University of Glasgow

García Blanco, Sonia (2003) *Electron-beam modification of silica for integrated optics.* PhD thesis.

http://theses.gla.ac.uk/5891/

Copyright and moral rights for this thesis are retained by the author

A copy can be downloaded for personal non-commercial research or study, without prior permission or charge

This thesis cannot be reproduced or quoted extensively from without first obtaining permission in writing from the Author

The content must not be changed in any way or sold commercially in any format or medium without the formal permission of the Author

When referring to this work, full bibliographic details including the author, title, awarding institution and date of the thesis must be given

Glasgow Theses Service
http://theses.gla.ac.uk/
theses@gla.ac.uk

Electron-beam Modification of Silica for Integrated Optics

Submitted for the degree of
Doctor of Philosophy
to the
Department of Electronics and Electrical Engineering, University of Glasgow

by
Sonia García Blanco
February 2003

© Sonia García Blanco, 2003

"To my parents and to Fraser
for all their love during the extent
of this work"

Abstract

Germanium-doped silica deposited by flame-hydrolysis deposition (FHD) is one of the materials most widely used for the fabrication of passive optical circuits for the telecommunication and bio-sensors industries. The development of novel fabrication techniques that reduce the number of processing steps while producing high-quality waveguides with tailored characteristics is desired. Electron-beam irradiation of silica increases the refractive index of the material, producing directly buried waveguides and leaving a flat wafer surface that allows easy integration with further processing steps.

The aim of this thesis is to characterise the physical processes involved in electron-beam irradiation of germanium doped FHD silica and the influence of the different material and irradiation parameters on the change of optical properties. The use of electron-beam irradiation is a convenient way of fabricating different kinds of communication and bio-sensing devices.

To that aim, the germanium-doped flame-hydrolysis silica employed was first characterized. A non-uniformity of the optical properties as a function of depth, was observed. In order to elucidate the origin of the graded-optical properties, compositional, structural and density analyses were carried out on the material. Once the properties of the initial material were known, the effects of electron-beam irradiation were studied. The electron-beam transfers energy to the material non-uniformly, which undergoes a structural rearrangement, which leads to change in the relative density and therefore, variation in the refractive index. The structural, density and refractive index changes were independently characterized and confirmed from theoretical calculations. Thermal annealing experiments were carried out in order to study the stability of the changes induced in the material and further information concerning the physical processes involved was found. Several waveguide devices were fabricated, exhibiting low-losses, thus confirming the suitability of the technique. Finally, the results obtained for electron-beam irradiation were compared with 2 MeV argon ion irradiation, finding that a common structural modification leading to the refractive index change mechanism must be present in both cases.

Acknowledgements

I would like to thank my supervisors, Prof. J.M. Cooper, Prof. J.S. Aitchison and Prof. R. De La Rue for their help and guidance during throughout this project and for their careful revision of this manuscript. I would like to thank also Prof. J.H. Davies for very useful discussions and helpful advice for the development and understanding of the densification theory.

To my FHD lab colleagues, Mr. Duncan Ross, Ms. Alison Cleary and Mr. Ian McNicholl I would like to express my thanks, for all the "hot" hours spent in the lab. Specially, I would like to thank Mr. Ian McNicholl for passing me all his large FHD experience and for all his help when something went wrong.

Dr. Andrew Glidle is acknowledged for his help and guidance in the material characterization techniques during our "non-sleeping" trips to Daresbury and Grenoble. His encouragement during those experiments is highly acknowledged, especially when he would allow me to go to bed while he would stay for the last measurement.

Dr. S. Thoms, Dr. D. McIntyre and all the technical staff from the Level 1 are acknowledged for their guidance in the use of the electron-beam writer and for helping me when I needed a "long" job. I would also like to acknowledge all the technical staff from the Level 6 cleanroom for all their help.

I would like to thank Dr. B. Poumellec and Ms. A.S. Jacqueline from the Université of Paris-Sud for fruitful discussions all along this work and for the warm welcoming during my visits to their lab. Dr. J.E.E. Baglin and Dr. A. Kellock are also acknowledged for their interesting, useful discussions and encouragement during the writing of this thesis and for performing the RBS analysis.

I would like to express my thanks to Dr. Daniel Ortega for his guidance during my first months of my PhD and for his friendship. I want also to express my gratitude to all the friends I made during these three years and "a bit" in Glasgow for all the good moments we spent together and their cheering during my writing up. I could not have made it without the support of all of them.

Finally, I would like to specially thank Fraser for being there with me during the good and not so good moments, always supporting and encouraging me. Fraser's family is specially thanked for putting me up during the last months of my PhD. I would like to express my gratitude to my family, who were always there, ready to listen to me and give me a warm word. Thank you!

List of publications

Journal papers:

[1] S. García-Blanco, A. Glidle, J.H. Davies, J.S. Aitchison, J.M. Cooper, Electron beam induced densification of Ge-doped flame hydrolysis silica for waveguide fabrication, Applied Physics Letters, 79, 18, 2889-2891, 2001.

[2] A-S. Jacqueline, S. García-Blanco, B. Poumellec, J.S. Aitchison, Dependence on Ge doping of specific volume change in silica induced by e-beam irradiation, accepted for publication in Journal of Non Crystalline Solids, 2003.

[3] S. García-Blanco, A.J. Kellock, J.E.E. Baglin, A. Glidle, J.M. Cooper, J.S. Aitchison, R.M. Delarue, Fabrication of optical waveguides by 2 MeV Ar+ irradiation of germanium-doped flame-hydrolysis deposited silica, accepted for publication in Nucl. Instrum. and Methods, May 2003.

Conference papers:

[1] S. García-Blanco, A. Kellock, J.E.E. Baglin, A. Glidle, J.M. Cooper, R.M. De La Rue, J.S. Aitchison, Ar^+ ion-implantation of Ge-doped flame hydrolysis deposited silica for the formation of optical waveguides, Proc. IBMM 2002 Conference, Kobe, Japan, 2002.

[2] A.S. Jacqueline, S. García-Blanco, B. Poumellec, J. S. Aitchison, Dependence on Ge doping of specific volume change in silica induced by electron beam irradiation, Proc. SiO_2 and Advance Dielectrics, Trento, Italy 16-18 September 2002.

[3] S. García-Blanco, J.S. Aitchison, J.M. Cooper, R.M. De La Rue, Low-loss controlled-birefringence waveguides fabricated by electron-beam irradiation of germanium doped FHD silica, Proc. IPRC 2002, Vancouver, Canada, 2002.

[4] S. García-Blanco, A. Glidle, J.M. Cooper, R.M. De La Rue, A.S. Jacqueline, B. Poumellec, J.S. Aitchison, Characterization of the densification induced by electron-beam irradiation of ge-doped silica for the fabrication of integrated optical circuits, Proc. of 2002-IEEE/LEOS Workshop on Fibre and Optical Passive Components, Glasgow, UK, 2002, 17-23.

[5] S. García-Blanco, A. Glidle, J.H. Davies, J.M. Cooper, J.S. Aitchison, Waveguide fabrication by electron beam modification of flame hydrolysis silica, Proc. OECC/IOOC 2001 Conference Incorporating ACOFT, Sydney, Australia, 2001, 35-36.

[6] S. García-Blanco, T.C. Kleckner, A. Glidle, J.H. Davies, J.S. Aitchison, J.M. Cooper, Fabrication of integrated optical circuits by electron beam modification of flame hydrolysis deposited silica, Proc. ECIO 2001, Padeborn, Germany, 2001, 121-124.

Electron-beam Modification of Silica for Integrated Optics

Abstract. i

Acknowledgements. ii

List of Publications. iii

Index iv

Chapter 1. Introduction. 1

Chapter 2. Material characterization techniques. 12

2.1. Introduction. 12

2.2. Fundamentals of the deposition of germanium-doped silica layers by Flame-Hydrolysis Deposition. 13

2.2.1. FHD setup description and deposition routine. 13

2.2.2. Preparation of substrates. 15

2.3. Compositional analysis. 16

2.3.1. X-Ray Photoelectron Spectroscopy (XPS). 16

2.3.1.1. Fundamentals of the technique. 16

2.3.1.2. Instrument for the collection of the XPS data. 20

2.3.1.3. Compositional quantitative analysis with XPS. 20

2.3.1.4. XPS analysis of the SiO_2/GeO_2 system. 21

2.3.1.5. Characterization of the germanium concentration depth profile. 24

2.3.2. Rutherford Backscattering Spectroscopy (RBS). 24

2.3.2.1. Fundamentals of the technique. 25

2.3.2.2. Instrument for the measurement of the RBS data. 29

2.3.2.3. Analysis of the RBS data. 29

2.4. Structural analysis. 30

2.4.1. Raman spectroscopy. 30

2.4.1.1. Basic principles. 30
2.4.1.2. Raman spectrum of the silica network. 32
2.4.1.3. Experimental instrument. 34
2.4.1.4. Qualitative analysis of the data. 35

2.4.2. X-ray Absorption Fine Structure (EXAFS). 36

2.4.2.1. EXAFS principle. 36
2.4.2.2. Structural information obtained from EXAFS analysis. 39
2.4.2.3. Different experimental configurations to collect the data. 39
2.4.2.4. Limitation factors in the analysis of EXAFS data. 41
2.4.2.5. Experimental details for the collection of data in this work. 42
2.4.2.6. Analysis of the data. 42

2.5. Density analysis. 44

2.5.1. X-ray reflectivity. 44

2.5.1.1. Fundamentals of the technique. 44
2.5.1.2. Experimental considerations. 47
2.5.1.3. Analysis of the experimental data. 50

2.5.2. Profilometry. 51

2.5.2.1. Atomic force microscopy. 51
2.5.2.2. Stylus profilometry (Talystep). 53

Chapter 3. Optical characterization techniques. 54

3.1. Introduction. 54

3.2. Experimental characterization of the refractive index profile. 55

3.2.2. Fundamentals of the m-line technique. 56
3.2.3. Description of the experimental setup used to measure the effective refractive index. 59
3.2.4. Fabrication of the in-coupling gratings. 60
3.2.5. Estimation of the measurement errors. 62

3.3. Theoretical analysis of the modes of propagation of a slab waveguide structure. 66

3.3.1. Propagation of light in a step-index slab guide. 67

3.3.1.1. Ray optics approach. 67

3.3.1.2. Electromagnetic approach. 70

3.3.1.3. The "cut-off" condition and the number of propagating modes supported by a slab waveguide. 72

3.3.2. Propagation of light in a graded-index medium. 73

3.3.2.1. Determination of the kind of refractive index profile from a n_{eff}^2 versus $(m+1)^2$ plot. 73

3.3.2.2. Ray optics approach. 74

3.3.2.3. The Wentzel-Kramers_Brillouin (WKB) method for solving the modes of a graded-index profile waveguide. 77

3.3.2.4. Reflectivity calculation method (RCM) for the calculation of the modes of propagation of an arbitrary refractive index profile structure. 78

3.3.3. Recovery of the refractive index profile of a slab waveguide from effective refractive index measurements. 83

3.3.3.1. Inverse-WKB method for the recovery of the refractive index profile from the measured effective refractive indices of the propagating modes. 83

3.3.3.2. Combination of the RCM method with a genetic algorithm for the recovery of the refractive index profile given by a stepwise approximation. 87

3.4. Aspects of analysis of 2-dimensional channel waveguides. 90

3.5. Characterization of the propagation losses of the electron-beam direct-written monomode waveguides by using a modified-Fabry-Perot technique. 92

Chapter 4. Characterization of as-deposited germanium-doped FHD layers. 97

4.1. Introduction. 97

4.2. Description of the $Ge:SiO_2$ layers. 99

4.3. Optical characterization of the as-deposited films. 100

4.3.1. Description of the samples. 100

4.3.2. Method for the refractive index characterization. 100

4.3.3. Relation of the refractive index with the composition and density of the material: Lorentz-Lorenz equations. 100

4.3.4. Measurement of the effective refractive indices of the propagating modes. 102

4.3.5. Calculation of the refractive index profile from the optical measurement of the propagating modes. 104

4.3.5.1. Step-wise approximation plus a complementary error function. Fitting with genetic algorithms. 106

4.3.5.2. *Inverse*-WKB method with asymmetry factor s. 109

4.3.6. Evolution of the n-profile for different $GeCl_4$ fluxes. 111

4.3.5. Influence of the sintering conditions on the n-profile. 112

4.3.6. Birefringence of the as-deposited layers. 113

4.4. Compositional analysis. 114

4.4.1. XPS study of the germanium depth profile. 114

4.4.1.1. Preparation of the samples. 114

4.4.1.2. Comparison of the profiles for FHD layers before and after sintering. 114

4.4.1.3. Germanium depth profile of the sintered $Ge:SiO_2$ FHD layers. 116

4.4.2. RBS analysis of FHD silica layers germanium depth profile. 117

4.4.2.1. Preparation of the samples. 117

4.4.2.2. Germanium depth profiling using RBS. 118

4.4.3. Effect of the sintering conditions on the germanium profile. 122

4.5. Structural analysis. 124

4.5.1. Confocal Raman spectroscopy. 124

4.5.1.1. Preparation of the samples. 124

4.5.1.2. Raman scattering spectroscopy of as-deposited $Ge:SiO_2$ FHD layers. 125

4.5.2. X-Ray Absorption Fine Structure (EXAFS) Analyses. 127

4.5.2.1. Preparation of the samples. 127

4.5.2.2. ReflEXAFS study of the germanium environment. 128

4.6. Density profile measurement by X-ray reflectivity. 136

4.6.1. Preparation of the samples. 136

4.6.2. Measurement of the density profile. 137

4.7. Conclusions. 139

Chapter 5. Study of the effects induced in the germanium-doped FHD silica layers by electron-beam irradiation. 141

5.1. Introduction. 141

5.2. Irradiation technique. 144

5.2.1. Preparation of the samples. 144

5.2.2. Method for the irradiation at 50 keV. 144

5.2.3. Irradiation technique using 10 keV electrons. 145

5.3. Interaction of the electron-beam with the material. 146

5.3.1. Sceleton: Monte-Carlo simulation of interaction of electrons with the material. 146

5.3.2. Calculation of the local volume energy density deposited by the electron-beam. 146

5.3.3. Local volume density of energy deposited by a 50 keV electron-beam. 148

5.3.4. Local volume density of energy deposited by a 15 keV electron-beam. 151

5.3.5. Evolution of the density of energy profile in depth with the energy of the incident electrons. 151

5.4. Structural changes after electron-beam irradiation of FHD silica layers. 153

5.4.1. Raman spectroscopy studies. 153

5.4.1.1. Introduction. 153

5.4.1.2. Sample preparation. 154

5.4.1.3. Raman study of the change in structure after irradiation. 154

5.4.2. ReflEXAFS studies of the change in structure around the germanium atoms upon electron-beam irradiation. 157

5.4.2.1. Preparation of the samples. 157

5.4.2.2. Variation of the local structure around the germanium after irradiation. 158

5.5. Densification induced by electron-beam irradiation on Ge-doped FHD silica layers. 163

5.5.1. Introduction. 163

5.5.2. Fundamentals of electron-beam densification of silica. 163

5.5.3. Elastic calculations to obtain the strains and stresses appearing

in the structure due to densification. 166

5.5.3.1. Elastic calculations for obtaining the permanent strain from the measurement of the total change in density. 166

5.5.3.2. Theoretical model based for the calculation of the permanent component of the densification. 169

5.5.4. Measurement of the densification by X-ray reflectometry. 171

5.5.4.1. Preparation of the samples. 171

5.5.4.2. Irradiation performed with a 10 keV electron-beam. 172

5.5.4.3. Irradiation performed with a 50 keV electron-beam. 173

5.5.5. Measurement of the densification by profilometry (Talystep). 174

5.5.5.1. Profile of densification in depth. 174

5.5.6. Evolution of the relative change in volume with the different irradiation and material parameters. 178

5.5.6.1. Dependence of the depression on the surface on the writing parameters. 178

5.5.6.2. Evolution of the depression on the surface with dose and germanium content. 179

5.5.6.3. Dependence of the depression in the surface on the energy of the electrons used. 181

5.5.6.4. Dependence on the structure of the initial silica layers. 182

5.6 Refractive index change induced in Ge-doped FHD silica by electron-beam irradiation. 187

5.6.1. Evolution of the effective refractive index of the different propagation modes with irradiation dose and germanium content. 187

5.6.2. Calculation of the refractive index change from the relative change in density. 189

5.6.2.1. Theoretical model. 189

5.6.2.2. Refractive index profile expected from density change measurement in Ge:SiO_2 FHD layers. 191

5.6.2.3. Analysis of the refractive index profile from the study of the modes of propagation. 193

5.6.2.4. Comparison of the refractive index profiles obtained from densification with the ones from optical measurements. 195

5.6.3. What happens with the birefringence. 199

5.7. Stability of the changes induced by irradiation: Isochronal annealing experiments. 203

5.7.1. Thermal annealing experiments of the refractive index. 204
5.7.2. Thermal recovery of the electron-beam induced densification. 208

5.8. Conclusions. 211

Chapter 6. Fabrication of integrated optical devices with electron-beam direct writing of germanium doped FHD silica. 213

6.1. Introduction. 213

6.2. Fabrication of multimode waveguides. 214

6.2.1. Fabrication method. 214
6.2.2. Characterization of multimode waveguides. 214

6.3. Fabrication of monomode waveguides: characterization of the propagation losses. 215

6.3.1. Fabrication of the waveguides. 215
6.3.2. Characterization of the monomode waveguides: study of the propagation loss. 216

6.4. Fabrication of Y-branches. 220

6.4.1. Preparation of the samples. 221
6.4.2. Beam propagation method (BPM) simulation of the Y-branch. 221
6.4.3. Experimental characterization of the Y-branches. 224

6.5. Conclusions. 225

Chapter 7. Other irradiation technique to fabricate optical waveguide on Ge:SiO_2 FHD: Ion implantation with 2 MeV Ar^+ ions. 226

7.1. Introduction. 226

7.2. Preparation of the samples. 227

7.3. Deposition of energy into the FHD silica after Ar^+ implantation. 228

7.4. Optical measurements after irradiation with 2 MeV Ar^+. 230

7.5. Measurement of the densification induced by 2 MeV Ar^+ irradiation. 233

7.5.1. X-ray reflectivity measurements of the change in density. 233

7.5.2. Measurement of the densification from height-step measuments. 233

7.6. Calculation of the change in refractive index expected from the change in density. 234

7.7. Isochronal annealing experiments. 237

7.8. Conclusions. 239

Chapter 8. Conclusions and suggestions for further work. 240

8.1. Conclusions. 240

8.2. Suggestions for further work. 242

References. 244

Appendix 1. A1-1

Appendix 2. A2-1

Chapter 1

Introduction

In 1851 John Tyndall, as part of a lecture demonstration at the Royal Institution, 'piped' light down a jet of water and prophesied that one day this phenomenon would prove useful in communications [Tyndall, 1851]. Much work had to be done in order to fulfill Tyndall's prophecy and, it was not until the early 1960's that the development of the laser provided the first stable source of coherent light for communication applications. In 1966, Kao and Hockman envisaged the application of a continuous glass fibre, of a kind that had been already employed for endoscopes, for telecommunications [Kao, 1966]. The development of fibres was pushed forward due to the high capacity for information transfer in comparison with the traditional electrical coaxial wires. Optical fibres offer other advantages, such as immunity from electromagnetic interference, freedom from electrical short circuits, security from monitoring, low price, reliability and ease of maintenance [Hunsperger, 1991]. It was not until the manufacturing processes for silica optical fibres produced propagation losses less than 2 $dB \cdot cm^{-1}$, in the middle 1970's [Gowar, 1983] that the real expansion of the optical communications occurred. Since then, the evolution toward higher capacity and higher speed systems has not stopped, and, at present, long haul transmission at 40 $Gb \cdot s^{-1}$ is becoming a reality [Chao, 2002], [Inada, 2002].

Fibre optic devices have the disadvantage of being bulky and not very robust. Integration of several functions onto a single substrate appeared as the logical direction to follow. The term Integrated Optics was first introduced in 1969 by Miller [Miller, 1969], who proposed a compact optical receiver by integrating guided wave optics, optical detection and amplification on a single substrate. This approach soon received interest from the scientific community due to the potential advantages of mass production, low cost, performance and reliability. The rapid advance of microfabrication

techniques and material developments in the semiconductor microelectronics industry made the development of optical integration techniques easier. Optical integrated circuits present a number of potential advantages such as increased bandwidth, expanded frequency division multiplexing, low-losses, smaller sizes, lower power consumption, batch fabrication economy, improved reliability and immunity to vibration [Hunsperger, 1991].

There are a number of different material systems that are relevant for the production of integrated optical circuits, such as polymers, glass (high silica, multicomponent silica glasses and chalcogenides), single ferroelectric crystals (such as $LiNbO_3$ and Li TaO_3) and semiconductors (such as silicon and different III-V compound semiconductors such as GaAs or InP). Different materials are chosen for different applications.

Silica is one of the most extensively used materials for the fabrication of passive integrated optical components [Soref, 1993], [Fardad, 1996], [Jalali, 1996], [Tang, 1996], [Jones, 1996], [Kawachi, 1990], [Kawachi, 1996]. Planar silica layers are normally deposited on silicon substrates, constituting what it is known as silica-on-silicon technology. The high degree of compatibility between silica-based devices and optical fibres in terms of modal characteristics and refractive index, which give low coupling losses and parasitic reflections, have made planar silica technology extensively used in the fabrication of planar lightwave circuits (PLC's). This technology is commercially available and a range of components released, such as arrayed-waveguide gratings (AWG's), NxN star couplers [Grant, 1994], NxN AWG multiplexers [Bretoiu, 2002], Mach-Zehnder interferometers, waveguide array routers (WGR's) and Bragg filters [Li, 1996], [Eldada, 2001].

Several techniques can be used to deposit silica layers: chemical vapor deposition (CVD) [Izawa, 1981], which has several variants, such as plasma-enhanced CVD (PECVD) [Grand, 1990] and low pressure CVD (LPCVD) [Henry, 1989], sol-gel deposition [Almeida, 1994], [Holmes, 1993], radio-frequency (RF) sputtering [Goell, 1985], electron-beam vapor deposition [Song,2002], thermal oxidation [Zelmon, 1983] and flame-hydrolysis deposition (FHD) [Kawachi, 1983]. Among these techniques, CVD and FHD are the most commonly used for the deposition of silica layers [Eldada, 2001]. FHD deposition was first used in 1942, when a patent was issued to Hyde [Hyde,

1942]. The technique was later developed to produce low-loss optical fibres and as an efficient technique for the deposition of titanium doped silica in planar format [Kawachi, 1983].

In the FHD silica deposition process, vapors of the glass precursors are fed to a H_2/O_2 flame where a hydrolysis/oxidation reaction produces glass particles, around 0.1 μm in diameter, which deposit on top of a silicon or silica substrate to form a porous white soot. This is then sintered in a furnace at high temperature (1350 °C) in an oxidizing atmosphere to produce a transparent bubble-free layer. This glass, when processed as an optical waveguide gives very low propagation losses. The refractive index of the layer can be controlled by varying the relative concentration of gases fed to the torch. Typical precursors used in the deposition of FHD layers are silicon tetrachloride ($SiCl_4$), germanium tetrachloride ($GeCl_4$), boron trichloride (BCl_3), phosphorus oxychloride ($POCl_3$) or titanium tetrachloride ($TiCl_4$). As well as controlling the refractive index of the material, the different dopants also reduce the melting point of the glasses, thus reducing the temperature of the sintering step [Marques, 2000]. This may be desirable when several different layers are to be integrated on the same substrate.

The technique most often used to define optical waveguides in silica is based upon standard photolithography followed by reactive ion etching (RIE). This latter technique often leads to considerable roughness in the waveguide walls, thus increasing the scattering loss [Eldada, 2001]. Different post-processing techniques can be used in order to reduce the waveguide walls roughness, but they imply further fabrication steps. Furthermore, the definition of optical waveguides by photolithography and dry-etch involves several fabrication steps, thus increasing the time and cost of the fabrication process.

Alternative techniques to produce optical waveguides in glass have been investigated, such as ion-exchange in soda-lime glasses [Stewart, 1979], diffusion, implantation and different types of ion-beam irradiation [Townsend, 1994]. These techniques can produce optical waveguides in a smaller number of fabrication steps and reduce the sidewall roughness.

Since the discovery of the UV-photosensitivity of silica by Hill *et. al.* [Hill, 1978] a large amount of work has been carried out to explore the possibility of fabricating integrated opticalwaveguides based on the UV sensitivity of silica. By exposing the sample to different sources of UV radiation (e.g. ArF laser at 193 nm wavelength [Takahashi, 1997], KrF laser at 248 nm [Nishii, 1995], [Tsai, 1997], [Nishii, 1999], [Shigemura, 1999], [Brambilla, 1999], XeCl laser (4.0 eV) [Hand, 1990], [Dong, 1995], [Nishii, 1995], [Hosono, 1996], [Dianov, 1997], [Douay, 1997], [Nishii, 1997], Xe_2 laser [Morimoto, 1999], excimer laser [Hosono, 1999a], [Hosono, 1999b], [Kuzuu, 1997], CW laser at 244 nm [Poumellec, 1996] or Ti:sapphire at 820 nm [Homoelle, 1999]) a refractive index change up to about 10^{-3} can be obtained. This change is large enough to allow the formation of optical waveguides.

The UV-photosensitivity of silica has mainly been used as a way of fabricating fibre Bragg gratings [Hill, 1993], [Meltz, 1989], [Xie, 1993], [Zhao, 1998], [Lee, 1999], [Liu, 1997] by means of a phase mask or a space optics interferometer, i.e. a Lloyd's mirror type of interferometer [Douay, 2000]. Such gratings have already found industrial applications. The next generation of applications of laser photosensitivity of silica will be in the field of planar lightwave circuits. The direct writing of optical circuits by focusing an intense laser light has been investigated [Maxwell, 1993], [Maxwell, 1995], [Monro, 1996], [Monro, 1998], [Monro, 1999], [Svalgaard, 1997], [Zauner, 1998b]. Other applications involve laser trimming of phase errors in array waveguide gratings (AWG's) [Zauner, 1998a], [Takada, 2000], laser fabrication of bandpass filters [Kashyap, 1993], [Albert, 1999] and laser-induced birefringence control [Canning, 2000a], [Chen, 2002].

The mechanisms responsible for the refractive index change through photosensitivity are not yet completely understood and much work has been done in the last few years in this area. It seems that the photosensitivity effect may be due to the presence of oxygen deficient centres, that absorb light in the UV region, forming "E'-centres" that are responsible, through the Kramers-Krönig relations, for the changes in refractive index observable in the visible and near infra-red [Nishii, 1996]. Other phenomena, such as densification and changes in polarizability, are also found after UV-irradiation of silica and they too play an important role in the change in refractive index via the Lorentz-Lorenz equations [Schenker, 1997].

Different deposition techniques with different dopant composition, will produce silica with different photosensitivity [Canning, 2000b]. The different post-processing of the substrates also plays an important role in determining the photosensitivity of the material [Canning, 2000b]. Much work is still being carried out in order to find the best way of fabricating photosensitive silica glass [Ferraris, 2000]. In this area, germanium has been found to increase the photosensitivity of silica glass through the reduction of the electronic band-gap of the material [Nishii, 1995].

The formation of colour centres in different silicas and in germanium doped silica has been the subject of many studies. The formation of defects in the structure upon UV-irradiation is produced in two different ways [Hanafusa, 1985], [Hand, 1990], [Simmons, 1991], [Hosono, 1992], [Tsai, 1993], [Nishii, 1995], [Nishii, 1996], [Hosono, 1996], [Poumellec, 1996], [Taunay, 1997], [Takahashi, 1997], [Nishii, 1999], [Shigemura, 1999], [Heaney, 1999], [Grubsky, 1999]. Firstly, colour centres can be formed by using the oxygen deficient centres (Ge-Ge, Ge-Si and Si-Si) present in the structure; and secondly, by forming defects by changing the configuration of germania or silica tetrahedra that constitute the basic silica network. The bonds involved in the oxygen deficient centres are weaker than the basic silica network tetrahedra and, therefore the presence of that kind of defect increases the sensitivity to UV-irradiation. The number of oxygen deficient centres depends on the deposition parameters for the original glass structure.

These defect groups introduce excess losses in the UV region of the spectrum. The Kramers-Krönig relations can be used to calculate the refractive index, Δn, change due to colour centres formation [Leconte, 1997], [Poumellec, 1996], [Takahashi, 1997], [Bernardin, 1990], [Dong, 1995], [Douay, 1997], [Nishii, 1996], [Hand, 1990]:

$$\Delta n^{KK} = \frac{1}{2\pi^2} \int_{\lambda_1}^{\lambda_2} \frac{\Delta\alpha}{1-\left(\frac{\lambda}{\lambda'}\right)^2} d\lambda \qquad (1.1)$$

where Δn^{KK} is the refractive index change calculated through the Kramers-Krönig relations, λ' at which the refractive index change is evaluated, $[\lambda_1, \lambda_2]$ is the spectral

range contributing significantly to Δn, normally between 190- and 800 nm and $\Delta\alpha$ is the excess loss in the UV region.

This relationship alone cannot explain the entire variation in refractive index induced in the sample by the radiation. The change in volume and internal strain due to structural changes in the silica are also responsible for a large amount of the change in refractive index. The influence of the densification process on the refractive index change has been subjected to various studies [Douay, 1997], [Schenker, 1997], [Poumellec, 1996], [Niay, 1999], [Nishii, 1996], [Bernardin, 1990], [Primak, 1968]. Densification of the material is also known to induce stresses and strains in the structure that modify its polarisability.

The changes in volume and in the polarisability of the material are related to the refractive index change by means of the Lorentz-Lorenz relation [Poumellec, 1996]. The strains that appear in the material following densification also contribute to the change in refractive index through the photo-elastic effect [Poumellec, 2002]. Recent studies have shown that for high germanium concentrations [Nishii, 1997] and for high fluences [Canning, 2000b], a dilation of the material is produced instead of a compaction, leading to a reduction in the refractive index.

The change in refractive index achieved after UV irradiation of pure silica or germanium-doped silica is usually very small, $\Delta n<10^{-3}$. For the fabrication of waveguide-based integrated-optical circuits, a higher change in refractive index is required. Different post-deposition techniques have therefore been used in order to increase the sensitivity of the silica.

A large amount of work is being carried out to find adequate dopants in order to further increase the photosensitivity of the silica [Ferrari, 2000]. In that direction, co-dopant ions such as nitrogen [Dianov, 1997], tin [Dong, 1995], rare earth ions (Ce^{3+}) [Selvarajan, 2001] and silver [Montero, 1999] have all been explored. Some of these ions enhance the photosensitivity by a large amount but normally at the cost of increased propagation losses.

A further technique that has been used to increase the UV-sensitivity of the silica is flame-brushing. This procedure [Bilodeau, 1993], [Ferraris, 2000] consists of heating

the sample with a hydrogen-rich flame at 1700°C. At this elevated temperature, H_2 diffuses very quickly in the silica, making it locally photosensitive. The main disadvantage of this process is the possible weakening of the material.

Hydrogen loading has been used extensively as a technique for the increase of sensitivity of fibres and planar silica samples before UV-writing. This process [Fokine, 2000], [Tsai, 1997], [Heaney, 1999], [Grubsky, 1999], [McLaughin, 1998] consists of introducing the sample into a high pressure (20-800 atm) hydrogen rich atmosphere at high (500 °C) or low (20-75 °C) temperatures. The H_2 diffuses into the glass structure, increasing the sensitivity to the irradiation as the hydrogen reacts under the radiation and increases the formation of Ge-E' centres. The hydrogen is also thought to stabilize the Ge-E' centres.

Samples loaded at low temperature have to be stored at low temperature to avoid out-diffusion of the hydrogen, whilst those loaded at high temperature suffer a permanent change in the refractive index, due to the formation of stable bonding of hydrogen with the glass.

The main problem with this technique is the formation of OH- radicals, which increases the losses in the optical communications band (800-1600 nm wavelength) [Keiser, 2000]. This problem can be overcome by replacing the hydrogen by deuterium [Færch, 2002], but in this case the problem that arises is the large increase in the cost of the process. Other drawbacks of this technique are the short lifetime and poor long-term stability of the loaded-silica [Erdogan, 1994], which are especially important in planar circuits, due to the rapid hydrogen out-diffusion through thin cladding layers. The stability of the photosensitivity enhancement by hydrogen loading can be locked by irradiating the hydrogen-soaked PLC with 248 nm KrF laser light [Åslund, 1999], [Åslund, 2000].

Other techniques used to increase the sensitivity of the silica to UV-irradiation involve pre-irradiation either with different laser wavelengths or with other particles such as protons. The pre-irradiation creates absorption bands in the material that enhance the effect of the UV-irradiation. The photosensitivity of the samples can be increased by irradiating the material with a high-intensity CO_2 laser [Brambilla, 1999]. This procedure increases the concentration of oxygen deficient centres in the material by thermal

effects, thus increasing the photosensitivity. Pre-irradiation of a sample heated at 800 °C with >1×10^{17} cm^{-2} 300 KeV protons produces an absorption band at 240 nm due to Ge-Ge or Si-Ge bonds that, after UV-irradiation, will produce the colour centres responsible for the change in refractive index [Kyle, 1995]. Nevertheless, proton implantation at room temperature does not produce any change in the photosensitivity of the silica.

Chen *et al.* [Chen, 2000] extended the UV-sensitivity for silica to the shorter 157 nm wavelength of an excimer F_2-laser which involves a single photon absorption mechanism. This arises due to the fact that the 7.9 eV energy of the F_2-laser photons exceeds the typically 7.1 eV bandgap of a 5 mol % GeO_2 germanosilicate glass [Nishii, 1995], increasing the efficiency of the irradiation. A refractive index change as high as 5.4×10^{-3} has been reported by Chen et al [Chen, 2003] for a 3 mol % GeO_2 sample without hydrogen loading.

Electron-beam irradiation was first reported as a technique for the direct-writing of optical waveguides in silica in 1976 by Houghton *et al.* [Houghton, 1976]. They reported a change of 0.4% in the refractive index for pure silica irradiated with 16 keV electrons. Since then, different optical devices have been written in different kinds of pure-silica by electron-beam direct-writing technique, such as waveguides [Bell, 1991], [Madden, 1990], [Barbier, 1991], [Lewandowski, 1994], [Lewandowski, 1991], [Syms, 1994a], [Syms, 1994b], Y-branches and directional couplers [Syms, 1995] and thermooptic interferometric switches [Syahriar, 1998]. Among the advantages of electron-beam direct-writing, in comparison with its counterpart of UV-direct-writing, are the production of a refractive index change large enough for the fabrication of optical waveguide devices without the need for any pre-sensitization techniques. This reduces time consuming fabrication steps and decreases the losses of the material that can be produced due to the introduction of dopants. Furthermore, electron-beam direct-writing allows the independent controllability of the depth and refractive index difference of the written waveguides by the control of the electron energy [Everhart, 1971] and dose of the electrons used [Barbier, 1991]. Nevertheless the electron-beam writing of optical circuits is still intrinsically a slow process, thereby limiting the size of the devices that can be direct-written.

Other effects, such as non-linear optical properties, have been reported to be induced in silica glass upon electron-beam irradiation of different kinds of silica [Nakanishi, 1999], with the added advantage of easy fabrication of device patterns with high spatial resolution such as periodically poled structures for nonlinear optical gratings.

The mechanisms involved in the change in refractive index due to electron-beam irradiation have been reported to be similar to those responsible for the increase of refractive index by UV irradiation, i.e. the formation of colour centres [Spaargaren, 2000], the densification and change of the polarizability of the structure [Primak, 1968], [Dellin, 1977], [Barbier, 1991], [Lewandowski, 1991],

Germanium was found to increase the sensitivity of the silica under UV-irradiation [Nishii, 1995]. The influence of germanium content in the silica on electron-beam irradiation have not yet been fully addressed. In particular, germanium-doped silica deposited by flame-hydrolysis is one of the most widely used materials in planar silica technology, and as mentioned before, exhibits very low losses [Kominato, 1990]. It is therefore of considerable interest to study the effects produced in this material by irradiation with an electron-beam and to thereby control the quality of the waveguides formed. The advantages of this technique for the fabrication of integrated optical circuits are numerous and include the direct formation of waveguides embedded in the silica matrix, leaving a very flat surface suitable for further integration steps. As a consequence of the mechanism by which the electrons deposit their energy in the material, very smooth sidewalls can be expected, thus reducing the scattering losses due to sidewall roughness. The circuits fabricated by this technique can also have applications in the telecommunications industry as well as in the optical sensor market.

In this thesis, the effects of electron-beam irradiation of germanium-doped flame-hydrolysis silica have been studied and the quality of the waveguides fabricated using this technique have been assessed. To that end, the optical, compositional and structural properties of the germanium-doped flame-hydrolysis layers used in this work were firstly analyzed so as to address the modifications induced in these properties by irradiation with an electron-beam.

Chapter 2 and 3 summarize the material and optical characterization techniques used throughout this work. Chapter 2, in particular, describes the fundamentals of the techniques used in the compositional (X-ray photoelectron spectroscopy and Rutherford backscattering spectrometry), structural (Raman spectroscopy and X-ray absorption fine structure) and density (X-ray reflectivity) characterization techniques used in Chapters 4 and 5.

Chapter 3 summarizes the technique employed in this work to characterize the refractive index profile, the m-line technique. The modal analysis of step and graded index slab waveguides are also addressed theoretically and two techniques for the recovery of the refractive index profile from the measurement of the effective refractive index of the propagating modes, the inverse-WKB technique and the reflectivity calculation method (RCM), together with a optimization algorithm, are described. Some theoretical considerations concerning the study of channel waveguides are presented and the measurement of the propagation losses in monomode channel waveguides are described.

Chapters 4 and 5 describe the results of the analysis of the germanium-doped flame hydrolysis silica slab waveguides. In Chapter 4, the layers are studied before irradiation. The refractive index profile of these layers was investigated and related to the compositional and density profiles. The structure of the as-deposited layer is also studied in this chapter.

In Chapter 5, the change in refractive index due to electron-beam irradiation of the as-deposited films was addressed. In order to understand the main contributions to the change in refractive index, the structure after irradiation and the densification produced due to the electron-beam were analysed and related to the change in refractive index.

Chapter 6 demonstrates that, from the results of Chapters 4 and 5, optical waveguide based circuits can be directly-written in germanium-doped flame-hydrolysis silica. The losses obtained in monomode waveguides were characterized and asymmetrical Y-branches were fabricated and characterized, obtaining good agreement between theory and experiment.

Chapter 7 studies the irradiation of germanium-doped FHD layers by a different technique, irradiation with 2 MeV argon ions. The results obtained with these techniques were compared with the effects of electron-beam irradiation.

Finally, Chapter 8 summarizes the conclusions from this work and presents ideas for further investigation.

Chapter 2

Material characterization techniques

Chapter summary.

The present chapter intends to introduce the basics of the different material characterization techniques used throughout this thesis. The methods are classified into compositional analysis methods (X-ray photoelectron spectroscopy (XPS) and Rutherford Backscattering Spectroscopy (RBS)), structural analysis methods (Raman spectroscopy and X-ray Absorption Fine Structure (EXAFS)) and density analysis (X-ray reflectivity and surface profilometry).

2.1 Introduction.

It is anticipated that the optical and propagation characteristics of electron-beam direct-written waveguides are influenced by the material composition and physical properties, such as the density of the material and the bonding of the structure. Electron-beam irradiation of Ge-doped flame hydrolysis deposited (FHD) silica layers is expected to alter the structure of the as-deposited material. The optical characteristics of the as-deposited layers are controlled by the concentration of dopants, in this case germanium, that have been introduced in the material. Therefore, the analysis of the composition and structure of the flame-hydrolysis layers before and after irradiation with an electron-beam is needed to understand both the optical properties and the changes in these properties after irradiation.

The FHD layers used throughout this work were deposited by the author in the flame-hydrolysis deposition facility of the Department of Electronics and Electrical Engineering of the University of Glasgow. A complete description and operation of the system can be found in previous PhD theses [Maxwell, 1990], [Barbarossa, 1992], [Bebbington, 1993], [Bonar, 1995], [McLaughlin, 1998], [Marques, 2000], [Ruano, 2000]. Therefore, only a brief introduction to the technique will be presented in this work. Nevertheless, the recipes used for the deposition of the different samples used in this work will be specified as required.

This Chapter begins with a brief description of the flame-hydrolysis deposition technique used to deposit the germanium-doped silica layers. Next, the techniques used for compositional characterisation, X-ray photoelectron spectroscopy (XPS) and Rutherford Backscattering Spectroscopy (RBS), are briefly described. These techniques allow the measurement of the depth profile of the germanium composition.

A brief summary of the techniques used in this work for the structural characterization of the FHD layers is then presented. In particular, Raman spectroscopy and X-ray Absorption Fine Structure (EXAFS) have been used.

Finally, the techniques used to characterize the densification induced by the electron-beam, surface profilometry using Atomic Force Microscopy (AFM) or a Talystep stylus profilometer and grazing angle X-ray reflectivity, are presented. From measurements of the depression of the surface, simple elastic calculations were performed in order to obtain the extent of densification in the bulk of the material. An independent measurement performed by X-ray reflectivity has also been carried out in order to check the validity of the surface profilometry analysis described. Thus, in this chapter, the fundamentals of X-ray Reflectivity are also highlighted.

2.2 Fundamentals of the deposition of germanium-doped silica layers by Flame-Hydrolysis Deposition.

Flame-hydrolysis deposition, together with the plasma enhanced chemical vapor deposition (PECVD) technique, are the most widely used techniques for the deposition of silica layers for the telecommunications industry. In the Department of Electronics and Electrical Engineering of the University of Glasgow, the FHD facility has been used for many years [Maxwell, 1990], [Barbarossa, 1992], [Bebbington, 1993], [Bonar, 1995], [McLaughlin, 1998], [Marques, 2000], [Ruano, 2000].

2.2.1 FHD system set-up description and deposition routine.

The basic set-up used in this work for the deposition of silica layers by FHD is shown in Figure 2.1 (a). A zero-grade nitrogen flux is passed through "bubblers" where different precursors for the deposition of the glass are contained. These

bubblers are kept at a fixed temperature, 20 °C, in order to maintain a constant vapor pressure. The bubblers are contained in a sealed perspex box, which is permanently purged with a nitrogen flux and the temperature maintained at 23 °C in order to avoid condensation and hydrolysis in the pipes.

(a)

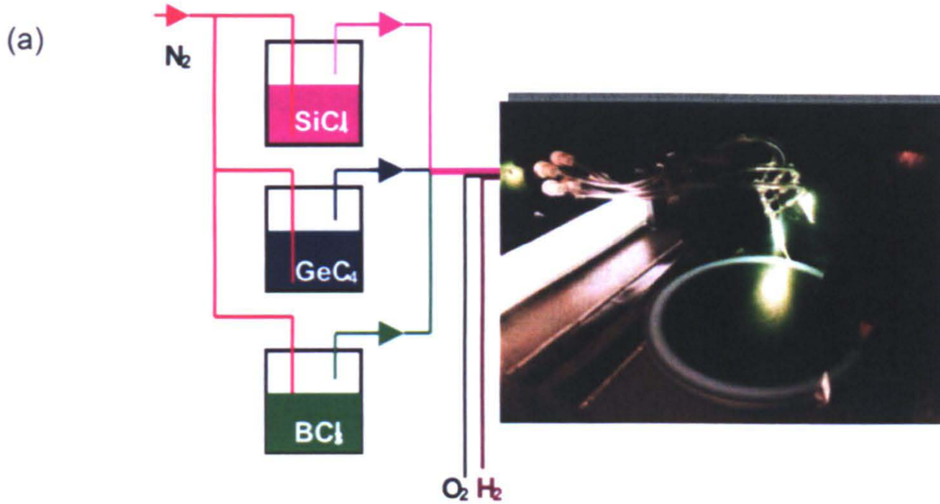

(b)

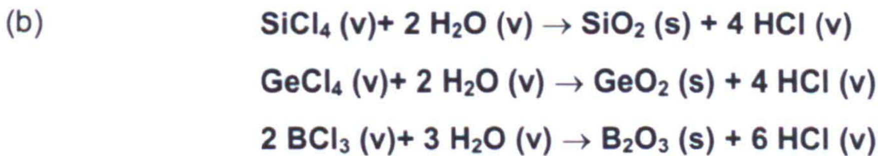

$$SiCl_4\,(v) + 2\,H_2O\,(v) \rightarrow SiO_2\,(s) + 4\,HCl\,(v)$$

$$GeCl_4\,(v) + 2\,H_2O\,(v) \rightarrow GeO_2\,(s) + 4\,HCl\,(v)$$

$$2\,BCl_3\,(v) + 3\,H_2O\,(v) \rightarrow B_2O_3\,(s) + 6\,HCl\,(v)$$

Figure 2.1. (a) Schematic of the FHD system: A nitrogen flux is passed through the bubblers containing the halides of the different glass constituents, carrying their vapour to a H_2/O_2 torch; (b) reactions occurring in the torch. They produce the oxide particles that constitute the glass.

The rate flow of nitrogen, carrying the vapours of the halides can be varied and it is measured by different mass flow controllers (after passing through the bubblers). Depending on the flux of halides to the torch, different amounts of dopant are introduced into the deposited silica layers. The amount of vapour from the halide carried in the nitrogen flux is directly related to the flux of nitrogen. The vapours of the halides are carried to the torch through polytetrafluoroethylene (PTFE) pipes. Hydrogen and oxygen are also carried to the torch, their flux also being controlled by a mass flow controller.

The substrates on which the FHD silica layers are deposited are placed in a silicon carbide turntable, inside the deposition chamber (Figure 2.1 (a)). The reactions shown in Figure 2.1 (b) take place in the flame and particles of SiO_2, GeO_2

and B_2O_3 form a low-density white soot on top of the substrates. A heater underneath the turntable keeps its temperature constant (≈ 140 °C) throughout the deposition process.

As a consequence of the reactions occurring in the flame, HCl is produced. Consequently, a centrifugal fan is connected to the chamber in order to extract the HCl gases and carry them to a scrubber unit, in which they are neutralized by making them pass through highly pressurised water. The scrubber unit is emptied and refilled after each deposition.

After the deposition of the soot, the samples are subjected to a high-temperature sintering step in a vertical furnace. Different times and atmospheres are used for different compositions of soot. For germanium-doped FHD silica layers (Ge:SiO_2 FHD); a 2 h sintering at 1350 °C in an oxygen and helium atmosphere (0.5 $l \cdot min^{-1}$ and 100 $cm^3 \cdot min^{-1}$ fluxes respectively) was the standard recipie. After this sintering step, high optical quality germanium-doped silica layers are formed and are ready for further processing and characterization.

2.2.2 Preparation of the substrates.

Ge:SiO_2 FHD layers were deposited on different substrates: bare silicon, silicon with a 15 μm thermal oxide and quartz substrates. Only substrates that can withstand the 1350 °C sintering step can be utilised. It is important to note here that the substrates used for the deposition need to be carefully cleaned in order to produce a defect-less silica layer. Normally, a standard clean in Opticlear, acetone and methanol, followed by a standard acid clean in sulphuric acid and peroxide mixture at 80 °C is sufficient. For the bare silicon substrates, a special cleaning in a NH_4OH:H_2O_2:D.I. water 1:1:5 solution for 15 min followed by rinsing in D.I. water needed to be done after the standard acid clean step.

The exact recipes used along the present work for the deposition of the different layers will be detailed when appropriate. The refractive index of the material can be controlled by varying the germanium content in the glass [Gowar, 1983].

2.3 Compositional analysis.

2.3.1 X-Ray Photoelectron Spectroscopy (XPS).

X-ray photoelectron spectroscopy (XPS), also known as ESCA (Electron Spectroscopy for Chemical Analysis), is a powerful technique used for the surface analysis of materials [Vickerman, 1997], [Walls, 1989], [Carlson, 1975], [Briggs, 1990]. Qualitative and quantitative elemental analysis can be performed on the structure (apart from H and He) with detection limits in the range 0.1-1 % at. Information on the chemical environment of the different elements can also be obtained.

In the next section, a brief summary of the technique and its applications to the analysis of the composition of germanium-doped FHD silica samples are given.

2.3.1.1 Fundamentals of the technique.

An XPS experiment consists of irradiating a sample with monochromatic X-rays and measuring electrons that are subsequently ejected. The X-rays photons have sufficient energy to excite some of the electrons in the sample so that they can escape from the surface as "photoelectrons" (Figure 2.2). The emitted photoelectrons are subsequently instrumentally separated by their energy and counted by the detector. The energy of the photoelectrons is characteristic of the atomic and molecular environment from which they originated whilst the number of photoelectrons emitted is proportional to the amount in the X-ray irradiated material.

When an X-ray photon impinges upon an atom, it may transfer all its energy to the electrons of the core-level of the atom. If the energy of the incident X-ray photon is large enough, the electron has enough energy to be emitted from the atom and become a "photoelectron". The kinetic energy of the photoelectron leaving the atom is given by

$$E_K = h\upsilon - E_B - E_W \quad (2.1)$$

where $h\upsilon$ is the energy of the X-ray source, E_k is the kinetic energy of the detected photoelectron, E_B is the binding energy of the core electron and E_W is the work function of the spectrometer (Figure 2.2 (b)).

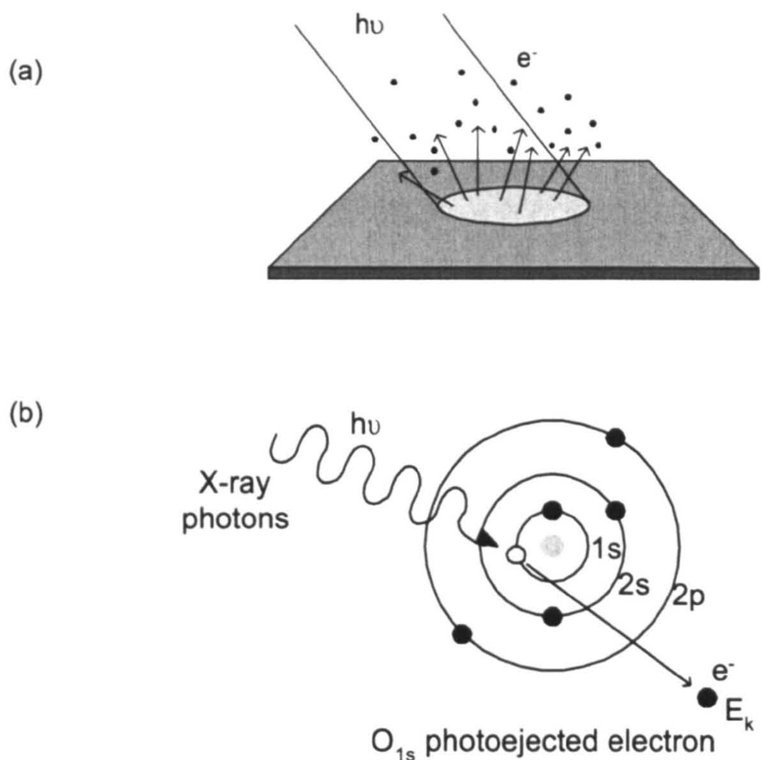

Figure 2.2. XPS principle: (a) Representation of the principle of XPS: photons of energy hυ are incident on the sample producing the emission of photoelectrons; (b) Orbital representation of the same principle for the case of the emission of an O_{1s} electron.

After the photoelectron leaves the atom, it has to escape from the surface of the sample by overcoming the specimen work function and arrive at the detector without loss of energy, in order to contribute to the measured photoemission peak characteristic of that orbital. This condition is only satisfied by the electrons escaping from the outer 10 nm of sample [Vickerman, 1997]. Although the penetration of the X-rays in the material is much larger than 10 nm, photoelectrons emitted at a greater depth will suffer loss of energy due to interaction with the matter. Even if they still have enough kinetic energy to arrive to the detector, they will not contribute to the photoemission peak but to the background peak at a lower energy (Figure 2.3). This is the reason why XPS is described as a strictly surface analytical technique.

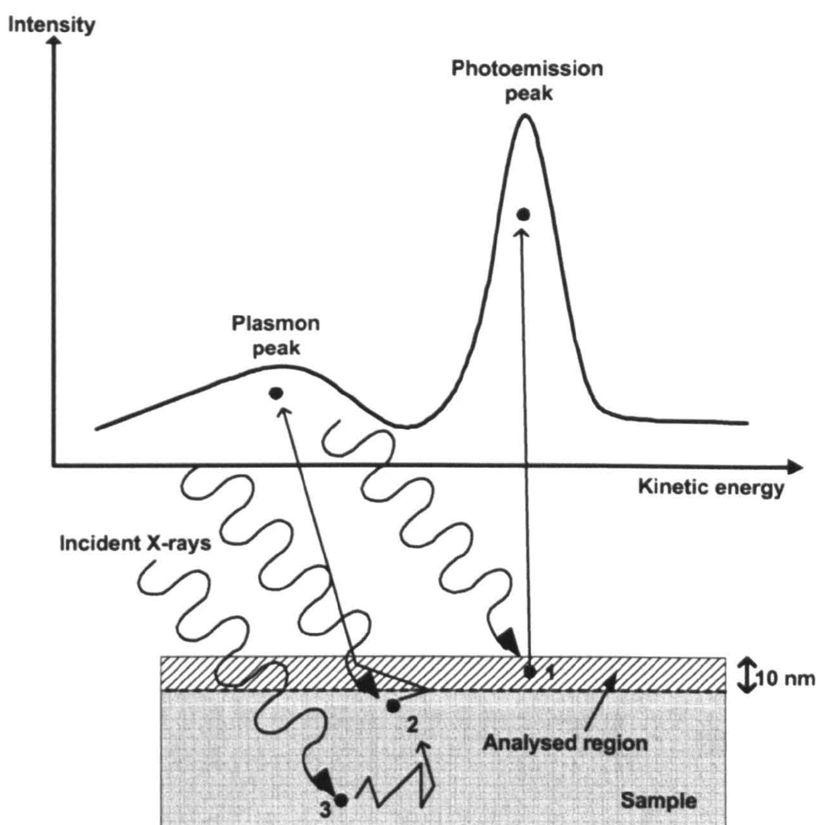

Figure 2.3. XPS emission peak and plasmon peak: After excitation, Electron-1 leaves the sample without loss of energy in scattering events, contributing to the emission peak. Electron-2 loses some energy in inelastic events before reaching the detector, contributing to the background "plasmon" peak. Finally, electron-3 loses all its kinetic energy before leaving the sample [Vickerman, 1997].

The detector has to be calibrated in order to be able to obtain the binding energies from the measurement of the kinetic energies of the photoelectrons emitted. After counting the number of electrons reaching the detector for each binding energy in the measurement energy range, a spectrum is obtained, in which each peak corresponds to a different core level of the different atoms present in the material (Figure 2.4). Since the binding energies for a particular element fall within a narrow range, the different elements can be uniquely identified.

If the sample being analyzed is an insulator, it will become positively charged due to the loss of electrons, producing a distortion in the photoemission peak shape. Thus, for a quantitative analysis, the loss of electrons needs to be compensated by flooding the sample with a mono-energetic source of low-energy (<20 eV) electrons from a nearby thermal source, called a flood-gun.

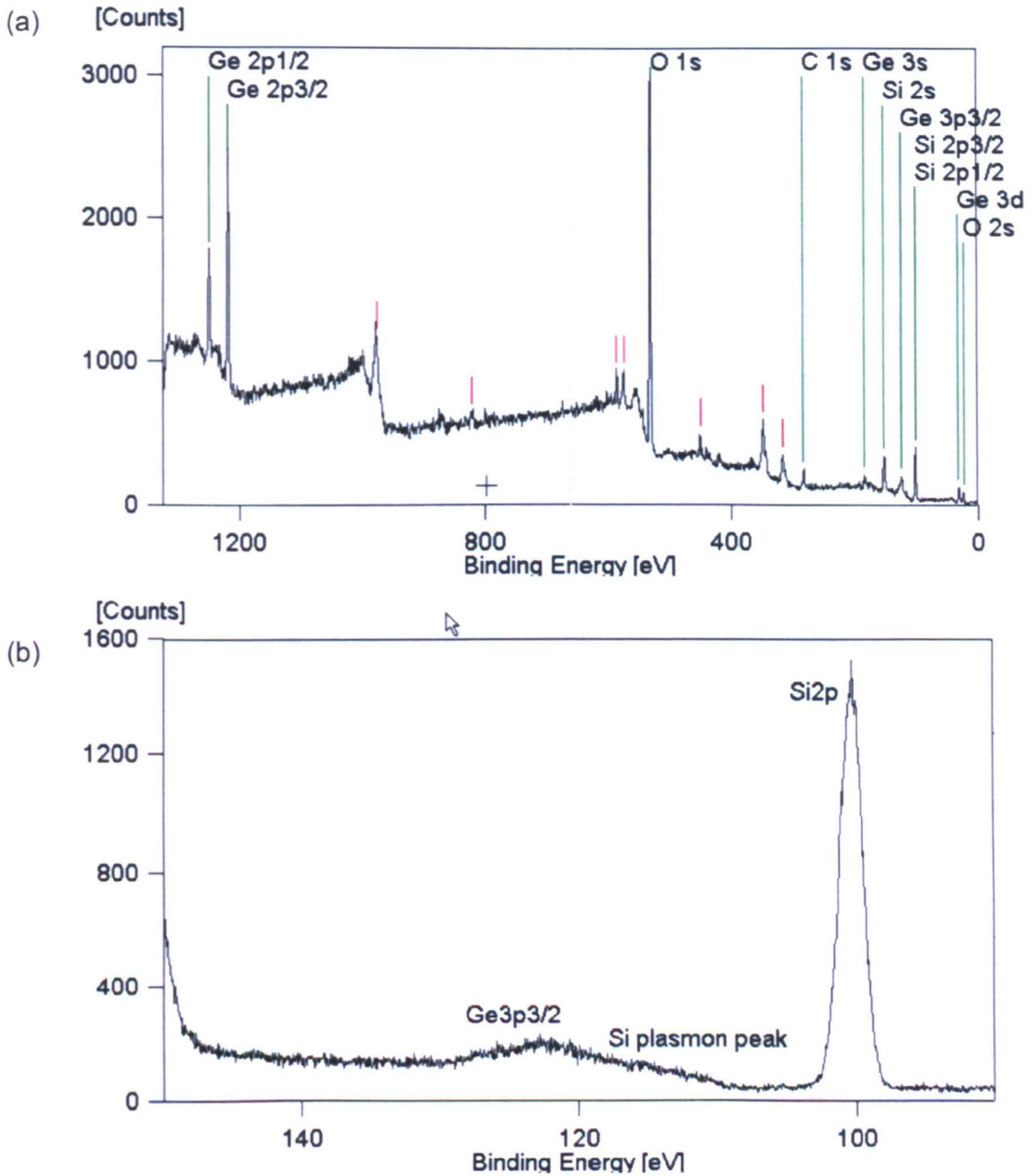

Figure 2.4. Ge-doped FHD silica XPS spectrum: (a) Scan spectrum after 10 min wet etch in buffered 4:1 HF; (b) Scan of the region corresponding to the Si2p peak.

The atoms of the different elements in the solid are not isolated, but bound together. Even though the electrons involved in a chemical bond are not the core-level electrons but the valence electrons, the latter will affect the value of the binding energies of the former, varying slightly the binding energies. The shift of binding energies is called the “chemical shift” and involves a shift in the position of the

measured peaks in the XPS spectrum, thus providing an indication of the chemical environment.

2.3.1.2 Instrument for the collection of the XPS data.

The experiments carried out in the present work were performed in RUSTI, at CLRC Daresbury Laboratory (Warrington, UK). The spectrometer used was an ESCA300 photoelectron spectrometer, which can be seen in Figure 2.5.

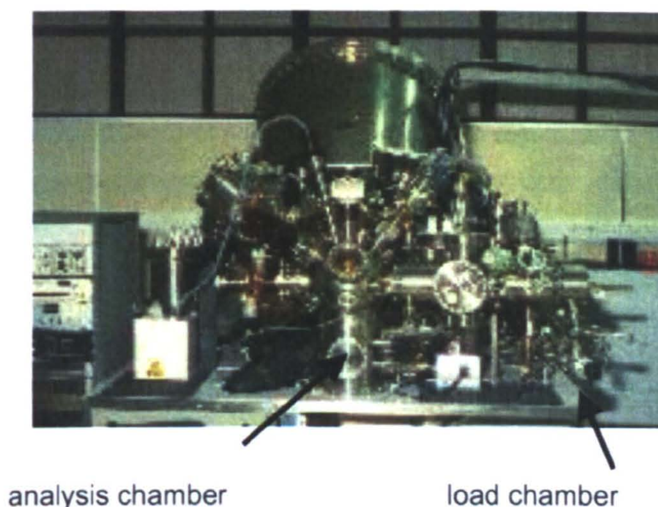

analysis chamber load chamber

Figure 2.5. XPS analysis intrument: ESCA300 machine in RUSTI at Daresbury Laboratories.

The incident X-ray energy is 1486.7 eV (Al $K\alpha$ line) sampling an area of 6 mm × 0.5 mm of sample. As the FHD silica samples studied in this work are insulators, flood-gun electrons at 3 eV were used. The measurements were performed placing the samples in the analysis chamber at an angle of 45° with respect to the incident X-ray beam.

2.3.1.3 Compositional quantitative analysis with XPS.

As mentioned above, the number of counts in a certain photoemission peak is proportional to the number of atoms of the corresponding element present in the sample. The steps for the quantitative compositional analysis of the specimen are:

1. Identification of the peaks corresponding to the different elements by comparing with the tabulated [Crist, 1999] information.

2. Background subtraction of counts due to emission of low keV electrons from other orbitals: the background subtraction proposed by Shirley [Shirley, 1972] has been used in this work.

3. Integration of the number of counts under the peak. This will give the number of counts corresponding to that orbital. Both the background subtraction and the integration of the area under the peaks are performed with the help of the Scienta analysis software.

4. The number of atoms of each element can be calculated as counts/sensitivity.

The empirical sensitivity factor is a function of both the element orbital and the XPS instrument. Thus, whilst the sensitivity factor for silicon and oxygen had already been determined for the ESCA300 machine, it was necessary to measure a standard (Ge_2N_3) to determine the sensitivity factor of the germanium orbitals.

2.3.1.4 XPS analysis of the SiO_2/GeO_2 system.

In the study of flame-hydrolysis deposited silica samples, the elements of interest are silicon, germanium and oxygen. Even when boron chloride was also introduced in the flame during the deposition process, the presence of boron was not observed in any of the spectra taken, suggesting its evaporation at some point during the deposition of the soot (in the flame) or sintering steps.

An example of a typical XPS spectrum for a Ge-doped FHD sample is shown in Figure 2.4 (a), in which the different peaks are indicated. The regions used for the quantitative compositional analysis are indicated in Table 2.1 and an example of each region is shown in Figure 2.4 (b) and Figure 2.6.

Region	Energy window /eV
Si2p	90-110
Ge3d	10-50
O1s	520-540

Table 2.1. Regions for the different elements present in the flame hydrolysis deposited samples.

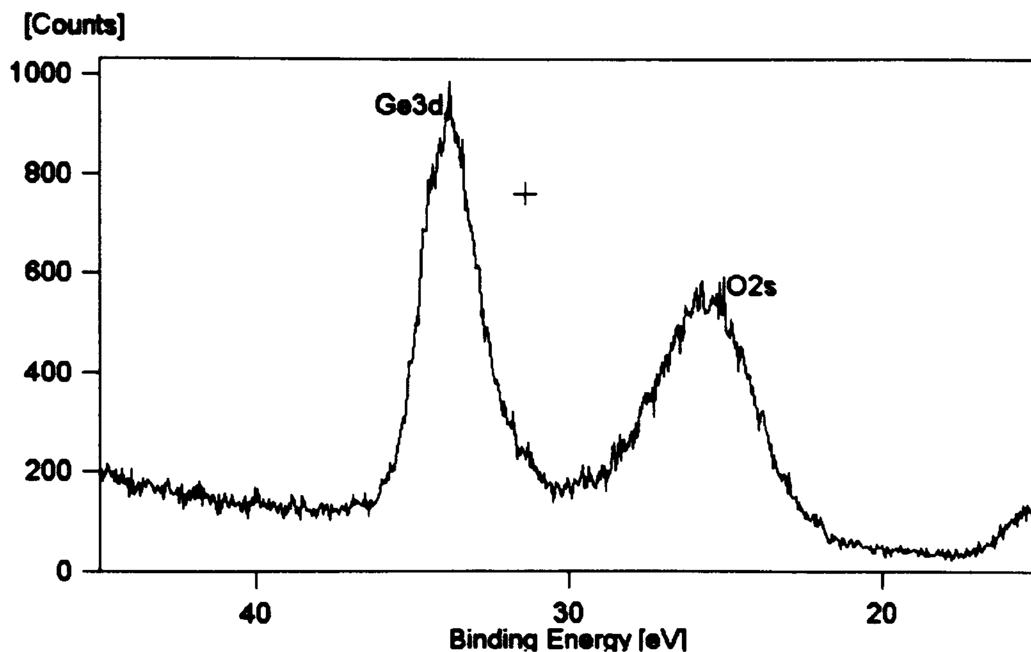

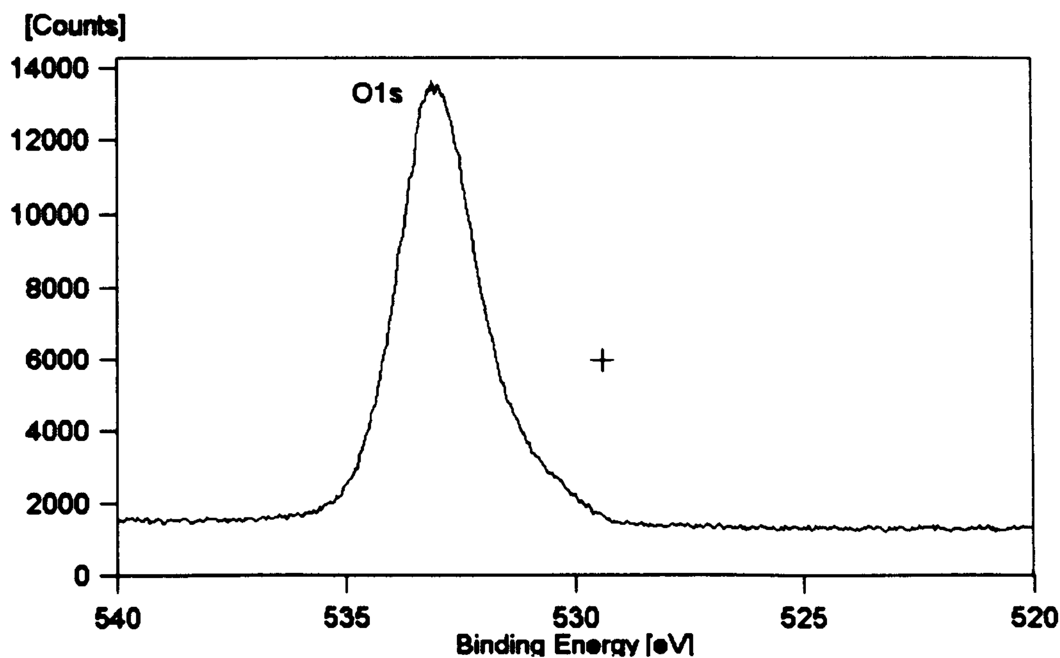

Figure 2.6. Ge and O peaks in the XPS spectrum: (a) Scan of the region corresponding to the Ge3d peak in the sample; (b) Scan of the region corresponding to the O1s peak.

The sensitivity of the instrument to the different elements has to be known in order to carry out a quantitative analysis. The sensitivity for the Si2p and O1s peaks are already known for this machine to be 1 and 2.93 respectively. Therefore, only a calibration standard for the germanium needs to be prepared.

The calibration standard was prepared by making a pellet of a compound having germanium and another element for which the sensitivity of the machine is known and whose XPS peaks are not close to the peaks for the germanium. In the present study Ge_3N_4 has been utilised. The sensitivity for the N1s peak is 1.73 and the position of the peak is at $\approx$ 410 eV.

The number of counts corresponding to the N1s and Ge3d peaks were evaluated and the number of atoms of nitrogen were calculated knowing the sensitivity, as can be seen in Table 2.2. As the stoichiometry of the compound is known, the number of germanium atoms has been calculated by using

$$(\textit{number of Ge atoms}) = (\textit{number of N atoms}) \times \frac{3}{4} \qquad (2.2)$$

The sensitivity of the instrument for the Ge3d peak is therefore calculated as 2.36.

Element peak	Counts	Sensitivity	Number of atoms
N1s	1519	1.73	878
Ge3d	1554	**X=2.36**	659

Table 2.2. XPS measurement of the nitrogen and germanium peak for the calibration for the germanium sensitivity.

The absolute measurement error in the number of counts for each element can be calculated as the square root of the number of counts, as they are statistical sampling errors. The errors in the composition given in weight percent can be evaluated as follows.

Let the function for evaluating the composition in weight percent from the number of atoms of each element be:

$$f = \frac{Ge_{atoms} \cdot m_{Ge}}{Ge_{atoms} \cdot m_{Ge} + Si_{atoms} \cdot m_{Si} + O_{atoms} \cdot m_{O}} \times 100 \qquad (2.3)$$

where Ge_{atoms}, Si_{atoms} and O_{atoms} are the number of atoms of germanium, silicon and oxygen respectively, and m_{Ge}, m_{Si} and m_{O} are the masses of germanium, silicon and oxygen. The absolute error in this function is given by

$$\sigma_f = \sqrt{\sigma_{Ge}^2 \cdot \left(\frac{\partial f}{\partial Ge_{atoms}}\right)^2 + \sigma_{Si}^2 \cdot \left(\frac{\partial f}{\partial Si_{atoms}}\right)^2 + \sigma_O^2 \cdot \left(\frac{\partial f}{\partial O_{atoms}}\right)^2} \quad (2.4)$$

in which the absolute errors for the different atoms can be calculated as

$$\sigma_x = \sigma_{x\,counts} \cdot \frac{1}{sensitivity\ factor\ of\ x} = \frac{\sqrt{x_{counts}}}{sensitivity\ factor\ of\ x} \quad (2.5)$$

where x represents germanium, silicon and oxygen.

2.3.1.5 XPS characterization of the germanium concentration depth profile.

The concentration of germanium was evaluated at different depths in the material by repeated etching of the silica with 4:1 buffered HF (solution of hydrofluoric acid and ammonium fluoride) followed by XPS analysis. To determine the depth at which the XPS analyses were performed a drop of Shipley S1828-photoresist was put on the edge of the sample prior to every immersion in HF. The photoresist prevented the material underneath from being etched during subsequent immersions in HF. After all the measurements had been made, the photoresist was removed in acetone and the resulting depth profile measured with a Talystep profilometer.

2.3.2 Rutherford Backscattering Spectroscopy (RBS).

Rutherford Backscattering Spectroscopy (RBS) is a powerful technique for material analysis. One of its most important advantages is that it is fully quantitative not requiring the use of standards. It also allows the determination of the elemental composition of the sample up to depths of 3 μm, with errors smaller than 1 %, as well as the depth profiling of the different elements present in the material, with depth resolutions better than 100 Å [Wolf, 1989]. Its specificity for elemental analysis is better for lower atomic number elements (as it is explained later in this section). Its detection limits lie between 0.01-10 % at., dependent on the element under study. RBS can be used also for structural analysis of single crystals by applying the channeling effect.

2.3.2.1 Fundamentals of the technique.

In Rutherford-Backscattering Spectroscopy, the sample to be analyzed is bombarded by a beam of energetic ions, typically hydrogen and helium ions, with energies in the range 1-4 MeV. The incident ions undergo elastic collisions with both the outer surface atoms and with the atoms below the surface. After the collision, the ions are scattered in a backward direction and leave the sample, arriving at a solid-state detector with a certain kinetic energy. The detector is located at a fixed viewing angle.

The energy with which the backscattered ions arrive at the detector depends on the energy of the incident ions, E, the loss of energy suffered by the ions during their penetration in the sample, the loss of energy due to the scattering event, the loss of energy of the backscattered ions in their way out of the sample and the number of backscatter atoms. Therefore, by analyzing the energy of the backscattered ions, information concerning the elemental concentration and the composition depth profiling of the material can be obtained.

The loss of energy by the incident ions as they travel through the sample is due to the interaction of the incident particles with the electronic clouds of the atoms in the target (electronic stopping) and to the glancing collisions with the nuclei of the target atoms (nuclear stopping). The energy lost by the ions in their way through the sample is given by the stopping cross section, ε:

$$\varepsilon \equiv \left[\frac{1}{N} \frac{dE_o}{dx} \right] \quad (2.6)$$

where N is the volume density of the target material and dE_o/dx is the total stopping power for the sample. Theoretical calculations of the electronic and nuclear stopping powers are complicated and inaccurate. Therefore, for the analysis of the RBS data, tabulated values from experimental data for many target elements are used [Ziegler, 1985]. Since ions backscattered in the same kind of target atom at different depths in the sample reach the detector with different energies (Figure 2.7), compositional depth profiling is possible by analyzing the RBS data.

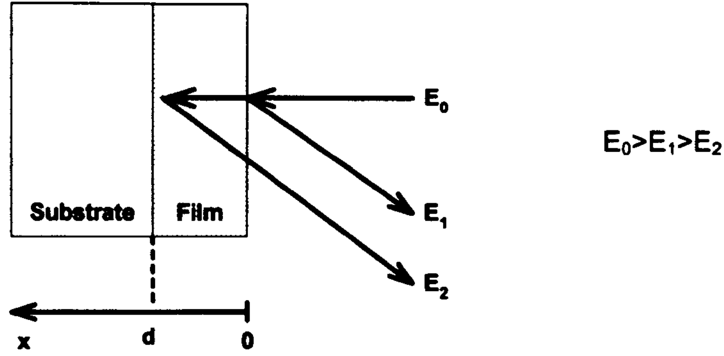

Figure 2.7. Principle of depth profiling using RBS: the energies E_1 and E_2 correspond to the energy with which the ions backscattered at different depths arrive to the detector. In both cases the ions undergo the energy loss associated with the collisional event with the atoms of the target. The ion backscattered by the atoms at the surface does not suffer any extra loss while the atom backscattered at a certain depth, d, will experience an extra loss of energy on the way in and out of the material, determined by the stopping cross-section of the material.

During the elastic collision between the incident ions and the atoms of the target, part of the energy of the projectile is transferred to the atoms in the sample. The relation between the incident and backscattered energies of the ions is called kinematic factor, K, which is given by [Vickerman, 1997], [Walls, 1989],

$$K = \left[\frac{\sqrt{\left(M_2^2 - M_1^2 \sin^2\theta\right)} + M_1 \cos\theta}{M_1 + M_2} \right]^2 \qquad (2.7)$$

where M_1 is the mass of the incident ion, M_2 is the mass of the target ion and θ is the scattering angle. But the detector will only count the ions that are backscattered within a certain solid angle Ω. The probability of an ion being backscattered within the solid angle of the detector is given by the Rutherford scattering cross section, which is given by [Walls, 1989]

$$\frac{\partial\sigma}{\partial\Omega} = \left[\frac{Z_1 Z_2 e^2}{4E} \right]^2 \cdot \frac{4}{\sin^4\theta} \cdot \frac{\left[\sqrt{1 - \left[\frac{M_1 \sin\theta}{M_2} \right]^2} + \cos\theta \right]^2}{\sqrt{1 - \left[\frac{M_1 \sin\theta}{M_2} \right]^2}} \qquad (2.8)$$

where Ω is the solid angle of the detector, in steradians, E is the energy of the incident ion before backscattering, Z_1 and Z_2 are the atomic numbers of the incident ion and target atom respectively and θ is the scattering angle.

The number of backscattered ions detected at the detector placed a scattering angle θ is given by [Walls, 1989]

$$Y = QNt\frac{d\sigma}{d\Omega}\Omega \tag{2.9}$$

where Y is the yield, Q is the number of particles that strike the target, N is the volume density of target atoms, t is the target thickness and $d\sigma/d\Omega$ is the scattering cross-section.

From the kinematic factor in Equation 2.7 it can be seen that the energy lost after a collision with different target atoms is dependent on the mass of the target atom. Thus, for two target atoms placed at the same depth in the sample, the energy with which the backscattered atoms arrive at the detector will be smaller for the smaller mass target atom. Therefore, RBS allows the discrimination between different target atoms. This discrimination will be larger for atoms of smaller mass, as the loss of energy in the scattering event is larger in those cases than for atoms of large mass.

From Equation 2.9 it is possible to see that the number of backscattered ions detected after scattering with one type of the target atoms is related to the concentration of that kind of atoms in the material. Therefore, the amplitude of the RBS spectrum is related to the concentration of the different atoms in the material under study.

It is also important to note that the incident ions cannot be backscattered by H or He atoms present in the sample. Therefore, those elements cannot be detected by this technique. Nevertheless, a change in the geometry of the experiment can be performed in which the forward scattered ions are detected, thus allowing detection of these light atoms.

Finally, Figure 2.8 shows an example of how an RBS spectrum is formed, considering all these effects: The loss of energy through electronic and atomic stopping in and out of the sample, the stopping cross-section (which allows the depth profiling of the different elements present in the sample), and the loss of

energy due to collision events, kinematic factor, which allows the separation amongst peaks corresponding to different atoms in the sample. The concentration of each element in the sample can be analyzed from the yield, or number of counts obtained at each energy.

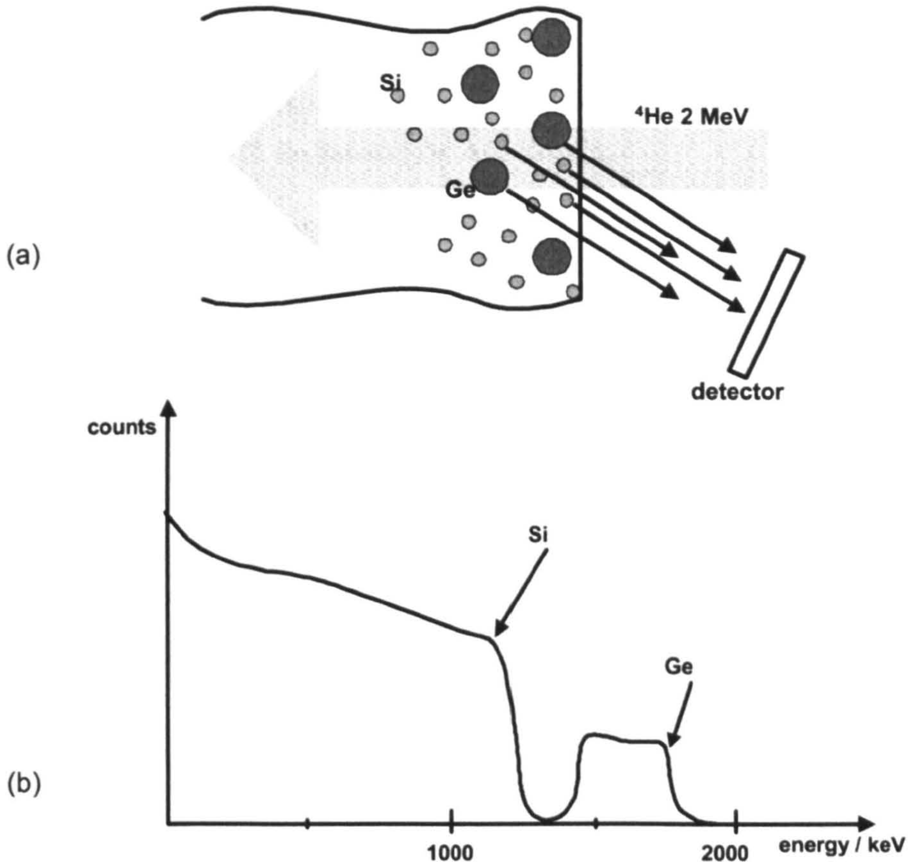

Figure 2.8. Construction of an RBS spectrum: (a) Backscattered beam as the incident beam passes through the sample; (b) Resulting RBS spectrum.

In Figure 2.8, the helium ion incident beam is backscattered by the two kinds of atoms in the sample, germanium and silicon. Due to their higher mass, the germanium atoms produce less loss in the collision event, and therefore the backscattered ions posses higher energy than in the case of the silicon atoms. The ions arriving at the detector are counted for the different energies and the number of counts obtained for each energy (or channel) is plotted (Figure 2.8 (b)). Two peaks, corresponding to the silicon and germanium atoms can thus be separated. Each of these peaks extends over a range of energies, the higher energy corresponding to the ions scattered by atoms at the surface and the subsequent lower energies

corresponding to ions scattered by atoms progressively deeper into the material. The heights of the peaks corresponding to the different elements are proportional to the elemental concentration and the scattering cross section, as shown in Equation 2.9.

2.3.2.2 Instrument for the collection of the RBS data.

The RBS measurements performed in this work have been carried out in the Ion Beam Laboratory of the IBM Almaden Research Center, San Jose, California, in collaboration with Dr. J.E.E. Baglin and Dr. A.J. Kellock.

The instrument used is an NEC Pelletron-particle accelerator, which can accelerate helium ions to energies of up to 3 MeV. The ion beam is focused and directed toward the target chamber by means of a system of magnets, quadrupoles, and collimators through an evacuated line. A solid-state detector is used to measure the kinetic energy of the backscattered ions.

Analyses were performed using both H^+ and He^+ ions as probe ions. For the analyses performed with He^+ ions a typical energy of 2.3 MeV was used with an incident current of 40 nA. For the analyses carried out by using H^+ ions, an energy of 2.3 MeV was also used, but with a lower incident current of 5 nA.

2.3.2.3 Analysis of the RBS data.

Several software packages are available for simulating and analyzing the RBS spectra (RUMP, SIMRA, HYPRA, etc). In this work, the spectra taken were fitted by using the software RUMP (Rutherford Universal Manipulation Package) [Doolittle, 1985]. For model fitting, the sample is divided into a certain number of layers, *i*, of thickness Δx_i. For each layer a certain composition is assumed. By means of the RUMP software, the RBS spectrum corresponding to that assumed structure is calculated and compared to the actual measured spectrum. The parameters of the different layers (thickness and composition) are varied until a good fit is obtained between the calculated (RUMP) and measured spectra.

2.4 Structural analysis.

2.4.1 Raman Spectroscopy.

Predicted by Smekal in 1921 and first observed by Sir Raman in 1928, the Raman effect relies upon the polarization of the electron cloud associated with a chemical bond by the incident electromagnetic radiation. The electromagnetic radiation modulates the polarization of the electron cloud with a time dependency due to the vibration of the atoms forming the bond [Vickerman, 1997]. Through its sensitivity to the vibrational properties, Raman scattering offers a valuable tool for the understanding of structural aspects in disordered materials [Umari, 2002]. In the case of the silica structure, information concerning the bond angle between the different tetrahedra, as well as the presence of defects in the structure, responsible for narrow lines in the spectrum, such as 3– and 4-fold small rings can be easily obtained. In this work, a confocal Raman microscope was used, further introducing the possibility of exploring the structural variations of the silica network with depth.

2.4.1.1 Basic principles.

When a molecule is irradiated with light, a small portion of the light can be scattered either elastically (Rayleigh scattering) or inelastically (Raman scattering). The scattering of the incident light is due to the formation of dipole moments in the atoms by the incident electric field, through the polarisability of the electron cloud. The polarizability without atoms displacement (vibration) leads to Rayleigh scattering. On the contrary, with atom displacement (or with atom vibration), the polarizability is modulated and leads to Raman scattering [Yates, 1987].

The different vibration motion of N atoms of a system (3N) are distributed in a series of modes (3N-6) solutions of the ion Schrödinger equation. Modes can make the polarizability of the electron cloud oscillate at different frequencies. This can be written as

$$\alpha = \alpha_0 + \alpha_0 \, cos(2\pi \upsilon_1 t) \qquad (2.10)$$

where α is the susceptibility of a certain mode under vibration, α_0 is the static susceptibility of equilibrium and υ_1 is the vibrational frequency of the given mode.

If the sample is irradiated with incident light of frequency υ_0,

$$E = E_0 \cos(2\pi\upsilon_0 t) \tag{2.11}$$

a dipole moment is induced by the electric field (polarisability) as

$$\begin{aligned}\mu &= \alpha E = \alpha_0 E_0 (1+\cos(2\pi\upsilon_1 t))(\cos(2\pi\upsilon_0 t)) = \\ &= \alpha_0 E_0 \cos(2\pi\upsilon_0 t) + \frac{1}{2}\alpha_0 E_0 \cos 2\pi(\upsilon_1 + \upsilon_0)t + \frac{1}{2}\alpha_0 E_0 \cos 2\pi(\upsilon_0 - \upsilon_1)t\end{aligned} \tag{2.12}$$

Therefore, the scattered light is modulated by the vibrations of the different modes in the material. The first term with unshifted frequency υ_0 is called the Rayleigh scattering (Equation 2.12), the second term at a frequency $\upsilon_0+\upsilon_1$ is called the anti-Stokes Raman scattering and the third term, at a frequency $\upsilon_0-\upsilon_1$ is the Stokes Raman scattering. The intensity of the anti-Stokes Raman scattering is much weaker than the one corresponding to the Stokes peak, as has been explained using quantum mechanics [Yates, 87]. In order for a bond to be Raman active, its polarizability needs to change with the vibrational modes of that bond. Therefore, not all the bonds are Raman active and therefore, detectable by Raman spectroscopy. Complementary vibrational techniques, such as infrared absorption spectroscopy, in which the activity of the bonds is associated with the electric dipoles instead of symmetry, can be used to map out the complementary part of the spectrum.

In a Raman spectroscopy experiment, the sample under study is irradiated with a highly monochromatic light of a certain frequency (the exact frequency is not important, as Raman spectroscopy measures the shift in frequency of the scattered light, although the frequency has to be enough to excite the vibrations in the different bonds). In a very simplified vision, the light will suffer elastic and inelastic events. In the elastic scattering events, no loss of energy is produced in the scattering event. Therefore the scattered photon has the same frequency than the incident photon, representing the Rayleigh scattering. Other photons might excite a vibrational mode of the material vibrating with frequency υ_1, as described in Figure 2.9.

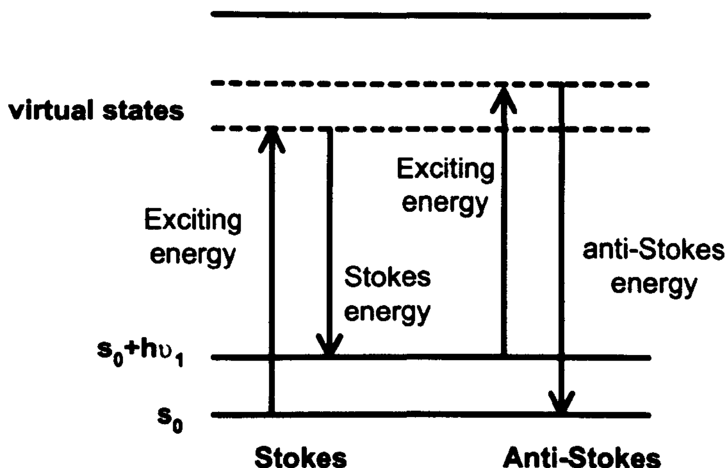

Figure 2.9. Representation of the Raman effect: Stokes and anti-Stokes scattering events [Yates, 1987]. S_0 is the energy of the ground state of the bond. Light experiences pseudo-absorption to the called "virtual states", before decaying producing the Stokes (if the original state of the bond was the ground state) or anti-Stokes scattering (if the bond was originally vibrating with frequency υ_1).

The energy of the scattered photon equals the difference between the exciting and absorbed radiation. It presents a shift in its frequency of $+\upsilon_1$ (anti-Stokes) or $-\upsilon_1$ (Stokes) compared to the exciting frequency. In the anti-Stokes scattering, therefore, the photon of scattered light presents an energy that is the energy of the exciting light plus the energy difference between the fundamental vibrational state in which the bond was prior to the irradiation and an excited vibration state. Thus, in order to produce anti-Stokes scattering, the initial state of the bond is in an excited vibrational state whereas the final state of vibration is the ground state. As the probability that a bond is in a vibrational state is much smaller than the probability of it being in ground state, the intensity of the anti-Stokes line in the Raman spectrum is much less intense than its Stokes counterpart.

2.4.1.2 Raman spectrum of the silica network.

Figure 2.10 shows an example of a silica spectrum (the spectrum was taken from a quartz slide) where all the typical features are named. Galeener [Galeener, 1979] justified the different broad bands appearing in the spectrum as determined by the vibrations of the different bonds of the silica network by using the central-force network model developed by Sen and Thorpe [Sen, 1977].

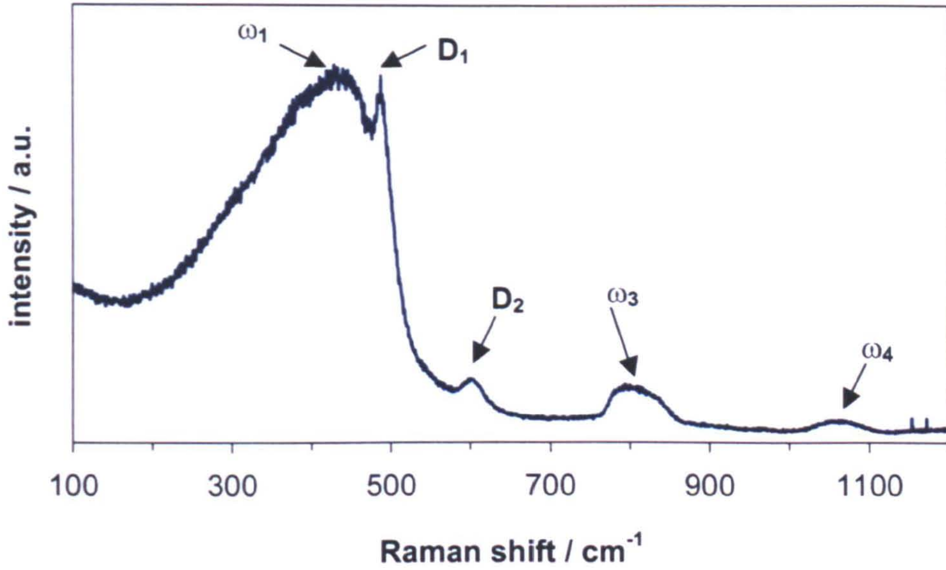

Figure 2.10. Raman spectrum of a quartz sample: The different features characteristics of the spectrum are indicated.

According to that model, the position of the different bands can be calculated as [Galeener, 1979]:

$$\begin{aligned}
\omega_1^2 &= \left(\frac{\alpha}{m_x}\right)(1+\cos\theta) \\
\omega_2^2 &= \left(\frac{\alpha}{m_x}\right)(1-\cos\theta) \\
\omega_3^2 &= \omega_1^2 + \left(\frac{4\alpha}{3m_A}\right) \\
\omega_4^2 &= \omega_2^2 + \left(\frac{4\alpha}{3m_A}\right)
\end{aligned} \qquad (2.13)$$

where ω_i are the angular frequencies in rad·sec^{-1}, α is the A-X bond stretching constant, θ is the angle A-x-A and m_x and m_A are the masses of the oxygen and silicon atoms, respectively. Due to the spreading of the angles between tetrahedra along the silica network, those frequencies appear as bands rather than as peaks. Figure 2.11 shows a schematic of the vibrational modes of the silica structure.

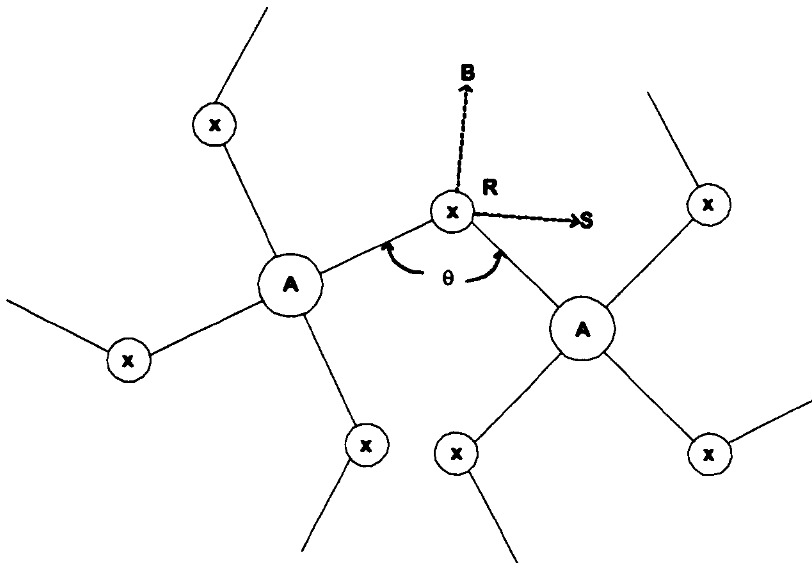

Figure 2.11. Ax_2 glass structure: In the case of silica, A represents the silicon and x the oxygen. The vibration modes of the network are indicated: B (symmetric-stretch motion), S (antisymmetric-stretch motion) and R (rocking motion) [Galeener, 1979].

The band ω_1 is produced by the symmetric-stretch motion of the bridging oxygen atom, indicated in Figure 2.11 as B, in which not movement of the silicon atom is produced. The band ω_4 is due to the anti-symmetric stretch motion, noted in Figure 2.11 as S and the band ω_3 is due to the stretching motion of the oxygen atom accompanied by motion of the silicon atoms depending on the ratio of the masses m_x/m_A, the average angle of the bond and the coordination of the cation (A atom, in this case the silicon) [Galeener, 1979].

The narrow peaks named as D_1 and D_2 in Figure 2.10 cannot be explained as random vibrations of the silica network. Galeener proposed that they are produced by the symmetric-stretch motion associated of the oxygen bridging atoms in 4- and 3- membered planar ring structures embedded inside the silica network [Galeener, 1982a], [Galeener, 1982b]. This explanation has been later confirmed by quantum mechanical simulations of the silica structure based on first-principles by Pasquarello *et. al.* [Pasquarello, 1998].

2.4.1.3 Experimental instrument.

The Raman spectra studied in this work were collected in the University of Paris at Jussieu, in collaboration with Dr. D.R. Neuville. The measurements were done with

a T64000 Jobin-Yvon confocal microRaman spectrometer, which was equipped with a cryogenic EG&G Model 1433-C CCD (charge-coupled detector). The confocal configuration of the microRaman instrument allows depth profiling of the samples, permitting the detection of the Raman spectrum from a volume as small as 1 μm^3 focusing at different depths into the sample.

The excitation light used was a monochromatic 514.532 nm wavelength light from a Coherent model 70C5 Ar^+ laser operating at a power of 2 W. A 100-fold objective lens was used for the focusing so that only a volume of 1 μm^3 was sampled. The data was collected for 600 sec.

2.4.1.4 Qualitative analysis of the data.

In the subsequent chapters, only qualitative information is sought from the Raman spectrum. However, it is important to consider firstly, that a shift in the silica network bands is due to a change in the Si-O-Si angle, following the expression [Liu, 1997], [Galeener, 1983], [Galeener, 1979]

$$\Delta\omega_i = \pm\left(\frac{\alpha}{m_o}\right)\frac{\Delta\theta}{2\omega_i}\sin\theta \qquad (2.14)$$

where ω_i are the frequencies (rad·sec^{-1}) of the different silica Raman bands, $i=1$ to 4, α is the Si-O bond-stretching force constant (all the other force constants are assumed to be zero according with Galeener [Galeener, 1979]), m_o is the mass of the oxygen atom and θ is the angle of the Si-O-Si bond. The sign before the right hand side of Equation 2.14 is negative for $i=1$ and 3 and positive for $i=4$, i.e. $(-1)^i$.

Secondly, the relative intensities of the defect lines D_1 and D_2 with respect to the other bands in the spectrum are indicative of the proportion of 4- and 3- membered rings in the silica structure. Since the 4- and 3- fold ring structures occupy less volume than the silica tetrahedra, a high content of small rings will involve a more highely compacted structure [Dianov, 1997], [Chan, 2003], [Bazylenko, 1997], [Chan, 2001].

The absolute intensities of the peaks of the spectra in this work cannot be used to obtain structural information as the same amount of material was not always excited.

2.4.2 X-Ray Absorption Fine Structure (EXAFS).

X-Ray Absorption Fine Structure is a useful technique for the study of the structure of materials that do not possess long-range order. The coordination number of the different elements and their distances to the element under study can be obtained, thus making this technique valuable for different applications such as the determination of metal ion coordination in molecules, the study of glasses and gels, the determination of metal cluster size in supported metal catalysts, the study of impurity sites in semiconductors and the study of local coordination in complex materials, such as high temperature superconductors [Vickerman, 1997]

In the following section, the basics of the EXAFS technique will be presented. For more detailed information, the Web page of the XAFS group at Daresbury laboratory (and references therein) are a good source of references.

2.4.2.1 EXAFS principle.

In an EXAFS experiment, the sample is irradiated with a monochromatic X-ray beam of increasing energy. As the X-rays penetrate the sample, their energy can be used to eject a core electron. In order for this to be possible, the energy of the incident X-ray has to be larger than the binding energy of the core electron that is excited. The main difference with the XPS principle is that the range of energies used in EXAFS are much larger, therefore exciting different core electrons.

The ejected photoelectron can be considered as a wave the frequency of which is dependent on the energy of the photoelectron. This wave will interact with the atoms surrounding the excited atom producing interference waves (Figure 2.12). The characteristics of the oscillations produced by the interference between the photoelectron wave and the waves of the electrons from the surrounding atoms will depend on the distance between the central atom and the neighboring atoms and the number and nature of the neighboring atoms. As the amplitude of the electron wave is inversely proportional to the distance from the emitter atom, the oscillations produced by interaction with the first or even second shell of atoms will play the most important role in the EXAFS oscillations. Therefore, EXAFS allows the study of the local environment of the atoms of interest.

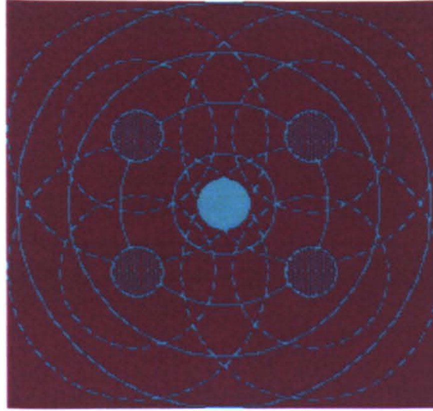

Figure 2.12. EXAFS principle: Representation of the photoelectron ejected from the atom whose environment is studied as a wave, which is scattered by the surrounding atoms producing oscillations in the absorption spectrum.

Normally, in an absorption EXAFS experiment, the spectrum which describes the relationship between the transmitted and incident intensities is measured for a range of incident energies around the binding energy of the element whose environment is to be analyzed, using an experimental configuration similar to the one shown in Figure 2.13. A double crystal monochromator produces a monochromatic X-ray beam. The energy of the X-ray photons in the beam is varied over a range of energies around the critical edge of the element under study (in this case, the K-edge of the germanium).

The main features in the measured spectrum are the absorption edge of the excited element, which is marked by a pronounced step in the absorption, and the oscillations due to the effect of the other atoms surrounding the excited atom (Figure 2.14)

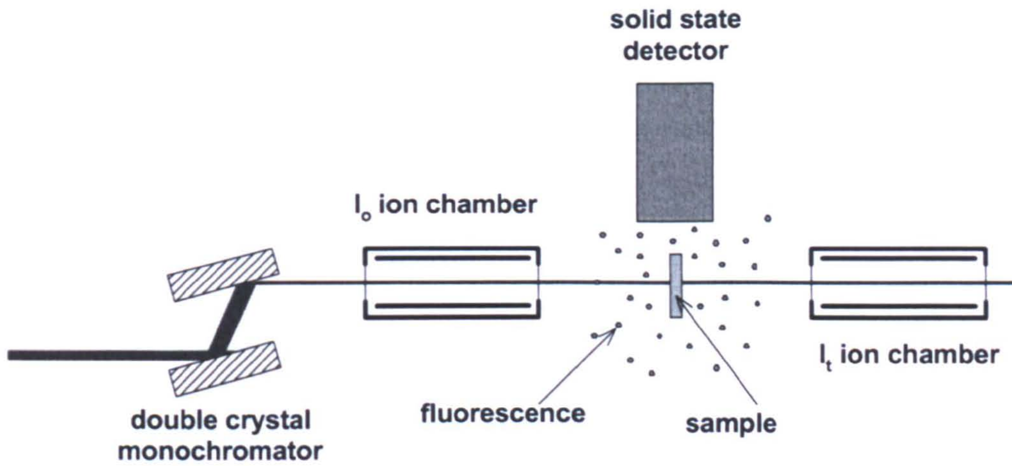

Figure 2.13. Typical EXAFS' configuration: The double crystal monochromator produces a monochromatic beam of different wavelengths. The intensity of the beam is measured by two ion chambers placed before and after the sample to be analyzed. As the core electrons are excited, fluorescence is produced that can also be detected by a solid state detector.

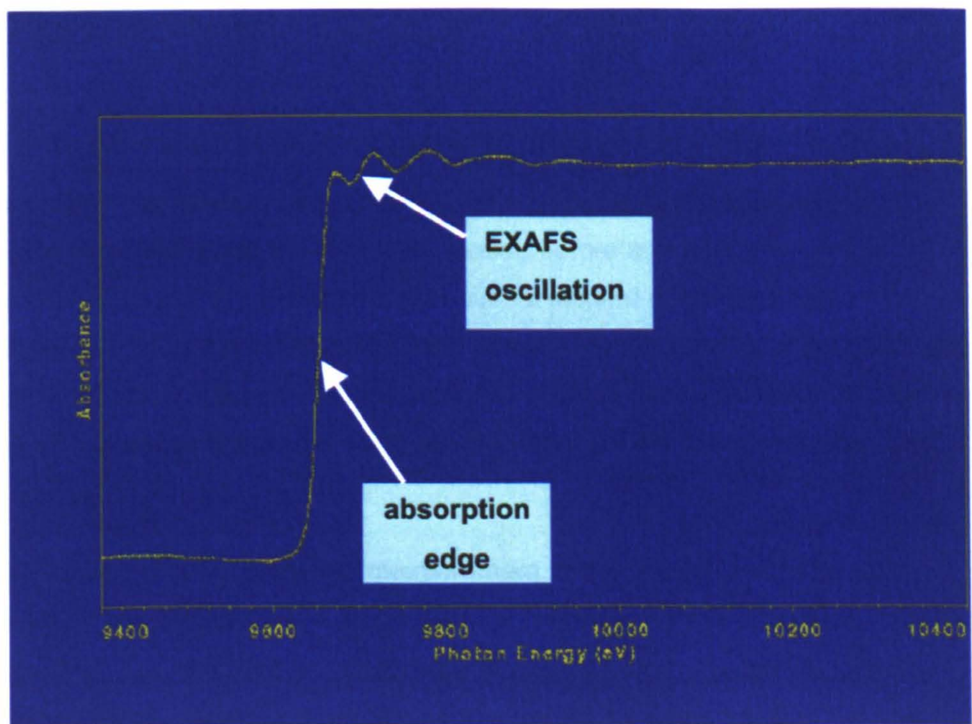

Figure 2.14. Example of critical edge: an increase of the absorbance can be observed after the critical edge for absorption, followed by the EXAFS oscillations.

2.4.2.2 Structural information obtained from EXAFS analysis.

From the analysis of the oscillations measured in the absorption spectrum, information concerning the local environment of the excited atoms (central atom) can be obtained:

1. Type of scattering atom (atomic number ± 2 for inner shell, ± 3-5 for outer shells, these errors can be larger for poor quality data or data range shorter than k=15 $Å^{-1}$)

2. Coordination number (accuracy ± 10% for inner shell, ± 25% for outer shell, at best).

3. Distance of the neighboring atoms to the excited atom (± 0.02 Å for inner shells, ± 0.05 Å for outer shells).

4. Measurement of the disorder of the basic shell (i.e. Debye-Waller type factors, thermal plus static contributions, ±10% for inner shell, ± 25% for outer shells, at best).

2.4.2.3 Different experimental configurations used to collect EXAFS data.

Absorption: The intensity of the beam before and after passing through the sample are collected in two ion chambers placed before and after the sample (Figure 2.13). The first ion chamber is filled with a mixture of gas to absorb approximately 20% of the incident flux and the second ion chamber is filled with gas to absorb 80% of the incident flux. The absorption of the sample is calculated as ln (I_0 / I_t), and changes across the edge, as the energy of the incident photons is varied.

Fluorescence: For fluorescence measurement, the sample is normally set at 45 degrees to the incident beam. Absorption of the energy of the incident X-rays by a core electron from the K-shell, produces a core-hole, which can be occupied by another electron from a more energetic shell, such as the L-shell, losing the extra energy as a fluorescence photon. The energy of the fluorescence photon is less than the energy required to eject an electron from the K-shell to the free space (energy of the K-edge).

The fluorescence detected for a certain incidence energy is related to the amount of absorption, thus presenting the information contained in the oscillations of the absorption spectrum.

Fluorescence is usually used for dilute samples (less than ca. 2 % of the element of interest). At lower concentrations, fluorescence gives a better signal-to-noise ratio than transmission, where just a small signal on a steep background would be seen. At concentrations higher than about 4 % of the element of interest the fluorescence signal becomes distorted due to self-absorbance (see section 2.4.2.4).

Electron yield: This technique is used instead of fluorescence when the element under analysis is a light element for which the fluorescence would be low. The method involves the collection of the Auger electrons. In these experiments, the sample is biased and the drain current is collected (Total Electron Yield). In order for this technique to be applied, the sample needs to be electrically conductive.

EDEXAFS: This form of EXAFS collects in only "one shot" the absorption spectrum corresponding to all the incident wavelengths. A curved polychromator focuses all the light onto a spot of approximately 100-200 μm of diameter at the sample. The light then expands after passing through the sample and arrives to a position sensitive detector. The position on the detector therefore represents an energy scale, and the whole spectrum can be collected at the same time.

Fluorescence mode ReflEXAFS: In this technique, the incident beam is directed to the sample at a glancing angle, around the critical angle for reflection. Depending on the incidence angle, different penetrations on the sample will be obtained. The fluorescence produced by the incident beam is collected by a solid-state fluorescence detector, placed on top of the sample. The height of the detector will be chosen to maximize the number of fluorescence counts without producing saturation of the detector. A schematic of the technique is shown in Figure 2.15.

Since the flame-hydrolysis deposited silica layers to be analyzed are very thin (≈2-6 μm) and deposited on top of a thick 500 μm silicon substrate, transmission measurements are not possible, i.e. for a 500 μm thick silicon substrate the transmission at 10 keV would be 0.02 %, requiring data collection for an unpractical length of time. On the other hand, as only the first few microns of the sample need to be measured, a reflEXAFS setup can be used. The penetration depth of the X-

rays in the sample, and therefore the depth from which the EXAFS data is collected, depends on the angle of incidence.

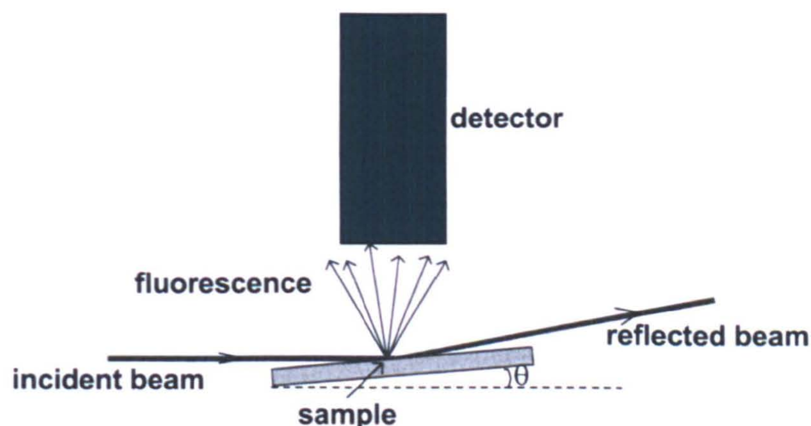

Figure 2.15. ReflEXAFS configuration: The sample is hit by the incidence beam at a glazing angle around the critical angle for reflection. The fluorescence produced is measured by the solid-state detector.

2.4.2.4 Limitation factors in the analysis of EXAFS data.

There are different factors that limit the amount of information that can be obtained from the analysis of the EXAFS oscillations. In concentrated samples, more than 4 % at., at angles at which the penetration of the incident X-rays is on the 100's of Å range, the signal due to the atoms deeper in the material will contribute less to the EXAFS signal than the atoms from the surface of the sample. This is particularly important if the structure varies within the depth of the sample. Another factor that can contribute to a distorted EXAFS signal in samples with a high concentration of the element under study (> 4% at.) is self-absorption of the fluorescence signal on its way through the sample to the detector [England, 1999]. Self-absorbance occurs when the fluorescent photons are absorbed by other atoms of the element of interest (i.e. they excite a core electron to an outer orbital), leading to a decrease in the amplitude of the observed oscillations, and consequent under-estimation of co-ordination numbers. But this effect does not make the periodicity of the oscillation change, and the values obtained from fitting the EXAFS signal still give correct distances to the surrounding atoms [England, 1999]. Self-absorption is usually not a problem in ReflEXAFS because the penetration depth at low angles of incidence (half the critical angle) is very low (ca. 50-100 Å) so the fluorescent photons are not absorbed, even in high concentration samples. However, at higher incident angles,

greater than the critical angle, the penetration depth is several hundred Å's, and the fluorescent signal will be distorted with lower than expected coordination numbers obtained. The same effect is obtained in rough samples.

2.4.2.5 Experimental details for the collection of data in this work.

The data was collected in Station 9.3 of Daresbury Laboratory Radiation Source with a reflEXAFS configuration. The incident beam was scanned around the energy of the K-edge of germanium (11.12 keV). A Si (220) monochromator, detuned to reject 50 % of the signal in order to minimize harmonic contamination, was used in the measurements. The size of the incident beam was defined by using a 3 mm horizontal slit together with a 50 μm vertical slit. Typical beam conditions in this station are a minimum current of 125 mA at 2 GeV.

The ion chambers before and after the sample are filled with Ar; 20% absorbing I_o and 80% absorbing I_t, backfilled to 1000 mbar with He. The system was calibrated by using a platinum foil standard to measure the platinum edge (11.554 KeV).

A 13-element solid-state Canberra fluorescence detector was used, for which the energy acquisition window was selected to correspond to the fluorescence peak of germanium, 9.886 KeV. The channels in the solid-state detector were calibrated by using the $L\alpha 1$ line of a platinum foil and the $L\alpha 1$ line of a gold foil. The detector was placed above the sample at an angle approximately perpendicular to the plane of the surface. For data collection the detector channels were "windowed" on the Ge $K\alpha$ fluorescence, and the total and windowed fluorescent signals for the 13 elements were recorded separately in the raw data files.

Four scans were collected of each sample and then summed in order to improve the quality of the data (i.e. noise $\sqrt{n}$).

2.4.2.6 Analysis of the data.

Once the data was collected, the EXAFS spectra have to be extracted from the absorption spectra. Theoretical calculations using a model for the atomic level description of the surrounding environment of the element under study were then performed in order to find the atomic environment that best matches the measured EXAFS data.

In this study, the software available at Daresbury laboratory has been employed in order to perform these calculations [Ellis, 1995], [Binsted, 1998]. The data collected by the different elements of the solid-state detector in the four scans taken is added by using the program EXCALIB. In this data reduction stage, possible glitches in the measured data can be observed, in which case the different spectra can be edited and the point corresponding to the glitch can be deleted.

The background before and after the absorption edge was then substracted by using the program EXSPLINE, which is based on the original program SPLINE of Ellis [Ellis, 95]. After background substraction, the EXAFS data can be analyzed by using the program EXCURV98 [Binsted, 98], by adding shells of backscatterers around the central absorber atom.

From the fits, information concerning the coordination numbers of the different atoms present in the structure around the excited atoms, the distances of the different atoms to the central (excited) atom and some information about the disorder of the structure can be obtained.

The quality of the fit is calculated by a statistical test, the reduced-χ^2 test, which is given by

$$Reduced\ \chi^2 = \frac{absolute\ \chi^2}{nind - npars} \tag{2.15}$$

where *npars* is the number of parameters that are modified during the fitting and *nind* is defined by

$$nind = \frac{2\Delta k \cdot \Delta R}{\pi} + 1 \tag{2.16}$$

where Δk is the range of analysed wavevectors, k, in the reciprocal space ($k=\{(4\pi m_e/h^2)(E-E_o)\}^{1/2}$ where E_o is the threshold energy for the absorption edge and m_e is the mass of the electron) and ΔR is the range of distances from the central atom. The Reduced-χ^2 should become significantly smaller after adding an extra shell to the structure in order to justify the addition of the shell.

2.5 Density analysis.

2.5.1 X-Ray Reflectivity.

The theory of reflectivity in single and multilayered structures has been widely developed in optics [Born, 1959] and various optical characterization techniques, such as ellipsometry, use the reflectivity theory in order to characterize the optical properties of the materials under analysis.

The density of a material is related to its refractive index through the Lorentz-Lorenz relation (an equation in which the density of the material, together with the polarizability and composition are combined to obtain the refractive index of the material) [Born, 1959]. Therefore, the estimation of the density of the material by optical methods should be complemented by non-optical structural characterization, to support the use of the Lorentz-Lorenz relation.

Since X-rays, due to their high energy, can excite all the electrons in the sample [Wallace, 1995], and since the refractive index of the material at the X-ray wavelength is directly related to the electron density, using X-ray reflectivity it is possible to measure the electron density in a material independently of the chemical bonding. Since the first classical work by Compton in 1923 [Compton, 1923], X-ray reflectometry has become a powerful tool for analysis of surfaces and thin film interfaces. This technique allows the determination of surface and interfacial roughness, layer thickness of thin films and multilayer samples, surface density gradients and layer density. It has the advantage of not being sensitive to either crystal structure, dislocations or defects, so that many different kinds of structures can be probed by this technique, including crystalline, poly-crystalline and amorphous structures, such as glasses. This arises due to the fact that the reflectivity depends only on the electron density of the material and not on its structure [Stoev, 1997] although this insensitivity to the structure of the material under analysis does also have the drawback of not being able of distinguish between interface roughness or grading, for example (as both produce the same effect on the electron density).

2.5.1.1 Fundamentals of the technique.

The refractive index for X-ray radiation is given by

$$n = 1 - \delta - j\beta \qquad (2.17)$$

where

$$\delta = \frac{\lambda^2}{2\pi} r_o \rho_{elec} \qquad (2.18)$$

and β accounts for the X-ray absorption of the material ($\beta = \lambda\mu/4\pi$ where μ is the linear absorption coefficient of the material).

In equation 2.18, λ is the wavelength of the X-rays, r_o is the classical radius for the electron $r_o = 2.82 \cdot 10^{-5}$ Å, and ρ_{elec} is the electron density, i.e. the number of electrons per unit of volume in the material [Stoev, 1997].

The same formalism used in electromagnetic theory for the calculation of the reflectivity of a system composed of one or more layers [Born, 1959] can be applied to X-ray wavelengths by substituting the optical refractive index for the corresponding refractive index for X-rays [Parrat, 1954]. Since the refractive index of the material under analysis is $n<1$ (i.e. smaller than the refractive index of air, $n=1$), a critical angle exists. For angles of incidence below the critical angle, total reflection occurs at the interface between air and material, while for angles larger than the critical angle, radiation can be partially refracted into the material. It is important to note that, in this section, the incidence angle, θ_i, is being considered as the one formed by the incident beam with the surface of the material, as shown in Figure 2.16.

Figure 2.16 shows a typical reflectivity curve. For angles below the critical angle, the reflectivity equals 1 (total external reflection). For angles over the critical angle, some transmission into the sample occurs, producing a drop on the reflectivity. Therefore, from the analysis of a measured reflectivity curve, the position of the critical angle can be determined.

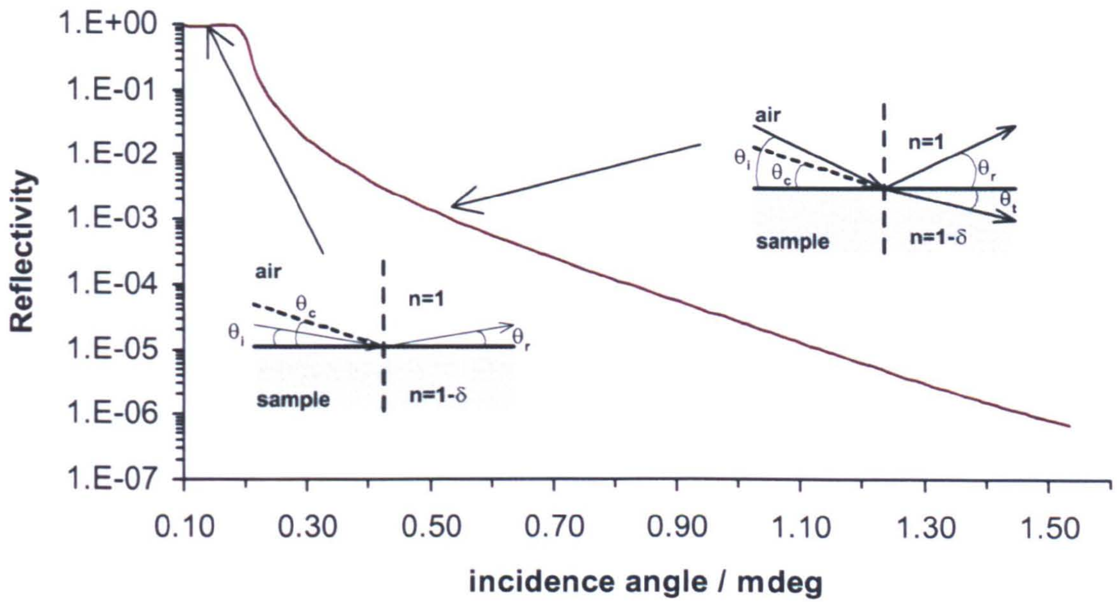

Figure 2.16. Typical example of reflectivity curve: For the angles below the critical edge, the reflectivity is approximately 1. For incidence angles over the critical edge, the reflectivity begins to drop. As $\delta \ll 1$, the critical edge is very close to 1. The critical edge normally occurs at grazing incidence.

Considering Figure 2.16, by applying Snell's law to the incidence and refracted angles, it is possible to say

$$\cos\theta_c = (1-\delta) \quad (2.19)$$

given the refractive index of the air as 1, and when the incidence angle corresponds to the critical angle, the refracted angle is 0 deg. As δ is $\ll 1$, the critical angle is close to 0 (the reflectivity experiments are normally performed at grazing incidence), and the first term in Equation 2.19 can be replaced by a Taylor series as

$$1-\frac{\theta_c^2}{2} \approx 1-\delta \Rightarrow \theta_c \approx \sqrt{2\delta} \quad (2.20)$$

From Equations 2.18 and 2.20, the electron density of the material can be directly determined from the position of the critical angle. The electron density, ρ_{elec}, can be directly related to the density of the material as [Stoev, 1997]

$$\rho_{elec} = N_A \frac{f_{molecule}}{M.W} \rho \quad (2.21)$$

where N_A is the Avogadro's number, $f_{molecule}$ is the atomic scattering factor which represents the number of electrons in a molecule, *M.W.* is the relative molar mass (in grams) and ρ is the density of the material. The critical angle is taken normally as the angle for which the reflectivity has dropped to 0.5.

Nevertheless, the determination of θ_c is not straightforward due to other factors contributing to the reflectivity, such as roughness of the interfaces and presence of a graded refractive index structure. Therefore, in order to analyze the density of the samples in those cases, a more detailed model for the reflectivity, introducing the effect of those factors is needed [Als-Nielsen, 1991], [Stoev, 1997], [Nevot, 1980].

Software, which introduces the effects mentioned above, is readily available [Braun, 1999]. In this work, the software Parratt32, which is based on the methodology described by Parrat [Parrat, 1954] including the roughness effect [Nevot, 1980], was used. The software uses a one dimensional Newton-Raphson fitting algorithm to fit the experimental data. A value for $Re(rho)=2\pi\delta/\lambda^2$ is obtained from the fitting algorithm. From that value, the electron density and consequently the density of the material can be obtained:

$$\rho = \frac{Re(rho)}{N_A\, r_o} \frac{M.W.}{f_{molecule}} \qquad (2.22)$$

where r_o is the electron radius in Å, *M.W.* is the relative molar mass (in grams), NA is the Avogadro's number and $f_{molecule}$ is the atomic scattering factor of the molecule.

2.5.1.2 Experimental considerations.

The data for this experiment was collected in Station 16.2 at the Daresbury Laboratory Synchrotron Radiation Source. The measurements were taken at wavelengths of 1.36 Å and 0.52 Å. The X-rays were incident on the sample at a grazing incidence, where the detector was placed at an angle of twice the incidence angle. The sample and the detector were scanned for a range of incidence angles, θ_i, from 0.1 to 1.75 deg at steps of 0.00125 deg in the region of the critical edge (from 0.15 to 0.245 deg) and 0.005 deg elsewhere for the spectra collected at 1.36 Å, and at steps of 0.0005 deg around the critical edge (from 0.05 to 0.1 deg) and 0.001 deg elsewhere for the data collected at 0.52 Å. The intensity of the

reflected X-rays were detected by the detector. Vertical and horizontal slits were used before the X-rays arrived to the sample and before the detector, to define the size of the beam. Different filters were placed in front of the detector to avoid its saturation. The number of counts was high enough so that a count error of <2 % could be routinely obtained. The depth of material sampled by the X-rays at the critical angle is larger the smaller the wavelength.

Alignment.

It is important to take into account the importance of the alignment of the sample on the accuracy of the measurements. As an example, a misalignment error of 1 mdeg in the determination of the incidence angle will introduce an error of 1 % in the calculation of the density of the material. In order to align the sample as well as possible, several scans of the height and the incidence angle were taken prior to the collection of the data, in order to make sure that the sample was centrally located in the beam (of width 50 μm) and reflected the beam into the centre of the detector positioned at a designated angle ($2\theta_i$). Figures 2.17 (a) and 2.18 (a) show schematically the alignment procedure. The height and incidence angle scans were repeated until the maximum of intensity was always obtained at height "0" and angle of incidence equal to half of the detector angle. In Figure 2.17 (b) and 2.18 (b) an example of height and θ_i scans are shown.

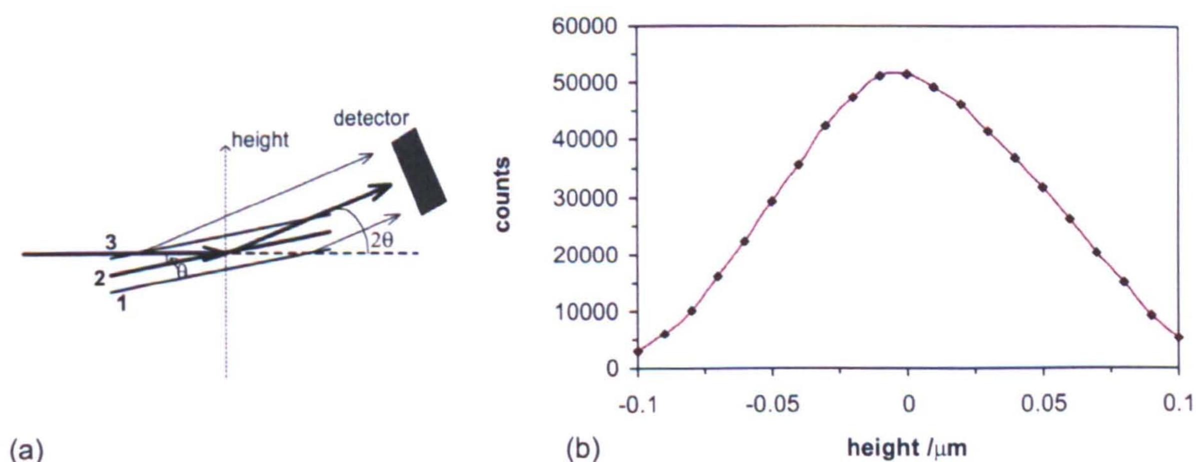

Figure 2.17. Height scan: (a) The height of the sample is scanned from positions 1 to 3. At position 2, the reflected beam is completely detected by the detector while at position 1 and 3, part of the reflected beam lies out of the detector; (b) Graph obtained from a height scan. The peak occurs for the height for which the full reflected beam is detected.

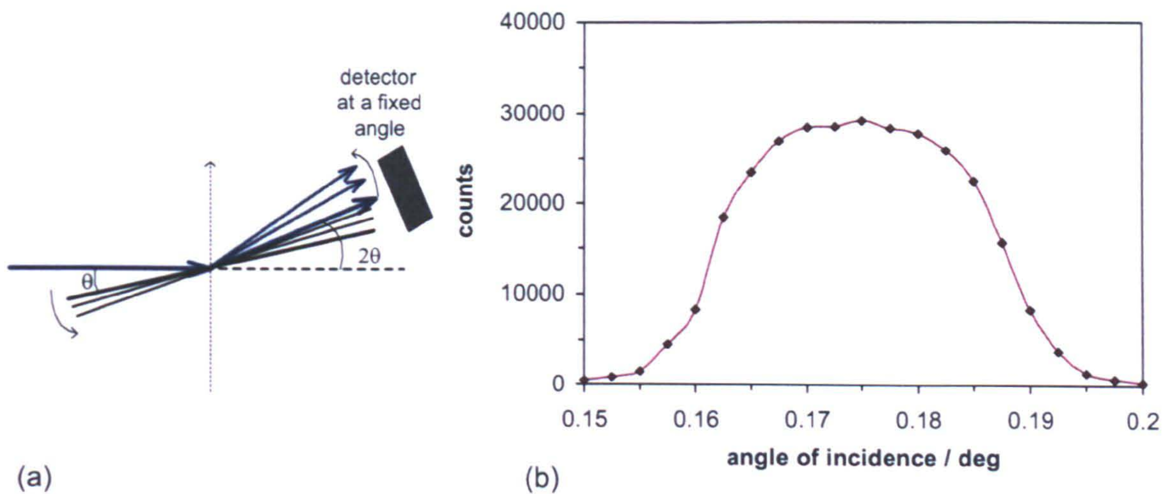

Figure 2.18. Angle of incidence scan: (a) The angle of the detector is kept at a fixed position and the angular position of the sample is scanned. The maximum of intensity will be obtained when the incidence angle into the sample corresponds to half the detector angle; (b) The detector angle was fixed at 0.35 deg. The maximum in the measured intensity was obtained for an incidence angle of 0.175 deg.

Sample flatness.

Another important consideration to take into account is the possible bow of the sample. If the sample is not completely flat, the X-rays incident on the surface of the sample will hit the sample at different angles, thus suffering a different amount of reflection. This effect will distort the shape of the reflectivity curve. Due to the different thermal expansion coefficients between the silicon and the FHD silica, a bow of the silicon substrate occurs during the high temperature sintering process. In order to avoid this effect, the substrates on which the FHD silica layers were deposited for the X-ray reflectivity experiment, were silicon polished blocks 5 mm thick.

Background noise.

Finally, roughness of the surface of the sample will produce off-specular scattering. In order to determine the magnitude of this scattering, scans of the detector angle were made, keeping the incidence angle constant. The background noise was represented by the percentage of the signal peak that is under the background line. As can be seen in Figure 2.19, the background noise can be considered zero in these measurements.

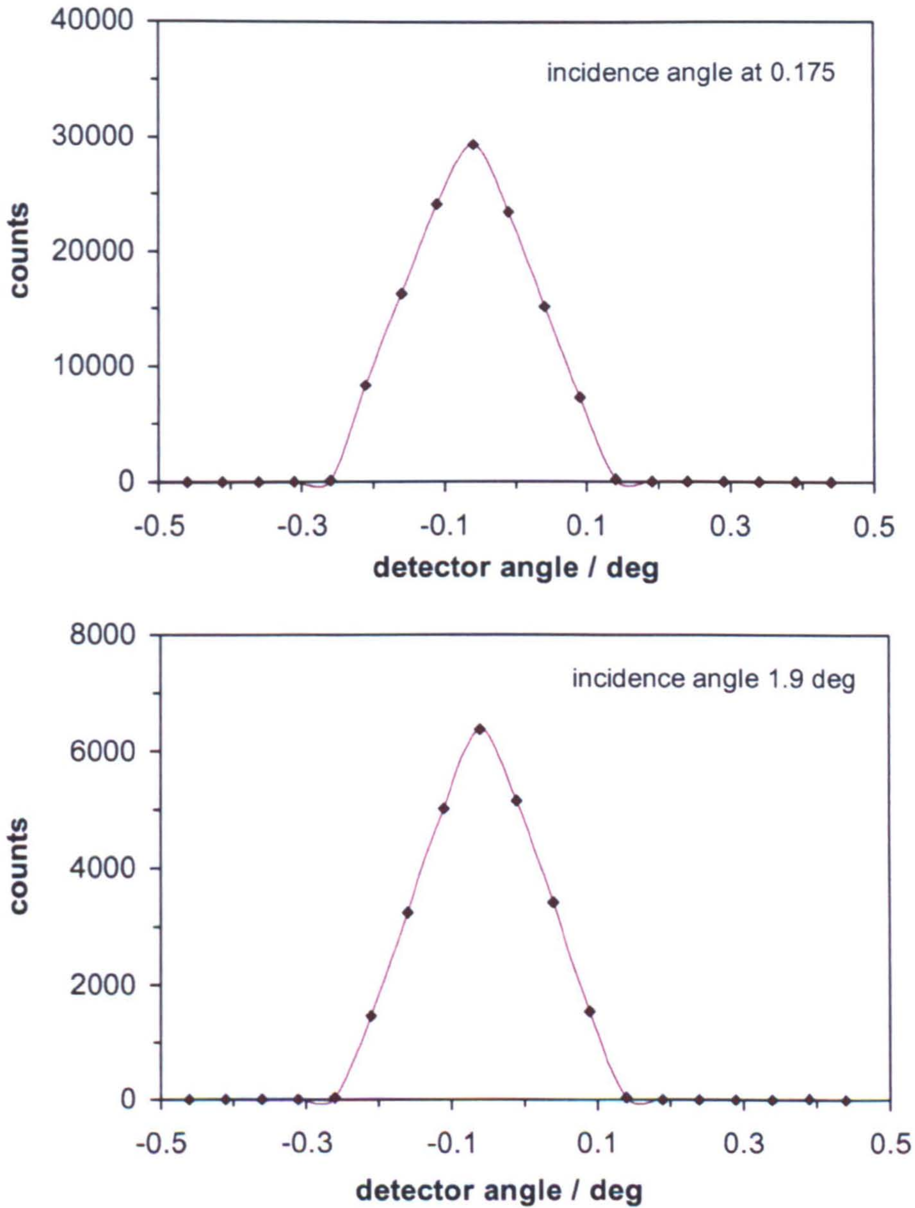

Figure 2.19. Scan of detector angle at two θ_i for background measurement: It can be observed that in both cases the background noise can be considered zero.

2.5.1.3 Analysis of the experimental data.

The software Parratt32 [Braun, 1999] was used in order to analyze the experimental data from the X-ray reflectivity measurements. From the measurements, the number of counts in the detector, placed at an angle $2\theta_i$ were obtained as a function of the incidence angle θ_i. The number of counts was normalized using the number of counts on the detector when the beam was switched off (dark current) and the

number of counts of the monitor, which measures the number of counts of the incident beam. As a result, the reflectivity as a function of the incidence angle was obtained. The Parratt32 software requires the absolute error in the measurement for each point. Using statistical theories, the errors in the monitor and detector counts can be estimated as $\sqrt{counts}\,/\,counts$.

For the measurements taken at the short wavelength, 0.52 Å, over-illumination of the sample can occur due to the smaller incidence angles used in this case (over-illumination occurs when the beam is illuminating a length longer than the length of the sample). If over-illumination occurs, the measured intensity reflected from the sample will be smaller than if not over-illumination happened, as part of the beam is not being reflected. Therefore, a correction factor needs to be applied to the measured data in order to compensate for this effect for those incident angles for which over-illumination was occurring. If this is not done, a distorted reflectivity curve is obtained.

2.5.2 Profilometry.

After irradiation of a limited area of the FHD layers by an electron-beam [Blanco, 2001], a depression on the surface can clearly be seen. The depression is large enough to be measured by surface profilometry using atomic force microscopy or a stylus profilometer. From the depression measured, the densification of the material can be estimated using an elasticity model, as described in Chapter 5.

2.5.2.1 Atomic Force microscopy.

AFM (Figure 2.20) operates by measuring attractive or repulsive forces between a tip, which is scanned very close to the surface of the sample [Binnig, 86]. The forces between the tip and the sample can be kept constant during the measurement. Consequently, as the tip is scanned over the surface, it suffers deflections related to the surface topography. The deflection of the scanning tip due to the surface topography can be measured by different methods, such as measuring the tunneling current between the tip and the sample [Binnig, 1986] or by optical interferometry [Meyer, 1988]. Tips are typically made from Si_3N_4 or Si, and extended down from the end of a cantilever.

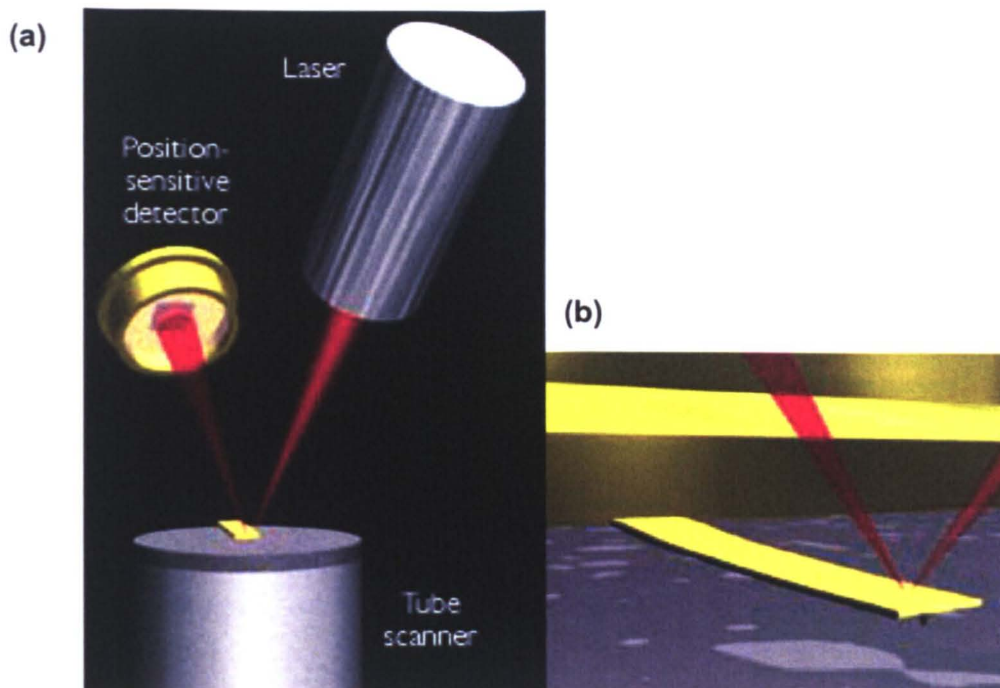

Figure 2.20. AFM principle: (a) Laser system used to detect the deflection of the cantilever during an AFM scan; (b) Tip of the AFM touching the surface of a sample.

AFM measurements can resolve lateral features as small as 30 nm and depth resolutions are below 1 pm

AFM measurements can be taken in several modes that can be classified as non-contact, contact and intermittent-contact modes. In the contact modes, the cantilever is scanned across the specimen in close proximity to the surface and changes in the cantilever deflection are monitored. In the non-contact mode the cantilever is close enough to the surface of the sample so that the attractive or repulsive forces of the surface towards the cantilever are measured. Finally, in the intermittent-contact mode, also known as tapping mode, the cantilever is driven at a fixed frequency close to its free resonant frequency. At each point of the scan, the tip is forced to approach the surface. As the cantilever approaches the surface, its resonant frequency falls. The tip approaches the surface until the resonant frequency has dropped to a fixed set-point. From the amount of displacement suffered by the cantilever, the topography of the surface can be obtained [Midha, 99]. The measurements performed in this work were done using the tapping mode

2.5.2.2 Stylus profilometry (Talystep).

In this type of surface profilometer, a stylus or tip is scanned above the sample with a certain force reproducing the surface topography of the sample. In the present work, a Taylor-Hobson Talystep was used, which allowed a high resolution of 1 % of the full scale (better than 6.4 nm for the typical scale used).

Chapter 3

Optical characterization techniques.

Chapter summary.

The present chapter describes the optical methods that will be used in this thesis work for the characterization of the FHD silica layers. The experimental setup for the optical measurement of the refractive index distribution, the so called "m-lines" setup, is described. Different methods for the theoretical analysis of the mode of a certain waveguide structure are explained, both, for the direct analysis (i.e. calculation of the propagation modes of a given structure) and for the indirect analysis (from a certain distribution of modes, calculate the refractive index profile present in the structure under study). The Fabry-Perot method for the characterization of the losses of channel waveguides is also outlined.

3.1 Introduction.

A collection of techniques are presented in the present Chapter, which were used in the following chapters for the optical characterization of the waveguides fabricated by flame-hydrolysis deposited silica, before and after the irradiation with an electron-beam.

Since one of the aims of this work is the characterization of the refractive index profile of the FHD silica waveguides before and after irradiation with an electron-beam, the experimental method used for the measurement of the refractive index profile, the m-line technique based on grating couplers, is presented in Section 3.2. From this technique, a set of measured values corresponding to the effective refractive indices of the different modes propagating along the waveguide was obtained. In order to obtain the refractive index profile from this set of modes, theoretical calculations need to be carried out.

In Section 3.3, the propagation of light in slab waveguides with both step and graded index profiles is described by the use of a geometric-optics approach and a

more accurate electromagnetic approach, showing how the propagation modes of a waveguide structure can be calculated. In the case of graded index waveguides, two methods for the calculation of the modes of the structure are described: the Wentzel-Kramers-Brillouin (WKB) approximation and the Reflectivity Calculation Method (RCM) based on the use of dark lines.

If the known data is the effective refractive index of the different modes, an inverse method needs to be utilized. The inverse problem is described by the use of two methods: firstly, a step-wise approximation of the profile together with a fitting algorithm to obtain the shape of the refractive index profile that best fits the measured modes; and secondly, by means of an *inverse*-WKB method which allows the direct calculation of the refractive index profile from the measurement of the modes. Both methods are used in Chapter 4 and 5 for the characterization of the germanium-doped FHD silica films before and after irradiation, and a comparison of the profiles obtained with each method is made.

Section 3.4 gives a brief discussion of the modal analysis of 2-D channel waveguides by the use of the effective index method and finally, in Section 3.5, a method for the measurement of the propagation losses of the buried waveguides fabricated using an electron-beam is presented.

3.2 Experimental characterization of the refractive index profile.

In the design of complex integrated optical circuits, the variation in refractive index within a waveguide determines its detailed propagation characteristics. Methods for the determination of the refractive index distribution have been reported in the literature. They can be classified into three major groups [Shiozawa, 1990]:

1. Methods based on the far-field radiation pattern of the guided mode [Hotate, 1979].

2. Methods based on the near-field radiation pattern of the guided mode [McCaughan, 1983], [Morishita, 1986].

3. Methods based on the measurement of the effective refractive index of the different propagation modes [Ding, 1983], [Ulrich, 1973], [White, 1976],

[Chiang, 1985], [Hocker, 1975], [Chandler, 1990], [Sarid, 1980], [Adams, 1979], [Tien, 1974].

The methods belonging to the last set have the advantage of being based only on the measurement of the coupling angle, which can be measured with high accuracy. Amongst these methods, it is the m-line technique based on grating couplers that was used in this work. However, it should be noted that, in common with other coupling methods, this technique also has the disadvantage that the only information available for reconstruction of the refractive index profile is the value of the effective refractive index of the different modes.

An aim of the present work is the determination of the refractive index profile of FHD layers after irradiation with different electron doses. Two obvious options are available for coupling light into the waveguide, which are: firstly, the use of a prism [Ulrich, 1973], [Tien, 1970], [Ulrich, 1970], [Hunsperger, 1991], [Lee, 1986]; and secondly the use of a grating [Hunsperger, 1991], [Dakss, 1970]. Since, in the present work, only a limited region of the waveguide can be electron-beam irradiated, it is important to couple the light into exactly the same spot after each irradiation. Thus, since the waveguide structure could be accurately aligned in the electron-beam writer prior to each irradiation, etching of a grating on the surface of the waveguide in the area that is to be irradiated was chosen as the most appropriate way of coupling technique. In contrast, if a prism coupler were to be used, a large irradiation area would be required because of the difficulty of repeatedly positioning the prism in exactly the same position.

3.2.1 Fundamentals of the m-line technique.

Figure 3.1 depicts the various parameters associated with the coupling of light into a grating of period Λ and depth d.

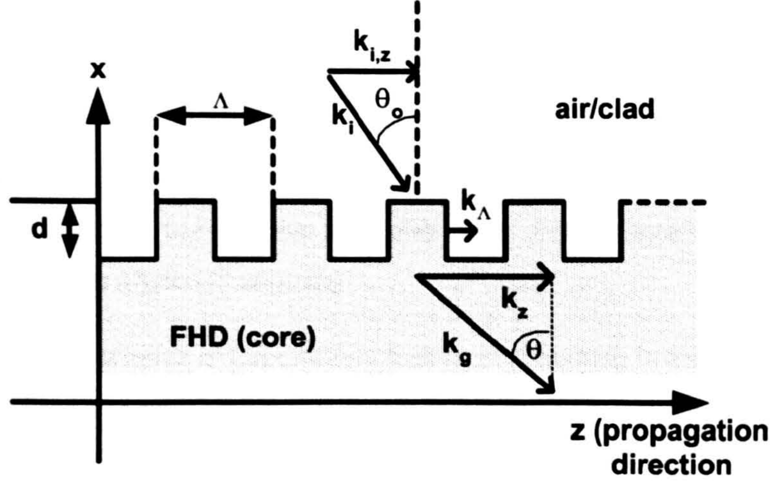

Figure 3.1. Grating-coupling mechanism: The component in the z-direction of the propagation constant of the incident wave, $k_{i,z}$, has to be matched to the propagation constant of the wave propagating in the grating area, k_z+k_Λ.

In order for the incident wave to be coupled into a waveguide mode, the component of the propagation constant in the propagation direction, k_z, needs to satisfy [Ogawa, 1972], [Hunsperger, 1991]:

$$k_{i,z} = k_z + m \cdot k_\Lambda \tag{3.1}$$

where *m* is the grating order and can take the values $m = \pm 1, \pm 2 \ldots$, $k_{i,z} = (2\pi/\lambda) n_a \sin\theta_0$ and $k_z = \beta = (2\pi/\lambda) n_{eff}$ are the components in the propagation direction, *z*, of the propagation constants of the incident wave and the guided mode, $k_\Lambda = (2\pi/\Lambda)$ is the grating vector, n_a is the refractive index of the air, θ_0 is the incident angle, λ is the wavelength of the light in vacuum and $n_{eff} = n_g \sin\theta$ is the effective refractive index of the propagating mode. The angle θ_0 has been taken in this work as the angle formed between the propagation vector and the perpendicular to the propagation direction.

After substituting each term ($k_{i,z}$, k_z and k_Λ) in Equation 3.1 by the values required for coupling of light between the two media, it becomes

$$\frac{2\pi}{\lambda} n_a \sin\theta_0 = \frac{2\pi}{\lambda} n_{eff} + m \cdot \frac{2\pi}{\Lambda} \tag{3.2}$$

which implies

$$n_{eff} = n_a \sin\theta_0 - m \cdot \frac{\lambda}{\Lambda} \quad (3.3)$$

This is known as the phase matching condition of a grating coupler. Equation 3.3 allows the calculation of the effective refractive index of the different modes from the measurement of the angles of coupling.

Since the effective index of the different modes propagating in the structure are needed and the measurements are made in the grating area, it is necessary to take into account the error introduced in the measurement by the presence of the grating. In order to evaluate the magnitude of the error that is introduced into the measurements, the modes of a structure such as the one shown in Figure 3.2 have been calculated.

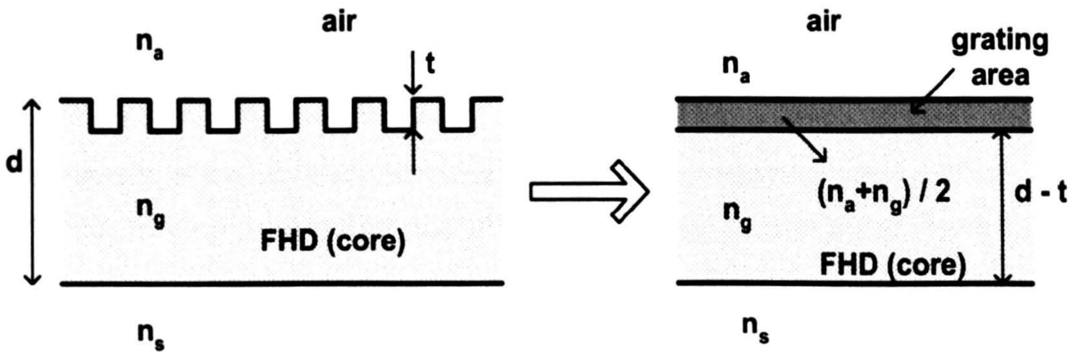

Figure 3.2. Influence of the grating in the measurements: Model used to evaluate the error introduced in the measured modes by the grating coupler. In the figure n_s, n_g and n_a are the refractive indices of the substrate, the FHD core and the air, respectively, d is the thickness of the FHD layer and t the depth of the etched grating. The following values have been used in the calculation: n_a=1, n_g=1.4818, n_s=1.4582, d=5 μm.

The grating area has been approximated as an upper layer having a thickness corresponding to the depth of the grating and a refractive index equal to the average between the refractive indices of the waveguide layer and that of air. Calculations of the effective indices for different grating thicknesses (using methods described later, Section 3.3) are shown in Table 3.1.

It can be seen that the effect on the effective waveguide index is most pronounced for the higher order modes. This is consistent with the higher confinement of the lower order modes to the centre of the waveguide, and

consequently of them having less interaction with the grating. The calculations of Table 3.1 were carried out considering a step-index profile. As it will be seen in the next chapter, the FHD silica samples used in this work have a graded index profile, and the refractive index in the region near the surface is smaller than in the core of the waveguide. Therefore, less influence of the grating would be expected on the measured modes.

mode	without grating	t=70nm	t=100nm	t=200nm
0	1.4807	1.4807	1.4806	1.4806
1	1.4773	1.4772	1.4772	1.4770
2	1.4717	1.4716	1.4715	1.4711
3	1.4642	1.4639	1.4637	1.4631

Table 3.1. Comparison of calculated modes with and without gratings of different depths.

3.2.2 Description of the experimental setup used to measure the effective refractive index.

A schematic of the setup used to measure the effective refractive indices of the different modes of propagation supported by the waveguide is shown in Figure 3.3.

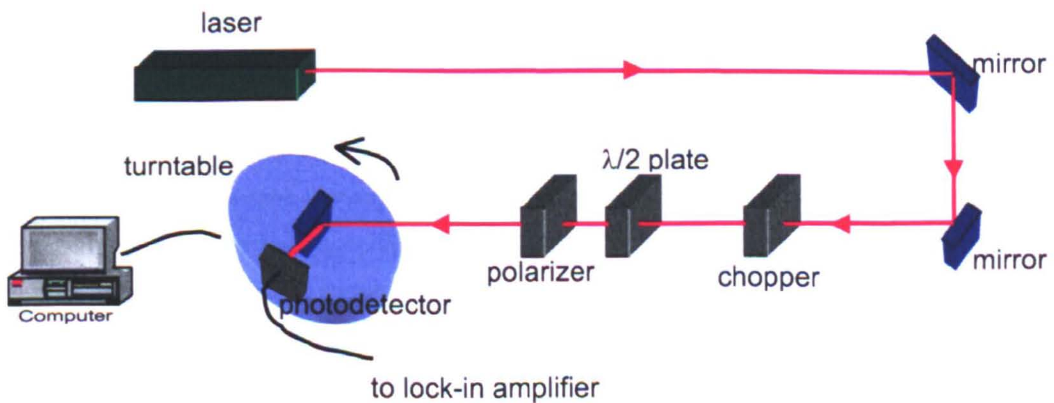

Figure 3.3. Description of the "m-line" setup for the measurement of the effective refractive index of the waveguide modes.

The light from a laser is passed through a half-wave plate and a polarizer, in order to select the polarization of the light incident on the gratings (see Section 3.3.1.2 for a definition of the TE and TM polarizations). The beam has to be aligned to pass

through the middle of the rotary table where the sample must be placed, and the sample is placed perpendicular to the beam.

Figure 3.4 shows an example measurement of the light transmitted at the edge of the waveguide as a function of the incidence angle. The peaks of intensity correspond to the coupling of light into the waveguide, as detected by the photodetector.

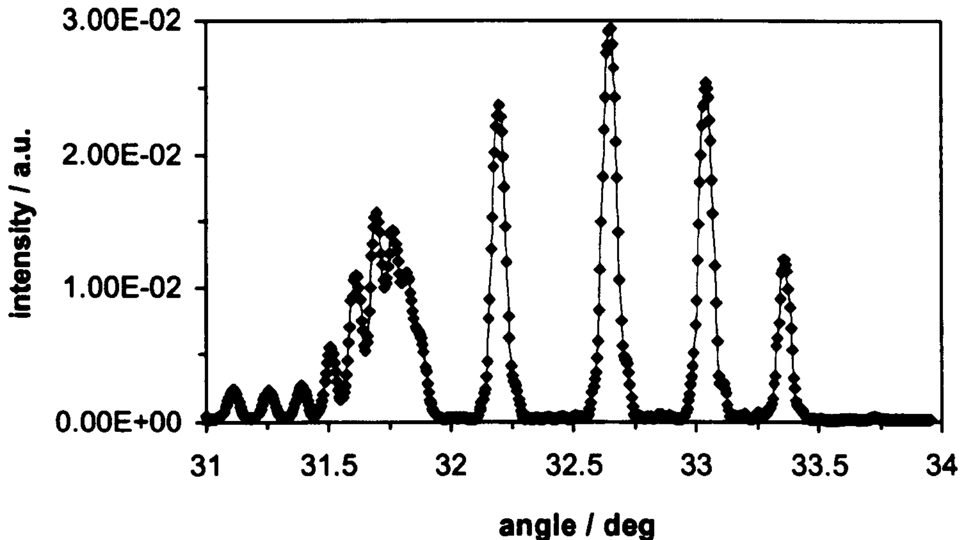

Figure 3.4. Example of measurement with the "m-line" setup: Each peak corresponds to the intensity measured by the photodetector when the light is coupled into a mode supported by the waveguide.

The Newport MM4005 (Newport, UK) motion controller was used to control the rotary stage with an angular resolution < 1 mdeg. The angle of incidence of the light on the grating is scanned with an angular step of 5 mdeg and the light intensity at the output of the slab waveguide was measured with a silicon photodetector, connected to a lock-in amplifier EG&G-5207. Both the motion controller and the lock-in amplifier were controlled from a computer using LabView.

3.2.3 Fabrication of the in-coupling gratings.

The gratings were fabricated by a combination of electron-beam lithography [Campbell, 1996] and reactive ion etching. The protocol followed for the fabrication of the gratings was as follows:

First, the FHD substrates were cleaned in an ultrasound bath in opticlear (5 min), acetone (5 min), methanol (5 min) and rinsing with de-ionized (D.I.) high purity water for 5 min followed by blow drying with nitrogen (standard cleaning procedure). An acid cleaning step was usually also used after the standard cleaning step, in a solution of sulphuric acid and hydrogen peroxide (7:3) at 80 °C for 15 min to remove any possible excess of organics.

Secondly, a layer of poly (methyl methacrylate), PMMA, E2041, 4% diluted in o-xylene was spun at 5000 rpm for 60 sec, giving a thickness of 106 nm. This step was followed by a 30 min bake at 180 °C to remove the excess of solvent in the resist. Another layer of PMMA E2041, 4% diluted in o-xylene (same conditions) was then spun and baked for 60 min at 180 °C.

A thin 30 nm layer of nichrome was then evaporated in a Plassys MEB450 metal evaporator system. The grating pattern was then written by the electron-beam writer, using a dose of 213 $C{\cdot}cm^{-2}$ (this dose was calculated after an exposure test and it is dependent on the nature of the substrate used and the size of the patterns written). After exposure, and prior to development, the nichrome layer was removed in a solution of 200 g ceric ammonium nitrite, 35 ml acetic acid and 1000 ml D.I. water.

Development of the exposed PMMA was performed for 60 sec in a solution 1:1 of IPA:MIBK (isopropyl alcohol and methyl isobutyl ketone) at exactly 23 °C and was immediately rinsed in D:I. water and blown dry with a flow of nitrogen.

It is possible that some remaining resist was still present in the exposed areas, even after development, giving a poor dry-etch. In order to eliminate these, the samples were subjected to an oxygen plasma in a Plasma Asher machine for 30 sec. This step was followed by a 30 sec soak in HCl (hydrochloric acid) diluted 1:4 in D.I. water. The wafer was then rinsed in D.I. water and blown dry.

A dry etch in BP80 machine, with CHF_3 gas as the active gas, RF power of 190 W and etch pressure of 30 mT during 80 sec was then performed. With these conditions, depths <80 nm were obtained, to minimize the error introduced in the measurement by the presence of the grating.

Finally, the removal of PMMA mask was carried out by immersing the sample in hot acetone during several hours. After that, acid cleaning in a sulphuric-peroxide

H_2SO_4:H_2O_2 7:3 solution at 80 °C was performed followed by a standard cleaning procedure.

The evaporation of a thin layer of NiCr prior to electron-beam exposure was necessary in order to avoid charging of the sample during exposure, which would affect the definition of the pattern.

Figure 3.5 (a) shows an SEM picture of the gratings just after dry etch step. The hardening suffered by the resist during the etch step leads to a rough surface. After immersion in hot acetone, Figure 3.5 (b) shows that the PMMA has not been completely removed. Thus, an acid cleaning step is required to remove the residues of resist, Figure 3.5 (c).

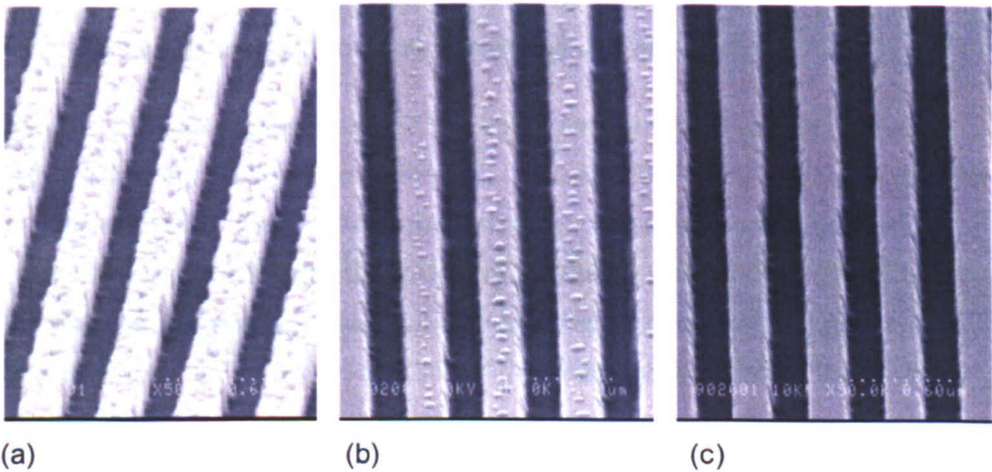

(a) (b) (c)

Figure 3.5. Removal of resist in dry-etched gratings: (a) Gratings directly after the dry etching step. It can be seen the modification that the resist, smooth originally, has suffered during the plasma etch. (b) Same grating after several hours in hot (50 deg) acetone. (c) Same grating after acid cleaning step.

3.2.4 Estimation of measurement errors.

In the characterization of the refractive index profile by the m-line technique it is very important to make accurate measurements of the coupling angles. There are several major sources of error, the most important of which are the fabrication errors in the grating period, the possible instability of the wavelength of the He-Ne laser and the misalignment in the determination of the angular zero position.

Concerning the errors in the fabrication of the gratings, the parameter having most influence on the coupling angle is the period of the grating. The estimated

averaged variation (given by the manufacturer of the electron-beam writer machine) in the period of such a kind of structure written by the electron-beamwriter used is 0.01%, which in the case of a period of 680 nm represents 0.068 nm. However, it should be noted that the ratio of etched/un-etched profile does not influence the angle of coupling of the modes, although it does influence the efficiency of the coupling.

The 632.8 nm wavelength He-Ne laser (JDS Uniphase) used can also exhibit instability in the wavelength, thus affecting the evaluation of the effective refractive index. Nevertheless, for the laser used in this work, this fluctuation was neglible.

Finally, the alignment of the sample with respect to the coupling laser beam is important, in order to have a correct definition of the angle "0". The "from measurement to measurement" variation must be minimized and, in order to achieve this, the following alignment routine was utilized:

Firstly, the beam was positioned in the middle of the rotation stage, since it is critical that the laser beam passes through the axis of the rotation stage. Once the beam was aligned on the middle of the turntable, the sample was aligned to the beam. If the beam were not in the middle of the stage, when turning the turntable to scan the angle, the sample would not only experience a rotation, but also a translation (which will move the position of the beam with respect to the grating).

Secondly, the sample was aligned perpendicular to the laser beam. This position determines the definition of the origin of the angles (i.e. the angle "0"). If the sample were not perfectly perpendicular to the beam when the position of the beam indicated in the motion controller is 0, an offset on the definition of the angle that affects the accuracy of the measurements would be introduced. This is shown in Figure 3.6. In order to perform this alignment, an aperture was located 27.5 cm in front of the sample in the path of the beam. The sample was placed in a "micro-block" in which the rotation was adjusted until the reflected beam from the surface of the sample would overlap with the incident beam. This was accomplished by making the reflection pass back through the aperture. However, as the size of the aperture is ≈100 μm, some offset in the angle will still be present.

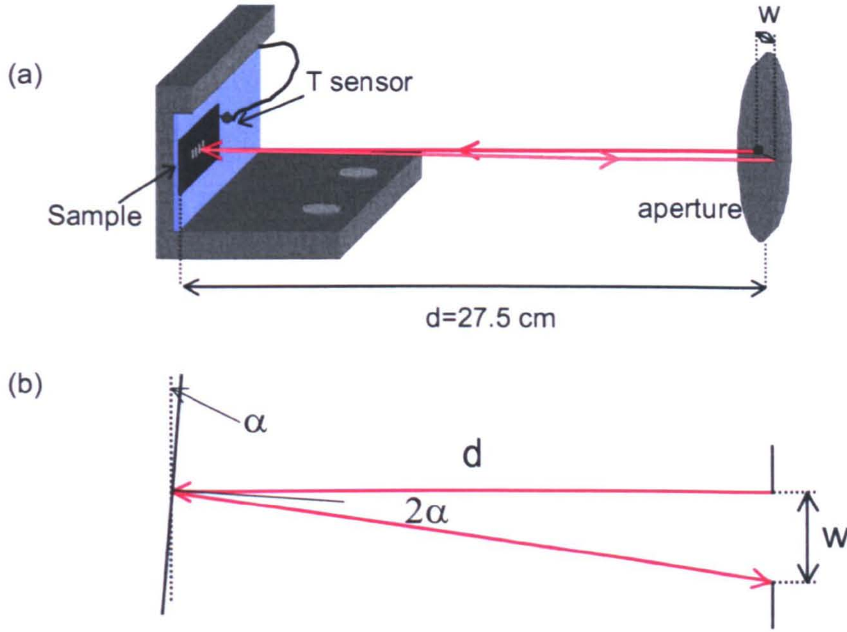

Figure 3.6. Alignment of the angle "0": (a) Sample holder and aperture used for the experiment; (b) Ray representation of the incident beam. It can be seen that, due to the finite size of the aperture, an error of ±α can be introduced in the definition of the angle "0".

From Figure 3.6 (b) the magnitude of the angular offset can be calculated as:

$$\alpha = \frac{tan^{-1}\frac{w}{d}}{2} = 0.0104\,(deg) \tag{3.4}$$

From the measured angles, the effective refractive index was calculated as $n_{eff} = n_a\, sin\theta + \lambda/\Lambda$ for a first order grating. The error in the calculation of n_{eff} can be calculated as

$$\sigma_{neff}^2 = \sigma_\theta^2 \cdot \left(\frac{\partial n_{eff}}{\partial \theta}\right)^2 + \sigma_\lambda^2 \cdot \left(\frac{\partial n_{eff}}{\partial \lambda}\right)^2 + \sigma_\Lambda^2 \cdot \left(\frac{\partial n_{eff}}{\partial \Lambda}\right)^2 = \sigma_\theta^2 \cdot \cos^2\theta + \sigma_\lambda^2 \cdot \frac{1}{\Lambda^2} + \sigma_\Lambda^2 \cdot \left(\frac{\lambda}{\Lambda^2}\right)^2 \tag{3.5}$$

In Table 3.2 the values that correspond to the present case are shown. The only part of the error that can be minimized is the one dependent on the alignment on the beam, as the error in the period due to the beam-writer cannot be changed.

Parameter	Value
σ_θ	0.0104 (deg) (Eq. 3.4)
σ_λ	≈ 0
σ_Λ	0.068 (nm)
Λ	680 (nm)
λ	632.8 (nm)
θ	31.5-34 (deg)
error squared due to σ_θ (1st term Eq. 3.5)	$2.40\ 10^{-8} - 2.26\ 10^{-8}$
error squared due to σ_λ (2nd term Eq. 3.5)	≈ 0
error squared due to σ_Λ (3rd term Eq. 3.5)	$1.274\ 10^{-7}$
total maximum error	**$3.89\ 10^{-4} - 3.87\ 10^{-4}$**

Table 3.2. Variability of the different parameters involved in the m-line technique.

In order to evaluate the measurement error experimentally, a series of measurements were performed on the same grating during a certain period of time, making sure that the setup was both misaligned and then re-aligned between consecutive measurements. The total number of measurements was 18, from which the mean and standard deviation were calculated and are shown in Table 3.3.

mode 0	mode 1	mode 2	mode 3
$1.4804 \pm 1.58\ 10^{-4}$	$1.4759 \pm 1.65\ 10^{-4}$	$1.4702 \pm 1.8\ 10^{-4}$	$1.4635 \pm 1.63\ 10^{-4}$

Table 3.3. Experimental estimation of the measurement errors.

The experimental results are typically better than the maximum error calculated theoretically. Therefore, error bars of $\pm\ 2.10^{-4}$ have been assigned in the graphs concerning measurement of the refractive index.

3.3 Theoretical analysis of the modes of propagation of a slab waveguide structure.

By using the m-lines technique based on grating couplers (Section 3.2), a set of effective refractive indices of the different modes supported by the waveguides was obtained. A particular distribution of modes is representative of a certain refractive index profile. Thus, beginning with the known (measured) effective refractive index of the different modes, the refractive index distribution in depth of the waveguide structure under study was obtained.

In order to achieve this goal, understanding of the theoretical analysis of planar optical waveguides was first required, after which, the methods to calculate the refractive index profile from the knowledge of the propagation modes were studied.

The study of the propagation of light in different media was carried out by solving the electromagnetic equations (Maxwell's equations) with the appropriate boundary conditions. In this case, an exact solution of the propagation modes was obtained. Nevertheless, in cases for which the refractive index varies by only a small amount in a distance comparable to the wavelength of the propagating light, a more intuitive, geometric ray-optics approach can be followed in order to obtain an approximated description of the propagation of light. In this approach, the electromagnetic waves travelling in the waveguide are represented by their wavevector, $\vec{k}$, which determines the path followed by the wave inside the waveguide. The trajectory followed by the wave depends on the refractive index distribution across the perpendicular to the direction of propagation z.

For the two kind of index distribution studied in this section, the step index and graded index distributions, a ray optics treatment was first described in order to understand the propagation of light in such media and then, a treatment based on the electromagnetic theory was developed and the results obtained with the two different methods were finally compared.

3.3.1 Propagation of light in a step-index slab guide.

3.3.1.1 Ray-optics approach.

A guide with the uniform index distribution shown in Figure 3.7 (a) was considered. When a light beam propagates inside the film, one dimension of the beam, in this case *x*, is confined by the thickness of the film, whilst in the other dimension, *y*, the wave can propagate freely. The light propagating along the propagation direction, *z*, is considered as formed by two fronts of plane waves bouncing back and forth between the two surfaces of the guide [Lee, 1986], [Hunsperger, 1991]. The plane waves are represented by their propagation vectors, $\vec{k}_g$, which are perpendicular to the plane of constant phase. The path traveled by the wave is represented by a ray with the direction of the propagation vector, as can be seen in Figure 3.7 (b).

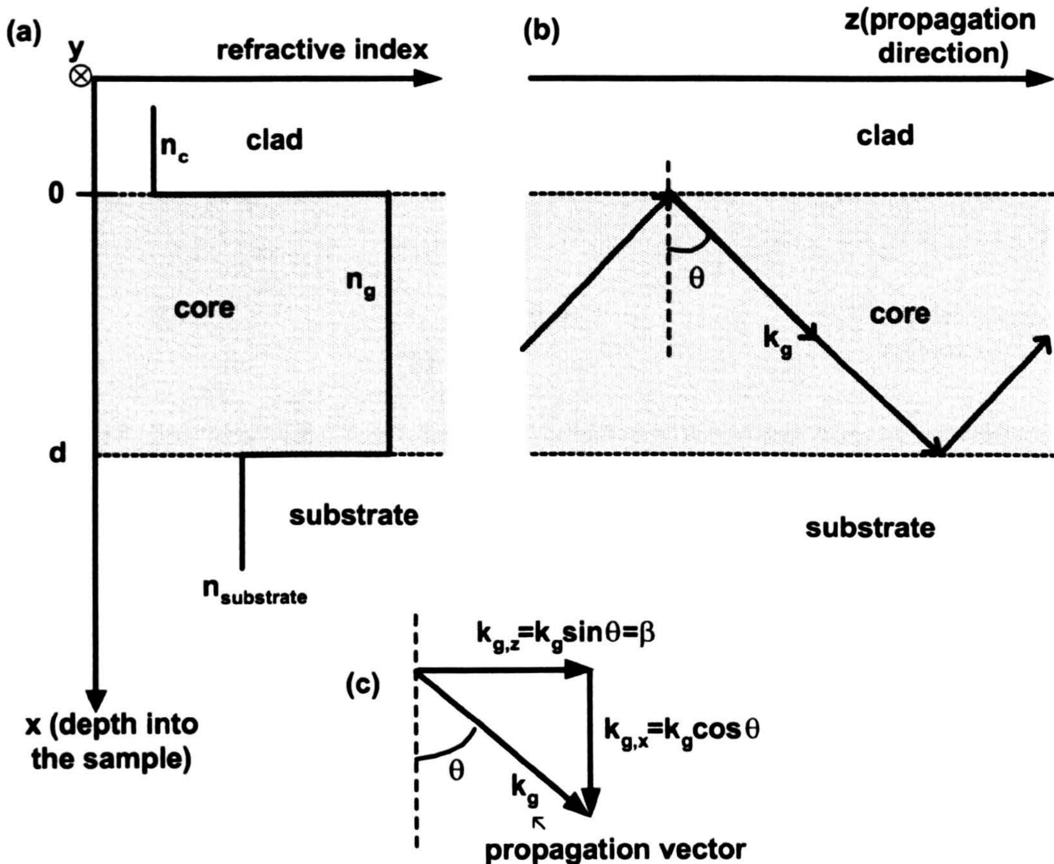

Figure 3.7. Ray-propagation in a step-index waveguide: (a) Refractive index profile corresponding to a step-index waveguide; (b) Propagation of a wave along the waveguide, represented by the ray trajectory of its propagation vector $\vec{k}_g$. (c) Components of the propagation vector in the *x* and *z* directions.

At the interface between two media with different refractive indices, guide and cladding or guide and substrate, the angles of the incident, reflected and transmitted rays follow the Snell's law relation (Figure 3.8) [Hunsperger, 1991]:

$$n_a \sin\theta_i = n_b \sin\theta_t \qquad (3.6)$$

If $n_a > n_b$, a critical angle exists such that for incident angles larger than the critical angle there is no transmitted beam. This situation is known as "total internal reflection" and is represented in Figure 3.8 (c). The condition for total internal reflection determines the range of angles that the incident ray can adopt in order for the light to be confined inside the structure.

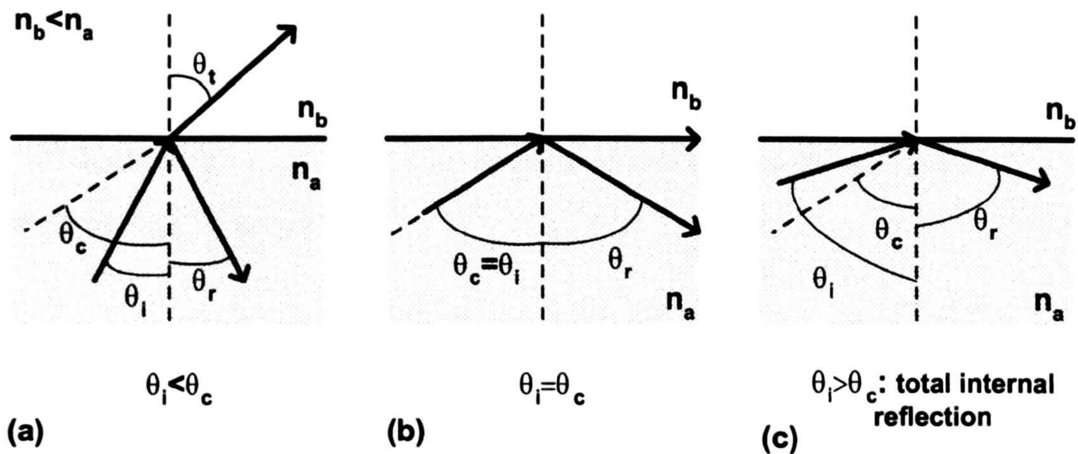

Figure 3.8. Schematic of the Snell's law for the reflection at a boundary between two media with refractive indices n_a and n_b such as $n_b<n_a$: (a) Incident angle smaller than the critical angle; (b) Incident angle equal to the critical angle: the transmission angle is 90 degrees; (c) Incident angle larger than the critical angle: total internal reflection at the interface.

The "total internal reflection" condition is not the only restriction that has to be satisfied for a wave to propagate along the waveguide. Also, the wavefronts of the different propagating waves into the waveguide need to be in-phase in order to interfere constructively. This situation is illustrated in Figure 3.9, in which the propagation of the wave is indicated by the ray path. The wavefront or plane of constant phase is depicted by the dashed line. From Figure 3.9 it can be seen that points A and C need to be in phase, i.e. their phase difference needs to be a multiple of 2π, as their belong to the same phase front, i.e. both are on the dashed line. The phase change from the point A to the point C can be calculated as the sum of the phase change accumulated during the path l_{ABC} plus the phase shifts due to reflections at the cladding and substrate interfaces.

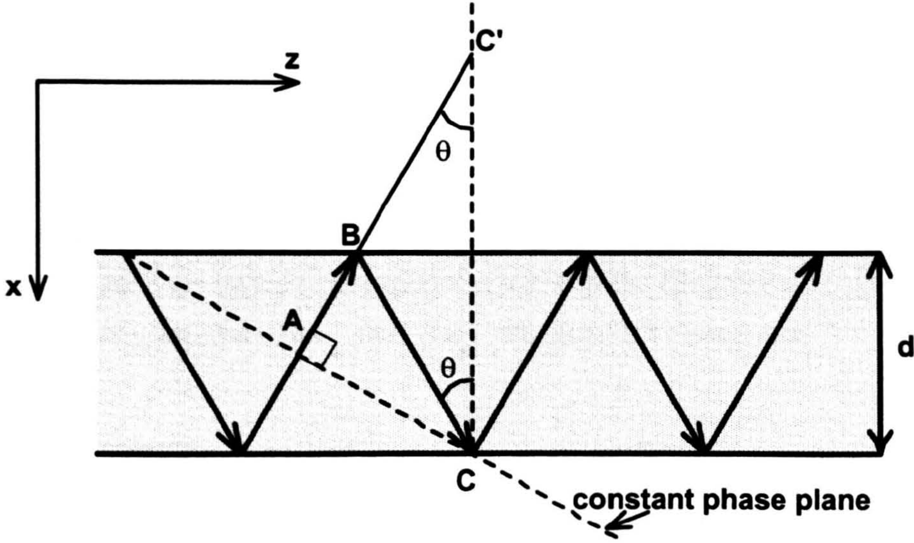

Figure 3.9. Transmission of light through a waveguide. The points A and C are in the same wavefront, thus, their phase difference must be a multiple of 2π. In order to evaluate the distance ABC the graphical construction depicted here can be used.

The path length l_{ABC} can be determined by unfolding it into the equivalent distance l_{ABC}' (Figure 3.9):

$$l_{ABC} = l_{ABC'} = 2d\,cos\theta \tag{3.7}$$

Therefore, the phase change after this distance is given by

$$\phi_{path} = 2dk_g \cos\theta \tag{3.8}$$

where k_g is the magnitude of propagation constant in the guide region: $k_g = (2\pi/\lambda)n_g$.

The phase shifts on reflection at the boundaries between two media with refractive indices n_a and n_b are given by [Born, 1959]:

$$\phi_{a-b,TE} = -2\,tan^{-1}\left(\frac{\sqrt{n_a^2\,sin^2\theta - n_b^2}}{n_a\,cos\theta}\right) \tag{3.9}$$

$$\phi_{a-b,TM} = -2\,tan^{-1}\left(\frac{n_a^2}{n_b^2}\frac{\sqrt{n_a^2\,sin^2\theta - n_b^2}}{n_a\,cos\theta}\right) \tag{3.10}$$

Therefore, the condition for constructive interference between the wavefronts can be expressed as

$$\phi_{path} + \phi_{guide_clad} + \phi_{guide_substrate} = 2m\pi \qquad (3.11)$$

After substitution of the phase shift produced at the guide-clad and guide-substrate interfaces by their corresponding expressions (Equations 3.9 and 3.10) and taking into account that $n_g \sin\theta = n_{eff}$, Equation 3.11 becomes

$$2\,d\,k\sqrt{n_g^2 - n_{eff}^2} - 2tan^{-1}\left(\frac{\sqrt{n_{neff}^2 - n_c^2}}{\sqrt{n_g^2 - n_{eff}^2}}\right) - 2tan^{-1}\left(\frac{\sqrt{n_{eff}^2 - n_s^2}}{\sqrt{n_g^2 - n_{eff}^2}}\right) = 2m\pi \qquad (3.12)$$

for TE modes and

$$2\,d\,k\sqrt{n_g^2 - n_{eff}^2} - 2tan^{-1}\left(\frac{n_g^2}{n_c^2}\frac{\sqrt{n_{neff}^2 - n_c^2}}{\sqrt{n_g^2 - n_{eff}^2}}\right) - 2tan^{-1}\left(\frac{n_g^2}{n_s^2}\frac{\sqrt{n_{eff}^2 - n_s^2}}{\sqrt{n_g^2 - n_{eff}^2}}\right) = 2m\pi \qquad (3.13)$$

for TM modes, which represent what is known as the "transverse resonance condition" [Adams, 1981].

By solving Equations (3.12) and (3.13), the effective refractive index corresponding to the allowed modes of the waveguide structure under study can be calculated by numerical methods.

3.3.1.2 Electromagnetic approach.

Consider again the waveguide structure of Figure 3.7, in which the regions corresponding to cladding and substrate are infinite along the -*x* and +*x* directions respectively. The properties of the structure were considered to be uniform in the *y*-direction ($\frac{\partial}{\partial y} = 0$).

From Maxwell's equations, it can be demonstrated [Lee, 1986] that only two polarizations, TE, with only field components ($0,E_y,0$) and ($H_x,0,H_z$) and TM, with field components ($E_x,0,E_z$) and ($0,H_y,0$) can propagate along the structure. For the

case of a time-harmonic TE plane travelling in the *z*-direction, with propagation constant $\beta=k_z$, the electric field, $E_y(x,z,t)$, needs to obey the wave equation

$$\nabla^2 E_y = \frac{n^2}{c^2}\frac{\partial^2 E_y}{\partial t^2} \tag{3.14}$$

where *n* represents the refractive index of the different regions of the waveguide and *c* is the speed of light in vacuum. Equation 3.14 has a solution of the form

$$E_y(x,z,t) = E'_y(x)\exp i(\omega t - \beta z) \tag{3.15}$$

Substituting Equation 3.15 into the wave-equation (Equation 3.14) gives:

$$\frac{\partial^2 E_y'}{\partial x^2} + \left(k^2 n^2 - \beta^2\right)E_y' = 0 \tag{3.16}$$

where $k \equiv \omega/c$ is the magnitude of the propagation vector in vacuum and *n* is the refractive index of the region in which the Equation 3.16 is applied. The solution to Equation 3.16 in the different waveguide regions depends on whether $\left(k^2 n^2 - \beta^2\right)$ is positive or negative in that region. In a waveguide in which the refractive index of the core is larger than the refractive index of the cladding and of the substrate, the solutions of the electric field in the different regions are:

$$\begin{array}{ll} A\exp(-qx) & 0 \le x \le \infty \\ B\cos(hx) + C\sin(hx) & -d \le x \le 0 \\ D\exp[p(x+d)] & -\infty \le x \le -d \end{array} \tag{3.17}$$

where $q = \left(\beta^2 - n_c^2 k^2\right)^{\frac{1}{2}}$, $h = \left(n_g^2 k^2 - \beta^2\right)^{\frac{1}{2}}$ and $p = \left(\beta^2 - n_{substrate}^2 k^2\right)^{\frac{1}{2}}$ are obtained by substituing Equations (3.17) into the wave equation (3.16). Applying the boundary conditions of continuity of the tangential components of the electric and magnetic fields at the core-cladding and core-substrate boundaries, i.e. *x=0* and *x=-d*, the following relation between the different parameters, *p*, *q* and *h*, can be obtained [Hunsperger, 1991], [Adams, 1981]

$$\tan(hd) = \frac{p+q}{h\left(1-\frac{pq}{h^2}\right)} \qquad (3.18)$$

which is equivalent to the transverse resonance condition obtained by the ray-approach method. The solution of Equation (3.18) is a set of effective refractive indices corresponding to the allowed propagation modes in the structure.

3.3.1.3 The "cut-off" condition and the number of propagating modes supported by a slab waveguide.

As has been mentioned in Section 3.3.1.1, the angle that the propagation vector makes with the normal to the interface must be larger than the critical angle for both the cladding and the substrate in order for the wave to be confined in the core of the structure. If the angle is smaller than the critical angle for the cladding, radiation into the cladding will occur. If the propagation angle is smaller than the critical angle for the substrate, radiation of energy to the substrate will take place. It is important to note that the refractive index of the substrate is closer to the core index than the refractive index of the air.

The "cut-off" condition, i.e. the condition for which the mode is no longer confined in the core of the structure, is therefore given by

$$\beta = kn_a \qquad (3.19)$$

where n_a is the larger of the refractive indices of the cladding and substrate (it determines which radiation begins to take place first). Since in our case $n_c=1$ and $n_s=1.4582$, the cut-off condition will be determined by the beginning of the radiation modes into the substrate.

In order to calculate the number of modes that can be guided in a particular structure, the cut-off condition is substituted in the transverse resonance condition (Equations 3.12 and 3.13) and the number of modes, N, is evaluated [Adams, 1981]:

$$N = \frac{1}{\pi}\left\{kd\sqrt{n_g^2-n_s^2} - \tan^{-1}\left(\frac{\sqrt{n_s^2-n_c^2}}{\sqrt{n_g^2-n_s^2}}\right)\right\}_{\text{int}} \qquad \text{for TE modes} \qquad (3.20)$$

$$N = \frac{1}{\pi}\left\{ kd\sqrt{n_g^2 - n_s^2} - \tan^{-1}\left(\frac{n_g^2}{n_c^2}\frac{\sqrt{n_s^2 - n_c^2}}{\sqrt{n_g^2 - n_s^2}} \right) \right\}_{\text{int}} \quad \text{for TM modes} \tag{3.21}$$

where the subscript "int" means the next largest integer.

3.3.2 Propagation of light in a graded-index medium.

3.3.2.1 Determination of the kind of refractive index profile from a n_{eff}^2 versus $(m+1)^2$ plot.

It is known [Chandler, 1986], [Townsend, 1994] [Tien, 1974] that the spacing of the effective refractive indices of the modes supported by a waveguide is related to the refractive index distribution inside the structure. In a step-index guide, a plot of the squared effective refractive index as a function of $(m+1)^2$, where m represents the mode order, should be a straight line with negative slope. It should be pointed out that, due to the discrete nature of the modes, this graph represents discrete points and not a continuous function.

This could be explained, for a step-index distribution, by considering the transverse resonance condition across the depth of the waveguide structure:

$$2k_x d + \phi_{clad-core} + \phi_{substrate-core} = 2m\pi \tag{3.22}$$

For the case of a step index distribution, the phase shifts due to reflection at the clad-waveguide and waveguide-substrate boundaries can be approximated to π. Therefore, Equation 3.22 becomes

$$2k_x d - \pi - \pi = 2m\pi \Rightarrow d\, k\left(n_g^2 - n_{neff}^2(m)\right)^{\frac{1}{2}} = \pi(m+1) \tag{3.23}$$

which leads to

$$n_{eff}^2(m) = n_g^2 - \left(\frac{\lambda}{2d}\right)^2 (m+1)^2 \tag{3.24}$$

As m can only take integer values $m=0,1,2...$ Equation (3.24) represents a straight line with negative slope and discrete values.

3.3.2.2 Ray-optics approach.

Let the refractive index profile of a planar waveguide which occupies the half-space $x>0$ be monotonically decreasing (the discussion will easily be changed for profiles with other characteristics) as shown in Figure 3.10, where, again, z is the direction of propagation of the electromagnetic field.

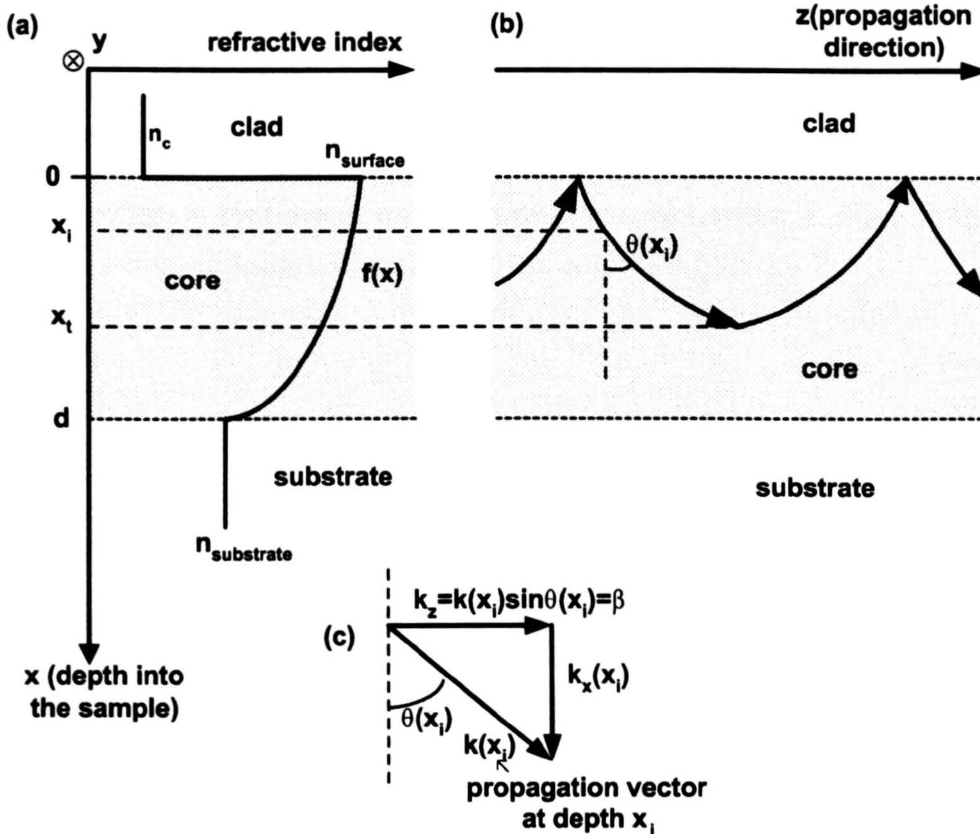

Figure 3.10 Ray-propagation in a graded-index profile waveguide: (a) Refractive index profile (monotonically decreasing) of a waveguide for which the propagation vector has a single turning point; (b) Ray-trajectory of the wave traveling along the structure and physical meaning of the turning point; (c) Propagation vector k at a certain depth, x_i, and its components in the propagation direction z, $k_z = n(x_i)k_0 \sin\theta(x) = n_{eff}k_0$ and in the x-direction, $k_x(x_i)$.

The electric and magnetic fields propagating in the waveguides adopt different distributions in the different regions defined by the refractive index, but they have to be matched along the interfaces between regions with different refractive index, forcing the component in the propagation direction of the propagation constant, $k_z=\beta$, to be the same at all points in the guide. As can be seen in Figure 3.10 (c), the z-component of the propagation constant is given by:

$$k_z = \beta = n(x_i) \cdot \sin\theta_i \cdot k_0 \qquad (3.25)$$

where x_i refers to the different points along the profile of the waveguide, θ_i is the angle formed by the propagation vector and the normal to the direction of propagation, z, and $k_0 = 2\pi/\lambda$ is the free-space phase constant. The term k_z is known as β and the quantity $n(x_i) \cdot sin\theta_i$ is the effective refractive index , $n_{eff}(m)$, for the propagation mode m. Therefore, as β is constant along the waveguide structure, the effective refractive index will be constant in all the regions of the structure, being the characteristic parameter of each propagating mode.

At the depth x_i, the wave mode has a total propagation vector, k, which makes an angle θ_i with the propagation direction z. The angle θ_i is given by

$$\theta_i = sin^{-1}\left(\frac{n_{eff}(m)}{n(x_i)}\right) \qquad (3.26)$$

where, as has just been stated, $n_{eff}(m)$ is a constant characteristic of the mode. As the wave advances a distance Δz in the propagation direction, it penetrates a depth Δx_i into the structure, where $\Delta z_i = \Delta x_i \, tan\theta_i$ as can be seen in Figure 3.10 (c). The refractive index at the point x_i+Δx_i will be $n(x_i)+\Delta n_i$, where the increment of the refractive index depends on the shape of the refractive index profile. In the case of a monotonically decreasing profile, $n(x_i)+\Delta n_i < n(x_i)$. Therefore, $\theta_{i+1} > \theta_i$, and the direction of the propagation vector will begin to change until the depth, x_t, at which $n(x_t)=n_{eff}(m)$. At this depth, Equation (3.26) indicates that the propagation vector will be parallel to the propagation direction, z. For $x>x_t$, $n(x)$ will be smaller than n_{eff} , making θ_i imaginary. Therefore, the ray cannot propagate in that region, bouncing upwards at the depth x_t, Figure 3.10 (b). The point x_t is therefore known as the turning point for that propagating mode [Hocker, 1975].

As for the case of the step index distribution (Section 3.3.1.1), only certain modes are allowed to propagate in the waveguide. In order for a mode to propagate, the total phase change in a round trip in the direction perpendicular to the propagation direction has to be an integer multiple of 2π [Lee, 1986], [Hocker, 1975]. In order to calculate this phase change, the infinitesimal change of phase, $d\phi$, after an incremental displacement dx needs to be considered:

$$d\phi = n(x)\cdot k_0 \cdot \cos\theta_i \cdot dx = k_0\left[n(x)^2 - n_{eff}(m)^2\right]^{\frac{1}{2}} dx \qquad (3.27)$$

where $n_{eff}(m)$ is the effective refractive index of the mth mode of propagation.

In the case of a waveguide with a refractive index profile that is monotonically decreasing with depth, only one turning point, at x_t will be present. The wave will therefore propagate, bouncing between the air or cladding interface and the turning point, if the refractive index profile satisfies the following integral equation that requires the total phase change to be a multiple of 2π ("transverse resonance condition"):

$$2\int_0^{x_t(m)} k_0\left[n(x)^2 - n_{eff}(m)^2\right]^{\frac{1}{2}} dx + \phi_1 + \phi_2 = 2\pi m \qquad (3.28)$$

where x_t is the depth corresponding to the turning point (Figure 3.10), ϕ_1 is the phase change at the air or cladding surface and ϕ_2 is the phase change at the turning point (x_t) for the mode m.

If, in contrast to the refractive index profile described above, there is a maximum in the refractive index profile (Figure 3.11), the propagation vector is bounded between two different depths, buried in the waveguide structure. This oscillation of the vector is also described as being confined between two turning points. Thus, in the case shown in Figure 3.11, the limits in the integral equation are changed to x_{t1} and x_{t2}:.

$$2\int_{x_{t1}(m)}^{x_{t2}(m)} k_0\left[n(x)^2 - n_{eff}(m)^2\right]^{\frac{1}{2}} dx + 2\phi = 2\pi m \qquad (3.29)$$

In the last two equations, $n_{eff}(m)$ represents the refractive index of the mth-mode, and is equal to $n(x_t)$ at the turning point. Only the propagation modes the effective refractive index of which obeys this equation are guided in the waveguide.

The phase-shift suffered by the field due to reflection at the turning point can be calculated by taking into account the fact that, if the refractive index change with depth is slow, the refractive index at $n(x_{t2}^{+})$ is equal to the refractive index $n(x_{t2}^{-})$. Therefore, the phase shift at that point tends to $\phi = -\pi/2$ (Equations 3.9 and 3.10). Again, the phase shift experienced by the beam at the boundary with the cladding or

with the substrate can be evaluated by using Equations 3.9 and 3.10, together with the appropriate values for the refractive indices corresponding to mode *m*.

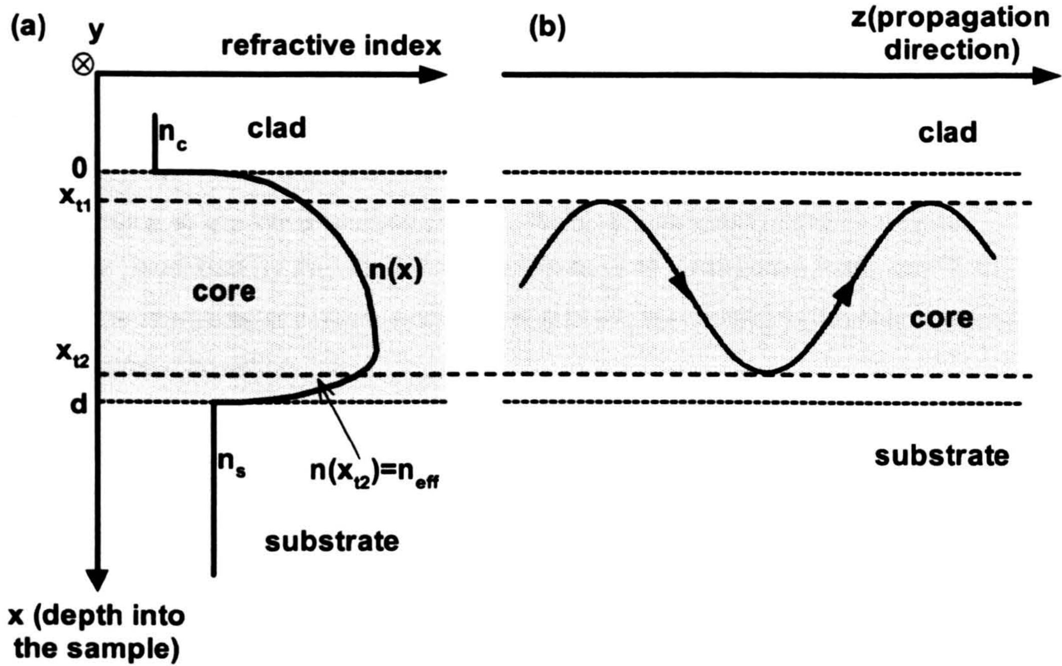

Figure 3.11. Ray tracing in a profile of refractive index with two turning points: (a) Profile of refractive index; (b) The trajectory of the propagation mode bounces between x_{t1} and x_{t2}.

3.3.2.3 The Wentzel-Kramers-Brillouin (WKB) method for solving the modes of a graded-index profile waveguide.

Let the refractive index profile of a waveguide be *n(x)*, with *x* perpendicular to the cladding-core interface and to the direction of propagation *z*. For the TE modes, the modal field distribution for the electric field, $E'_y(x)$ satisfies the Helmholtz equation (Equation 3.16).

Equation 3.16 is similar to the eigenmode equation of an electron in a quantum well, and the different allowed energy levels of the electron in the quantum well correspond to the modes of the waveguide and the different eigenmodes correspond to the wavefunction for those allowed levels. In our case, the eigenvalues of Equation 3.16 represent the different propagation constants, β, of the different allowed propagation modes in the waveguide and the eigenmodes, the field distribution, $E'_y(x)$, of the different allowed modes.

Due to the analogy with the well-known problem in quantum mechanics , the methodology used there can be applied to determine the modes in a waveguide in the present context [Chandler, 1986]. Among the different methods used in quantum mechanics, the Wentzel-Kramers-Brillouin (WKB) method has been largely demonstrated to lead to very accurate solutions when the refractive index function is a slowly varying function of the transverse position [Marcuse, 1973] [Chiang, 1985] [White, 1976] [Gedeon, 1974], [Tien, 1974].

According to the WKB-method [White, 1976], the solution of the eigenvalue problem described by Equation 3.16, for the case of a refractive index profile for which the ray-trajectory has a single turning point, is reduced to the resolution of the characteristic equation

$$2\int_0^{x_t(m)} k_0\left[n(x)^2 - n_{eff}(m)^2\right]^{\frac{1}{2}} dx + \phi_1 + \phi_2 = 2\pi m \qquad (3.30)$$

where $n(x)$ is the refractive index profile, $n_{eff}(m)$ is the effective refractive index for each of the allowed propagation modes, $x_t(m)$ is the turning point for the mode m, where $n(x_t(m)) = n_{eff}(m)$ as discussed in the previous section, ϕ_1 and ϕ_2 are the phase shifts at the surface and turning point respectively. Equation 3.30 is the same as has been obtained in Section 3.3.2.2 by the ray-tracing method.

Knowledge of the refractive index profile allows the calculation of the modes supported by the waveguide by solving the integral equation numerically, as discussed in the literature [White, 1976], [Chiang, 1995], [Gedeon, 1974], [Tien, 1974].

3.3.2.4 Reflectivity-calculation method (RCM) for the calculation of the modes of propagation of an arbitrary refractive index profile structure.

Chandler and Lama [Chandler, 1986], [Chandler, 1990] have detailed the reflectivity calculation method (RCM) for the calculation of the modes of an arbitrary structure. The method is based on the experimental technique of observing the “dark lines”: by means of a prism coupler of higher refractive index than the waveguide structure, light is coupled into the waveguide, as can be seen in Figure 3.12.

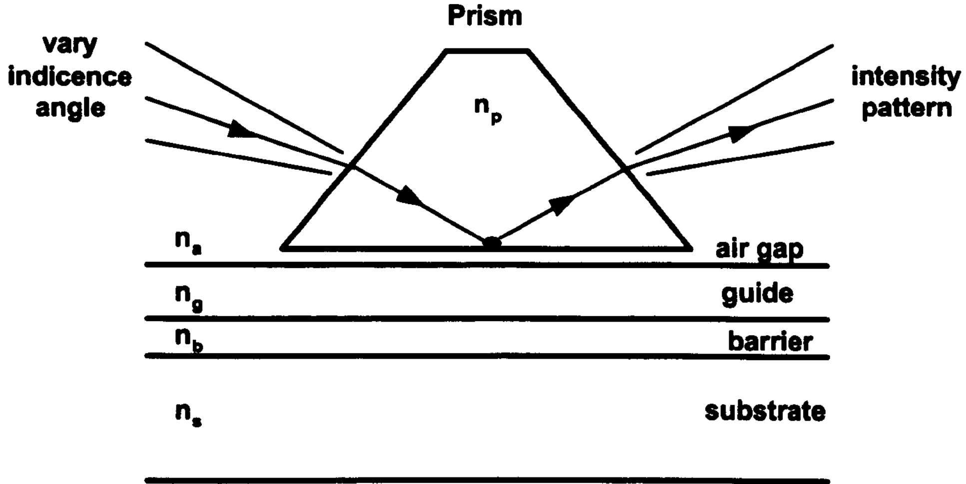

Figure 3.12. The dark-mode experimental setup: Varying the angle of incidence is equivalent to varying $n_{eff}(m)$, i.e. β/k. The values of $n_{eff}(m)$ for which a minimum in the intensity of the output is detected correspond to resonances in the guiding layer structure, i.e. the modes of the waveguide structure.

The light reflected at the prism-waveguide boundary is then observed. The incident angle of the light is varied, thus varying the propagation constant, β, of the light coupled into the structure. Only at certain angles, will the "resonance" condition be satisfied, resulting in the light being coupled into a waveguide mode (or a substrate mode) and therefore, a dip (dark line) in the intensity of the reflectivity will be observed.

In the calculations, the structure is divided into many thin layers (Figure 3.13). In each of them the wave field is composed of a forward and a backward spatial component in the *x*-direction, perpendicular to the surface of the structure, as has previously been discussed in Section 3.3.1.1. In each layer, the electric field component has a spatial distribution of the shape

$$E_y^{'}(x) = A\,exp(+ik_x x) + B\,exp(-ik_x x) \qquad (3.31)$$

where $k_x = kn(x)cos\theta(x) = k\left(n^2(x) - n_{eff}^2(m)\right)^{\frac{1}{2}}$ is the *x*-component of the propagation vector in the medium. In Equation 3.31, the structure is considered to be uniform and infinite in the *y*-direction. Light propagates along the waveguide along the *z*-direction (Figure 3.13). The spatial component of the electric field has an oscillating nature in the regions of the structure where $n_{eff}(m) < n(x)$

(confinement region), and a decaying nature in the other regions (evanescent field regions).

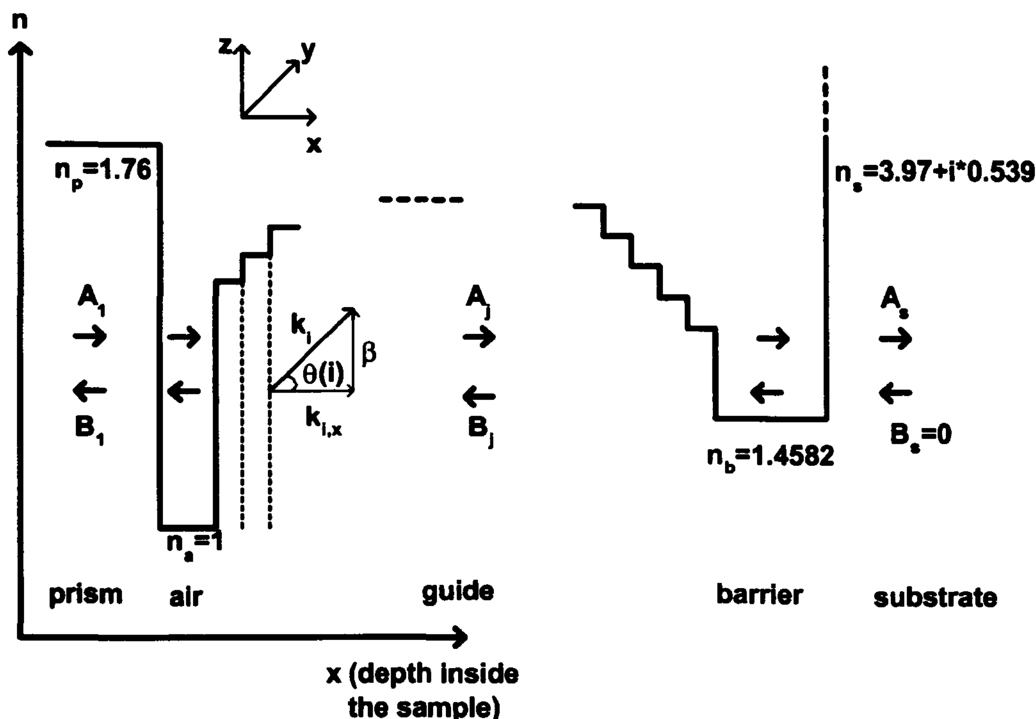

Figure 3.13. Layered structure representing a graded index waveguide for the RCM: The value of the refractive index as a function of depth is represented. Also, the propagation vector for the layer *i* with its two components can be seen. In order for the method to work mathematically, the width of the barrier has to be small enough so that the light sees the lossy substrate. In this study, a value of 2 μm has been shown to give accurate results in the determination of the effective refractive index of the modes of known waveguides.

The wave-components in two adjacent regions are related by the boundary conditions, for which the continuity of the electric , and magnetic field components parallel to the interface, has to be satisfied. For the TE polarization, the boundary conditions can be represented by a 2×2 matrix product:

$$\begin{aligned} A_j \exp(ik_jT_j) + B_j \exp(-ik_jT_j) &= A_{j+1}\exp(0) + B_{j+1}\exp(0) \\ k_jA_j \exp(ik_jT_j) - k_jB_j \exp(-ik_jT_j) &= k_{j+1}A_{j+1}\exp(0) - k_{j+1}\exp(0) \end{aligned} \quad (3.32)$$

where the *x*-origin of each region has been taken at its first boundary, and the thickness of each region is given by T_j . These equations can then be written as

$$\begin{pmatrix} A_j \\ B_j \end{pmatrix} = \begin{pmatrix} \frac{\left(1+\frac{k_{j+1}}{k_j}\right)}{2E_j} & \frac{\left(1-\frac{k_{j+1}}{k_j}\right)}{2E_j} \\ \frac{\left(1-\frac{k_{j+1}}{k_j}\right)E_j}{2} & \frac{\left(1+\frac{k_{j+1}}{k_j}\right)E_j}{2} \end{pmatrix} \begin{pmatrix} A_{j+1} \\ B_{j+1} \end{pmatrix} \tag{3.33}$$

where $E_j = exp(ik_jT_j)$. Repeating this 2×2 matrix system for each layer in the structure, the (A_1, B_1) amplitudes at the coupling prism can be related to the (A_s, B_s) amplitudes at the substrate by the product of the *s-1* matrices M_j representing the *s-1* interfaces of the system:

$$\begin{pmatrix} A_1 \\ B_1 \end{pmatrix} = \left(\prod_{j=1}^{s-1} M_j\right) \begin{pmatrix} A_s \\ B_s \end{pmatrix} = \begin{pmatrix} P_{11} & P_{12} \\ P_{21} & P_{22} \end{pmatrix} \begin{pmatrix} A_s \\ B_s \end{pmatrix} \tag{3.34}$$

taking into account the fact that B_s represents the component traveling in the backwards direction, in the substrate region $B_s = 0$. Therefore, the reflection at the prism interface is given by:

$$R = \left|\frac{B_1}{A_1}\right|^2 = \left|\frac{P_{21}}{P_{11}}\right|^2 \tag{3.35}$$

In the RCM, the calculation of the dark lines is achieved by varying continuously $n_{eff}(m)$, which is equivalent to continuously varying the incidence angle, and for each value of $n_{eff}(m)$ the reflectivity is calculated.

However, for this calculation to be possible for a confined waveguide, a small loss has to be introduced into the system, a loss that is always present in real systems due to scattering or absorption. In the mathematical model described previously, there is no such mechanism for loss and therefore, the reflectivity calculation could not detect any dark line. In our system, this loss mechanism could be achieved by allowing some tunneling into the substrate by selecting the appropriate thickness of the thermal silicon dioxide layer between the core and the silicon substrate [Chandler, 1986]. This approach is simpler than that of introducing the losses through specifying complex refractive indices in the layers and does not introduce errors in the positions of the modes.

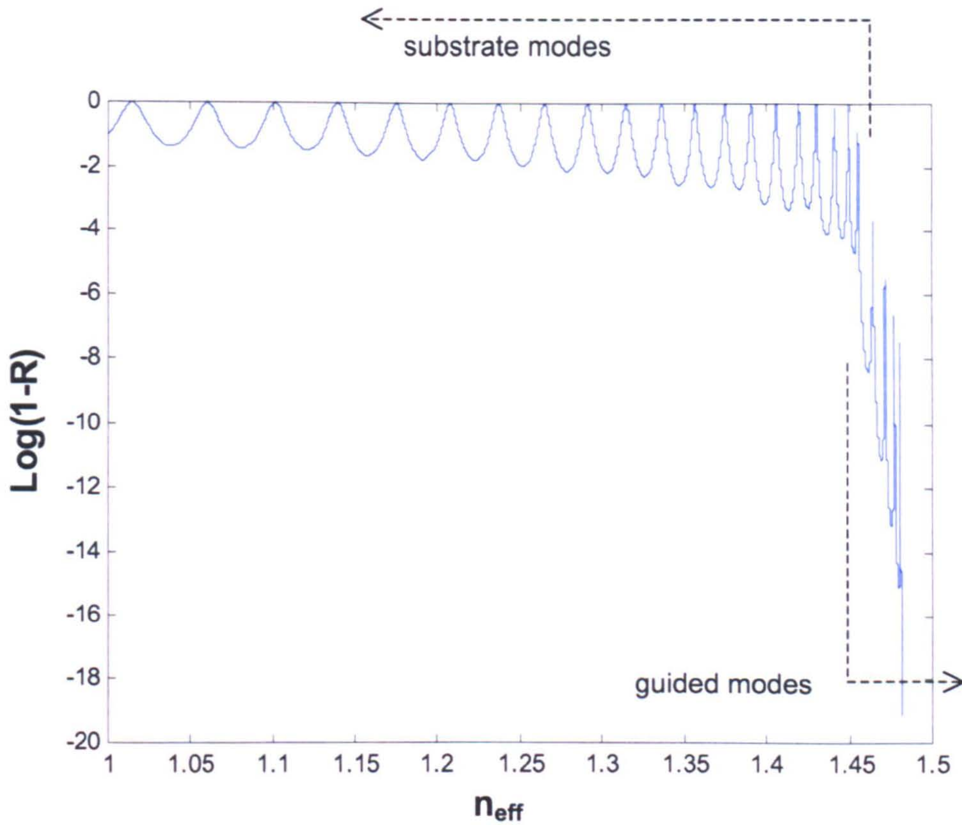

Figure 3.14 Calculation of modes using the RCM: Set of modes calculated using the Reflectivity Calculation Method for a guiding structure with step refractive index 1.4818 and width 5 μm on a layer of thermal oxide of index 1.4582. The thickness of the thermal oxide was chosen so that leakage to the silicon substrate was allowed and therefore the mathematical calculation of the "dark lines" was possible.

A program in Matlab was written by the author of this thesis in which these calculations were performed. The refractive index profile for which the modes were to be calculated was introduced either manually or through an imported file. The profile was divided into an enough number of layers of constant refractive index and the boundary condition matrix was calculated for each of those layers. Finally the reflectivity is calculated, as described above, for a set of values of "effective refractive index", $n_{eff}(m)$. A function, as shown in Figure 3.14, was obtained in which some well defined "spikes" can be seen for the higher values of $n_{eff}(m)>n_{thermal\ oxide}$, corresponding to the guided modes. The peaks become wider as the value of $n_{eff}(m)$ decreases, representing modes that leak into the substrate, which are called "substrate modes".

3.3.3 Refractive index profile of a slab waveguide from effective refractive index measurements.

3.3.3.1 *Inverse*-WKB method for obtaining the refractive index profile from the measured effective refractive indices of the propagating modes.

In the previous section, how the effective refractive index of the different modes of propagation can be obtained accurately by solving the WKB equation numerically, if the refractive index profile, $n(x)$, is known and varies slowly in the x-direction was discussed.

Conversely, in the inverse problem, the objective is to find the refractive index profile that is the best fit to a particular set of modes. A method that makes it possible to obtain the refractive index profile from a set of known modes is useful in various situations, such as the recovery of the profile from measurements of the waveguide modes or the design of a waveguide with the required characteristics determined by a specific distribution of the modes of propagation.

As the only information that is available is the value of the effective refractive index for a limited set of modes, there is a limited amount of information that can be obtained for the refractive index profile. For each mode, the refractive index at the turning point corresponds to the effective refractive index of that mode. Therefore, by calculating the position of the turning points corresponding to the modes in the waveguide, the refractive index can be evaluated at specific depths within the waveguide. This means that only a limited number of points are available to reconstruct the continuous refractive index profile [White, 1976].

Chiang *et. al.* [Chiang, 1985] introduced the concept of the "effective-index" function that eliminates the limitation on the number of available points for the recovery of $n(x)$. The effective-index function of the continuous variable m, $N(m)$, is such that when m takes integer values, $N(m)$ corresponds to the effective refractive index of the mode m. A particular refractive index profile uniquely determines an effective-index function, and the two properties are related through the WKB equation. The methodology proposed by Chiang [Chiang, 85] involves, firstly the determination of the effective-index function and, secondly the calculation of the corresponding refractive index profile by the application of the WKB method.

The effective-index function can be obtained by fitting the measured effective refractive index of the different modes by a polynomial. The order of the polynomial has to be chosen carefully in order for the difference between the fitted effective refractive index and the measured refractive index for all the waveguide modes to be smaller than the measurement errors. The effective-index function has to be monotonically decreasing, as the effective refractive index of the modes always decreases with increasing mode number. If the maximum of the refractive index profile is placed at *x=0*, as shown in Figure 3.15, the peak index can be calculated from the effective-index function.

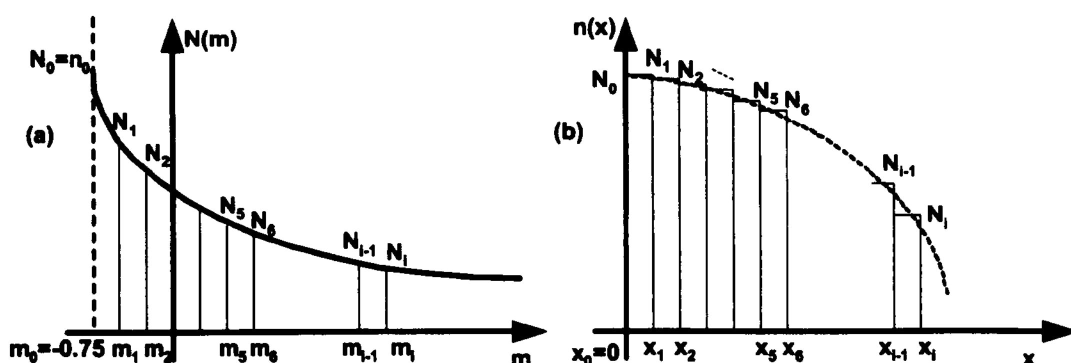

Figure 3.15. *Inverse*-WKB method: (a) Effective-index function sampled at the points m_0 to m_i, with m_0=-0.75 corresponding to the maximum of the refractive index profile, n_0. (b) Profile reconstructed by applying the WKB-equation to the sampled effective index profile.

As the peak index occurs at *x=0*, then $n_0=n(0)=N(m_0)$, where m_0 can be obtained by putting $x_t(m_0)=0$ into the WKB equation (Equation 3.30), which then reduces to:

$$2\pi m_0 - \phi_1 - \phi_2 = 0 \qquad (3.36)$$

In the case of a single turning point, ϕ_1, the phase shift at the cladding boundary, is given by

$$-2\cdot tan^{-1}\left[r_o^2 \cdot \frac{\left(n^2(0)-n_{clad}^2\right)^{\frac{1}{2}}}{\left(n^2(0)-n^2(0)\right)^{\frac{1}{2}}} \right] = -\pi \qquad (3.37)$$

and the phase shift at the turning point is $-\pi/2$. From Equation 3.36 the value $m_0=-0.75$ was obtained, and therefore, the peak refractive index was determined as

$n_0=N(-0.75)$. Similar calculations can be carried out for the situation where there are two turning points. In that case, both phase shifts, ϕ_1 and ϕ_2 are $-\pi/2$ giving $n_0=N(-0.5)$.

The effective-index function calculated in this way will be closer to the corresponding real effective-index function the greater the number of modes and, therefore, the refractive index profile will be closer to the actual one.

Once the effective-index function is specified, it is necessary to invert the WKB equation. This is not straightforward, as it is an integral equation and therefore, a numerical method was employed. The effective-index function was sampled at the points $m_0<m_1<...<m_i$, that correspond to the values $N_0=n_0<N_1<...<N_i$, as can be seen in Figure 3.15. To determine the x_i's, a stepwise approximation of the profile was used in which the index of the step i, $\overline{N}_i$, is given by the average value of N_i and N_{i-1}, i.e. $\overline{N}_i=(N_i+N_{i+1})/2$, for i=1,2,3... The WKB-integral from Equation 3.29 can then be replaced by a sum [Chiang, 1985]:

$$k\int_0^{x_i}\left(n^2(x)-N_i^2\right)^{\frac{1}{2}}dx\cong k\sum_{j=1}^{i}\left(\overline{N}_j^2-N_i^2\right)^{\frac{1}{2}}\left(x_j-x_{j-1}\right)=k\left[\left(\overline{N}_1^2-N_i^2\right)^{\frac{1}{2}}\left(x_1-x_0\right)+\right.$$
$$\left.+\left(\overline{N}_2^2-N_i^2\right)^{\frac{1}{2}}\left(x_2-x_1\right)+...+\left(\overline{N}_i^2-N_i^2\right)^{\frac{1}{2}}\left(x_i-x_{i-1}\right)\right]=k\left\{x_i\left(\overline{N}_i^2-N_i^2\right)^{\frac{1}{2}}+\sum_{j=1}^{i-1}x_j\left[\left(\overline{N}_j^2-N_i^2\right)^{\frac{1}{2}}\right.\right.$$
$$\left.\left.-\left(\overline{N}_{j+1}^2-N_i^2\right)^{\frac{1}{2}}\right]\right\}=m_i\pi+\frac{\phi_1(N_i)}{2}+0.25\pi \qquad (3.37)$$

where $x_0=0$, $i=1,2,3...$ and $\phi_1(N_i)/2$ is half the phase shift suffered by the wave at the boundary where no turning point is encountered.

From the previous equation, the x_i's can be computed iteratively by means of Equation 3.38.

$$x_i=\frac{m_i\pi+\dfrac{\phi_1(N_1)}{2}+0.25\pi-k\sum_{j=1}^{i-1}x_j\left[\left(\overline{N}_j^2-N_i^2\right)^{\frac{1}{2}}-\left(\overline{N}_{j+1}^2-N_i^2\right)^{\frac{1}{2}}\right]}{k\left(\overline{N}_i^2-N_i^2\right)^{\frac{1}{2}}} \qquad (3.38)$$

for $i=1,2,3...$

The refractive index profile of the waveguide was then determined by the set of points, (x_i, N_i), where the values of the N_i's correspond to the values of the *i*-sampled point of the effective-index function. The advantage of this method is that the recovered profile can be made as smooth as desired by increasing the number of sampling points.

If the refractive index profile presents two turning points, Equation 3.30 can be written as

$$2\int_{-x_t(m)}^{x_t(m)} k_0 \left[n(x)^2 - n_{eff}(m)^2\right]^{\frac{1}{2}} dx = 2\pi m + \pi \qquad (3.39)$$

where the phase change at the turning points is set as $\pi/2$. Asymmetrical profiles can also be analysed by breaking up Equation 3.31 into two parts with the introduction of an asymmetry factor *s*, which can vary from 0 to 1:

$$2\int_{0}^{x_t(m)} k_0 \left[n(x)^2 - n_{eff}(m)^2\right]^{\frac{1}{2}} dx = 0.5(1+s)(2\pi m + \pi) \qquad (3.40)$$

$$2\int_{-x_t(m)}^{0} k_0 \left[n(x)^2 - n_{eff}(m)^2\right]^{\frac{1}{2}} dx = 0.5(1-s)(2\pi m + \pi)$$

Each of the Equations 3.40 represents half of the profile of refractive index. A similar algorithm to Equation 3.37 would be applied for the resolution of the profiles defined by Equations 3.39 and 3.40.

It is also important to note the limitations of this method. Firstly, depending on which order is used for the fitting polynomial to form the effective-index function, a slightly different refractive index profile is obtained. The results depend on the quality (how close it is to the actual one) of the effective-index function. The quality of the effective-index function increases with the number of modes supported by the waveguide. In this work, the effective refractive index of the different modes were fitted with the polynomial of the smallest order that accomodates the modes to within an error smaller than the experimental error. Also, due to the characteristics of this method, small oscillations (or "bumps") in the refractive index profile cannot be detected, as they are not directly visible in the measurement of the modes and with this method only smooth refractive index profiles can be constructed.

Finally, the errors produced in the measurements of the modes will also affect the quality of the recovered profile.

Nevertheless, this method of calculation has important advantages. First of all, it allows the recovery of the profile without having to assume its shape *a priori*, even when the accuracy in the shape of the profile is not very high, as is the case for a small number of modes. Also, the computing time required is minimal.

A simple Matlab program was written to perform this computation in order to recover the refractive index profile of the flame-hydrolysis waveguides fabricated in this work.

3.3.3.2 Combination of the RCM method with a genetic algorithm for the recovery of the refractive index profile given by a stepwise approximation.

As has been shown in Section 3.3.2.4, the reflectivity calculation method allows the determination of the effective refractive index of the different modes of propagation of a given waveguide structure by dividing the structure into a sufficient number of layers each of them having an uniform refractive index. As has been discussed in the previous section, the *inverse*-WKB method allows only the recovery of monotonic profiles, thus limiting the kind of problem that can be performed. In the waveguides studied in this work after irradiation with an electron-beam, a monotonic profile cannot be considered as valid *a-priori* assumption.

A more general method for the recovery of the refractive index profile given the values of the effective refractive index supported by the structure is therefore desirable. With this aim, a convenient approach would be to assume the profile to be constituted by a certain number of layers of variable refractive index and thickness. The values of the effective refractive indices of the structure can be calculated by the RCM method and the values obtained can be compared with the effective refractive index measured for the actual structure. The refractive index and thickness of each layer was varied until the effective refractive indices of the structure modelled fit the measured effective refractive indices of the actual structure in a least-squares approach.

Due to the complexity of the optimization problem, a minimization algorithm that does not get trapped at a local minimum needs to be used. Genetic algorithms have been demonstrated to yield good results for the optimization of complex functions

with a large number of variables and local minima [Goldberg, 1989], [Holland, 1992], [Ingber, 1992], with results being independent of initial estimates. Genetic algorithms have also found application in calculations of the optical constants of solids [Djurisic, 1997], [Djurisic, 1998]. Genetic algorithms were used in the present work to find a value in the proximity of a global minimum and the set of parameters obtained from the genetic algorithm was then used as the departure point for a direct search simplex method, the Nelder and Mead method, in order to refine the search in the surroundings of the point given by the genetic algorithm. The Nelder and Mead method [Wolfe, 1978] will converge rapidly to the closest minimum to the departure point.

Genetic algorithms search for the optical solution by using mechanisms present in Darwinian evolution: selection, mating and mutation. A set of parameters which are a possible solution to the problem is called an individual. A set of individuals is called a population. In a genetic algorithm, an initial population of a predetermined size (parameter of choice) is generated and the function to minimize is evaluated for each individual, assigning to it a "fitness" value. Each individual is codified as a string of numbers called a chromosome. Each element of the chromosome is called a gene. In the genetic algorithm used in this work, integer codification was used, which allows a wide number of possible solutions with smaller chromosomes than in the case of binary encoding [Alfaro-Cid, 2001a], [Alfaro-Cid, 2001b]. The next generations are formed by crossing the different chromosomes of the previous generation according to their fitness, as is schematically shown in Figure 3.16. Highly fit individuals will present higher probability to pass or transmit their genes to the next generation. In the particular algorithm used in this work, a two-point crossover was utilized [Alfaro-Cid, 2001a]. In order to expand the search to other domains and reduce the risk of getting trapped in a local minimum, a certain amount of chromosomes in each generation will suffer mutation in their genes. This mutation will occur with a certain probability (a parameter to be chosen), depending on the nature of the problem. The optimization can stop when an individual with fitness better than the convergence fitness has been found or when a fixed number of generations have been generated. Nevertheless, there is a need to take into account the fact that it is not possible to know whether the value found corresponds to "the global minimum".

Among the advantages of genetic algorithms is the fact that they are not dependent on the initial conditions, that they find the global minimum by sampling a

broad spectrum of possible solutions with a high probability of locating the global minimum [Holland, 1992]. Nevertheless, these advantages involve large amounts of memory and CPU time. Also, once they arrive at the proximities of the global minimum, the refinement is generally limited by the precision with which the chromosomes are codified. In order to increase the precision in this final step, a larger number of genes is required to codify the chromosomes and, therefore, the memory and CPU time requirement grow consequently.

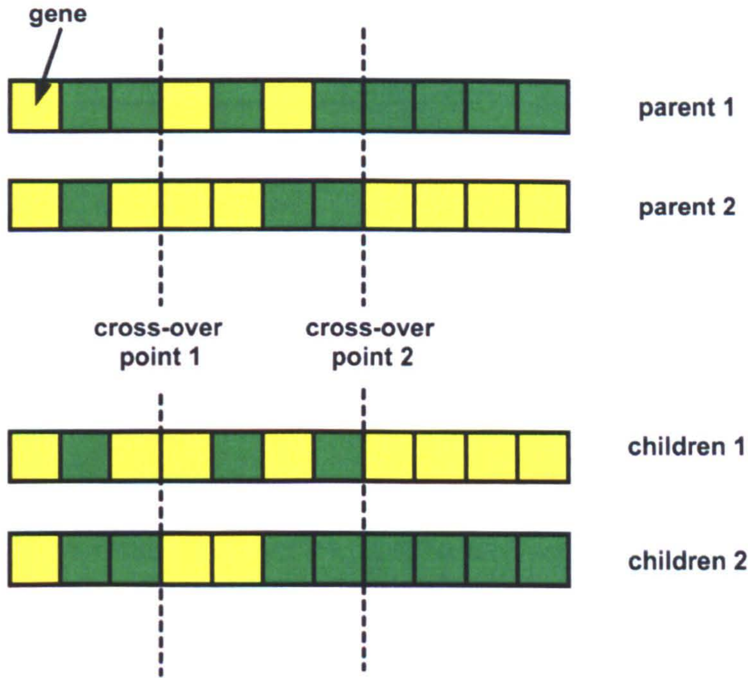

Figure 3.16. Schematic of the cross-over procedure in genetic algorithms: The two cross-over points are randomly chosen.

In order to overcome this last problem, once the genetic algorith converges to a minimum, the problem parameter codified in the chromosome corresponding to that minimum is used as a starting point for a direct search method, the Nelder-Mead algorithm, which will converge to a closer minimum to the starting point.

The genetic algorithm used has been described by Alfaro et al. [Alfaro-Cid, 2001a], [Alfaro-Cid, 2001b] to control the propulsion and direction of a ship and has been adapted to the problem of the present work. The parameters of the algorithm that can be freely chosen are the size of each population, the probability of mutation and the number of generations. The Nelder-Mead algorithm used is codified in the Optimization Toolbox of Matlab.

3.4 Aspects of analysis of 2-dimensional channel waveguides.

In all the waveguides studied in the previous section, there was no confinement in the *y*-direction (parallel to the surface and normal to the direction of propagation). There are several ways of also confining the light into the *y*-direction, thus producing a channel (2-D) waveguide. Some of the possible configurations of these guides are shown in Figure 3.17.

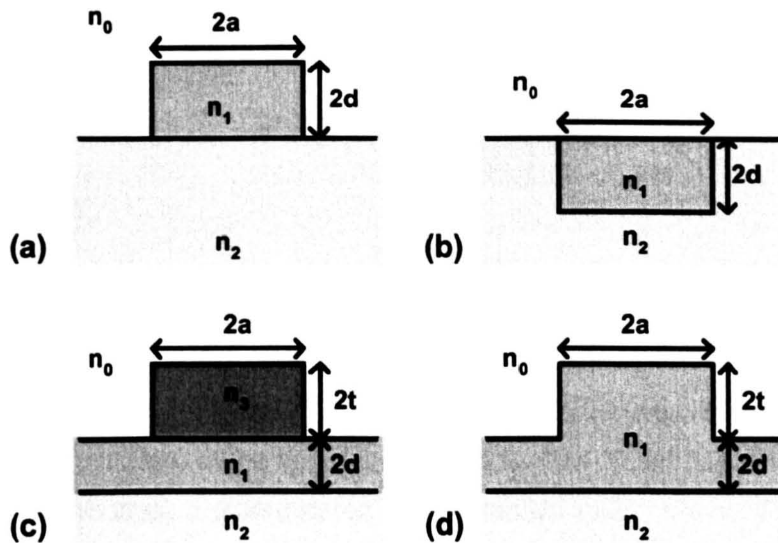

Figure 3.17. Different types of channel waveguides: (a) raised strip guide, (b) embedded strip guide, (c) strip-loaded guide, (d) rib guide [Adams, 1981].

In all cases, the light is confined in the region with the higher refractive index, n_1.

The analysis of channel waveguides is more complicated than the study of slab waveguides due to the increase in complexity of the Maxwell's equations with the introduction of the second dimension. Therefore, in most cases, approximate methods or numerical techniques are needed, such as the effective index method [Marcatili, 1974], [Hocker, 1975], [Adams, 1981], finite differences [Schulz, 1990], finite elements [Chiang, 1984] and Fourier decomposition methods [Henry, 1989]. Among them, the effective index method has been largely used due to its simplicity and the precision of its solutions [Adams, 1981].

The effective index method consists in dividing the 2-dimensional problem of a channel waveguide into two 1-dimensional ones as indicated in Figure 3.18, through construction of separable solutions.

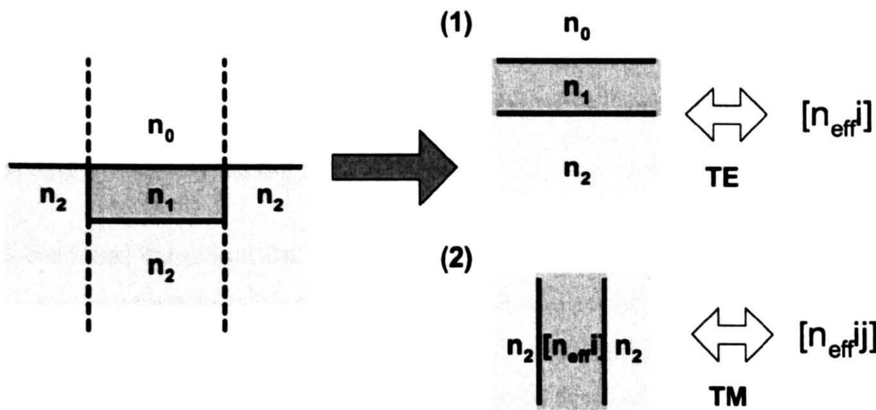

Figure 3.18. Representation of the "effective index method": The waveguide structure is shown on the left hand side. On the right hand side it is shown the realization of the effective index method for the calculation of the TE modes.

In the example shown in Figure 3.18., the initial channel waveguide structure is as shown in the left hand side of the figure. In order to find the TE propagating modes of the structure, two steps are considered in the effective index method. First, infinitely extending slab structure in the vertical direction is considered, as shown in (1) (Figure 3.18). The effective refractive index for the different TE modes supported by this structure can be calculated by the methods available for calculating the modes of propagation of a one-dimensional slab waveguide. The calculated effective refractive index can be denoted by $n_{eff}i$. In the second step of the calculation, the slab structure indicated in (2) is considered, in which the vertical structure $n_0/n_1/n_2$ is substituted by its correspondent effective refractive index. For each $n_{eff}i$, a new set of effective refractive index corresponding to the slab structure (2) are calculated, $n_{eff}ij$. For this second step, TM modes need to be considered due to the geometry of the problem.

Conversely, the calculation for the TM modes is carried out by beginning with the TM modes for the slabs in the vertical direction in the first step and TE for the second step.

This effective index method can also be applied to the analysis of graded index waveguides, such the ones obtained by diffusion [Hocker, 1975] or, in the case of this work, by electron irradiation of channel waveguides.

3.5 Characterization of the propagation losses of electron-beam direct-written monomode channel waveguides by a modified Fabry-Perot technique.

One of the most important parameters to characterize when studying a material and a technique in which to fabricate waveguides is the propagation loss exhibited by the waveguides fabricated by that technique. In the study of optical waveguides by electron-beam direct-writing of germanium-doped FHD silica, the propagation losses will determine the performance of the optical waveguide based devices fabricated and, therefore, the suitability of that method in different telecom and biosensor applications, as opposed to the usual waveguide fabrication techniques, such as lithography followed by reactive ion etching.

There are several origins to the propagation losses of a waveguide [Hunsperger, 1991]. One of the most important mechanisms responsible for the loss in the waveguides is scattering. Scattering losses can be due to imperfections (scattering centres) in the bulk of the material (volume scattering) or irregularities of the surfaces and interfaces of the waveguides. Since the size of the imperfections present in the silica is normally much smaller than the wavelength of the propagating light, volume scattering losses are typically negligible in comparison with the surface scattering. Ladouceur *et. al.* [Ladouceur, 1994] studied, mathematically, the effects of the sidewall roughness on the propagation scattering losses of channel waveguides. They calculated that in order to keep the losses due to scattering in the sidewalls below 0.01 $dB.cm^{-1}$, the oscillation on the width of the waveguide should be kepth within 1%. Furthermore, Bazylenko *et al* [Bazylenko, 1996] analyzed the effect of the sidewall roughness due to reactive ion etching techniques on the losses of the fabricated waveguides. They concluded that a roughness of 0.05 μm would lead to propagation losses of 2 $dB.cm^{-1}$. From these results, it becomes clear that a technique that reduces the sidewalls roughness would be convenient.

Another mechanism producing loss is the absorption of the material. Absorption by the material varies at different wavelengths and it is due to absorption by vibration of the different bonds in the structure. This type of losses is for the materials normally used for the fabrication of optical waveguides, and in particular, for germanium doped FHD silica, in general smaller than the scattering losses.

Losses can also be caused by radiation of the propagating light by coupling of the light to the modes of the cladding. This loss mechanism occurs mainly for higher order modes, as they are less confined in the core of the waveguide. Nevertheless, light traveling in a lower-order mode can also be coupled to a higher-order mode due to waveguide irregularities and inhomogeneities, which produce mode-conversion. This kind of loss is negligible in waveguides of reasonably quality and typically negligible in comparison to the scattering and absorption losses. Therefore, radiation losses are of considerable importance only in the case of bent waveguides.

Several techniques can be used for the characterization of the propagation losses, including the cutback method [Hungsperger, 1991], two- and three- prism methods [Weber, 1973], [Won, 1980], scattering-loss measurements [Hunsperger, 1991], [Okumura, 1986], and the Fabry-Perot resonator method [Walker, 1985], [Deri, 1991], [Adar, 1991]. Losses of an optical waveguide can also be deduced from the cavity finesse of a ring-resonator [Deri, 1991], [Walker, 1983]. The different methods are normally suited for different kind of waveguides. The two- and three-prim techniques are mostly used for characterizing slab waveguides while the Fabry-Perot and ring resonator methods are normally limited to channel waveguides. Cut-back and scattering loss measurements could be applied to both kind of waveguides.

The cut-back method is based on measuring the input and output power of a waveguide in order to deduce the propagation losses. As the insertion losses are not known, the waveguide is normally cut several times and the measurement taken repeatedly. The transmission power measured is then plotted on a log-linear graph as a function of the waveguide length. The slope of the graph determines the propagation loss. This technique has several disadvantages. Firstly, it is a destructive technique requiring a long enough waveguide to begin with, which is not always possible in integrated optical devices. Before each measurement polishing of the endfacets is needed, unless the material cleaves well (as for III-V

semiconductors). This requires a long preparation time. Secondly, it requires good reproducibility in the coupling in order for all the measured points to fall in a straight line.

The two-prism method allows the length of the waveguide to be varied by changing the distance between the input and output prisms. Nevertheless, the coupling efficiency of both prisms can vary, introducing scattering in the data. In order to reduce this effect, a third prism can be introduced [Won, 1980].

A modified Fabry-Perot technique was used in this work (Chapter 5), which allows the characterization of the propagation loss coefficient, α, of monomode channel waveguides without needing to consider the incident power in the waveguide, and therefore independently of the coupling losses [Clark, 1990], [Walker, 1985]. By the use of this technique, the propagation losses of monomode channel waveguides can be determined.

The set-up used in this experiment is shown in Figure 3.19. The laser used was a "Tunics" tunable laser, allowing steps in the wavelength as small as 0.001 nm. A fibre polarization controller was used to select only the TE polarization. The signal from the detector was analysed using a lock-in amplifier EG&G model 5207. Care was taken in order to not saturate the detectors during the measurements.

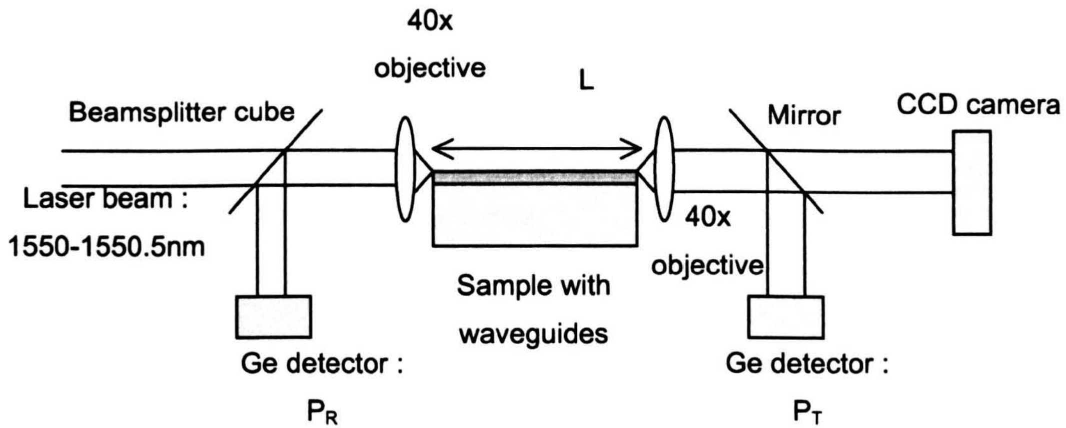

Figure 3.19. Experimental setup for the measurement of the losses using a modified Fabry-Perot technique.

The waveguide is considered to be a Fabry-Perot resonator, with a reflectance of the end-facets, R, and a propagation loss along the cavity of α (cm^{-1}).

The expressions for the transmitted and reflected power are given by:

$$E_T = \frac{E_o T e^{-\alpha L} e^{i\frac{\delta}{2}}}{(1 - \mathrm{Re}^{i\delta} e^{-2\alpha L})} \Rightarrow P_T = |E_T|^2 = \frac{E_o^{\,2} T^2 e^{-2\alpha L}}{1 + R^2 e^{-4\alpha L} - 2\mathrm{Re}^{-2\alpha L}\cos\delta} \tag{3.41}$$

$$E_R = -E_o \frac{(1 - e^{-2\alpha L} e^{i\delta})\sqrt{R}}{(1 - \mathrm{Re}^{-2\alpha L} e^{i\delta})} \Rightarrow P_R = |E_R|^2 = \frac{E_o^{\,2} R\left(1 + e^{-4\alpha L} - 2e^{-2\alpha L}\cos\delta\right)}{1 + R^2 e^{-4\alpha L} - 2\mathrm{Re}^{-2\alpha L}\cos\delta} \tag{3.42}$$

where E_T and E_R are the transmitted and reflected field strengths, P_T and P_R are the corresponding power intensities, L is the length of the sample, R is the reflectance of the facets and $T=1-R$. δ is the change in phase of the light in a round trip along the length of the sample, $k_0 n_{eff} 2L$, which is wavelength dependent through $k_0=2\pi/\lambda$. By tuning the wavelength of the laser, fringes can be observed in the measured P_R and P_T. The calculations to arrive at Equations 3.41 and 3.42 have been developed in more detail in the Appendix 1, for a more general case with different reflectivities at the two end-facets.

The maximum of the transmitted power, P_{Tmax} (and thus the minimum of the reflected intensity, P_{Rmin}), occurs when $cos\delta$ is 1. The opposite situation, P_{Tmin} and P_{Rmax}, occurs when $cos\delta$ is –1. Writing

$$G = \frac{P_{R_{min}} P_{T_{min}}}{P_{R_{max}} P_{T_{max}}} = \frac{(1 - e^{-2\alpha L})^2}{(1 + e^{-2\alpha L})^2} = \tanh^2 \alpha L \tag{3.43}$$

gives an expression from which the reflectivity of the end-facets is eliminated. Therefore, the propagation losses can be calculated from one single measurement, without the need to know the reflectance of the end-facets, which is an advantage over the traditional Fabry-Perot technique.

From Equation 3.43 the propagation loss is given by

$$\alpha\left[cm^{-1}\right] = \frac{1}{L}\tanh^{-1}\left(\sqrt{G}\right) \tag{3.44}$$

Two conditions are required for this method to be viable: firstly, the waveguide has to be monomode and secondly, the facets have to be perfectly polished at 90 degrees with the surface of the sample and with the propagation direction. If the first condition does not apply, the fringes measured can be distorted by the varying contribution of the different modes, which propagate with different periodicities. Since the contrast of the fringes is affected, Equation 3.44 will not calculate a real

value for the losses [Takeuchi, 1989]. Multimode waveguides could be measured by using this technique, but in order to get correct results, i.e. each mode should be excited separately by the use of a prism or grating coupler [Lee, 1998].

On the other hand, if the two end-facets are not polished perfectly at 90 degrees, the reflectance at each of the facets will be different, making it impossible to eliminate the reflectivities from the calculations. The errors introduced by this factor have been treated in more detail in Appendix 1.

Chapter 4

Characterization of as-deposited germanium-doped FHD silica layers

Chapter summary.

The present chapter presents the results from the characterization of the as-deposited sintered FHD silica layers. From the compositional (XPS and RBS) and density (X-ray reflectivity) characterizations, a gradient in the film properties, probably due to germanium diffusion and out-gassing during the sintering step, was observed. The structure of the film presents also this feature, which ultimately shows in the refractive index profile of the films, therefore influencing their optical characteristics. The films were optically characterized and the performance of the *inverse*-WKB method and the *inverse*-RCM were compared. The results from the optical characterization were finally compared with the compositional and structural results finding a good correlation. The properties of the films analyzed in this chapter are then responsible for the particular response of the material under electron-beam irradiation, as will be presented in Chapter 5.

4.1 Introduction

During the course of this research, the effects of electron-beam irradiation on silica, which allow the fabrication of optical buried waveguides, were studied. The modification of the silica is dependent on the structure and composition of the as-deposited material, and therefore, the methods outlined in Chapter 2 were used to understand the basis for the optical properties, that were subsequently investigated using the techniques described in Chapter 3. Since the cladding for such "buried" electron-beam fabricated waveguides (see Chapter 3) is essentially the as-deposited material, optical and structural details of this material are also necessary in order to reliably model the characteristics of the waveguides prior to fabrication.

In the present chapter, the characterization of the as-deposited Ge:SiO_2 FHD layers, before irradiation by an electron-beam, is described. First of all, optical analyses of the propagation modes supported by the slab waveguide using an m-line technique based on grating couplers are described [Tien, 1970], [Dakss, 1970].

From the spacing of the modes, a non-uniformity in the depth of the refractive index is evident. Two techniques for evaluating the refractive index profile from measurements of the modes, the *inverse*-WKB method and a step-wise approximation together with fitting based upon genetic algorithms, are compared. A study of the dependence of the refractive index profile on the sintering conditions is also presented together with the variations in the refractive index found when different $GeCl_4$ fluxes were used in the soot deposition stage. Another important optical parameter, the optical birefringence of the layers, is also characterized.

It was hypothesised that the non-uniformity of the refractive index profile is due to processes occurring during the sintering step of the deposition procedure, which, due to the high temperatures involved, can lead to a gradient in the germanium composition, density and structure through the depth of the as-deposited layers. Similarly, non-uniform germanium profile has been previously found in the germanium-doped silica preforms deposited by vapor-phase axial deposition process (VAD) [Potkay, 1988] and also, non-uniformity has been observed in the refractive index profiles of phosphorous doped PECVD layers due to diffusion and out-diffusion of phosphorus [Heimala, 1992]. As outlined in Chapter 5 (Section 5.5), composition, density and structure are the main parameters that determine the refractive index of the material. Several techniques, already described in Chapter 2, have been used here to characterize these properties: X-ray photoelectron spectroscopy (XPS) and Rutherford Backscattering Spectroscopy (RBS) were used for the measurement of the germanium composition profile, X-ray reflectivity was utilized for the characterization of the density profile whilst X-ray Absorption Fine Structure (EXAFS) and Raman spectroscopy were used for the structural characterization of the layers.

4.2 Description of the Ge:SiO_2 FHD layers.

Germanium-doped flame hydrolysis silica deposited layers (Ge:SiO_2 FHD) were deposited on top of silicon substrates with 15 μm of thermal oxide on them, as described in Chapter 2, Section 2.2. The deposition parameters used in the preparation of the samples for this chapter are given in Table 4.1.

Batch	Recipe (flux in sccm)				Thickness (μm)	EDX (Ge % wt.)
	$GeCl_4$	$SiCl_4$	BCl_3	N_2		
Apr'01	100	150	65	600	6.3	9.38±0.10
	120	150	65	580	6.6	10.24±0.10
	180	150	65	520	5.9	14.45±0.14
May'01	100	150	65	600	5.8	6.39±0.075
	150	150	65	550	4	11.22±0.13
	180	150	65	520	4.35	12.24±0.14

Table 4.1. Description of the samples characterized in this chapter.

In all cases H_2 and O_2 were also introduced in the torch with fluxes 5 and 7 $l\cdot min^{-1}$ respectively. The sintering step was performed at 1350°C for 2 h in O_2 and He atmosphere with fluxes 0.5 $l\cdot min^{-1}$ and 100 $cm^3\cdot min^{-1}$ respectively. The thickness of the samples was controlled by the number of traverses of the torch during the soot deposition step [Marques, 2000] and measured, after the deposition, by etching the layer in HF 40 % and subsequently measuring the resulting surface profile with a Talystep profilometer. The difference in etch rate between the FHD silica layer and the thermal oxide underneath marks the thickness of the FHD layer.

As the processes involved during the deposition are thermally activated, the time length of the sintering step was expected to have an influence on the shape of the refractive index profile. In order to investigate this behaviour, soot was deposited in three samples by using a 100 sccm flux of $GeCl_4$ in all cases, followed by different sintering times. The samples were introduced into the furnace at 1050°C and the temperature was then increased to 1350°C, at which temperature the samples were kept for 15 min (the first sample), and 120 minutes (the second and third samples). After this time the temperature of the furnace was ramped down to 600°C and the first two samples were taken out the furnace immediately. The third sample was left in the furnace overnight (8 h) at 600 °C. All the samples were observed under the optical microscope and none of them presented obvious signs of poor sintering.

4.3 Optical characterization of the as-deposited films.

In this section, firstly the refractive index profile of the as-deposited flame-hydrolysis deposited layers and its dependence on the germanium content of the sample and on the deposition parameters was characterized. Finally, the birefringence of the as-deposited films was studied.

4.3.1 Description of the samples.

The samples characterized in this section were described in Section 4.2.

4.3.2 Method for the refractive index characterization.

The refractive index profile of the as-deposited samples was characterized by measuring the effective refractive index of the different modes of propagation in a grating-coupler based "m-line" setup, followed by theoretical analysis of the measured data using the *inverse*-WKB with asymmetry factor 0.8 and the *inverse*-RCM, as described in more detail in Chapter 3.

4.3.3 Relation of the refractive index with the composition and density of the material: Lorentz-Lorenz equations.

In order to understand the physical origin of the particular refractive index profile obtained in a material, knowledge of the relation between composition and density of the material and its refractive index is needed. In this section, the basics of that relation are described.

The refractive index of a material is related to its density and composition by means of the Lorentz-Lorenz equation [Born, 1959]:

$$\alpha = \frac{3}{4\pi N}\frac{n^2-1}{n^2+2} \tag{4.1}$$

where α is the mean polarizability of the material, N is the number of molecules per unit volume and n is the refractive index of the material.

The number of molecules per unit volume can be expressed as:

$$N = N_m \frac{\rho}{W} \tag{4.2}$$

in which N_m is Avogadro's number (6.023.10^{23} molecules), ρ is the density of the material, and W is the molar mass (the mass of an Avogadro's number of molecules, which corresponds to the molecular mass in grams). Therefore, one can write

$$\frac{4\pi}{3}\alpha N_m = \frac{W}{\rho}\frac{n^2-1}{n^2+2} \tag{4.3}$$

where $A = \frac{4\pi}{3}\alpha N_m$ is known as the molar refractivity. Equation 4.3 is known as the Lorentz-Lorenz equation.

The mean polarizability for the different ions that constitute a compound can be found in the literature. For the ions that constitute the Ge:SiO_2 FHD glass, the following values have been reported [Dimitrov, 2002]: $\alpha_{O_2^-} = 1.720\ \AA^3$ and $\alpha_{Ge^{4+}} = 0.137\ \AA^3$ for the GeO_2 and $\alpha_{O_2^-} = 1.427\ \AA^3$ and $\alpha_{Si^{4+}} = 0.033\ \AA^3$ for the SiO_2. Assuming that the polarizabilities of these ions remain unchanged when forming the FHD silica network, the mean polarizability of a "molecule" of Ge:SiO_2 FHD can be calculated as

$$\alpha_{FHD} = \frac{N_{SiO_2}\alpha_{SiO_2} + N_{GeO_2}\alpha_{GeO_2}}{N_{SiO_2} + N_{GeO_2}} \tag{4.4}$$

where N_{SiO_2} and N_{GeO_2} are the percentage of silica and germania molecules present in the FHD glass and α_{SiO_2} and α_{GeO_2} correspond to the mean polarizability of the two components of the glass, which can be calculated as [Dimitrov, 2002]

$$\alpha_{SiO_2} = 1\times\alpha_{Si^{4+}} + 2\times\alpha_{O_2^-(SiO_2)} \tag{4.5}$$

$$\alpha_{GeO_2} = 1\times\alpha_{Gei^{4+}} + 2\times\alpha_{O_2^-(GeO_2)} \tag{4.6}$$

Therefore, the expression that relates the refractive index with the density and composition of the FHD silica glass is given by:

$$\frac{4\pi}{3}\alpha_{FHD}N_m = \frac{W_{FHD}}{\rho_{FHD}}\frac{n^2-1}{n^2+2} \tag{4.7}$$

4.3.4 Measurement of the effective refractive indices of the propagating modes.

The effective refractive indices supported by the waveguide structures described in Section 4.2 were measured as indicated in Section 4.3.2 (first column of Table 4.2).

It is known [Chandler, 1986], [Townsend, 1994] [Tien, 1974] that the spacing of the effective refractive indices of the modes supported by a waveguide is related to the refractive index distribution inside the structure. In a step-index guide, a plot of the squared effective refractive index as a function of $(m+1)^2$, where m represents the mode order, should be a straight line with negative slope (as demonstrated in Section 3.3.2.1). It should be pointed out that, due to the discrete nature of the modes, this graph represents discrete points and not a continuous function.

From the plot of the measured n_{eff}^2 for a particular mode, m, versus $(m+1)^2$ (Figure 4.1), it can be see that the straight line plot predicted for the case of a step index profile does not apply. This implies that the refractive index distribution is not uniform. In order to verify this point, the measured modes were fitted to a step refractive index profile waveguide, by doing a search in the solution space by varying the different parameters within the expected ranges at steps smaller than the experimental error. The results of this fit are shown in the third column of Table 4.2.

In order to compare the quality of the fit in the different cases, the fitting function shown in Equation 4.8 has been used

$$f = \frac{10^7 * \sum_{i=1}^{number\ modes}\left(n_{meas}(i) - n_{calc}(i)\right)^2}{number\ modes} \tag{4.8}$$

in which $n_{meas}(i)$ and $n_{calc}(i)$ represent the effective refractive indices measured and calculated, respectively, corresponding to mode i. The function was normalized to the number of modes, so that fittings corresponding to waveguides with different number of modes could be compared. It can be seen clearly in Table 4.2 the poor

agreement between the measured and fitted modes if a step profile were assumed, which translates in a high fitting function value.

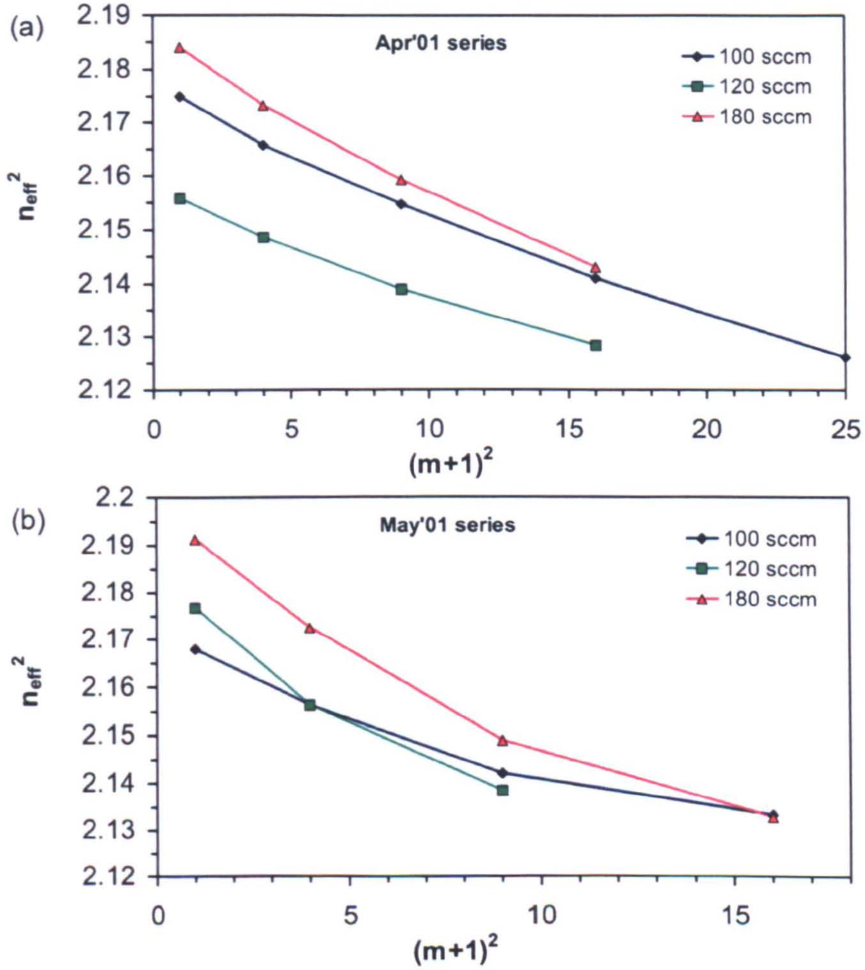

Figure 4.1. Squared measured effective refractive index of the propagation modes as a function of the squared mode number: The error bars corresponding to these measurements were plotted but are smaller than the size of the data points.

Since a non-uniformity in the material composition with depth was found for these FHD silica substrates (Section 4.4), the formulation of a more detailed model to describe the effective refractive index of the modes of propagation was undertaken, as described below.

Sample	m-number	n measured	n-step approx.	n-RCM+GA +optim	n-*inverse*-WKB	n-*inverse*-WKB+optim
100sccm, May'01	0	1.4724	1.4724	1.4724	1.4718	1.4725
	1	1.4684	1.4696	1.4682	1.468	1.4683
	2	1.4635	1.4651	1.4637	1.4641	1.4636
	3	1.4605	1.4593	1.4604	1.4598	1.4603
			fit=13.60	fit=0.23	fit=3.43	fit=0.18
150sccm, May'01	0	1.4750	1.4750	1.4750	1.4744	1.4750
	1	1.4668	1.4685	1.4668	1.4668	1.4668
	2	1.4596	1.4589	1.4596	1.4593	1.4596
			fit=11.26	fit=0.00	fit=1.50	fit=0.00
180sccm, May'01	0	1.4803	1.4803	1.4803	1.4795	1.4803
	1	1.4739	1.4757	1.4739	1.4732	1.4739
	2	1.4659	1.4681	1.4662	1.4668	1.4661
	3	1.4604	1.4586	1.4603	1.4596	1.4603
			fit=28.3	fit=0.25	fit=6.45	fit=0.13
100sccm, Apr'01	0	1.4748	1.4748	1.4749	1.4743	1.4748
	1	1.4717	1.4726	1.4717	1.4713	1.4717
	2	1.4679	1.4690	1.4678	1.4677	1.4679
	3	1.4632	1.4641	1.4631	1.4631	1.4632
	4	1.4581	1.4584	1.4580	1.4581	1.4582
			fit=5.84	fit=0.08	fit=0.90	fit=0.04
180sccm, Apr'01	0	1.4778	1.4778	1.4777	1.4777	1.4777
	1	1.4742	1.4753	1.4743	1.4734	1.4741
	2	1.4695	1.4712	1.4694	1.4689	1.4694
	3	1.4638	1.4656	1.4641	1.4642	1.4640
	4	1.4595	1.4589	1.4595	1.4592	1.4594
			fit=15.40	fit=0.24	fit=2.52	fit=0.16

Table 4.2. Values for the fitted effective refractive indices of the propagating modes of the different samples analyzed using different fitting procedures.

4.3.5 Calculation of the refractive index profile from the optical measurement of the propagating modes.

Several methods are described in the literature for determining the refractive index profile from the optical measurements of the modes of propagation. In the present work, the suitability of two of these methods was investigated: a step-wise approximation of the profile together with a fitting algorithm based on genetic algorithms [Chandler, 1986], [Holland, 1992]; and the *inverse*-WKB method [Chiang, 1985]. The principles of the methods have already been described in Chapter 3.

Due to the limited number of modes supported by the waveguides (<6), it is difficult to decide which profile best represents the actual profile, as each method introduces various forms of approximation. Thus, different profiles could produce a similar quality of fit. Therefore, physical information about the expected profile was included as a constraint in the analysis method.

In the present case, it was assumed that the refractive index profile beyond the interface of the FHD layer with the substrate, was a diffusion-like profile (gaussian or complementary error function) due to the nature of the physical processes involved: as described before, the germanium-rich soot deposited directly on top of the substrate or on the thermal silicon oxide layer can act as the source of germanium diffusing into the substrate. If this source were considered to be infinite, a complementary error function profile would be appropriate, as a first approximation, using Fick's 2nd law diffusion equation (as has been previously been studied in the context of diffused optical waveguides).

However, in the FHD layer region, the actual processes occurring involve a much greater number of phenomena. The variation of the diffusion constant as the soot is consolidated due to the change in structure of the material should also be taken into account in a more elaborated description of the physical processes occurring. Furthermore, due to the changes in temperature during the processing steps, different values of the diffusion constant should also be expected. Also, a decrease in the germanium content in some areas is likely to increase the sintering temperature for the consolidation of those regions, implying that different material densities are expected throughout the film. In Section 4.3.3 the relation between composition, density and refractive index of a material was discussed. As a consequence of all the processes involved, the use of a simple diffusion profile, as the candidate for the refractive index profile in this FHD region is likely to be a poor approximation.

4.3.5.1 Step-wise approximation plus a complementary error function. Fitting by genetic algorithms.

From the diffusion phenomena thought to occur during the sintering of the soot, discussed in the previous section, the refractive index profile was modeled using the profile shown in Figure 4.2.

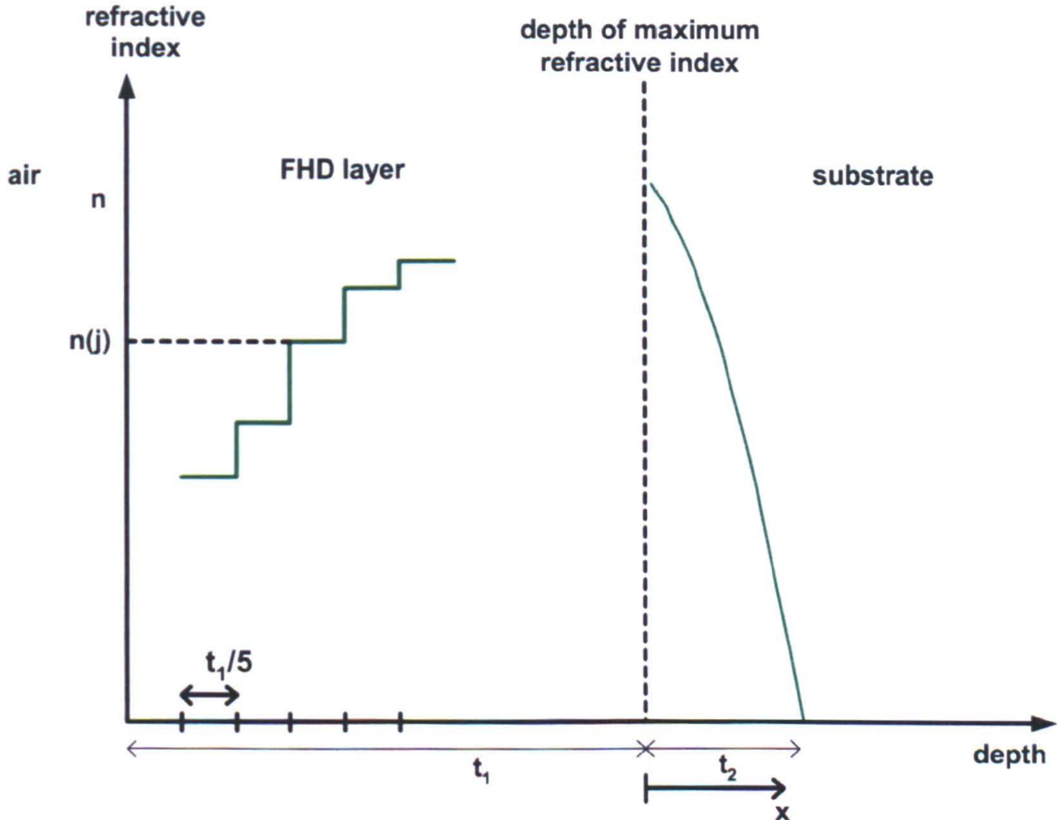

Figure 4.2. Graded-index profile expected in the Ge-doped FHD films: In the interface with the substrate, a refractive index profile following the expected diffusion of germanium into the substrate is expected. Towards the air interface, further structural and compositional mechanisms are expected, therefore using a stair-wise approximation for the fittings.

The unknown part of the profile was divided in *j* layers, each of which has assigned a refractive index *n(j)* (Figure 4.2). The total thickness of that region was defined by t_1, being, therefore, the thickness of each sub-layer defined by t_1 / j. A further constraint has been introduced for which the profile in that region is considered to be monotonically increasing until it reaches the interface with the substrate.

The part of the profile that corresponds to the diffusion of germanium into the substrate can be described by a function of the form

$$n_s + (n_{max} - n_s)\cdot(1 - erf(x/t_2)) \qquad (4.9)$$

where n_s is the refractive index of the thermal oxide, n_{max} is the peak refractive index at $x=0$, t_2 is the depth to which this shape of germanium profile extends and x is the distance from the substrate interface to the point at which the profile is being evaluated in that region. Thus, at the interface, $x=0$, the refractive index value given by Equation 4.9 is n_{max} and at $x=t_2$, the refractive index value is the refractive index of the substrate, as expected.

In the genetic algorithm, the values of the refractive indices of the layers in the FHD region have been allowed to vary from 1.46-1.49, the total thickness of the FHD region was varied from 4.0 to 6.9 μm for the Apr'01 batch samples and the 100 sccm sample from the May'01 series. The thickness was varied from 3.0 to 4.99 for the May'01 batch samples. In all cases, the thickness of the region of diffusion of germanium into the substrate has been varied from 0 to 1.9 μm. These ranges of variation of the different parameters constitute the space in which it is anticipated that the best solution should be, from the known optical properties of the FHD glass and physical measurements of its thickness.

In the model of Figure 4.2, 8 layers for the FHD region were used. A genetic algorithm was used in order to find the best fit to the experimental data using the least squares metric as in Equation 4.8. In the algorithm, the different parameters of the refractive index profile were codified using 28 genes, 200 individuals were used per population and the algorithm was left to run for 50 generations. The probability of mutation used was 1%. The explanation of genetic algorithms has been briefly outlined in Chapter 3.

From the genetic algorithm, values for the different parameters in the proximity of the global minimum were obtained. These values were used as the starting point for a simplex-search algorithm, the Nelder-Mead algorithm, implemented in the Optimization toolbox of Matlab. This algorithm converged to the first local minimum in the vicinity of the starting point, therefore, a refinement of the value obtained from the genetic algorithm was performed. Nevertheless, due to the multiple-minima nature of the problem, there was no guarantee that the best fit found corresponded to the global minimum of the fitting function. The algorithm was run until the fitted values were within the experimental error of the measurements.

The profiles obtained from these fits are shown in Figure 4.3 and 4.4 for the Apr'01 and May'01 series respectively. The values of the measured and fitted effective refractive indices of the different modes of propagation together with the value of the goodness, calculated using Equation 4.8 are shown in Table 4.2.

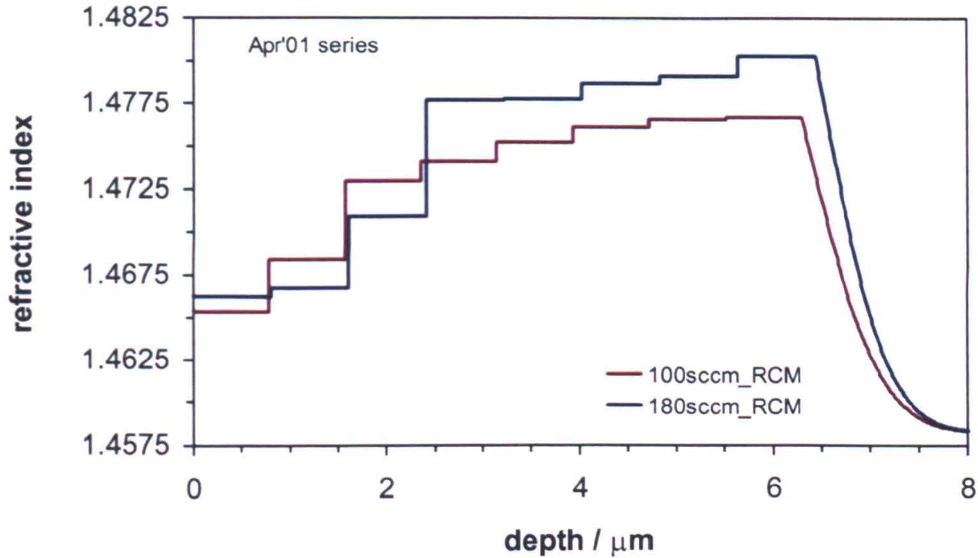

Figure 4.3. Refractive index profiles obtained after the *inverse*-RCM: Profiles obtained for the Apr'01 series samples using the RCM method with a genetic algorithm followed by a Nelder-Mead method to fit the experimental values of the effective refractive indices of the propagating modes.

The deviation of these fitted profiles from a step profile can be clearly seen. The quality of these fits can be observed in Table 4.2. The calculated effective refractive indices supported by the calculated profiles were within the experimental error of the measured modes.

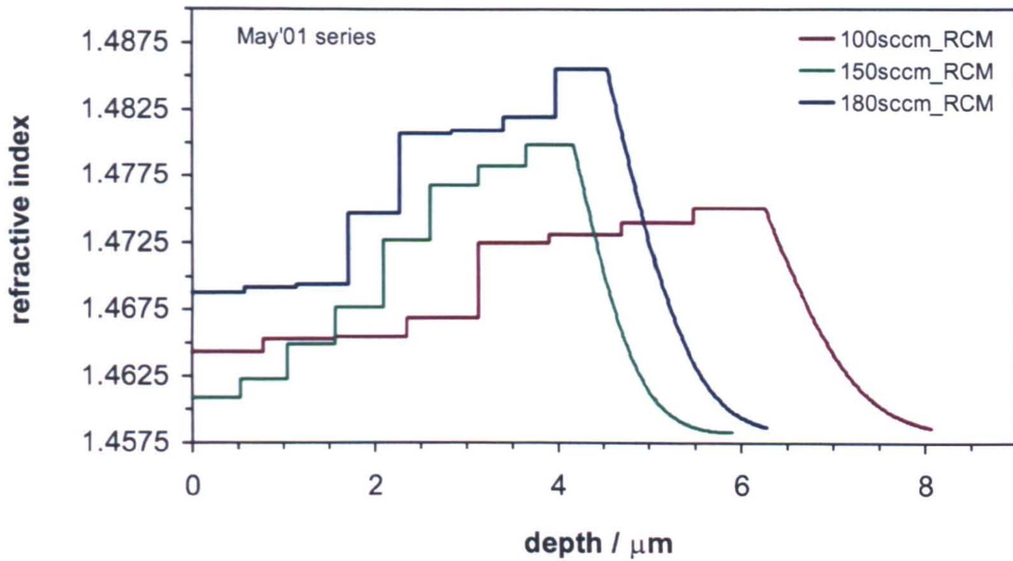

Figure 4.4. Refractive index profiles obtained for the May'01 series samples using the RCM method with a genetic algorithm followed by a Nelder-Mead method to fit the experimental values of the effective refractive indices of the propagating modes.

4.3.5.2 *Inverse*-WKB method with asymmetry factor *s*.

In Chapter 3, the theory of the *inverse*-WKB method for the calculation of the refractive index profile from the measurement of the modes, based on the technique developed by Chiang [Chiang, 1985] was described in Section 3.3.3.1. It was explained there how the introduction of an asymmetry factor, s, makes it possible to obtain profiles with different degree of asymmetry.

An *inverse*-WKB method with an asymmetry factor of 0.8 was used here to approximate the profiles, as that value yielded profiles the thickness of which were in agreement with the actual thickness of the layers, as measured by a Talystep profilometer (Table 4.1). From the profiles obtained by using the *inverse*-WKB method, the RCM method (Section 3.3.2.4) was used to evaluate the effective refractive indices of the different modes of propagation. The calculated modes n_{eff} values were separated from the experimental modes more than the experimental error of the measurements (Table 4.2, Column 5), implying that this function was not an optimal representation of the profile existing in the layer.

A further fitting step was performed in which the profiles obtained from the *inverse*-WKB method were divided into 20 layers and introduced into the optimization method (Nelder-Mead algorithm) until the effective refractive indices

calculated from the profile fitted the measured modes with an error smaller than the experimental error. The new fits can be seen in Column 6 of Table 4.2.

The profiles obtained using this method were compared to the ones obtained in the previous section using an *inverse*-RCM method and the genetic algorithm in Figure 4.5 and Figure 4.6. The step profile that best fits the measured modes was also represented for comparison.

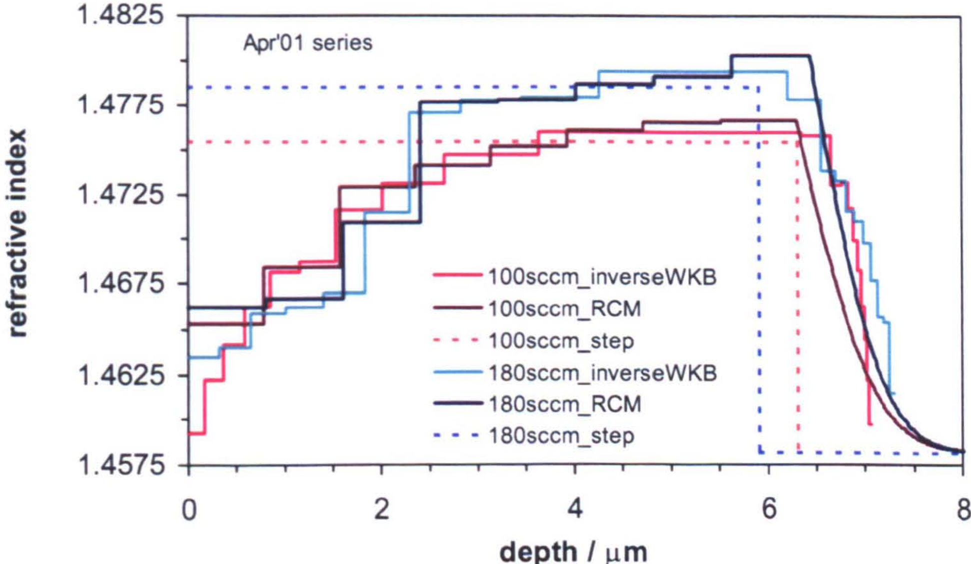

Figure 4.5. Comparison of the different calculation methods (Apr'01): Refractive index profiles corresponding to the Apr'01 series calculated by the step-approximation (dotted lines) and by the *inverse*-WKB following by an optimization step, and the RCM followed by an optimization step.

The close agreement between the profiles obtained from the two methods gave more confidence about the proximity of the model profile to the actual profile. Their clear difference with the step profile confirms the hypothesis of a graded structure in the as-deposited Ge:SiO_2 FHD silica layers, which will be further supported by the compositional analysis described in Section 4.4.

The *inverse*-WKB method followed by an optimization algorithm appears as the most convenient method to use if the computation time in each case is compared. Due to the nature of the genetic algorithms, their computation time is very large (in the case of the present computations, the function was evaluated 200x50=10000 times, which represents slightly less than 2.7 h). The *inverse*-WKB calculation can be performed in < 5 seconds. As the results obtained were similar in

both cases, the *inverse*-WKB method followed by a fitting algorithm will be used in the rest of the calculations in this Chapter.

Although the large computation time makes the genetic algorithm approach less convenient for the solution of the present problem, in case for which the *inverse*-WKB method is not applicable, such as when the profile is not monotonic in depth, the genetic algorithm will be very useful to get a possible fit to the refractive index profile.

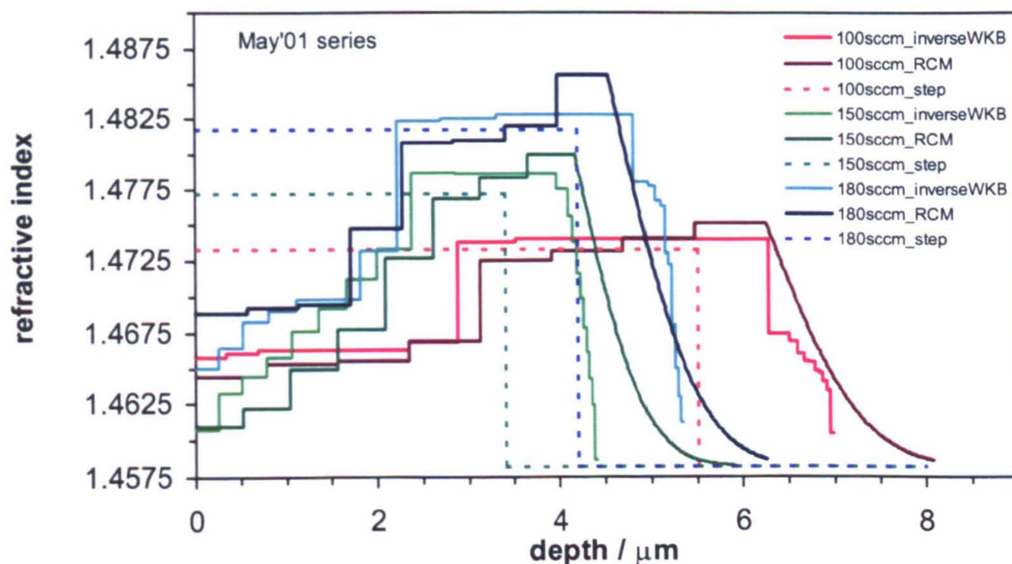

Figure 4.6. Comparison of the different methods (May'01): Refractive index profile calculated from the fitting of the measured effective refractive indices of the different modes of propagation by using different approximations.

4.3.6 Evolution of the n-profile for different deposition $GeCl_4$ fluxes.

The profiles of the refractive index for samples deposited with different fluxes of $GeCl_4$ in the torch (see Table 4.1 with the description of the samples) were calculated in the previous section. The corresponding profiles can be seen in Figures 4.5 and 4.6. As was expected, an increase in the flux of the germanium chloride in the deposition process produced an increase of the refractive index of the sintered layers. For all the compositions studied, the shape of the profile was similar.

4.3.7 Influence of the sintering conditions on the n-profile.

From the discussion in Section 4.1, it is proposed that the high temperature sintering allows the germanium present in the as-deposited soot to outgas and to diffuse both within the FHD silica layer that is being formed and into the substrate. Nevertheless, the loss of germanium was not large enough to prevent the proper sintering of the sample due to increase of the melting point as the germanium concentration decreases. Three samples were sintered for different times as described in Section 4.2. The sintered films had good optical quality as was determined by inspection under the optical microscope. The profiles of refractive index obtained by fitting the measured effective refractive index indices using the inverse-WKB method followed by a fitting routine (Section 4.3.5.2) are shown in Figure 4.7.

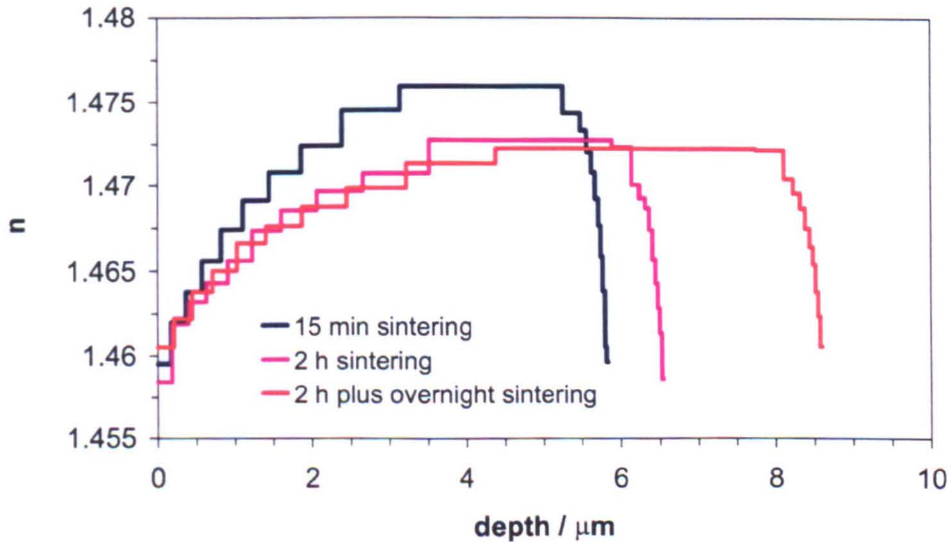

Figure 4.7. Influence of the sintering conditions on the refractive index profile: Refractive index profiles obtained after different sintering times of the FHD silica.

It can be seen in Figure 4.7 that the profile of refractive index in the samples sintered for 2 h at the high temperature had a different profile compared to the short sintering time sample. As it will be shown in a latter section (Section 4.4.3) the 2 h sintering sample and the 2 h sintering plus overnight at 600 C presented a higher depletion of germanium, consistent with the larger lapse of time spent at such a high temperature. However, the sample sintered for 2 h followed by overnight at 600 °C had a smaller content of germanium throughout its depth. Furthermore, in Section 4.6, the density of 3 samples deposited in the previous conditions was studied, obtaining a smaller density for the sample left in the furnace overnight than for the

sample removed immediately after the 2 h sintering step. In the refractive index profile, those effects, lower germanium content and lower density, can also been observed, being the refractive index of the sample sintered for 2 h and left overnight slightly lower than the sample sintered for 2 h.

4.3.8 Birefringence in the as-deposited layers.

As described in Chapter 2, a half-wave plate together with a polarizer were used in the m-line experiment, to select the polarization of the light incident on the films. Measurements were taken for both TE and TM polarizations. The birefringence could then be calculated as $B = n_{TE} - n_{TM}$.

Measurements were carried out for as-deposited FHD silica samples with different germanium contents (4-15 % wt. Ge). In all cases the birefringence measured was $< 3.10^{-4}$ a change that is less than the experimental error for the measurements (the estimated experimental error for the measurements of n_{TE} and n_{TM} is $\leq 2.10^{-4}$, therefore, the experimental error for the characterization of the birefringence is $\leq 4.10^{-4}$, which is larger than the values measured).

4.4 Compositional analysis.

In order to investigate the composition-refractive index relationship, the analytical techniques described in Chapter 2 were used. The representative results described here relate to the May'01 series of the previous section. The main compositional technique used, described in Chapter 2, was the collection of XPS spectra after wet-etching in 4:1 buffered HF (hydrofluoridric acid and ammonium fluoride) for increasing lengths of time. However, due to the lack of precise control over the etch rate and the small depth sampling distance of the technique, this method does not allow an accurate examination of the FHD layer/substrate boundary region. Thus, RBS measurements were carried out on two similarly prepared films in order to assess whether germanium diffuses across the FHD/substrate interface. The dependence of the germanium concentration profile on the sintering parameters has also been studied.

4.4.1 XPS study of the germanium depth profile.

4.4.1.1 Preparation of the samples.

The samples from the batch May'01 (described in Table 4.1) were subjected to depth profiling by means of consecutive etch in 4:1 buffered HF and XPS analysis, as described in Chapter 2, Section 2.3.1.5.

In order to determine whether there is a change in composition during the sintering of the soot, two samples were deposited at the same time with deposition parameters 100 sccm $GeCl_4$, 150 sccm $SiCl_4$, 600 sccm N_2, and 65 sccm BCl_3 as flux of gases to the torch. One of them was removed just after the deposition step and kept apart, while the second one underwent the high-temperature sintering step.

4.4.1.2 Comparison of the profiles for FHD layers before and after sintering.

XPS analysis of the soot before and after sintering was performed on the samples prepared as described in 4.4.1.1. In the spectrum corresponding to the as-deposited soot, Figure 4.8 (a), the peaks corresponding to the 2p1/2 and 2p3/2 of germanium can be clearly seen at 1217 and 1248 eV.

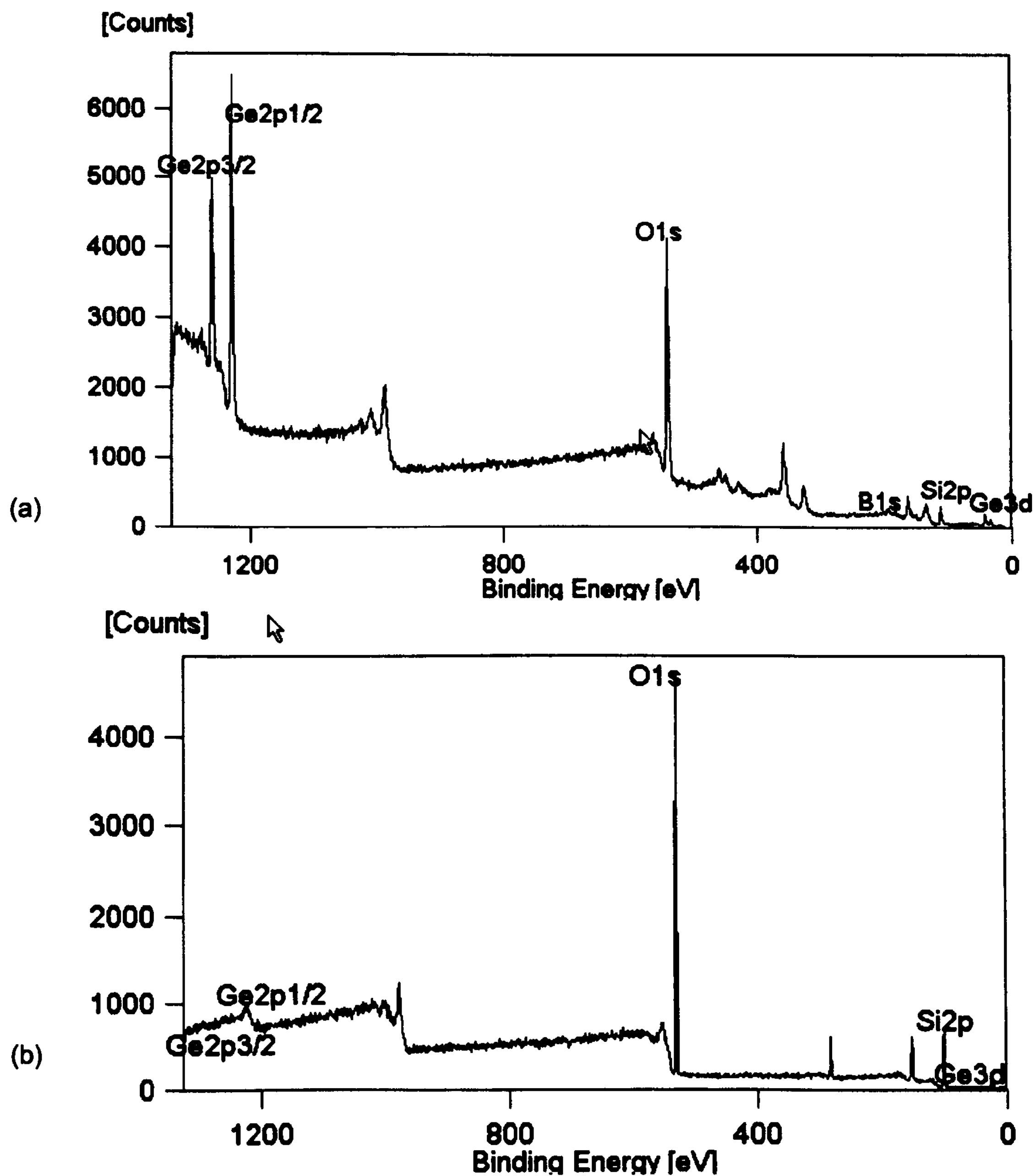

Figure 4.8. XPS spectra before and after sintering of the soot: FHD sample with halide fluxes of 100 sccm $GeCl_4$, 150 sccm $SiCl_4$, 65 sccm BCl_3: (a) XPS spectrum of the as-deposited soot; (b) XPS spectrum of the FHD layer after sintering of the soot at 1350 °C for 2 h. A decrease in the intensity of the germanium peaks is evident.

Quantitative analysis of the spectrum reveals a germanium composition of 15.1 ± 0.6 % wt. (Table 4.3). After the sintering step, the XPS spectrum shows clearly a decrease in the intensity of the germanium 2p peaks, implying a clear decrease of the germanium concentration at the surface of the sample, Figure 4.8 (b). The quantitative analysis is shown again in Table 4.3, yielding a germanium

content of 0.49 ± 0.12 % wt. This result clearly demonstrates the presence of a mechanism that results in the depletion of germanium species from the sample, probably explained by the volatility of the germanium oxide at such a high temperature.

Sample	counts			Ge %wt.
	Si	Ge	O	
soot	954	480	10288	15.11±0.6
sintered	1711	16	9444	0.49±0.12

Table 4.3. XPS compositional analysis of the surface of a FHD layer before and after high temperature sintering step.

4.4.1.3 Germanium depth profile of the sintered Ge:SiO_2 FHD silica layers.

Further XPS measurements were carried out on sintered FHD silica samples in order to find out the extent of the germanium-depleted region and to obtain the form of the germanium depth profile. The experiments were performed as described in Chapter 2 Section 2.3.1.5 for samples deposited using different gas flow rates during the soot deposition step. The results are shown in Figure 4.9.

A clear depletion region can be observed at the interface of the FHD silica layer with the air. At the interface between the FHD silica layer and the thermal oxide, again depletion of the germanium content was observed after a long enough HF etch time. However, it is possible that this effect might be due to the fact that the thermal oxide underneath the FHD layer was being exposed in certain areas, leading to the measurement corresponding to an average of the composition of the FHD silica layer and the germanium-free thermal oxide. In order to verify whether the reduction of germanium was due to the exposure of the un-doped thermal oxide or whether it was due to diffusion of the germanium species through the FHD silica layer and into the thermal oxide substrate, RBS analysis of a similarly prepared sample was carried out.

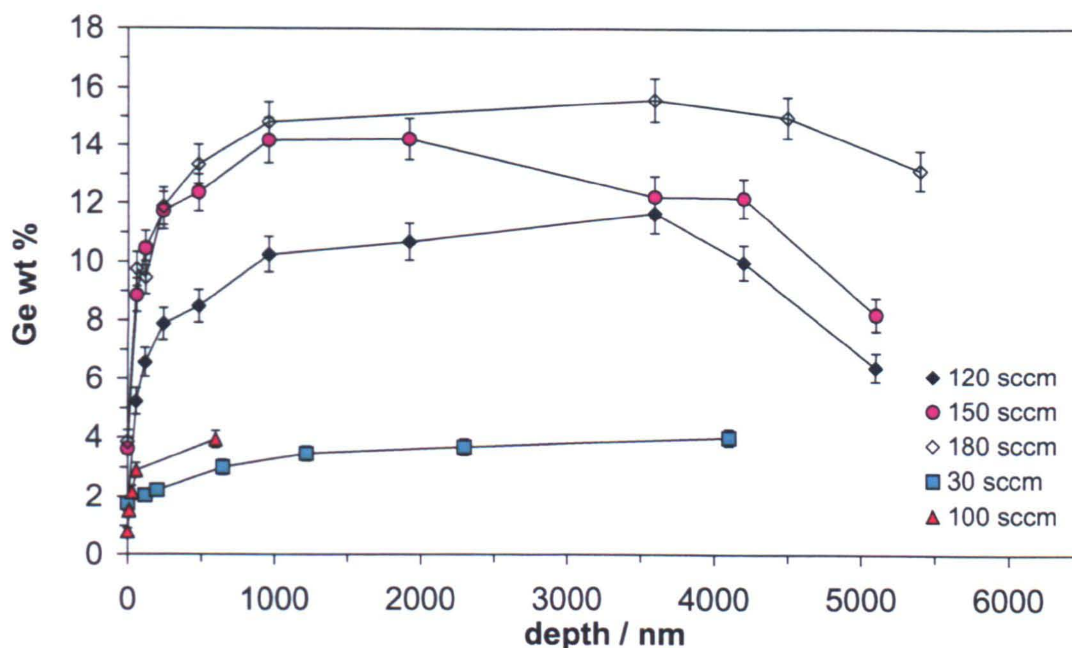

Figure 4.9. XPS-depth profile for FHD silica layers deposited with different $GeCl_4$ fluxes.

Furthermore, the destructive method used during the XPS germanium profiling implied that there was a possibility of a differential etch rate in HF of the SiO_2 compared with the GeO_2, that could lead to a germanium richer surface (or viceversa) as the etch advances. Thus, in order to corroborate the results shown in Figure 4.9, another measurement technique that does not require this HF etch step was used. As outlined in Chapter 2, RBS analysis provides a suitable non-destructive method to perform these analyses.

4.4.2 RBS analysis of FHD silica layers germanium depth profile.

4.4.2.1 Preparation of the samples.

For RBS analysis, two sets of samples were prepared, as shown schematically in Figure 4.10.

For the first set, 6 μm of FHD silica with a $GeCl_4$ flux of 100 sccm (150 sccm $SiCl_4$, 600 sccm N_2 and 65 sccm BCl_3) was deposited on a silicon substrate on which 15 μm of silicon dioxide had been thermally grown. For the second set, an FHD silica layer 9.2 μm thick was deposited directly onto a silicon substrate.

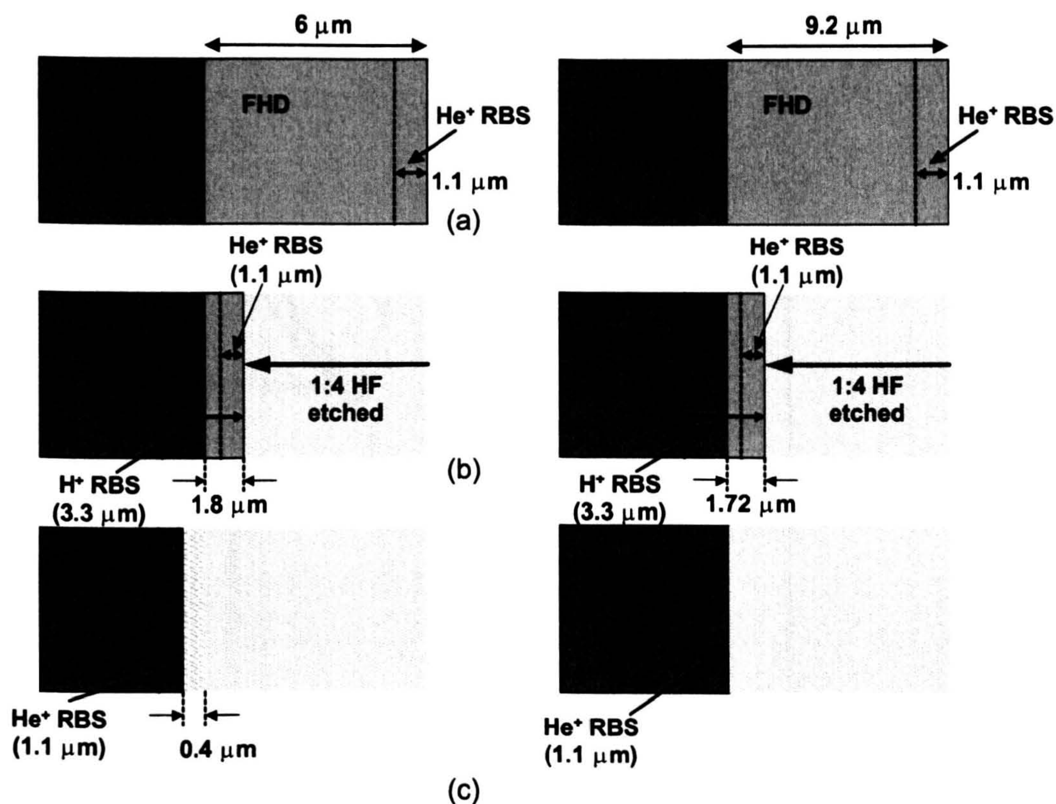

Figure 4.10. Schematic of the samples used for the RBS analysis: description of the etching carried out in buffered HF to perform the different RBS analysis: (a) As deposited FHD layer deposited on thermal oxide (left) and directly on silicon (right); (b) After etching in HF leaving only 1.8- (left) and 1.72 μm (right) of FHD layer; (c) Further etching step in HF removing the residual FHD layer from the previous step.

The possible analyzable depth using 2 MeV He^+ as incident ions is ≈1.1 μm and using 2 MeV H^+ ions is ≈3.3 μm before the Ge and Si peaks overlap in the spectrum. Thus, only the outer 1-3 μm of the films could be analyzed. In order to be able to explore the germanium composition profile at the interface with the thermal oxide or silicon, the Ge:SiO_2 FHD layers were etched in 4:1 buffered HF down to 1.8 and 1.72 μm thick respectively (Figure 4.10).

Further etching in HF was carried out in the films (Figure 4.10 (c)) until the FHD layer was completely removed. In the case of the sample deposited on thermal oxide, a further 0.48 μm of the thermal oxide were etched.

4.4.2.2 Germanium depth profiling using RBS.

The two as-deposited samples (Figure 4.10 (a)) were analyzed by RBS using 2 MeV He^+ ions in order to analyse the germanium distribution in the outer region of

the Ge:SiO_2 FHD layers, and the spectra can be seen in Figure 4.11 (a) (green and blue lines).

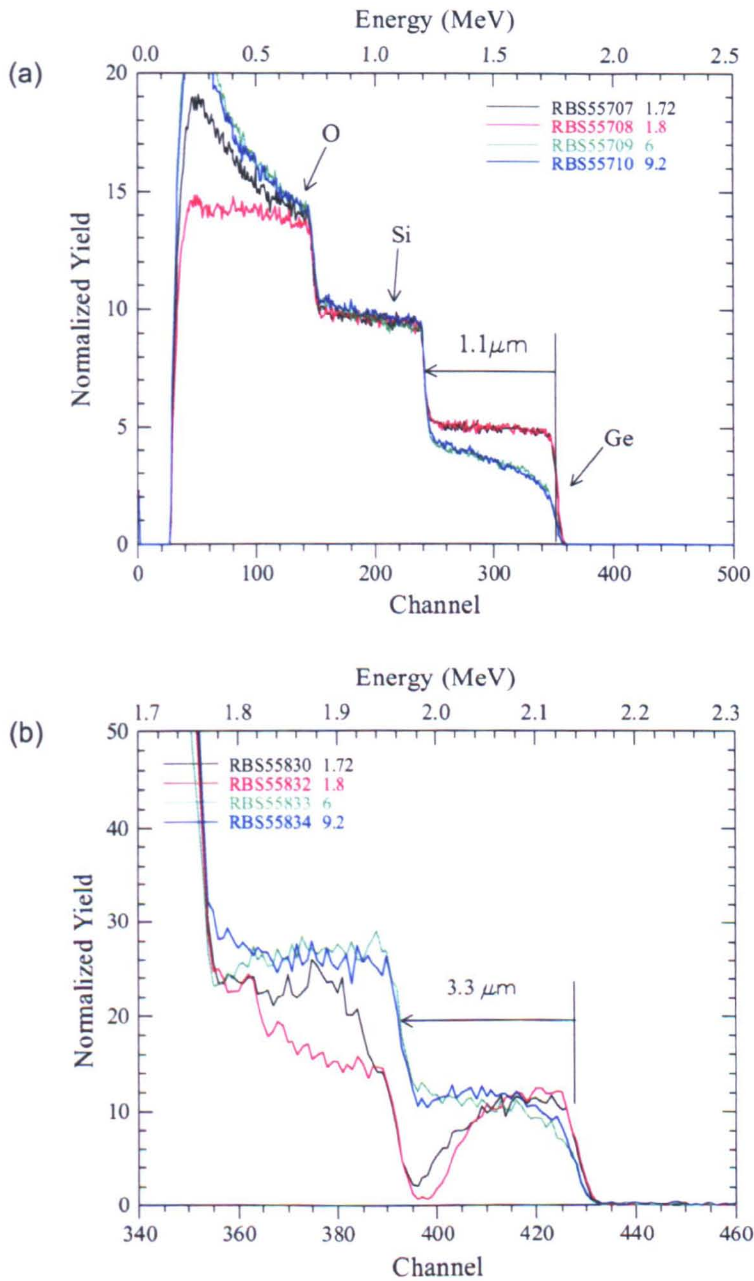

Figure 4.11. RBS spectra in the FHD/air and FHD/(silicon or silica) interfaces: (a) He+ RBS spectra of the samples shown in Figure 4.10 (a) and (b). The green and blue plots correspond to the samples deposited on thermal oxide and silicon respectively (Figure 4.10 (a)). The red and black correspond to the same samples after etching in HF (Figure 4.10 (b)). (b) H+ RBS spectra of the same samples.

In the spectra, the region corresponding to energies of the backscattered ions in the range between approximately 1.3 and 1.75 MeV corresponds to ions backscattered by germanium atoms in the sample. The energy 1.75 MeV corresponds to the energy of the ions backscattered by germanium atoms on the surface of the sample, as has been explained in Chapter 2 Section 2.3.2. As described in Chapter 2, the yield (number of backscattered ions) is proportional to the number of backscatterer atoms in the sample at the depth of collision that corresponds to that energy, which is determined by considering the kinematic factor and the scattering stopping cross-section. For the same kind of scatterer, the detected energy decreases the deeper into the sample the collision event occurs. If, at the same time, the yield increases considerably, this indicates that there is increase in concentration of that kind of atoms at that depth. This can be observed in Figure 4.11 (a), blue and green lines.

New RBS spectra using 2 MeV He^+ were taken of the samples for which the Ge:SiO_2 FHD layer was etched down to 1.72 and 1.8 μm (Figure 4.10 (b)). The spectra can be seen in Figure 4.11 (a) (red and black lines). From these spectra it can be seen that the germanium composition on the first 1.1 μm was constant and equal to the composition of the bulk (14.86±0.75 % wt. Ge). This implies that the diffusion of germanium into the substrate does not have influence in the germanium profile at that distance from the interface.

Since the penetration for 2 MeV H^+ is greater than in the case of He^+, additional spectra using H^+ ions were therefore taken on the etched samples (Figure 4.10 (b)) in order to analyze the composition to a greater depth. A drawback of using H^+ ions is that the cross-sections and stopping powers for H^+ backscattering are not as well known as those for He^+. An error worse than 10-15 % would be expected in the quantitative results from the analysis of the H^+ RBS spectra. Nevertheless, this measurement was able to show qualitatively that there was a gradient of germanium in the interface with the silicon and the thermal oxide, as can be seen in Figure 4.11 (b), (red and black lines). The point of 0 wt.% germanium is located at a point deeper than 3 μm from the surface of the etched films. As the depths of the films in which the analysis was done were 1.72 and 1.8 μm, it can be concluded that the germanium has diffused significantly into the silicon and thermal oxide respectively.

With the aim of performing a more accurate quantitative analysis of the germanium diffusion into the substrate, RBS spectra were taken with 2 MeV He^{+} from the samples shown in Figure 4.10 (c). The spectra are shown in Figure 4.12.

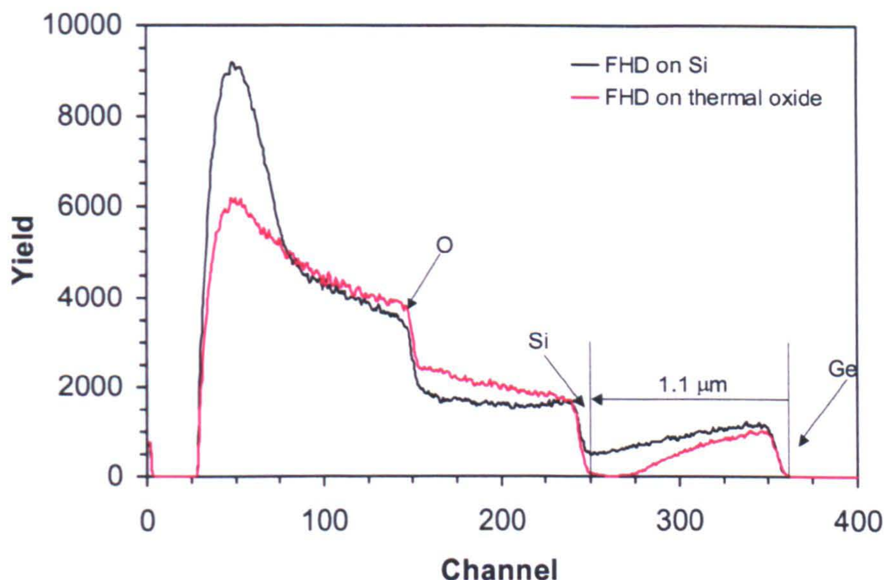

Figure 4.12. He+ RBS spectra of the FHD/Si and FHD/silica interfaces (Figure 4.10 (c)). In the case of the FHD layer deposited on thermal oxide, the end of the region where there is germanium present can be seen clearly in the spectrum.

A fit of the spectra corresponding to both samples was carried out by using the simulation software RUMP [Doolittle, 1985]. Both depletion regions, at the surface and in the interface with the substrate can be clearly seen (Figure 4.13), thus confirming our assumptions of germanium diffusion into the substrate and outside of the film.

The RBS results for the sample deposited directly on silicon are plotted in Figure 4.13 together with the XPS values obtained for a further sample from the same batch. It can be seen that both sets of data have a similar shape, supporting the conclusion drawn from the XPS germanium profiling by using HF wet etch of the layers to characterize the depletion of germanium in the FHD silica layers.

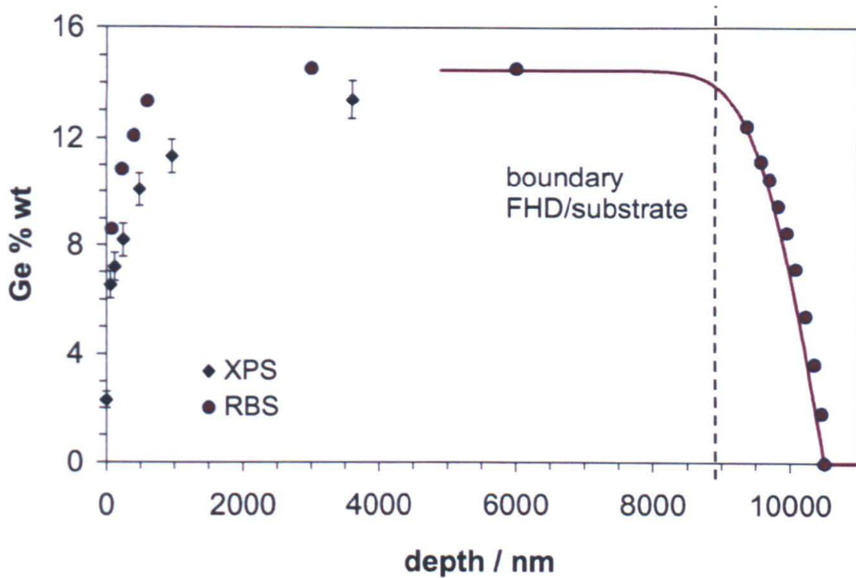

Figure 4.13. Germanium depth profile measured by XPS and RBS: a good agreement between the two sets of measurements can be observed.

4.4.3 Effect of the sintering conditions on the germanium profile.

XPS compositional analyses in depth were performed on the same set of samples that were sintered for different lengths of time, as described in Section 4.2 and whose refractive index profiles were analyzed in Section 4.3.7.

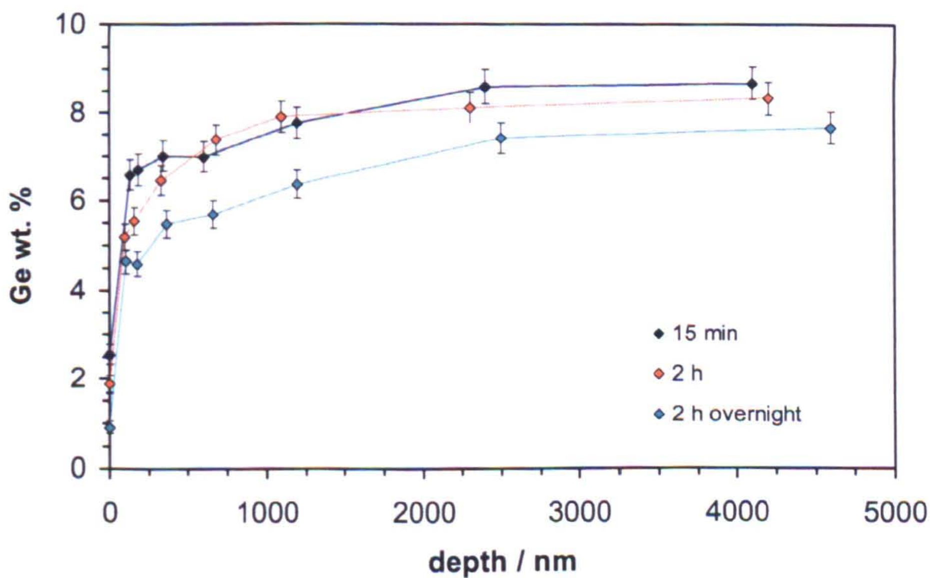

Figure 4.14. Effect of the sintering parameters on the germanium depth profile: XPS measurements taken on 3 samples sintered for different times at 1350 °C.

The results can be seen in Figure 4.14. The sample sintered only for 15 min presents a more abrupt depletion of germanium near the surface. The size of the larger germanium depletion region observed for the 2 h sintered sample is approximately 2 μm and for the sample left overnight at 600 °C is > 2 μm.

4.5 Structural analysis.

There are a large number of studies concerning the structure of silica [Gaskell, 1997] under different physical circumstances, such as high pressure [Sakka, 1969], different fictive temperatures [Brückner, 1970], [Chemarin, 1997] and of silica doped with different dopants, such as F [Yoshikawa, 1997], Sn [Chiodini, 1999], Au, Ag and Cu [Battaglin, 1998] and C [Johnson, 1998] among many others. In the present study, the study of the structure of the germanium-doped flame hydrolysis silica layers is interesting in order to understand the phenomena involved in the electron-beam irradiation of that material and the role played by the germanium concentration and the initial structure of the material in the electron-sensitivity of the silica and in the optical properties of the glass.

In the present work, Raman spectroscopy and EXAFS analysis of Ge:SiO_2 FHD layers, before (present chapter) and after irradiation (Chapter 5) with an energetic electron-beam have been carried out in order to examine the effect of the germanium in the structure and how it responds to the irradiation. Raman analysis allows the examination of the vibrational modes of the SiO_2 structure and how germanium affects them. It also brings information concerning the angles between tetrahedra in the structure, which determines the degree of compaction of the structure. EXAFS gives information about the local environment around the germanium atoms in the silica matrix, i.e. interatomic distances and the nature of the surrounding atoms.

4.5.1 Confocal-Raman spectroscopy.

4.5.1.1 Preparation of the samples.

Germanium-doped flame hydrolysis layers with a 14 % wt. germanium content were deposited on top of quartz substrates. The thickness of the layers was $\approx$7 μm. Quartz substrates were used in this case because the strength of the Raman peak of silicon is much stronger than that of silica. Even when a small portion of excitation light is transmitted to the substrate, a large signal from the silicon will introduce significant noise in the measured spectrum. It should be noted, however, that the results obtained on substrates deposited on quartz can vary slightly from the results that would be obtained if the substrate were silicon. This is due to the fact that the

stresses in the film will be different depending on the substrate on which they are deposited and that will affect the structure of the films. Nevertheless, it is anticipated that the general qualitative trend of the change in structure with germanium content and in depth should be similar for both type of substrates.

4.5.1.2 Raman scattering spectroscopy of as-deposited Ge:SiO_2 FHD layers.

The vibrational (Raman) spectra of amorphous solids consist primarily of broad bands, whose widths can be associated to disordered bond angles [Nian, 1989], [Galeener, 1979]. These bands are due to the different vibrational modes of the bonds in the structure, as discussed in Chapter 2 Section 2.4.1. In the SiO_2 network, these bands are named ω_1, ω_3 and ω_4, and appear at the wavenumbers of approximately 440 cm^{-1} (ω_1), 800 cm^{-1} (ω_3) and 1060 cm^{-1} and 1190 cm^{-1} for the transverse optic (TO) and for the longitudinal optic (LO) associated to ω_4 band [Galeener, 1979] [Chiodini, 1999].

Together with the broad bands associated with the vibrational modes of the continuous random network, two sharp features appear in the SiO_2 Raman spectrum. They are traditionally named "defect lines" D_1 and D_2 [Galeener, 1982b]. Its origin has been subject of some controversy. Galeener suggested that the D_1 and D_2 defect lines are due to a local arrangement of the SiO_2 structure in the shape of 4-fold and 3-fold unpuckered planar-ring structures [Galeener, 1982a] [Galeener, 1982b]. Other authors have suggested the impossibility of this model to produce such sharp features in the SiO_2 spectrum [Phillips, 1984], [Leeuw, 1985]. Pasquarello *et. al.* have recently performed quantum mechanics calculations based on first principles simulations of vitreous systems [Pasquarello, 2001] unambiguosly demonstrating that 3- and 4-membered ring structures embedded in the silica network are responsible for the defect lines D_2 and D_1 respectively.

When germanium is added to the silica structure, it is believed to substitute silicon atoms in the silica network [Nian, 1989], [Liu, 1997] still exhibiting the basic features of the un-doped silica network. Nevertheless, the presence of larger germanium atoms in the position of silicon atoms introduces distortion and strain in the glass structure, reducing the number and stability of small-membered rings. Therefore, the D_1 and D_2 lines in the spectrum get smaller as more germanium is introduced in the structure. This effect has also been studied for other dopants such as F [Yoshikawa, 1997] and Sn [Chiodini, 1999].

Figure 4.15 compares the Raman spectra of quartz (dark blue line) and 14 % wt. germanium doped FHD silica. All the spectra taken in this experiment were normalized with the ω_3 peak appearing at approximately 800 cm^{-1}, due to the fact that this peak is separated from the rest of the peaks appearing in the SiO_2 Raman spectrum [Chiodini, 1999]. The broad bands corresponding to the SiO_2 network are easily visible in both spectra. The D_1 and D_2 defect lines are readily observed in the quartz spectra and appear considerably diminished in the Ge:SiO_2 FHD films, supporting what has been previously discussed. The band centered at $\approx$ 440 cm^{-1} is narrower in the Ge-doped FHD silica sample. This has been proposed to be related to the Ge-O-Ge symmetric stretching vibration [Sharma, 1984], which introduces a narrow band at 416 cm^{-1}. The new broad band appearing at $\approx$ 670 cm^{-1} has been associated to the anti-symmetic vibration of the Ge-O-Ge and Ge-O-Si bonds [Dianov, 1997], [Sharma, 1984].

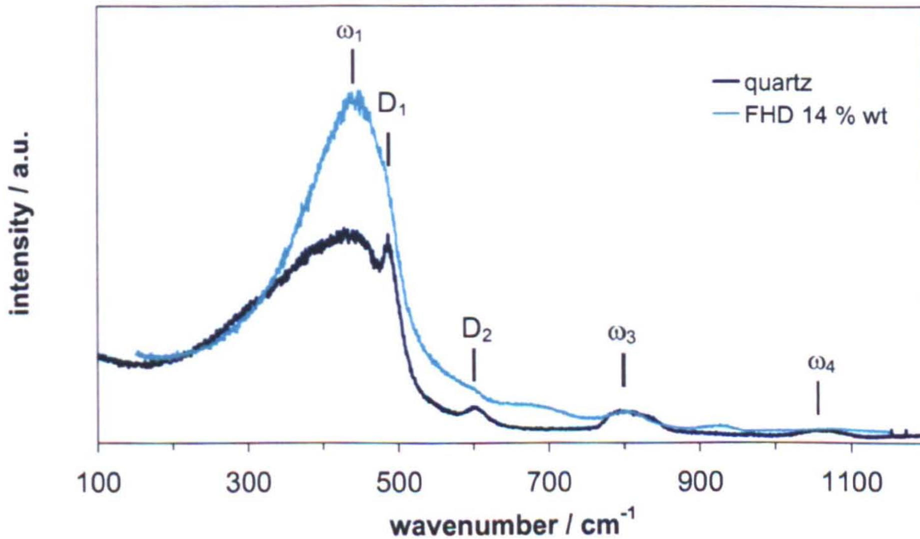

Figure 4.15. Comparison of the Raman spectrum of quartz and germanium doped FHD silica: The different features of the silica network can be observed in the spectra.

The confocal micro-Raman instrument used enabled depth profiling of the germanium doped silica with an observed volume of 1 μm^3. This is shown in Figure 4.16 for the as deposited 14 % wt. Ge:SiO_2 FHD silica sample. It is possible to observe the absence of noticeable D_1 and D_2 peaks for the first 6 μm of the material, appearing significantly stronger after the quartz substrate is reached. This result is consistent with the thickness of 7 μm of the Ge:SiO_2 FHD layers.

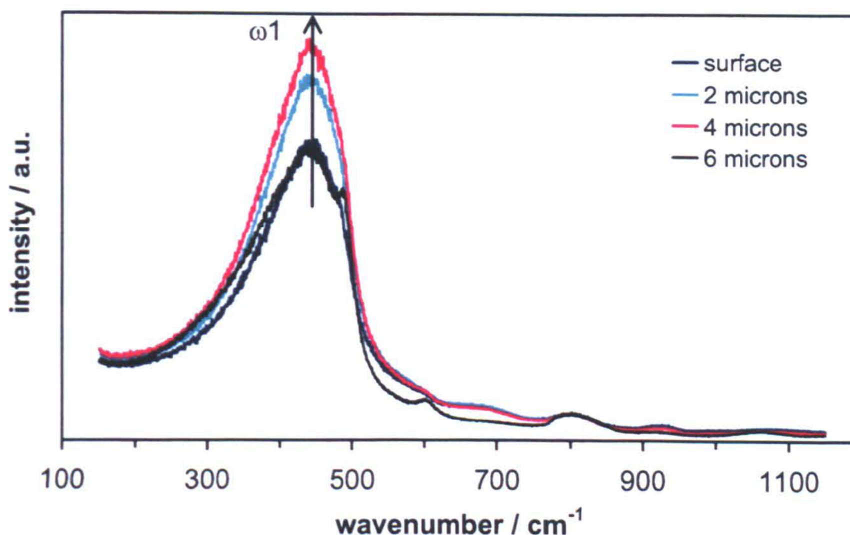

Figure 4.16. Evolution in depth of the Raman spectra: For a depth larger than 6 μm, the features of the quartz substrate appear. The germanium content of the film was 14 % wt.

The rest of the silica network peaks remain un-shifted with depth, probably suggesting an uniform structure of the layer in depth, for which the angles between tetrahedra remain constant. From the compositional analysis, a different germanium content in depth was found (Section 4.3). This variation in germanium content during sintering suggests that the consolidating silica matrix might adopt a slightly different structure. Nevertheless, the possible change in bond angle between tetrahedra does not appear to be evident in the Raman spectrum.

4.5.2 X-Ray Absorption Fine Structure (EXAFS) Analyses.

4.5.2.1 Preparation of the samples.

Flame hydrolysis deposited silica layers with different germanium contents (4, 14 and 15.5 % wt.) were deposited directly on silicon wafers (deposition recipes 100 sccm, 150 sccm and 180 sccm $GeCl_4$ respectively). The thickness of the layers was measured with a Talystep profilometer to be ≈7 μm thick (Section 4.2).

In order to compare the fitted interatomic distance and coordination number parameters for the FHD glass with a well-defined GeO_2 structure, a GeO_2 standard was prepared. To that end, GeO_2 powder bought from Aldrich-Sigma (Aldrich-Sigma, UK) was dissolved in ethylen-glycol and spun at slow speed on top of a microscope slide.

4.5.2.2 ReflEXAFS study of the germanium atomic environment.

ReflEXAFS measurements with fluorescence detection, as described in Section 2.4.2.5, were carried out in these as-deposited samples in order to investigate the local structure around the germanium atom before irradiation and the way in which this local structure changes with the germanium content. The measurements were taken at an incidence angle of 0.35 degrees. This angle is above the critical angle, θ_c, for reflection of the films, which is ≈0.178 deg as it can be seen from the reflectivity plot shown in Figure 4.17.

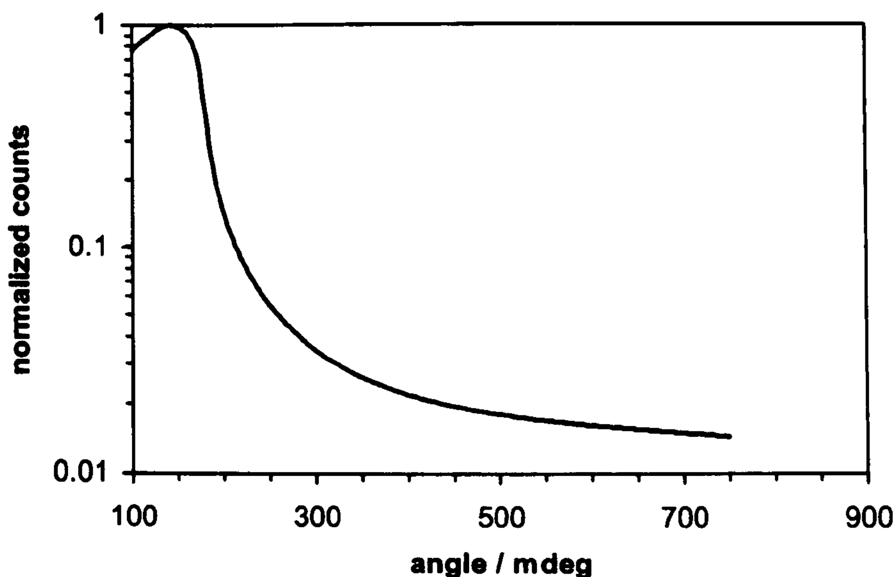

Figure 4.17. Reflectivity of the 14 % wt. germanium content as deposited sample: The critical angle, taken as the angle at which the reflectivity drops to half its maximum value, is around 178 mdeg. The EXAFS spectra were taken at 350 mdeg.

Fluorescence reflEXAFS data was collected from the GeO_2 standard, prepared as indicated in Section 4.5.2.1, in order to compare the fitted interatomic distance and coordination number obtained for the Ge:SiO_2 FHD glass with the one from a well defined GeO_2 structure. The data was collected at 0.350 deg of incidence angle. Figure 4.18 shows the measured EXAFS signal weighted with k^3 and the corresponding Fourier transform spectrum together with the results from the fitting.

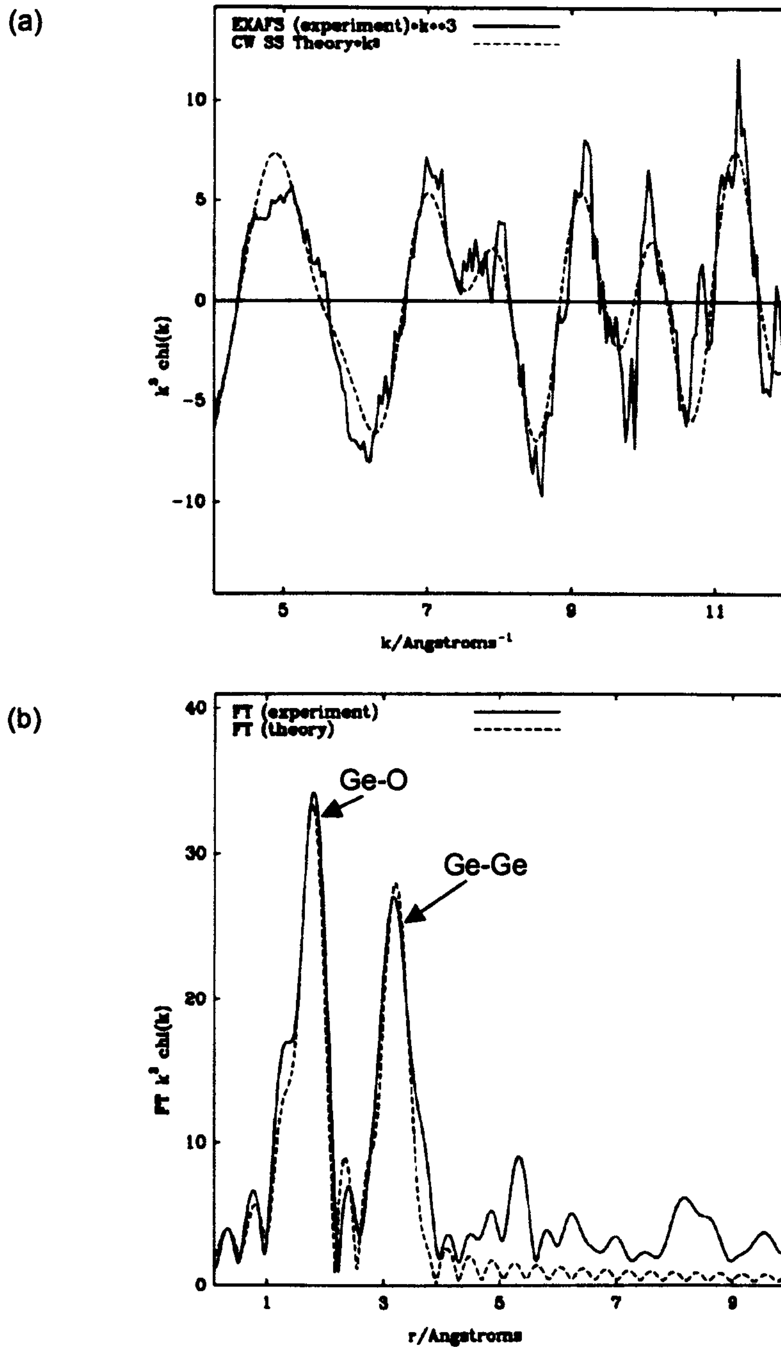

Figure 4.18. Fitting of the EXAFS data for a GeO_2 sample: (a) EXAFS signal; (b) Fourier transform signal.

In the Fourier transform, two clear peaks can be observed corresponding to the Ge-O bond and the Ge-Ge bond. The data was analysed as described in Chapter 2 Section 2.4.2.6. The values for the coordination number and the distances of the

different bonds obtained from the fit of the experimental data can be observed in Table 4.4.

Sample	Parameter					
	N			r / Å		
	Ge-O (1st shell)	Ge-Ge	Ge-O (2nd shell)	Ge-O (1st shell)	Ge-Ge	Ge-O (2nd shell)
GeO_2	3	1.7	0.09	1.73	3.19	1.61

Table 4.4. Coordination number and radius obtained from the fit of the EXAFS data for a GeO_2 in ethylene-glycol solvent layer spun on top of a microscope slide.

It can be seen that the coordination number obtained, 3, is smaller than the 4-6 coordination number usually expected for a hexagonal-tetragonal GeO_2 structure [Okumura, 1998]. This may be due to the effect of "self-absorption" arising due to the fact that the measurement was taken at a large incidence angle, as is further explained in Section 2.4.2.4. Also, the sample is concentrated and the surface was not very smooth, as could be observed by direct optical inspection, allowing the X-ray to arrive at steep angles to the material. Nevertheless, the distance obtained for the first and second shell around the central atom should be still the correct ones.

By comparing with the values reported by Okumura *et al.* [Okumura, 1999], [Wefing, 1999], [Skuja, 2000] for the distances of the Ge-O and Ge-Ge bonds in hexagonal GeO_2 obtained by different characterization techniques, 1.74 Å and 3.15 Å respectively, it is possible that the sample analyzed in this work could be considered to present that structure. In that case, the coordination number for the oxygen should be 4.

The values obtained for the FHD silica samples with different germanium contents are shown in Table 4.5, obtained from the fit of the experimental data with three shells, as shown in Figures 4.19-4.21.

Sample	Parameter					
	N			r / Å		
	Ge-O (1st shell)	Ge-Si	Ge-O (2nd shell)	Ge-O (1st shell)	Ge-Si	Ge-O (2nd shell)
4 wt. %	2	0.7	1.6	1.79	3.01	2.86
14 wt. %	1.1	0.3	0.9	1.79	3.04	2.84
15.5 wt. %	0.9	0.2	0.9	1.79	3.1	2.83

Table 4.5. Coordination number and radius obtained from the fit of the EXAFS data from Figures 4.19-4.21 for the as deposited samples with different germanium compositions.

Again, lower coordination numbers than the ones expected for GeO_2 were obtained. In order to remove the self-absorption effect, measurements at smaller angle than the critical angle for reflection should be taken. But the bulk of the sample was intended to be investigated, and, since the distances of the different bonds are still correct, these measurements are sufficient for the purposes of the present work. Furthermore, the reflEXAFS configuration is very sensitive to the roughness of the sample. If the roughness of the layers is above 10 Å, even at an angle below the critical angle for reflection, the beam impinges on most of the material with a much larger angle, therefore penetrating more than hundreds of angstroms, and therefore, self-absorption will lead again to incorrect coordination numbers.

(a)

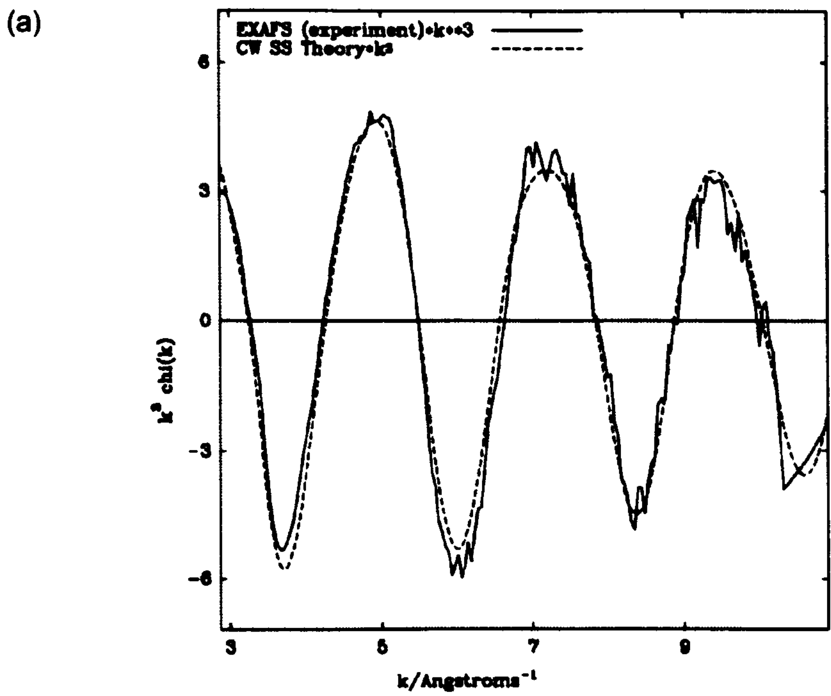

(b)

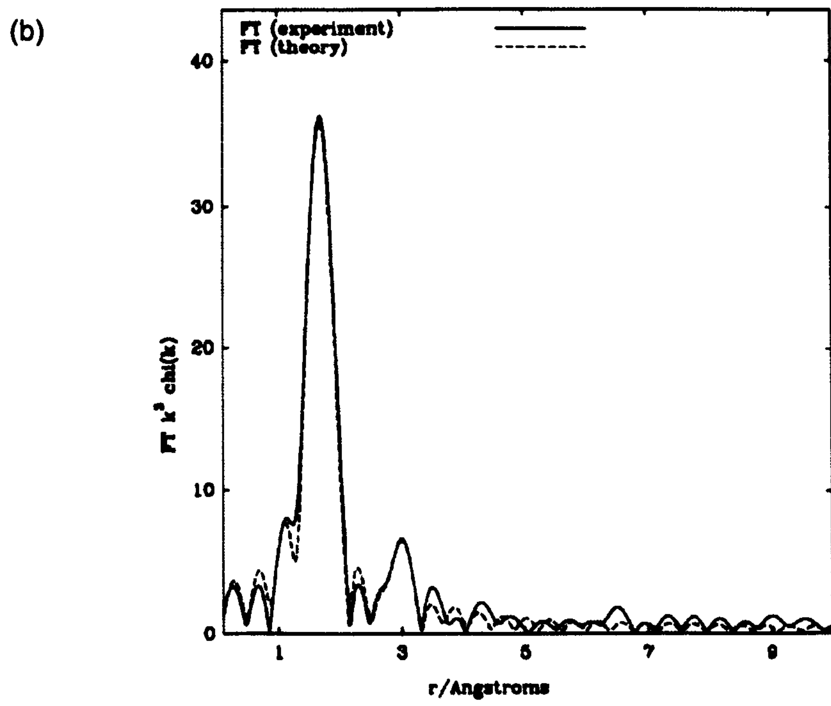

Figure 4.19. Fitting of the EXAFS data for a 4 % wt. Ge as deposited sample: (a) EXAFS signal; (b) Fourier transform signal.

(a)

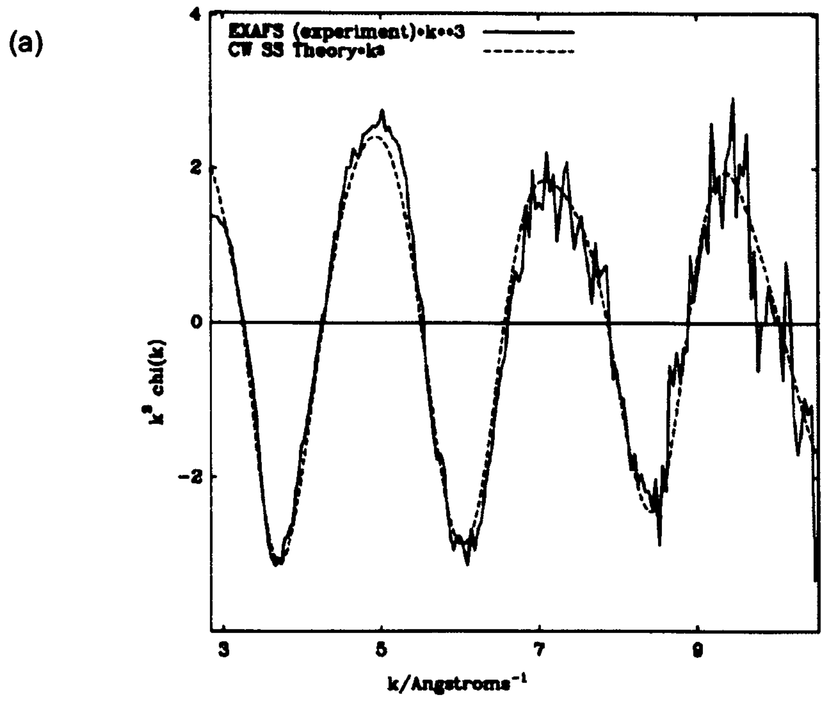

(b)

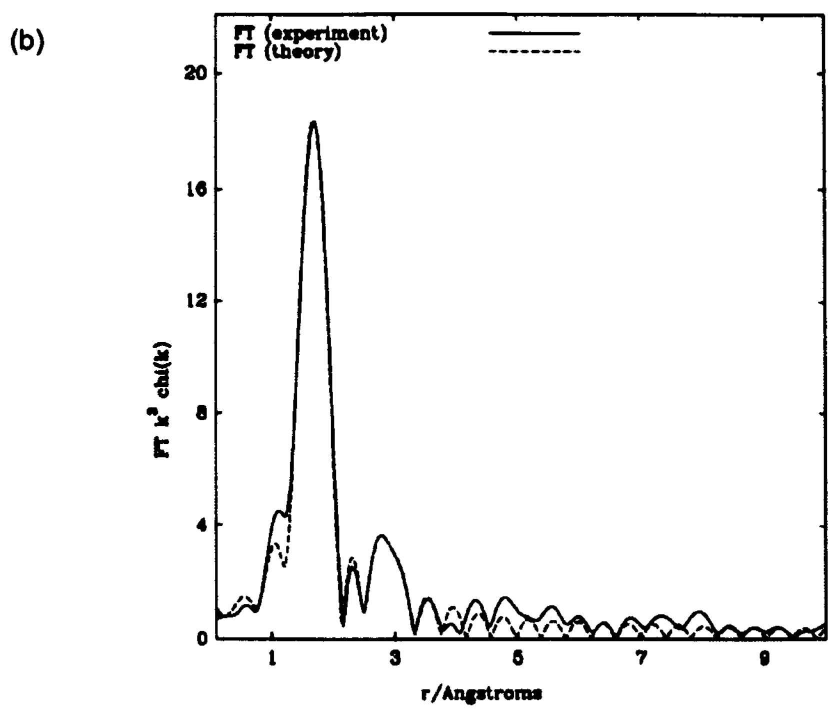

Figure 4.20. Fitting of the EXAFS data for a 14 % wt. as deposited sample: (a) EXAFS signal; (b) Fourier transform signal.

(a)

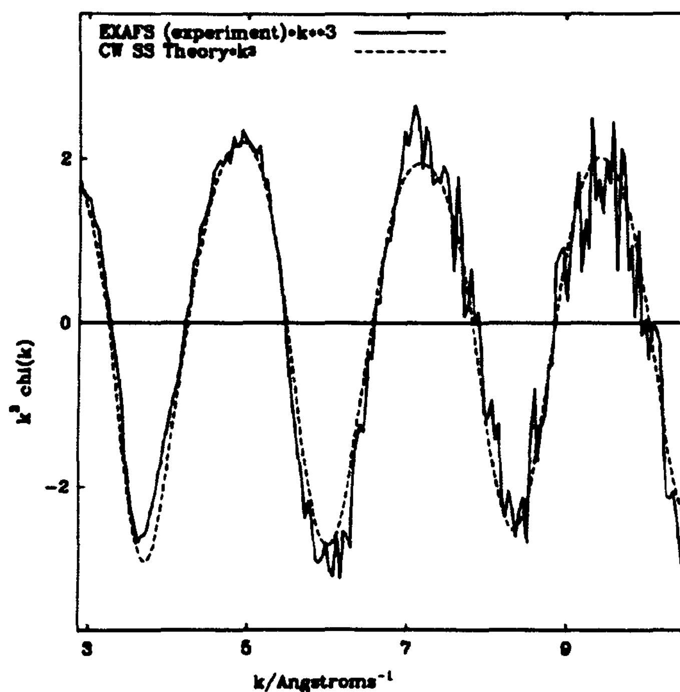

(b)

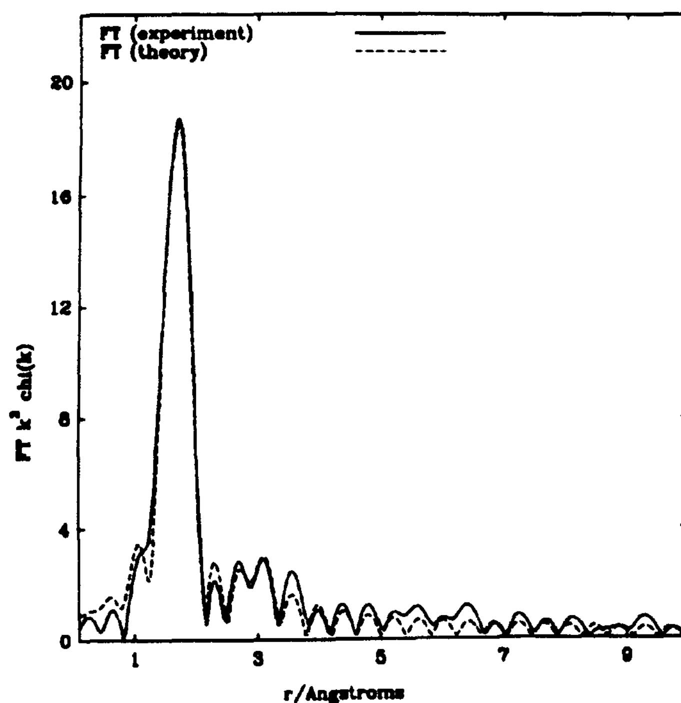

Figure 4.21. Fitting of the EXAFS data for a 15 % wt. Ge as deposited sample: (a) EXAFS signal; (b) Fourier transform signal.

The measured distances were independent on the germanium content, at least for the range of compositions used in this work. The length of the bond Ge-O obtained was larger than the one in pure GeO_2 (Table 4.4), implying a change of structure of the GeO_2 when immersed in the FHD silica network, probably due to the difference in inter-tetrahedral angle between the two networks [Hussin, 1999]. Another explanation can be that the oxygen is attracted closer to the silicon centre. Also, the formation of Ge-OH could also be possible. In the fitting of the EXAFS oscillations, the introduction of another shell of Ge-Ge bonds was not justified by a decrease of the fitting test (Section 2.4.2.6). This probably indicates that the germanium is incorporated into the silica network in Ge-O bonds instead of being clustered in Ge-Ge groups, as proposed previously by Greegor *et. al.* [Greegor, 1987].

Further work needs still to be done in order to fully understand the way in which germanium interacts with the silica structure.

4.6 Density profile measurement by X-ray reflectivity.

As has been stated in Chapter 2 (Section 2.5.1), X-ray reflectivity measurements allow the empirical measurement of the density of amorphous material through the fitting of the reflectivity curve with the appropriate reflectivity model. In this section, the influence of the sintering conditions of the flame hydrolysis soot on the density profile of the consolidated material was explored. This is important, as a different sintering procedure will translate in a different structure and this will determine the way in which the material will respond to the electron-beam irradiation.

4.6.1 Preparation of the samples.

The same set of Ge:SiO_2 FHD layers, the composition of which was studied in Section 4.4 to determine the influence of the sintering conditions on the germanium concentration depth profile, were prepared for this experiment, but in this case on top of 5 mm thick silicon blocks (Section 2.5.1). Three regions were defined by photolithography and then etched in 4:1 buffered HF in order to analyze the density at 3 depths (surface, 180 nm and 1680 nm) below the as-deposited sample surface interface. X-ray reflectivity measurements were taken at 1.36 Å of wavelength. At the critical angle, the depth of the sample that is being analysed can be calculated using the software available from the Center for X-Ray Optics at the E.O. Lawrence Berkeley National Laboratory. The software calculates the X-ray transmission through a material of certain thickness. In a reflectivity experiment, at the critical angle some X-rays enter inside the material, being reflected at a certain depth. In order to contribute to the measurement, the total transmission of the sample for a thickness equivalent to the way in and out of the material should be > 0. Calculating the thickness of sample that would make the transmission fall to 0.05, the depth of sample analyzed by a beam of 1.36 Å X-rays at the critical angle is ≈950 nm. It should be noted that the penetration is dependent on the composition and density of the material in each case, therefore, the value given is just orientative (calculated for a 7 % wt FHD sample with density 2.2 g·cm^{-2}).

4.6.2 Measurement of the density profile.

The data collected for the 3 different sintering time samples was analyzed as described in Chapter 2 Section 2.5. The values for the density of the different samples obtained from this experiment are summarized in Table 4.6.

It can be seen that for the 2 h sintered sample, an increase of density in depth was evident. This is consistent with the depletion of germanium from the surface observed by XPS and RBS compositional analyses. Those results, together with the present X-ray reflectivity results, suggested that out-gassing of germanium form the surface produces a region of lower density near the surface. The reasons for the lower density can be a decrease of germanium, which itself will reduce the density, but also, a reduced germanium content in the outer region of the layer during the sintering step will increase the temperature needed for a complete sinter of the soot. Therefore, the outer region will have a lesser degree of sintering than the bulk.

Sample		Density / g.cm^{-3}
15 min sintering	surface	2.40 ± 1.3%
	180 nm deep	2.40 ± 1.3%
	1680 nm deep	2.48 ±1.3%
2 h sintering	surface	2.46 ± 1.3%
	180 nm deep	2.53 ± 1.3%
	1680 nm deep	2.54 ± 1.3%
2 h overnight sintering	surface	2.36 ± 1.3%
	180 nm deep	2.43 ± 1.3%
	1680 nm deep	2.49 ± 1.3%

Table 4.6. Density measured by X-ray reflectivity for 3 different sintering routines for the FHD: 15 min at 1350 °C, 2 h at 1350 °C and 2 h at 1350 °C leaving it in the furnace at 600 °C overnight. The measurements were performed at 1.36 Å of wavelength.

In contrast, for the sample sintered during 15 min, a more uniform density profile was observed. This was again consistent with the more uniform germanium depth profile obtained from XPS measurements (Figure 4.14). The lower value of density obtained in this case, was also consistent with the shorter sintering time, which was probably insufficient to allow complete sintering of the material.

Further experiments would be needed in order to fully confirm this results, such as either SEM micrographs [Bonar, 1995] to investigate the sintering state of the samples or propagation losses measurements in order to test the propagation characteristics of the different degrees of sintering. Nevertheless, the results obtained in this study were enough to observe a difference in germanium content and density with which then justify a different behavior under electron-beam irradiation of samples sintered in different manner.

The density profile of a sample with a higher germanium content (15 % wt. in the bulk) and sintered by the normal routine (2 h at 1350 °C, cool down to 600 °C and removal from the furnace) was also investigated. As discussed later in Chapter 5, its density change after irradiation with a 10 keV electron-beam was analyzed. The results for the density profile of this as-deposited sample are shown in Table 4.7.

depth analysed	d / Å	rho / $Å^{-2}$	sigma / Å	chi^2	density /$g.cm^{-3}$
0	1.92 54.19 N/A	$2.826.10^{-5}$ $1.918.10^{-5}$ $2.035.10^{-5}$	8.5 12 73.3	1.58	2.39±1.3%
≈ 120 nm	0.28 2 N/A	$1.566.10^{-5}$ $1.734.10^{-5}$ $2.157.10^{-5}$	7.1 8.9 25.0	1.03	2.56±1.3%
≈ 480 nm	0.17 0.29 N/A	$1.597.10^{-5}$ $1.725.10^{-5}$ $2.185.10^{-5}$	6.9 9.4 28.5	0.82	2.61±1.3%

Table 4.7. Calculation of the variation in depth of a FHD sample with a germanium composition in the bulk of 15 % wt measured at a wavelength of 1.36 Å. The first column indicates the depth at which the reflectivity has been calculated. Columns 2-4 show the parameters resulting from the fit with the Parratt32 software with goodness of fit as indicated in column 5. In the last column, the density calculated from the fits is presented.

4.7 Conclusions.

In this chapter, the germanium-doped flame-hydrolysis deposited silica layers have been optically characterized. The spacing of the measured effective refractive indices of the different modes of propagation supported by the structure does not correspond to a step-index profile. Therefore, more complex modeling of the FHD silica layers was carried out which showed that there was a non-uniform refractive index profile with decreasing refractive index towards the surface of the layers.

Two methods were used and compared for the calculation of the refractive index profile from the values of the effective refractive indices of the propagating modes. Firstly, the profile was divided in layers and each layer varied between some limits by means of a fitting algorithm based on genetic algorithms, which led to a solution in the proximity of a global minimum. Subsequently, that solution was used as the starting point for a simplex fitting algorithm. The fits obtained with this method were better than the experimental error, which, provided a degree of confidence that this represented a good approximation. Nevertheless, the computation time for the genetic algorithm was very large, as the number of times it evaluates the function to minimize is large, in order to find the global minimum.

An alternative method consisting of a variation of the *inverse*-WKB method with asymmetry factor 0.8 was used, in which the profile solution from the *inverse*-WKB method was fed into a simplex search algorithm in order to refine the fit. The profiles obtained with this method were similar to the ones obtained from the genetic algorithm fit. Furthermore, the computation time for this method was considerably smaller. The *inverse*-WKB method takes few seconds to obtain a starting profile and the simplex method then refines the search in the proximity of that solution in a time scale of minutes while the result obtained is similar. Therefore, this method was more convenient for the search of the optimum refractive index profile.

Refractive index profiles for samples deposited with different germanium fluxes to the torch were analyzed and all of them showed a decrease in refractive index towards the surface and an increasing value of refractive index in the bulk when there is a higher germanium content in the sample.

The reason for the non-uniformity of the refractive index was then explored, obtaining a depletion in germanium concentration in the outer region of the films.

This result was obtained from XPS and RBS measurements. RBS measurements showed a diffusion of germanium in the FHD layer-substrate interface. Furthermore, density measurements performed by X-ray reflectivity also showed a gradient in the density profile in depth. The origin of this non-uniformity of the films might be the high-temperature sintering step during the deposition of the FHD layers, which allows the germanium species to diffuse along the films. Both, germanium content and density are related to the refractive index of the material through the Lorentz-Lorenz relations.

The structure of the films was also characterized in depth by Raman spectroscopy, not finding variation on the angle between tetrahedra in depth. EXAFS analysis allowed to characterize the length of the Ge-O bonds, arriving to the conclusion that the germanium introduced in the samples, for the concentrations studied in this work, was not clustered but incorporated into the silica network in the form of Ge-O bonds, which are deformed in comparison with the bonds present in pure GeO_2, probably due to the stresses induced in them by the silica network.

The results obtained in this chapter will be used in Chapter 5 for the characterization of the effect that the electron-beam irradiation produces in the germanium-doped FHD silica films.

Chapter 5
Study of the effects induced in the germanium-doped FHD silica layers by electron-beam irradiation

Chapter summary.

The present chapter deals with the effects that electron-beam irradiation induces in the germanium-doped FHD silica layers, making the technique suitable for the fabrication of optical waveguide devices. The interaction of the electron-beam with the material and the transfer of energy are analysed first. The density and structural changes induced in the silica are then characterized, using the techniques described in Chapter 2, as they are the main ones responsible for the change in refractive index. The refractive index change and its behaviour with depth were characterized optically and correlated with the density changes, which were thought to be the main contributors to the refractive index change. The magnitude of the index change was found to be large enough to allow the fabrication of optical devices. Finally, the stability of the change induced by the irradiation was studied by means of isochronal annealing experiments.

5.1 Introduction.

Integrated optical circuits potentially play an important role in many fields of application. In particular, integrated optical circuits in silica-on-silicon have been used extensively for both telecommunications and sensing applications. The detailed characterization of fabrication techniques that allow the production of these devices with specific properties is therefore desirable.

Typically, device fabrication using planar silica technology is based on the deposition of doped-silica layers followed by photolithographic pattern transfer of mask and dry-etch definition of the different elements. This technology has been investigated for many years [Miller, 1969] and is extensively used in the fabrication of integrated optical elements for communications and has also received attention in the sensors and bio-sensors industry [Ruano, 1999]. Nevertheless, the technique involves a number of processing steps in which critical control of silica deposition, sintering and dry-etching is required in order to obtain low-loss waveguides.

In recent years, a great deal of work has been carried out in order to develop novel fabrication techniques that allow the formation of low-loss optical waveguides with a minimum number of fabrication steps and further possible integrability. Among these techniques, irradiation of silica with different kinds of radiation has been a subject of great interest. Since its discovery [Hill, 1978], UV-irradiation of silica has found applications for the formation of directly-written gratings in fibers and planar silica structures. Trimming of optical circuits has also been performed using UV-irradiation [Kashyap, 1993] together with the direct-UV-writing of optical waveguides [Svalgaard, 1997]. However, the sensitivity of silica to the laser light normally used in making these structures, (244 nm and 198 nm) is not large enough and the use of pre-processing techniques such as hydrogen-loading [Lemaire, 1993] to enhance the photosensitivity is required. This problem may also be overcome by the use of shorter wavelength lasers, such as F_2-laser radiation at 157 nm or other kinds of ionizing radiation such as energetic electrons.

In the present work, the effect of electron-beam irradiation on germanium-doped flame-hydrolysis deposited silica has been studied. This technique allows the direct fabrication of buried channel waveguides immediately below the surface of the FHD-silica. The waveguides have smooth sidewalls, low propagation loss and low-birefringence. In order to be able to fabricate optical circuits using this technique, the effect of the electron-beam on the silica and its dependence on the different irradiation parameters, the composition and the initial structure of the silica needed to be investigated.

Electron-beam irradiation of silica has been reported to produce an increase in the refractive index of the material due to the formation of defects and to the densification of the exposed material [Barbier, 1991]. A number of components, including waveguides, Y-branches, and thermo-optical switches, have all been reported [Bell, 1991], [Madden, 1990], [Barbier, 1991], [Lewandowski, 1994], [Lewandowski, 1991], [Syms, 1994a], [Syms, 1994b], [Syms, 1995], [Syahriar, 1998]. Nevertheless, the study of the refractive index profile of the waveguides formed, the influence of the different writing parameters and the effect of the germanium content on the magnitude of the change induced by irradiation has not been systematically addressed.

This chapter begins (Section 5.2) with a description of the irradiation technique used. Then, the energy transfer from an energetic electron-beam to the material is

studied (since the effect of the electron-beam on the material should be related to the amount of energy deposited). The transfer of energy from the electron-beam to the silica structure produces structural rearrangements and the formation of different kinds of defects that also absorb in the ultraviolet. The rearrangement of the structure will lead to densification of the silica matrix, an effect that is accompanied by an increase of refractive index. The formation of colour centres also influences the change in refractive index through the Kramers-Krönig relations [Spaargaren, 2000]. Nevertheless, the magnitude of the contribution of the colour centre to the total change in refractive index is typically much smaller than the contribution from densification [Barbier, 1991]. Consequently, in Section 5.4, the structure of the germanium-doped silica layers after irradiation was studied by Raman scattering spectroscopy and EXAFS and compared to the results obtained in Chapter 4 for the as-deposited layers. In Section 5.5 the densification suffered by the material after irradiation was characterized. The dependence of the change in density on the dose, the germanium content and the pre-existing structure was investigated. Finally, an elastic model was used for the calculation of the strains that appear in the structure. Densification was related to the change in refractive index in Section 5.6. The evolution of the effective refractive index of the different modes with the irradiation dose was analyzed and compared with the evolution found for the densification. Their differences were explained and the birefringence induced in these layers by the electron-irradiation was characterized.

Finally, in Section 5.7, studies of the stability of the changes induced by the electron- beam, i.e. densification and change in refractive index, were described. Isochronal annealing was carried out and an activation energy was found for the thermal relaxation of the damage.

5.2 Irradiation techniques.

Irradiations were performed at electron energies of 50 and 10 keV.

5.2.1 Preparation of the samples.

Ge-doped flame hydrolysis deposited silica layers were deposited as described in Chapter 4, Section 4.2. To prevent the samples from charging, a 30 nm thick layer of nichrome was evaporated on top of the cleaned samples prior to irradiation in a Plassys MEB450 metal evaporator system. The nichrome was removed after irradiation in a solution of 200 g of ceric ammonium nitrite, 35 ml of acetic acid and 1000 ml of D.I. water.

5.2.2 Method for the irradiation at 50 keV.

The irradiations at 50 keV were carried out in a Leica Microsystems Beamwriter machine, model EBPG 5-HR-100. This is a commercial electron-beam lithography tool capable of writing features down to 20 nm over areas up to 126x126 mm^2. The Beamwriter is located in a class 10 cleanroom with the temperature controlled to +/- 0.25 °C. The beam current used during the irradiations was ≈ 100 nA with a spot size of 400 nm. The doses used in the present work ranged from 0.01 to 10 $C{\cdot}cm^{-2}$, with a resolution of 0.3125 μm.

The electron-beam is collimated by four sets of lenses on its way to the sample, and then scanned over the sample by means of deflection coils. The area that the electron-beam scanning can cover by this method is 800x800 μm^2, called a field, after which the stage has to be moved to the next position and then the electron-beam will be scanned again.

In order to avoid an increase in the temperature of the substrate that would anneal the effects of the writing process, the patterns were scanned 64 to100 times over the same area until the total dose was delivered. After irradiation, the nichrome layer was intact, thus no ablation of the material after irradiation is expected.

The patterns to be written in the FHD glass were designed using a mask design tool, WAM, which produces GDSII data. The GDSII data is transformed using another software, CATS, into a code that can be understood by the Beamwriter.

5.2.3 Irradiation technique using 10 keV electrons.

The beam of an electron-beam evaporator machine was scanned uniformly over the sample, located on top of the crucible. In order to avoid charging of the sample a 30 nm nichrome layer was evaporated before the irradiation. The maximum energy available in this evaporator was 10 keV, and the current used was 3 mA. The evaporator did not have any device to monitor the real dose deposited on the sample, i.e. a Faraday cup. Therefore, only an estimation of the applied dose was available for the irradiations performed at this energy.

5.3 Interaction of the electron-beam with the material.

As electrons enter the material, they interact with the atoms in the glass matrix and lose part of their energy by excitation processes, as their energy is not high enough to transfer into the sample by nuclear collision events [Everhart, 1971]. The electrons follow random trajectories inside the material, determined by scattering until they lose all their energy and stop. The loss of energy along this pathway gives rise to excitations of the silica atoms in the matrix, which relax in various ways, e.g. emitting photons (X-ray, UV, Vis), emitting electrons (secondary electrons, Auger electrons), producing breakage and rearrangements of bonds and dissipating heat into the lattice, e.g. phonons. These last three effects are believed to be responsible for the structural modification that will lead to densification and changes in refractive index [Barbier, 1991].

5.3.1 Sceleton: Monte Carlo simulation of interaction of electrons with the material.

A Monte-Carlo simulation program, Sceleton, which performs high precision Monte-Carlo simulations of electron trajectories in arbitrarily complex material structures, was used in this study. The software uses a single scattering model to follow the paths of the electrons as they move through the material. Different material stacks can be assembled, by describing the thickness and the material of each layer. The materials are described by their mass density and stoichiometry, which can be taken from the experimental data shown in Chapter 4 (a description of the material stacks used can be seen in Appendix 2). The result of the simulation is the transfer of energy per unit volume and per incident electron (in $eV \cdot \mu m^{-3} \cdot electron^{-1}$) as a function of depth and lateral distance from the point of incidence of the electron on the material.

5.3.2 Calculation of the local volume density deposited by the electron-beam.

In Figure 5.1 (a) a representation of the energy deposited into the material per incident electron and per unit volume as a function of depth and lateral radius from the point of incidence of the electrons is shown.

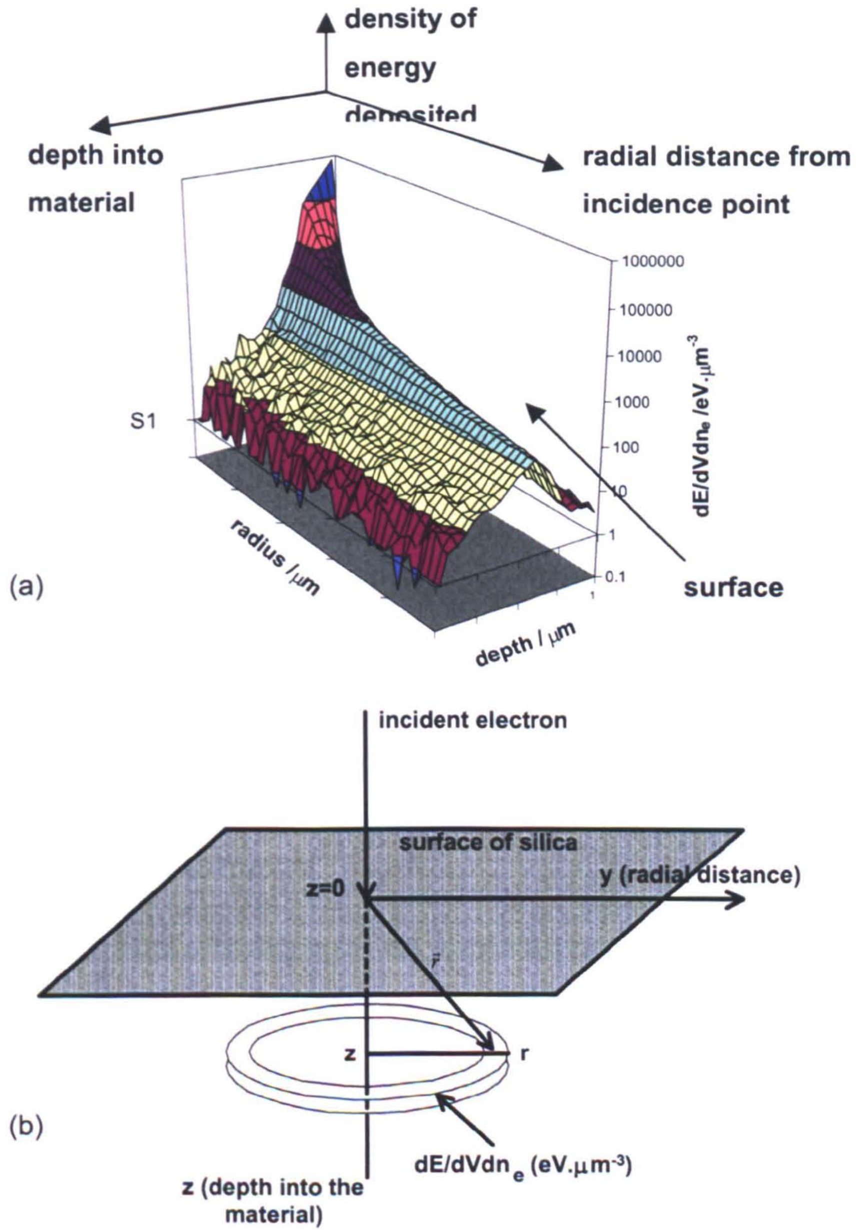

Figure 5.1. Deposition of energy in FHD silica by an energetic electron-beam: (a) dE/dVdn$_e$ (eV·μm^{-3}·electron^{-1}) as a function of depth and radial distance; (b) Schematic showing the coordinate system.

In order to calculate the total contribution of all the electrons incident on the sample to the energy per unit volume deposited at a depth *z* (Figure 5.1), the energy contributions of all the electrons hitting the surface need to be added. This calculation can be written as

$$\left(\frac{\partial E}{\partial V}(r,z)\right)^T = (n_e)\cdot\frac{\partial E}{\partial V \partial n_e}(r,z) \quad (5.1)$$

$$\left(\frac{\partial E}{\partial V}(z)\right)^T = \int_0^{\infty}\frac{\partial E}{\partial V \partial n_e}(r,z)2\pi N_e r dr \quad (5.2)$$

where $\left(\frac{\partial E}{\partial V}(r,z)\right)^T$ represents the total energy deposited per unit volume at the point, (r; z) (Figure 5.1), n_e is the number of electrons arriving at the position (*r; z=0*), $\partial E / \partial V \partial n_e (r,z)$ is the contribution of energy per unit volume and per electron hitting the surface of the sample at point (*r* ; *z=0*), N_e is the number of electrons per unit area, i.e. the dose, and $2\pi r dr$ is a radial area around the calculation point such that the electrons arriving to that area contribute with $\frac{\partial E}{\partial V \partial n_e}(r,z)2\pi N_e r dr$ to the calculation of deposited energy at the point of interest.

The value of $(\partial E / \partial V \partial n_e (r,z))$ is obtained from Sceleton and the electron-dose applied, N_e, is known. Simulations were performed for incident energies of the electrons of 15 KeV and 50 KeV.

The penetration depth of the electrons follows the expression below as a function of energy [Everhart, 1971]:

$$R_G(\mu m) = 0.0181E(keV)^{1.75} \quad (5.3)$$

5.3.3 Local volume density of energy deposited by a 50 KeV electron-beam.

The energy deposited as a function of the radial distance of the incident electrons is shown in Figure 5.2. In the same way, the energy density contribution as a function of depth, can be plotted for electrons at different radial distances from the point of calculation, as shown in Figure 5.3. The relationship given by Equations 5.1 and 5.2 can be evaluated and the result for different doses plotted in Figure 5.4.

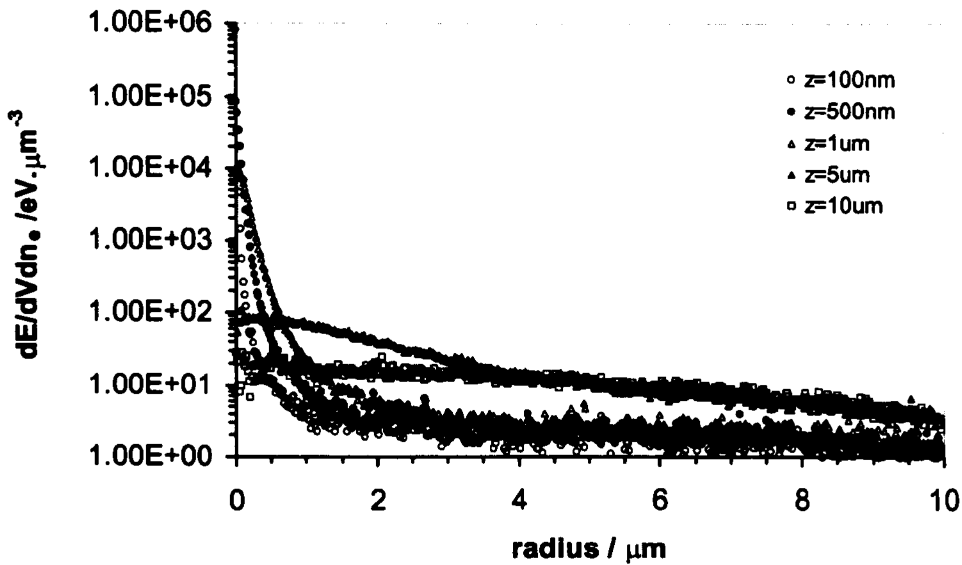

Figure 5.2. Energy density as a function of radial position, for five different values of z_i: as the depth increases the energy distribution decreases and broadens.

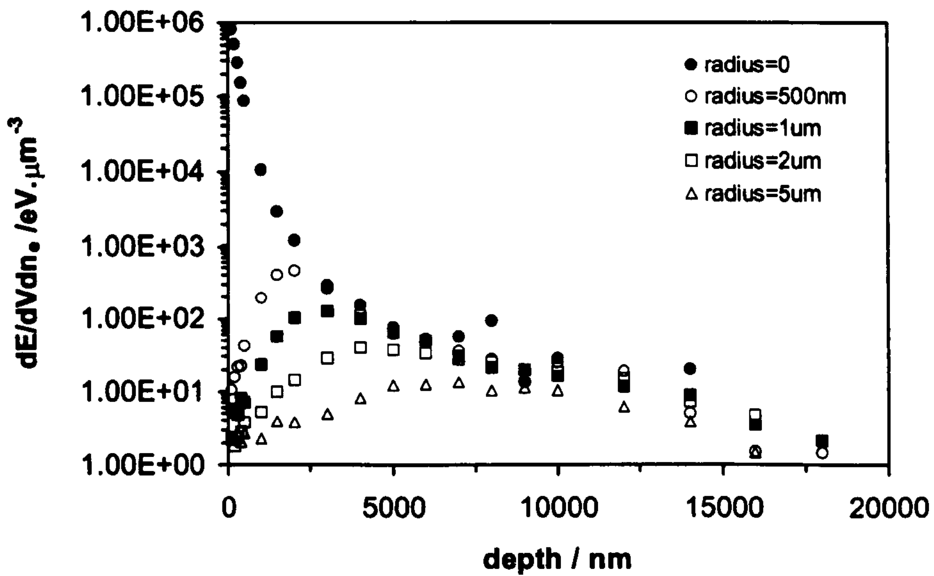

Figure 5.3. Energy density contribution in depth for electrons arriving at different radial distances.

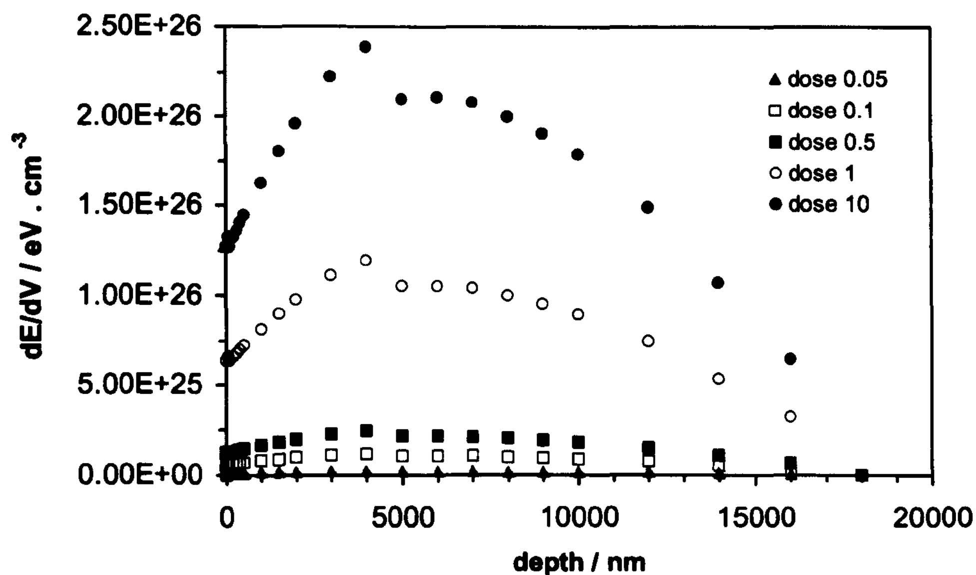

Figure 5.4. Depth profile of energy deposited by the electron-beam: Integral energy deposited as a function of depth for different doses of 50 keV electrons for a FHD sample with 2 % at. germanium, 4 μm thick, on top of thermal oxide.

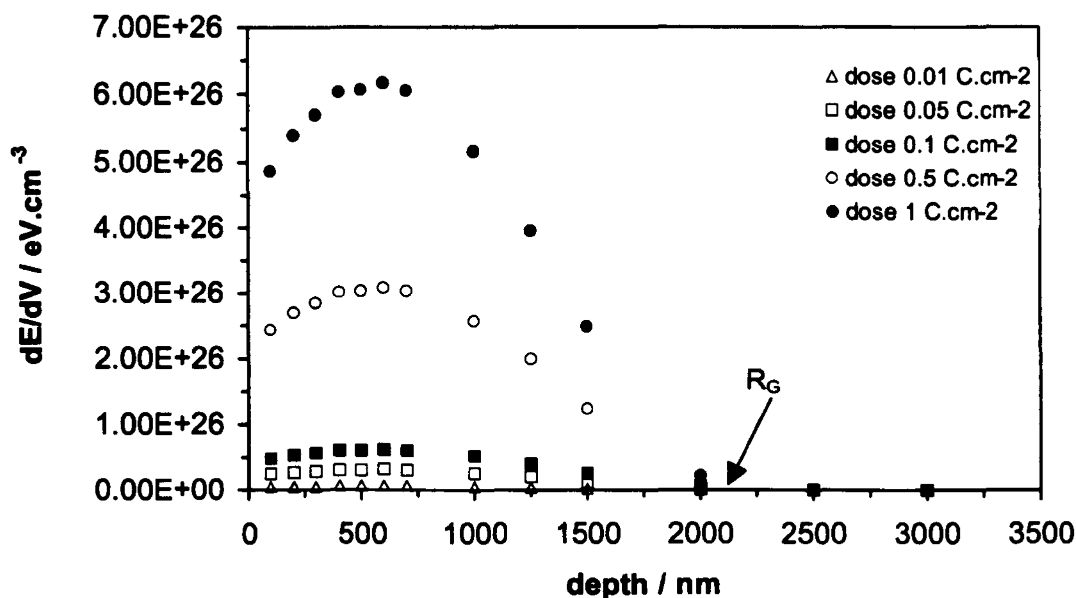

Figure 5.5. Integrated energy deposition different electron doses (15 keV): R_G (the Grün range) is defined as the depth at which the energy transferred by the electrons becomes zero. Sample simulated was 2 % at. germanium, 4 μm thick over a layer of thermal oxide.

5.3.4 Local volume density of energy deposited by a 15 KeV electron-beam.

The same calculations can be performed for the case of 15 KeV irradiation for example. Figure 5.5 shows the integral of the energy contributions of the electrons arriving in an surface area of radius the lateral straggle of the electrons as a function of depth, for an electron-beam of 15 keV and different doses.

5.3.5 Evolution of the density of energy profile in depth with the energy of the incident electrons.

As has been mentioned before, the electrons deposit their energy along their way inside the material. The penetration depth of the electrons depends on their initial accelerating energy, as can be seen in Equation 5.3. In order to see the evolution of the magnitude of the energy density deposited in depth for electrons arriving to the sample with different energies, the energy density deposition in depth was simulated using Sceleton for electrons arriving with 10, 15 and 25 keV to a 25 % wt. silica structure. The results of these simulations can be seen in Figure 5.6.

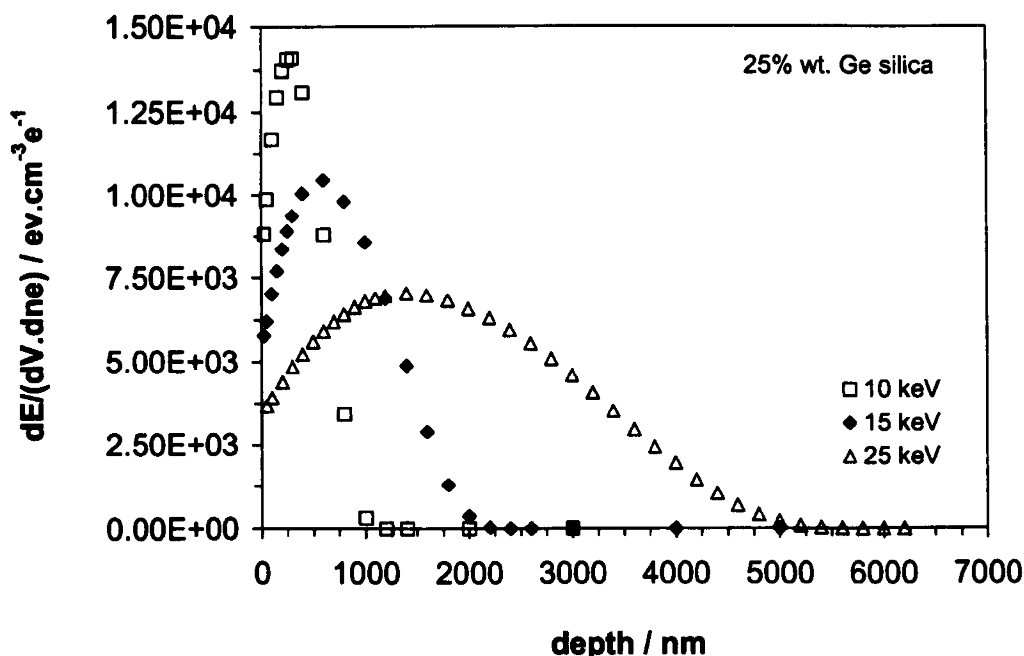

Figure 5.6. Evolution of the energy density deposited per electron into the silica structure as a function of the energy of the incident electrons: results obtained from simulations with Sceleton for 10, 15 and 25 keV electrons penetrating a 25 % wt. silica sample, 10 μm thick.

It can be observed that, the larger the energy of the incident electron, the smaller the energy density deposited but over a larger depth range.

5.4 Structural changes after electron-beam irradiation of FHD silica layers.

5.4.1 Raman spectroscopy studies.

5.4.1.1 Introduction.

As was discussed earlier (Chapter 2 Section 2.4.1 and Chapter 4 Section 4.5.1), the Raman spectrum of silica shows several bands, ω_1 to ω_4, representative of the silica network plus two additional defect lines that cannot be explained by random vibrations of the silica network. The defect lines, D_1 and D_2 are associated with planar 4- and 3-membered rings embedded into the silica matrix, which do not share atoms among each other [Galeener, 1982a], [Galeener, 1982b], [Pasquarello, 1998].

The angle of the Si-O-Si bonds in the small membered rings has to be smaller than in the case of the silica network structure, in order to comply with the closure and planarity of the rings [Pasquarello, 1998]. Therefore, 3- and 4-fold ring structures are expected to occupy less volume than the regular silica matrix, implying a structure with larger density and refractive index [Chan, 2003], [Bazylenko, 1997], [Chan, 2001], [Dianov, 1997].

Furthermore, the 3-fold and 4-fold ring structures contain higher strain energy than larger rings, indicating a situation outside thermal equilibrium. The formation of small-membered rings appears to be favoured when the system rearranges from a highly disordered configuration on short time scales [Pasquarello, 1998]. This situation can occur during irradiation with different high energy species, such as neutrons [Bates, 1974], where a large energy is transferred to the material in a very short period of time, leading to non-equilibrium structural modifications. Glasses with high fictive temperatures (i.e. the temperature at which the glass would find itself in equilibrium if suddenly brought to that temperature from its given state [Chan, 2003]) also show large concentrations of 3- and 4-membered rings [Galeener, 1985].

Formation of 3- and 4- membered rings has been reported after different treatments of the silica structure, such as thermal [Galeener, 1985], shock wave

compression [Okuno, 1999], neutron irradiation [Bates, 1972], [Bates, 1974] and UV irradiation with ArF (193 nm) and KrF (248 nm) irradiation [Liu, 1997], [Dianov, 1997] In the present work, the same effect has been found to occur after electron-beam irradiation of Ge:SiO_2 FHD silica.

5.4.1.2 Sample preparation.

Ge:SiO_2 FHD layers $\approx$ 7 μm thick and with 14 % wt. germanium content were deposited on quartz substrates. Areas of 1 mm^2 were irradiated using a 50 keV electron-beam with various irradiation doses.

5.4.1.3 Raman study of the change of structure after irradiation.

Figure 5.7 shows the spectra taken on the surface of an irradiated sample, for different doses. The blue line represents the as-deposited sample and shows the lack of narrow defect lines characteristic of germanium-doped silica (see Chapter 4 Section 4.5.1). After irradiation with different doses two effects can be seen. Firstly, the defect peaks D_1 and D_2, especially the latter, become more apparent. This suggests the appearance of 4- and 3-fold rings in the silica matrix after irradiation with the electron-beam. Secondly, the position of the ω_1 peak appears to be shifted towards higher frequencies. As was discussed in Chapter 2 (Section 2.4.1), a change in the bridging oxygen bond angle (Si-O-Si, Ge-O-Si or Ge-O-Ge) is related to a shift of the frequencies at which the different network Raman bands appear, given by the equation:

$$\Delta\omega_i = \pm\left(\frac{\alpha}{m_o}\right)\frac{\Delta\theta}{2\omega_i}\sin\theta \qquad (5.4)$$

where ω_i are the spectral positions (rad·sec^{-1}) of the different silica Raman bands, $i=1\text{-}4$, α is the Si-O bond-stretching force constant (all the other force constants are assumed to be zero), m_o is the mass of the oxygen atom and θ is the angle of the bridging oxygen bond. The sign in front of the right hand side of Equation 5.4 is negative for $i=1$ and 3 and positive for $i=2$ and 4. As discussed in Section 2.4.1.3, the volume analysed in each measurement is 1 μm^3.

From Equation 5.4, it can be seen that a shift of the ω_1 band towards higher wavenumbers, $\Delta\omega_i > 0$ implies a decrease in the bridging oxygen bond angle,

$\Delta\theta < 0$. Therefore, from the two effects observed in Figure 5.7, densification of the material is to be expected: the 3-membered rings occupy smaller volume than the silica tetrahedra [Dianov, 1997] and a reduction of the angle between different tetrahedra implies a compaction of the structure after irradiation.

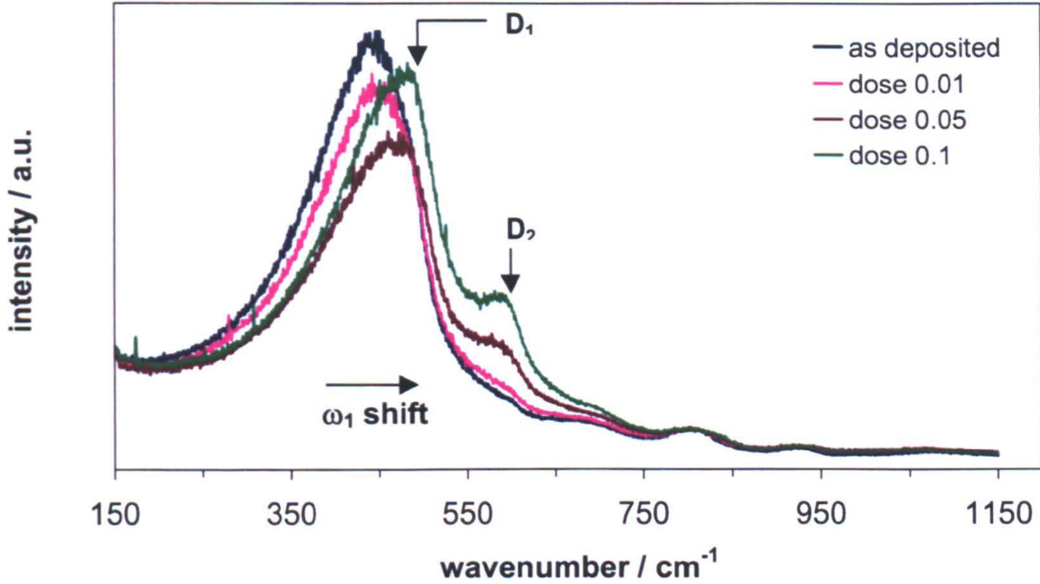

Figure 5.7. Evolution of the Raman spectra with the irradiation dose: the first micrometer of material of a 14 % wt germanium sample was probed. A noticeable increase can be observed in the magnitude of the D_2 defect line, implying an increase in the number of three-membered rings in the structure. The D_1 peak also increased, suggesting a slower increase in the number of four-membered rings. Finally, a shift of the ω_1 band towards higher wavenumbers was observed.

It is also interesting to study how the structure was modified as a function of depth. This can be done by using the confocal configuration of the Raman microscope. Figure 5.8 shows Raman spectra taken at different depths in the sample, which had been irradiated with a dose of 0.1 $C{\cdot}cm^{-2}$. The relative magnitude of the D_1 peak increased with respect to the D_2 peak as the depth increased. This implied that the proportion of 4-membered rings increased in relation to the number of 3-membered rings. Since the 4-membered rings occupy more volume than the 3-membered rings, this result appears to indicate a lesser degree of compaction deeper into the sample. Furthermore, the ω_1 peak appeared to shift towards smaller wavenumbers as the depth increases. From Equation 5.4, this result suggested an increase (or less of a decrease with respect to the as deposited sample) of the Si(Ge)-O-Si(Ge) bond angles, again implying a less compact structure with depth.

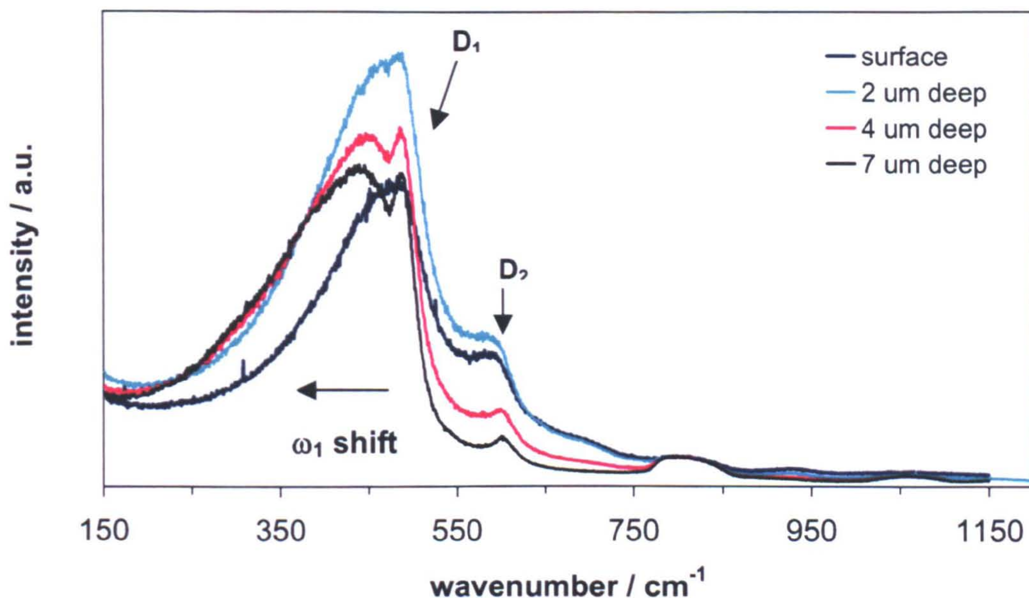

Figure 5.8. Raman spectra after an electron dose of 0.1 C·cm^{-2} as a function of depth: It can be seen that the D_2 peaks keeps constant in depth, while the D_1 peak increases with depth. Furthermore, the ω_1 peak shifts towards smaller wavenumbers in depth.

It is necessary to consider, however, that throughout the depth of the sample, some degree of compaction with respect to the as deposited sample occurred. The spectra of the as-deposited and samples irradiated with a dose of 0.1 C·cm^{-2} were compared for two different depths (2 and 4 μm) in Figure 5.9.

In both cases, a shift in the ω_1 band towards higher wavenumbers, suggesting a reduction of the Si(Ge)-O-Si(Ge) angle occurred, although it was larger for the spectra taken at 2 μm below the surface. An increase of the D_1 and D_2 was also observed at both depths, suggesting a more compacted structure.

These results are consistent with the measurements of the density of irradiated samples made using X-ray reflectivity and from the fitting of the data from profilometry (see Section 5.5.5.1): a higher degree of compaction occurs closer to the surface of the sample.

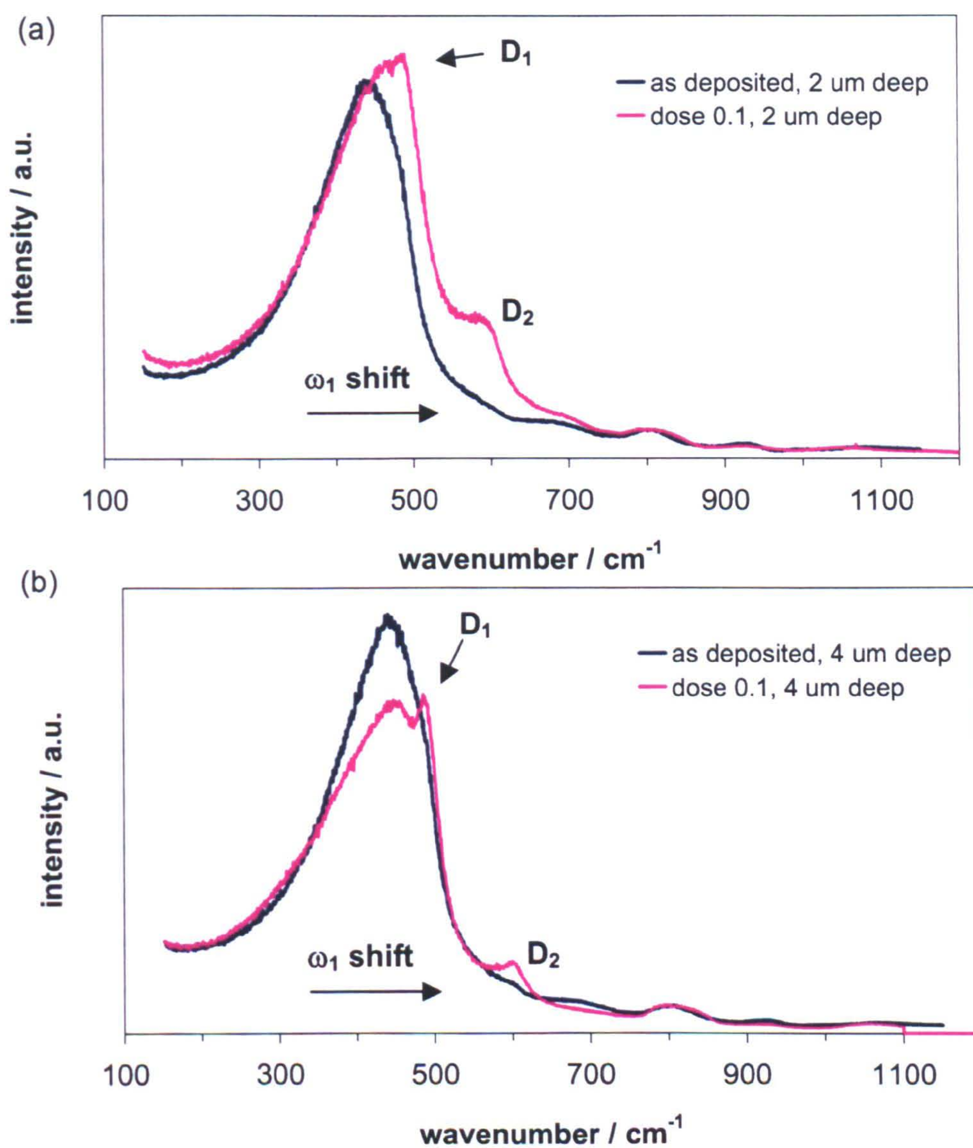

Figure 5.9. Raman spectra before and after irradiation: Comparison of the Raman spectra before and after irradiation with a dose of 0.1 $C{\cdot}cm^{-2}$ at two different depths: (a) Raman spectra 2 μm below the surface; (b) Raman spectra 4 μm deep.

5.4.2 ReflEXAFS studies of the change in structure around the Germanium atoms upon electron-beam irradiation.

5.4.2.1 Preparation of the samples.

The samples that were characterized by ReflEXAFS in Chapter 4 (Section 4.5.2) were irradiated with an electron-beam at 50 keV with a dose of 0.1 $C{\cdot}cm^{-2}$ (as

indicated in Section 5.2). The area irradiated was 5x25 mm^2, which was large enough to permit alignment into the incident X-ray beam, ensuring that only that area was illuminated.

5.4.2.2 Variation of the local structure around germanium after irradiation.

ReflEXAFS data was collected around the Ge-K edge (11.12 keV) with an incidence angle of 350 mdeg. The data was analyzed, as described in Chapter 2 (Section 2.4.2.6). The summary of the parameters obtained after the fit of the experimental data by adding successive shells (Ge-O, Ge-Si, Ge-O) until no further reduction in the reduced-χ^2 fitting test (Section 2.4.2.6) was obtained is shown in Table 5.1. The addition of a further Ge-Ge shell was not justified by the reduced-χ^2 test.

It should be noted that the coordination numbers are incorrect, probably due to self-absorption, as the concentration of germanium in the samples is larger than 1 % at. and as the penetration obtained for the incidence angle is of a few 100's of Å, as the collection has been carried out beyond the critical edge for reflection. The critical edge for reflection is 178 mdeg for these samples. Nevertheless, it is interesting to note that the coordination number for the Ge-Si shell is 0.0, which probably represents a real reduction of the number of oxygen-deficient centres. This is probably due to the weaker strength of the Ge-Si "wrong bonds" compared with the Si-O bonds. A similar result was found by Liu *et al.* [Liu, 1997] in their investigation of the UV-irradiation of Ge-doped silica by Raman spectroscopy. In that work, they suggest that the breaking of the Si-Ge "wrong bonds" leads to the formation of a GeE' centres, which is accompanied by a large lattice relaxation that stabilizes the GeE' centre by preventing its recombination. After UV-irradiation, probably due to the breaking of the Si-Ge bonds and subsequent relaxation of the network, a reduction of the size of the rings becomes possible and, therefore, the D_1 and D_2 lines again become apparent. This effect was also observed in the Raman analyses carried out in this work.

Comparing the values obtained by EXAFS for the as-deposited samples (Chapter 4, Section 4.5.2, Table 4.5) with the values obtained after irradiation (Table 5.1), the Ge-O distance passes from 1.79 Å before irradiation to 1.73 Å after irradiation. The bond length Ge-O for GeO_2 has been reported in the literature to be 1.74 Å [Okumura, 98], [Wefing, 1999], [Skuja, 2000]. The reduction in the Ge-O bond distance upon electron-beam irradiation may be related to the reduction observed in

the size of the rings that constitute the silica structure. If the size of the silica rings passed from > 6 to 3- and 4-fold rings, the angle of the oxygen bridging atoms would be reduced and the same would be expected for the Ge-O distance. The reduction in size of the silica rings was consistent with the observed breakage of the Ge-Si bonds and consequently, an increase in the density of the material was expected.

Sample	Parameter					
	N			r / Å		
	Ge-O (1st shell)	Ge-Si	Ge-O (2nd shell)	Ge-O (1st shell)	Ge-Si	Ge-O (2nd shell)
4 % wt.	1.1	0.0	0.6	1.73	---	2.77
14 % wt.	2.2	0.0	0.7	1.73	---	2.85
15.5 % wt.	1.0	0.0	0.5	1.73	---	2.84

Table 5.1. Coordination number, N, and radius, r, obtained from the fit of the EXAFS data from Figures 5.10-5.12 for the 0.1 $C \cdot cm^{-2}$ electron-beam irradiated samples for different germanium compositions.

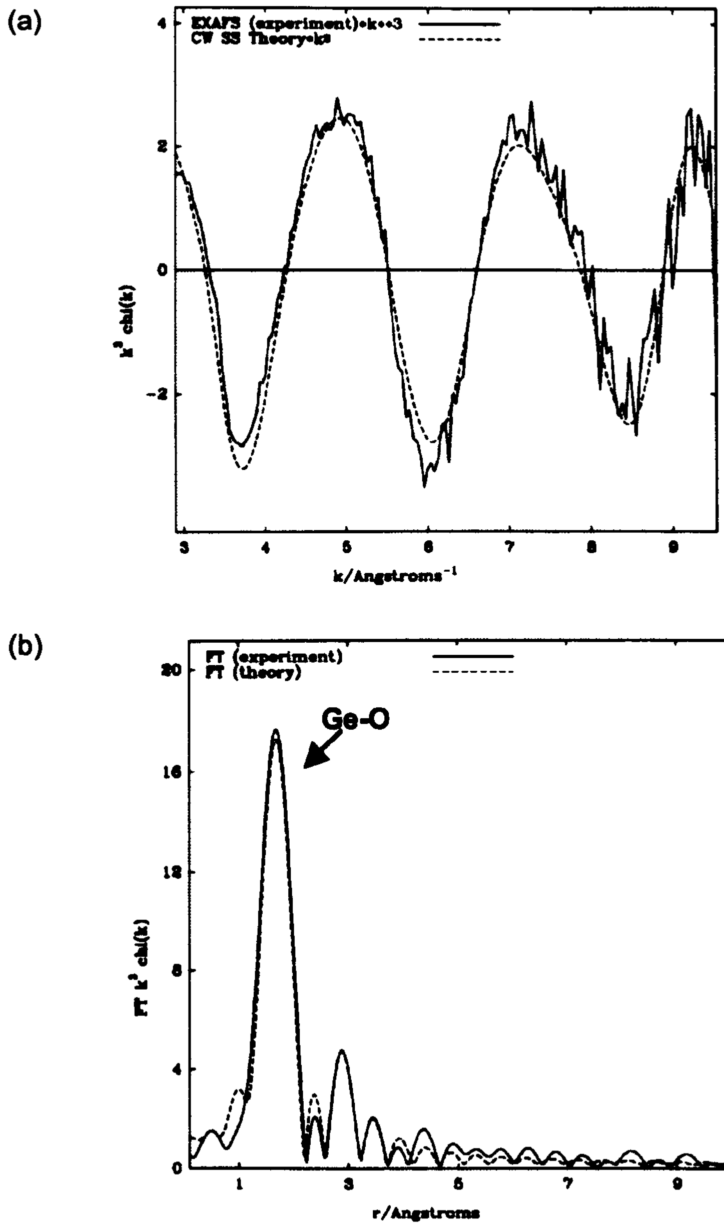

Figure 5.10. EXAFS data of a 4 % wt. sample after irradiation: Top corresponds to the EXAFS oscillations data and bottom to the Fourier transform data. Irradiation dose was 0.1 C·cm^{-2}.

(a)

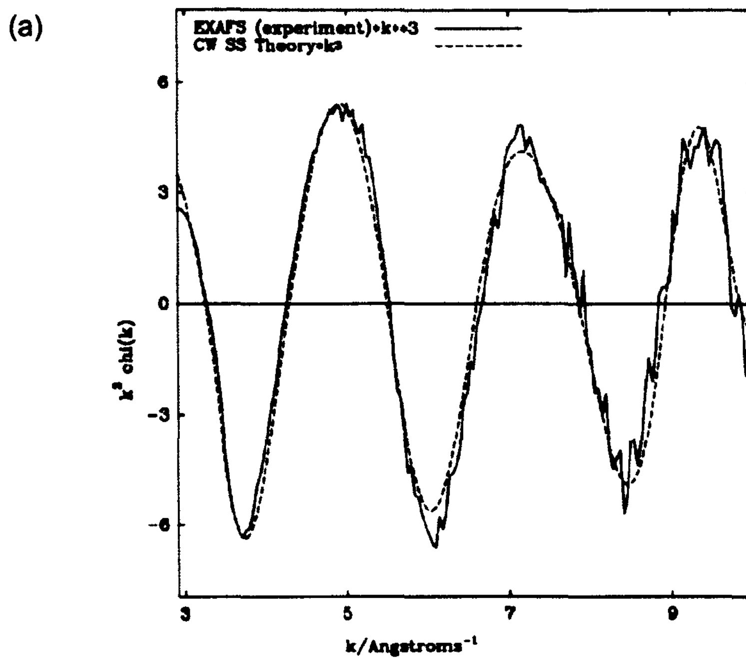

(b)

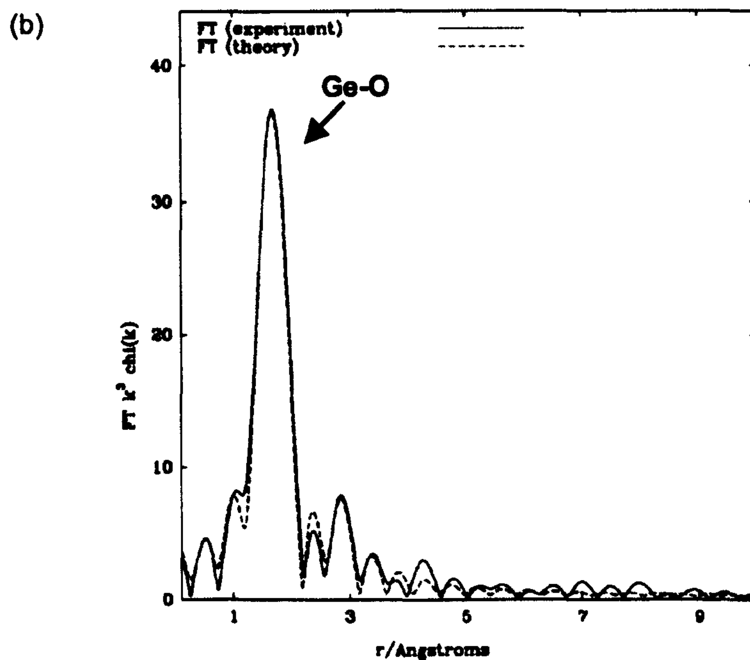

Figure 5.11. EXAFS data for a 14 % wt. Ge FHD sample irradiated with 50 keV and 0.1 C·cm^{-2}: (a) EXAFS oscillations; (b) Fourier transform fitting.

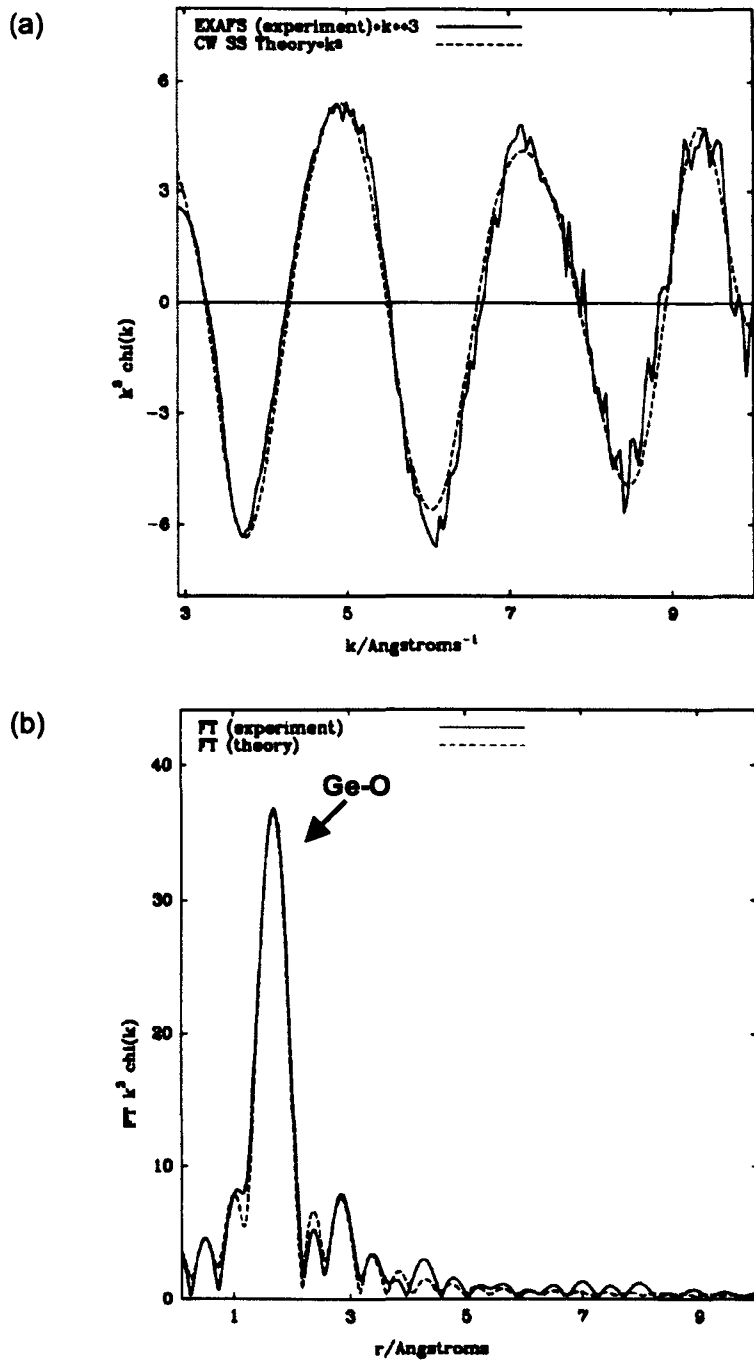

Figure 5.12. EXAFS data for a 15.5 % wt. Ge FHD sample irradiated with 50 keV and 0.1 C·cm^{-2}. (a) EXAFS oscillations. (b) Fourier transform fitting.

5.5 Densification induced by electron irradiation on Ge-doped FHD silica layers.

5.5.1 Introduction.

In the following sections, the densification induced by an energetic electron-beam (10 to 50 keV) in samples with different compositions of germanium-doped FHD silica was studied as a function of irradiation. The results obtained for this material were compared with those for other germanium-doped silica structures deposited by different techniques (MCVD, sol-gel, PECVD and HERA). A strong dependence of the densification on the structure of the deposited material and on the germanium content was found. The change in density after irradiation was also studied by X-ray reflectivity. The results obtained with this technique were then compared with the change in density obtained by measuring the depression observed on the surface after irradiation and calculating the change in density that will produce the observed surface depression, by means of elastic calculations. In both cases, a higher densification in the outer region of the material for the case of FHD silica was observed. This effect was not found for the same irradiation on MCVD silica and thermal silicon oxide, thus suggesting that it must be related to the particular structure of FHD silica layers.

5.5.2 Fundamentals of electron-beam densification of silica.

The vitreous state of silica can be considered as an essentially random network of SiO_4 tetrahedra joined by Si-O-Si bridging bonds. Successive tetrahedra cannot be infinitely close together, due to repulsive forces appearing between them, but they will present a random distribution of angles centered around a most probable value, which has been reported as $\approx$145 deg by several authors [Hosono, 2001], [Piao, 2000], [Mozzi, 1969], [Galeener, 1979].

The structure of vitreous silica can be compacted by various mechanisms [Primak, 1972], such as high pressure [Revesz, 1972], [Walrafen, 1981], [Bridgman, 1953], [Hemley, 1986], thermally [Bartolotta, 2001], polishing, shock waves [Wackerle, 1962] and different kinds of irradiation such as neutrons, electrons, different ions and gamma rays [Primak, 1968a].

Studies of the compaction induced by various irradiation sources suggest the existence of two distinct compaction mechanisms: one associated with knock-on atomic displacements (as applies ion implantation irradiation) and the other associated with ionization-induced rearrangements of strained Si-O bonds in the silica glass network. This last mechanism is relevant for UV and electron-beam induced compaction [Primak, 1968a], [Norris, 1974], [Primak, 1972] due to the fact that, as the electrons have negligible mass, they cannot directly produce atomic displacements by collisions [Piao, 2000].

Some authors have reported the mechanism of ionization-induced rearrangement of bonds as being produced by the absorption of an exciton [Borrelli, 1997], [Tugushev, 1998]. For a pure insulator, the absorption of photons of sub-bandgap energy generates electron-hole pairs through multi-photon band-to-band excitation. Electron-hole pairs can also be generated by the transference of energy from an incident energetic electron-beam. Electron-hole pairs are subsequently converted into excitons on a sub-picosecond time-scale [Williams, 1989]. The lifetime of a free exciton is less than 1 ns, although the excitons can be trapped with lifetimes as long as 10 ms [Tsai, 1991], [Skuja, 1984], [Fisher, 1990]. The trapped exciton will produce bond weakening, thus allowing the reconfiguration of the network and leading to a more compacted structure.

Other authors [Primak, 1972] explain the compaction mechanism for ionization events as being a "thermal spike" in which the heating induced along the entrance path of the electron into the material, due to the transference of energy to the Si-O bonds, determines a rearrangement of the silica structure, leading to densification.

In either case, the densification is related to the amount of energy that the electrons deposit into the material. As was discussed in Section 5.3, the deposition of energy is not uniform in depth. Therefore, a non-uniform densification with depth is expected. EerNisse *et al.* [EerNisse, 1974a] proposed a power-law dependence between the energy transferred to the material at a certain depth and the relative change in volume suffered by the material at that depth. The same kind of power-law dependence was suggested by Barbier *et al.* for the relationship between the change in refractive index with depth and the energy in depth deposited by the electrons [Barbier, 1991]. They found a power factor of 0.8 when they related the energy deposition profile calculated by Monte-Carlo simulations with the refractive index profile calculated using an *inverse*-WKB formulation. Primak *et al.* [Primak,

1968a] also found a power-law dependence relating densification with electron-dose. A power-law dependence has been routinely reported as an "universal" densification law for UV-radiation-induced densification [Ruller, 1991], [Liberman, 1999a], [Borrelli, 1999], [Griscom, 1993], [Liberman, 1999b], [Piao, 2000].

Other authors have reported a threshold energy after which the total densification (or effect of the electron-beam on the material) saturates. Houghton *et al.* [Houghton, 1976] found a value of 2×10^{23} keV·cm^{-2} for the saturation of the densification by ionizing radiation. The same value was reported by Devine *et al.* [Devine, 1993]. This saturation threshold has an influence on the profile of the modification because, due to the inherently non-uniform deposition of energy, saturation will occur first at certain depths. This will modify the shape of the densification (and consequently the change in refractive index) depth profile as the electron dose is increased. Furthermore, considering the total change in density occurring in the material as a function of the applied dose, saturation after a certain electron dose would be expected. This effect was not observed by Barbier *et al* [Barbier, 1991], EerNisse *et al.* [EerNisse, 1974a] and Primak *et al.* [Primak, 1968a] when they reported a power-law dependence of densification upon electron-irradiation, because they did not provide high enough irradiation doses to produce saturation of the compaction process.

The origin of the saturation in the change of the silica structure has been explained by considering the densification as a relaxation process [Borrelli, 1997]. In silica, as more sites become densified as a result of increasing the irradiation dose, the rate of change in density begins to decrease, because there is less material that can be densified. This result can be described by a differential equation of the form [Borrelli, 1997], [Primak, 1968a], [Seward, 1997]:

$$\frac{d\rho}{dD} = A(\rho_{eq} - \rho) \qquad (5.5)$$

where ρ is the density change as a function of the dose, ρ_{eq} is the density change when saturation is reached, D is the applied dose and A is a rate constant. The physical meaning of Equation 5.5 is that as the density approaches the saturation value, the rate of change in the density of the silica decreases. A solution to Equation 5.5 is

$$\rho = \rho_{eq}\left(1 - exp(-AD)\right) \quad (5.6)$$

Other kinetic equations, such as stretched exponential behavior [Primak, 1982], [Seward, 1997], [Allan, 1996], [Griscom, 2001], [Borrelli, 1997], [Griscom, 1993], or mixed exponential-power function [Poumellec, 1996a] have also been utilized to describe the dependence of the compaction on dose for ionizing irradiation. However, no universal agreement on the kinetics of the process has yet been found.

Furthermore, the dependence of the evolution of the densification with irradiation dose on the structure of the non-irradiated material also needs to be taken into account. The previous references deal with different kinds of silica, without any dopants. The influence of the germanium composition on the behavior of the silica under electron-beam irradiation and comparison with the results found in the case of germanium-doped silica irradiated by UV-irradiation has not been fully addressed.

In the case of UV-irradiated germanium-doped silica, germanium is known to increase the sensitivity of the material to the radiation, due to the reduction of the bandgap from ≈ 10 eV for pure silica to ≈ 7 eV for germanium-doped silica with 5 % mol of germanium. Therefore, the efficiency of the light absorption by the material at 244- and 198- nm is increased [Kristensen, 2001], [Leconte, 1998], [Jiang, 2002], [Borrelli, 1999]. The effect of germanium on the densification of germanium-doped silica under electron-beam irradiation has not yet been the subject of study [Jacqueline, 2003]. Nevertheless, the study of the impact of the germanium content on the densification upon electron-beam irradiation is relevant to this work, as it will help in choosing the best deposition parameters for the initial material.

5.5.3 Elastic calculations to obtain the strains and stresses appearing in the structure due to densification.

5.5.3.1 Elastic calculations for obtaining the permanent strain from the measurement of the total change in density.

The electron-beam transfers energy to the different bonds in the structure of the silica, allowing them to rearrange, adopting smaller bond angles by reducing of the angle between tetrahedra and by the formation of small-membered rings. A compaction of the silica therefore occurs in the irradiated region. This compaction

constitutes the "permanent" or "inelastic" densification, which has been called previously "unconstrained densification" [Seward III, 1997].

If it were possible to irradiate the whole volume of a free-standing FHD silica layer, i.e. not deposited on top of a substrate, the permanent densification would be the only effect appearing in the structure. The material would densify isotropically (Figure 5.13) being the linear component of the strain ε^p. The relative change in volume obtained under these conditions would be independent of the size of the irradiated region [Seward III, 1997] and could be approximated as $3\varepsilon^p$ [Craig, 1996].

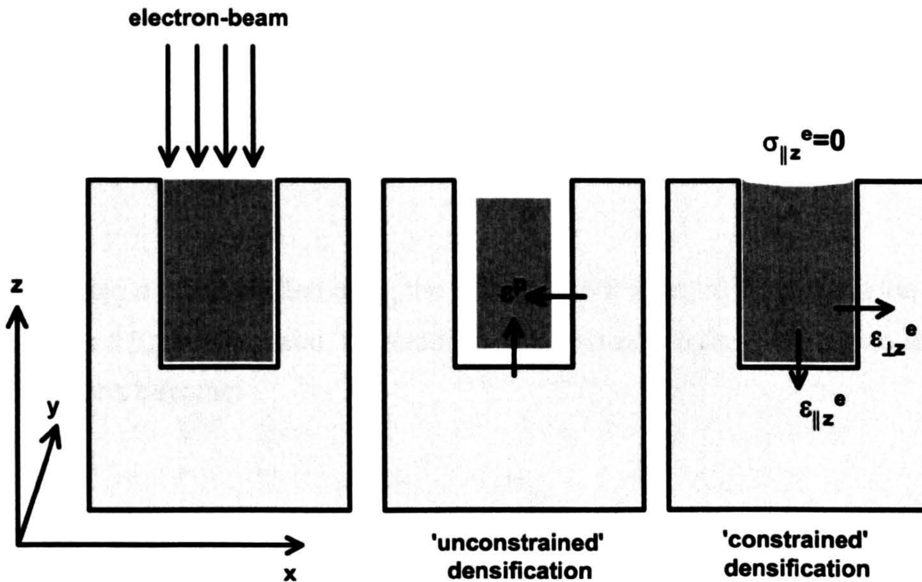

Figure 5.13. Unconstrained and constrained strains after irradiation: Left: region of sample being modified by the electron-beam; Middle: inelastic densification due to structural rearrangement leading to change in volume assuming no stress induced by the surrounding material; Right: The surrounding material induces some elastic stresses and strains. The global densification is less than in the absence of the surrounding material.

As the material is not free to densify, but is deposited on top of an "un-densified" substrate, strains appear in the irradiated region as a consequence of the "permanent" densification. In the middle of a wide, thin layer, the expression for the strain appearing in the directions parallel to the surface, the *x*- and *y*-directions, as an elastic reaction to the permanent strain, ε^p, can be approximated by:

$$\varepsilon_{xx}^{e} = \varepsilon_{yy}^{e} = \varepsilon^{e}{}_{\perp z} = -\varepsilon_{p} \qquad (5.7)$$

which means that the undensified material opposes the densification induced by the electron-beam in the direction parallel to the surface. In the direction

perpendicular to the surface (||z), the surface of the structure is free to depress, a condition that can be written as

$$\sigma_{zz} = \sigma_{||z} = 0 \tag{5.8}$$

i.e. the stress in the *z*-direction is 0.

Applying the basic expressions of elasticity for the middle of the densified region (far from the edges, where further stresses would occur) [Timoshenko, 1970], the following equations can be written:

$$\begin{aligned} E\varepsilon_{zz} &= \sigma_{zz} - \nu(\sigma_{xx} + \sigma_{yy}) \\ E\varepsilon_{xx} &= \sigma_{xx} - \nu(\sigma_{yy} + \sigma_{zz}) \end{aligned} \tag{5.9}$$

where E is Young's modulus and ν is Poisson's ratio, 0.17 in the case of fused silica.

Assuming a thin densified area, the assumption that $\sigma_{||z}=0$ throughout the material (Equation 5.8) can be made. Considering also that $\sigma_{xx}= \sigma_{yy}=\sigma_{\perp z}$ the previous expressions become:

$$\begin{aligned} E\varepsilon^{e}{}_{||z} &= -2\nu\sigma_{\perp z} \\ E\varepsilon^{e}{}_{\perp z} &= (1-\nu)\sigma_{\perp z} \end{aligned} \tag{5.10}$$

From the second of Equations 5.10, $\sigma_{\perp z}$ can be obtained and, substituting in the first of Equations 5.10, the following expressions are obtained:

$$\begin{aligned} \varepsilon^{e}{}_{||z} &= \frac{-2\nu}{1-\nu}\varepsilon^{e}{}_{\perp z} \\ \varepsilon^{e}{}_{\perp z} &= -\varepsilon_{p} \end{aligned} \tag{5.11}$$

which represent the elastic strains appearing in the structure as a consequence of the "permanent" densification induced by the electron-beam, due to the presence of the un-densified material underneath the densified region.

The total change in density is approximated by [Craig, 1996]:

$$\frac{\Delta\rho_T}{\rho_T} = 3\varepsilon_p + 2\varepsilon^{e}_{\perp z} + \varepsilon^{e}_{||z} \tag{5.12}$$

Thus,

$$\frac{\Delta\rho_T}{\rho_T} = 3\varepsilon_p - 2\varepsilon_p + \frac{2\nu}{1-\nu}\varepsilon_p = \frac{1+\nu}{1-\nu}\varepsilon_p \qquad (5.13)$$

Equation 5.13 relates the total relative change in density, which is the parameter measured by X-ray reflectivity, with the unconstrained densification.

5.5.3.2 Theoretical model for the calculation of the permanent component of the densification.

If the irradiated area extends all over the whole surface of the material, the only contribution to the elastic strains will be the presence of the un-densified substrate. In the case in which only a small area was irradiated, the un-densified material around that region will also oppose the global densification. In this case, a non-uniform distribution of elastic strains will appear across the irradiated region. As a result, the amount of total densification suffered by the structure will be dependent on the size of the patterns written.

If the irradiated area is large in comparison with its depth, in the middle of that region, the total displacement observed on the surface could be approximated as the total strain in the *z*-direction (perpendicular to the surface) multiplied by the depth of the region, *d*. In this case *d* is the penetration range of the electrons into the material. Therefore, an approximation to the surface displacement in these conditions can be expressed as:

$$t = \left(\varepsilon^p + \varepsilon^e{}_{\|z}\right)d = \frac{1+\nu}{1-\nu}d\varepsilon^p \qquad (5.14)$$

When the size of the irradiated area is not large enough to use the previous approximation a more complicated calculation needs to be used. In order to take into account the size of the patterns written, the following simple model has been used to calculate the deformation induced on the surface of the material after irradiation, *t*, as a function of the linear permanent strain component, ε^p, for different sizes of irradiated area [Blanco, 2001], [Davies, 2003]. The irradiated areas consisted of long stripes of different widths (5, 10, 20 and 40 μm).

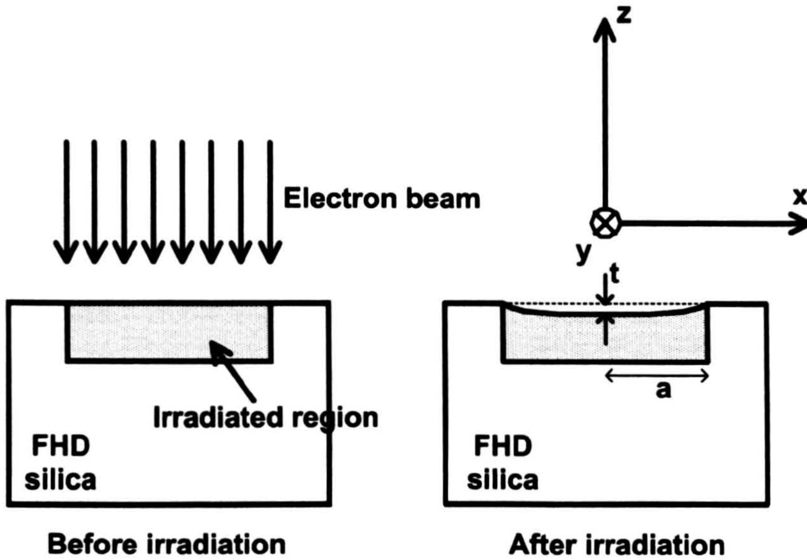

Figure 5.14. Model for the densification of silica after irradiation: The dotted area corresponds to the "damaged" region of width *2a*. The parameter *t* represents the depression appearing on the surface.

In the calculations, it has been assumed that the surface lies in the plane $z=0$ with *z* directed outward, *x* is perpendicular to the stripes, and the system is invariant along *y* (Figure 5.14). The sample was treated as semi-infinite, with the same elastic constants everywhere; the silicon substrate was considered to be deep enough that it did not affect the elastic field in the silica significantly. Irradiation was assumed to change the natural dimensions of the material isotropically by a linear fraction ε^p ("unconstrained" or "permanent" strain component). For simplicity it was assumed that $\varepsilon^p(x,z)$ is constant within the rectangle $-a< x< a$, $-d< z <0$ and vanishes outside. Integration over the elastic field of a center of dilation in a semi-infinite medium [Mindlin, 1950] shows that the surface is displaced by

$$t(x,0)=\frac{(1+\nu)\varepsilon^p d}{\pi}\left[f\left(\frac{x+a}{d}\right)-f\left(\frac{x-a}{d}\right)\right] \qquad (5.15)$$

where

$$f(u)=u\ln\left(1+\frac{1}{u^2}\right)+2\arctan u \qquad (5.16)$$

ν is the Poisson ratio for silica (0.17) and *d* is the penetration depth of the electrons in the material, given by $0.0181E(\text{keV})^{1.75}$ [Everhart, 1971], where *E* is the energy of the electrons in keV.

5.5.4 Measurement of the densification by X-ray reflectometry.

X-ray reflectivity measurements have been carried out before (Section 4.6) and after irradiation with an electron-beam, in order to measure directly the change in density experienced by the material.

5.5.4.1 Preparation of the samples.

For irradiations with a 10 keV electron-beam, an 8 μm thick layer of 15 % wt. Ge FHD silica was deposited on top of a silicon block 5 mm thick. A 30 nm NiCr layer was evaporated on top of the FHD layer and half the sample was irradiated with a 10 keV electron-beam at a current of 3 mA for 4 hours scanned over the whole surface of the sample (5 cm diameter circular sample). The dose that this condition produced cannot be calculated, as there was no Faraday cup installed in the electron-beam used for this irradiation.

After irradiation, different areas were defined by photolithography and etched for different times in diluted buffered HF (3 min and 6 min, which etch a depth of 120 nm and 480 nm respectively) in order to obtain a depth profile of the as-deposited and irradiated areas, X-ray reflectivity measurements were then performed at a wavelength of 1.36 Å.

For the case of 50 keV electron-irradiation, a layer of 8 % wt germanium-doped flame hydrolysis silica was deposited on top of a silicon block 5 mm thick and covered with a 30m NiCr layer. A 3 mm by 4 cm region was then irradiated by a 50 keV electron-beam with a dose 0.1 $C{\cdot}cm^{-2}$. The region exposed was made as long as possible in order to reduce the effect of over-illumination with the X-rays when incident at an angle as small as the critical angle. The region was wide enough for the analysis to be only in the irradiated region, as a horizontal slit of 0.4 mm was used.

X-ray reflectivity data was collected from the irradiated and the unirradiated areas at a wavelength of 0.52 Å. A correction factor had to be introduced into the data for the smaller angles to compensate for over-illumination. The curves measured were analysed by using the Parratt32 software [Braun, 1999].

5.5.4.2 Irradiation performed with a 10 keV electron-beam.

The results obtained from the fit of the reflectivity curves collected for the as-deposited sample have already been shown in Chapter 4 Section 4.6, in which the density was found to increase with depth. The results after irradiation can be seen in Table 5.2. It should be remarked that for the surface region of the irradiated sample, a fringe could be observed in the reflectivity data, corresponding to a more highly densified outer layer 8 nm thick. The reflectivity data is shown in Figure 5.15.

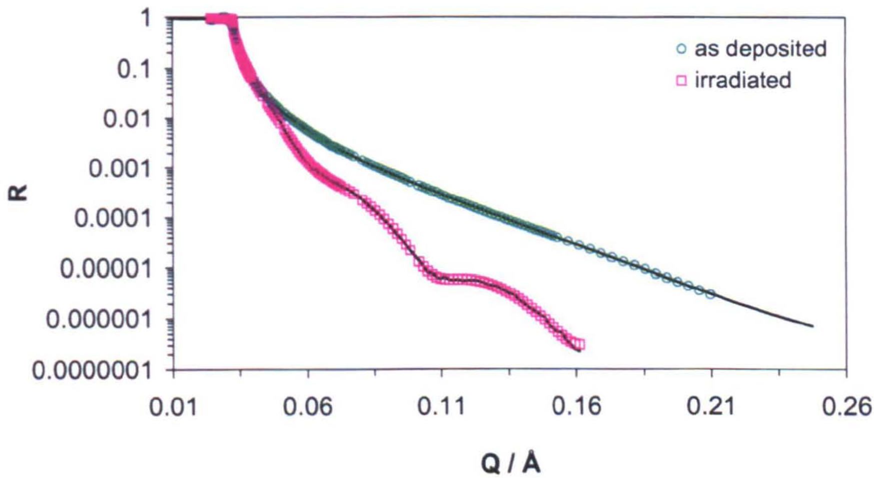

Figure 5.15. X-ray reflectivity curve of a 14 % wt. Ge-doped FHD silica sample before and after irradiation with a 10 keV electron-beam. Green circles represent the reflectivity curve before irradiation and pink squares represent the reflectivity curve after irradiation. The presence of a fringe indicated the existence of a higher densified outer layer 8 nm thick.

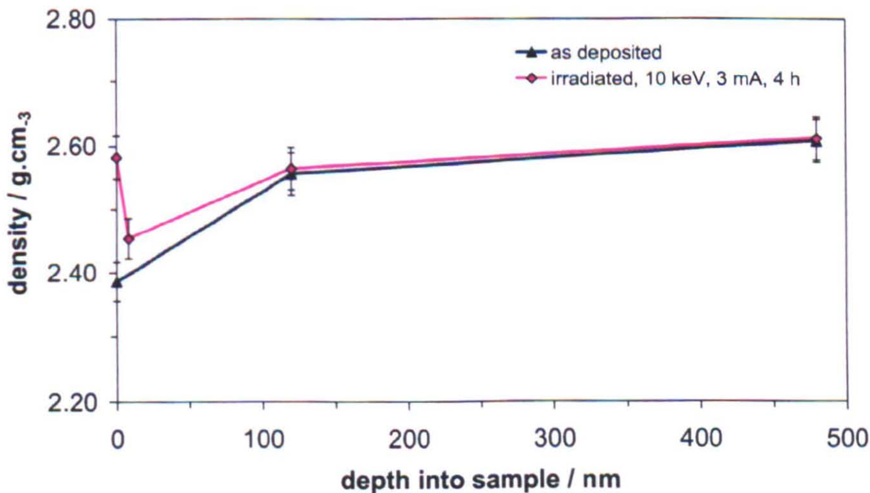

Figure 5.16. Density versus depth before and after irradiation with a 10 keV electron-beam: It is possible to see an increase of density with depth, while the biggest change in density occurs near the surface.

depth analysed	d / Å	rho / Å^{-2}	sigma / Å	χ^2	density /g·cm^{-3}
0	15.47	-5.838.10^{-7}	3.325	2.511	**2.45±1.3% (first 8 nm is 2.58±1.3%)**
	49.75	2.034.10^{-5}	18.572		
	75.79	2.202.10^{-5}	13.443		
	N/A	2.093.10^{-5}	5.104		
≈ 120 nm	0.09	5.497.10^{-6}	7.124	2.34	**2.56±1.3%**
	1.32	6.231.10^{-6}	7.796		
	N/A	2.164.10^{-5}	17.243		
≈ 480 nm	0.17	1.597.10^{-5}	6.921	1.09	**2.61±1.3%**
	1.1	7.988.10^{-6}	7.824		
	N/A	2.188.10^{-5}	16.605		

Table 5.2. Calculation of the variation in depth of a FHD sample 15 % wt after irradiation with a 10 keV electron-beam. The first column indicates the depth at which the reflectivity has been calculated. Columns 2-4 show the parameters resulting from the fit with the Parratt32 software with goodness of fit as indicated in column 5. In the last column, the density calculated from the fits is presented.

5.5.4.3 Irradiation performed with a 50 keV electron-beam.

From the analysis of the X-ray reflectivity data performed before and after irradiation with a 50 keV electron-beam, the values in Table 5.3 were obtained.

The depth analyzed by X-rays at 0.52 Å of wavelength at the critical angle was approximately ≈ 2900 nm, depending on the density of the material, calculated as indicated in Section 4.6 (calculated for a 7 % wt FHD sample with density 2.2 g·cm^{-3}).

sample	d / Å	rho / Å^{-2}	σ / Å	χ^2	density /g·cm^{-3}
as deposited	3.61	1.646.10^{-5}	3.75	0.53	**2.15±1.5%**
	N/A	1.813.10^{-5}	28.018		
50 keV irradiated	8.45	1.12.10^{-5}	4.007	0.3	**2.20±1.5%**
	N/A	1.846.10^{-5}	27.95		

Table 5.3. Values obtained from the fit of the X-ray reflectivity curves with the software Parratt32 for the density at the surface of a 7 % wt. germanium FHD silica layer before and after irradiation with a 0.1 C·cm^{-2} 50 keV electron-beam.

5.5.5 Measurement of the densification by profilometry (Talystep).

The change in density induced by the electron-beam in germanium-doped FHD silica was large enough to produce a depression of the surface, measurable by profilometry (Section 2.5.2, Chapter 2).

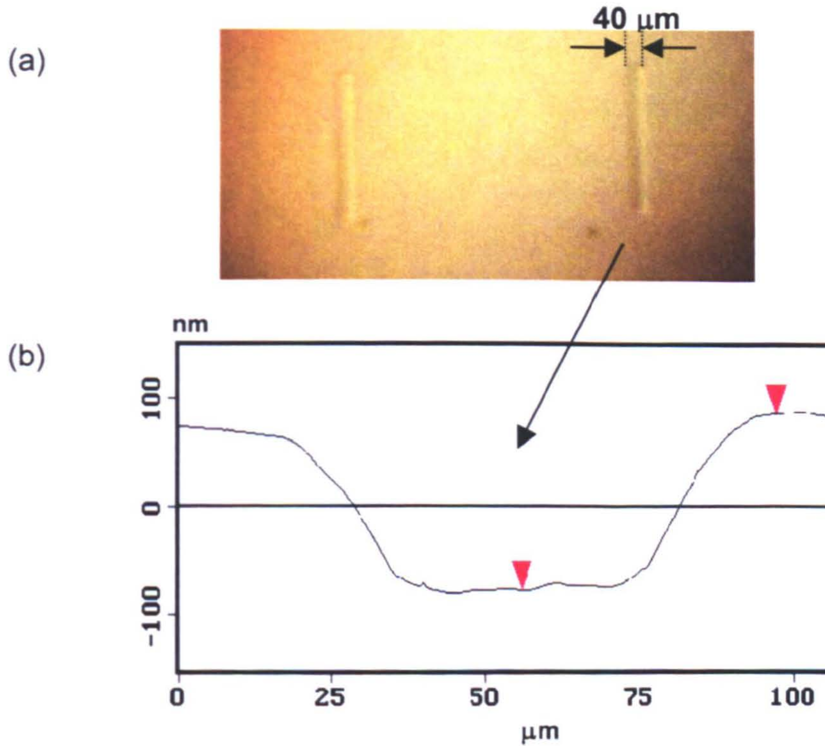

Figure 5.17. Surface profiling of the densification: (a) Optical micrograph of the densification after irradiation of a rectangular pattern. (b) AFM measurement of the surface profile due to the irradiation.

Figure 5.17 shows in (a) a picture of the depressions seen by an optical microscope and in (b) the depression measured by AFM. From the depression on the surface, elastic calculations can be carried out in order to calculate the change in the density of the irradiated material underneath.

5.5.5.1 Profile of densification in depth.

Patterns of different widths (5, 10, 20 and 40 μm) were directly electron-beam written into FHD silica, MCVD material and into thermal oxide using an irradiation dose of 1 $C{\cdot}cm^{-2}$. The depressions observed on the surface were measured by a Talystep profilometer. An example is shown in Figure 5.18. From Equation 5.15 it can be seen that the same irriadiation dose produces different surface depressions,

depending on the size of the pattern written. Moreover, the same irradiation dose induces the same unconstrained densification, as it does not depend on the geometry of the problem. The different depressions measured on the surface are therefore determined by the size of the trenches, as from Equation 5.15.

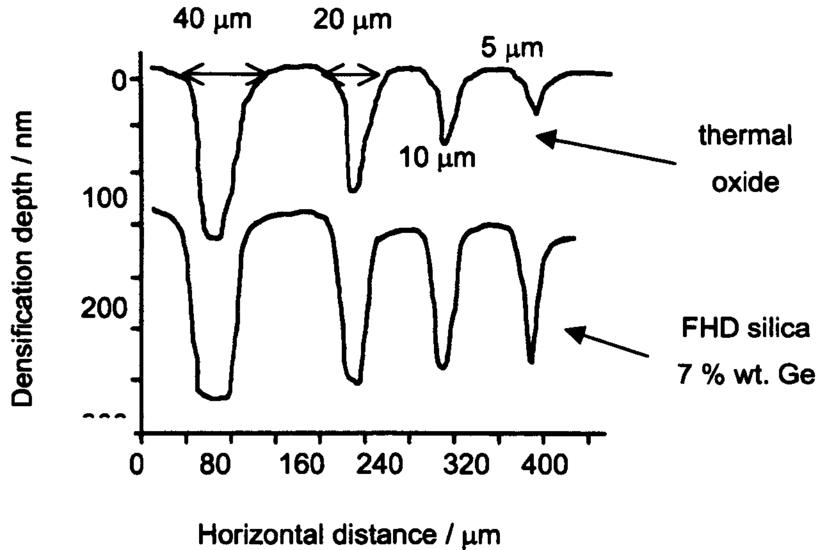

Figure 5.18. Dependence of the densification on the size of the patterns written: Top, thermal oxide; bottom, 7 % wt. Ge FHD silica. Both samples were irradiated with 50 keV electrons and dose 1 $C{\cdot}cm^{-2}$.

As can be seen in Figure 5.18, for the narrower trenches, a larger depression was obtained for the FHD silica sample than for the thermal silicon oxide. This suggests that the densification occurs deeper for the thermal oxide. The data measured for the case of thermal oxide could be explained by Equation 5.15, considering an homogeneous linear strain factor, ε^{P}. Nevertheless, for the case of FHD silica, a single strain factor for the whole irradiated area would not lead to a good fit to the depressions measured for the different widths. In this case, more than one layer needed to be used in order to predict the measured values for the surface depression from the permanent strains in the irradiated region [Blanco, 2001]. Two layers were already used [Blanco, 2001] to describe the densification of FHD silica. In the present work, an improved model with 6 layers was used in order to fit the experimental data of the surface depression. The results of these fits, for a sample with 9.4 % wt germanium content, are shown in Table 5.4. The width of the first 5 layers is 200 nm each and the last layer extends till the end of the penetration range of the electrons for this energy, i.e. ≈ 17 μm.

Dose	Fitting linear strain factors (×10^{-3})						Pattern width (μm)	Depth meas. (nm)	Depth fitted (nm)
	e^P_1	e^P_2	e^P_3	e^P_4	e^P_5	e^P_6			
1	140	20.8	4.4	4.2	3.5	3.5	5	124	117
							10	130	136
							20	153	157
							40	178	177
0.5	176	9.0	3.8	3.4	3.2	2.0	5	106	105.4
							10	124	118
							20	130	133
							40	146	146
0.01	58.6	7.4	3.0	2.5	2.5	2.4	5	42	54
							10	68	68
							20	86	85
							40	100	101

Table 5.4. Comparison of the values of strain in depth obtained from the fitting of the depressions measured on the surface with the expected depression calculated using the six-layers model described above. The calculations have been done for a sample with 9.4 % wt. germanium concentration. Irradiations performed at 50 keV.

The experimental error in the depth measurements was estimated to be smaller than ± 5 nm for these measurements, from the resolution of the Talystep profilometer used. It should be noted that the fitted values are within the experimental errors in almost all the cases.

The same technique of fitting was carried out in a FHD sample in which the same patters were written with an electron-energy of 20 keV and 1 C·cm^{-2} irradiation dose. In this case, the values of the parameters e^P_1 to e^P_6 were obtained as [95×10^{-3}, 19×10^{-3}, 1×10^{-3}, 0.8×10^{-3}, 0.8×10^{-3}, 0.8×10^{-3}], for which the most outer region thickness had to be chosen as 20 nm. A linear strain factor of 0.095 represents a relative change in density of ≈13% (Equation 5.13).

This phenomenon was not observed for the same kind of irradiation on thermal silicon oxide and MCVD silica, in which a uniform region was found in both cases to give a good fit to the experimental data. Therefore, these results appear to suggest that the outer region observed in FHD should not be related with the energy distribution with depth transferred by the electron-beam to the material, as this distribution is the same for the three materials.

The reason for the appearance of the outer more highly densified layer in the FHD silica material should be the particular structure of the germanium-doped FHD layers used in this work, probably in combination with the higher transference of energy density by the electron-beam at the surface of the material. One possibility could be migration of germanium atoms to the surface, as a consequence of the irradiation. A higher germanium content would increase the refractive index of the region. Ionic migration was reported previously for UV-irradiation of germanium-doped silica [Poumellec, 1996b]. In order to investigate whether that was the reason for the high increase in density, XPS measurements were carried out in Ge:SiO_2 FHD samples before and after irradiation with a ≈ 1 C·cm^{-2} 10 keV electron-beam. No increment in the germanium concentration was observed that could explain the large increase in density. In Chapter 4, a gradient was shown in the germanium concentration with depth in the FHD silica layers. Furthermore, a lower density was found by X-ray reflectivity measurements, for the outer region of the Ge:SiO_2 FHD layers (Chapter 4, Section 4.6). In this chapter (Figure 5.20) a higher densification effect was found for samples with smaller germanium content. All these factors may contribute to the higher densification obtained in the outer layer of the FHD silica material: the outer region contains less germanium and it is less dense before irradiation, which, together with a higher energy transfer from the electron-beam, makes that region more likely to densify. A large structural rearrangement towards the denser quartz structure could be expected in the outer region (the density of quartz is 2.65 g·cm^{-3}).

The existence of this more highly densified outer layer has been confirmed by X-ray reflectivity measurements (Section 5.5.4). In those measurements, the densification of the surface layer after irradiation with a 10 keV electron-beam led to a thin outer region with a higher change in density in comparison with the change suffered by the rest of the film.

A higher degree of densification was also indicated by the Raman spectroscopy analyses for the surface of the layer, showing a lesser degree of change in the angle between tetrahedra going at greater depths into the layer (Chapter 5, Section 5.4.1).

5.5.6 Evolution of the relative change in volume with the different irradiation and material parameters.

It is important to determine in which way the densification achieved can be controlled by varying the parameters used during the writing and deposition processes. Among these parameters, the ones that determine the characteristics of the waveguide formed are: the electron energy, determining the depth of the waveguide, as described in Section 5.3; the dose, which will determine the amount of change in densification (and, consequently, refractive index); and, finally, the germanium content, which will influence the behaviour of the material during the irradiation.

5.5.6.1 Dependence of the depression on the surface on the writing parameters.

The different patterns written in this thesis work were always done so with the same beam spot-size, 400 nm, and the same current density of 100 $nA{\cdot}cm^{-2}$ (Section 5.2). Due to the fact that during the writing process some heat can be generated in the sample and produce an *in-situ* annealing of the effects of the electron-beam, the total dose applied in each writing process was applied during several scans. It is important, however, to know whether the number of scans performed during the writing influences the final densification effect. In order to verify this point, the following experiment was performed.

Patterns of different sizes (5, 10, 20 and 40 μm) were written in a 7 % wt. germanium content FHD silica sample. The total dose applied, 1 $C{\cdot}cm^{-2}$, was delivered by writing the pattern on top of itself several times until the total dose was delivered. The dose delivered in each scan was, therefore, the total dose divided by the number of scans.

The same patterns were written in the same sample (to avoid variation from sample to sample) with 10, 20, 50, 70 and 100 scans, and the results of the depressions measured on the surface can be observed in Figure 5.19. It can be seen that the different points obtained for each size of pattern can be considered within the experimental error of the measurement, which is taken to be ≈ 10 nm in this particular case, as estimated from the resolution of the measurement technique. Due to the characteristics of the particular electron-beam-writer used in the

irradiation (Section 5.2), a smaller number of scans was not possible to deliver such a large dose, therefore making it impossible to test the possible heating effect when a number of scans < 10 was used. From this experiment it can be said that for a number of scans > 10, it was not possible to identify any clear self-annealing effect during the writing process.

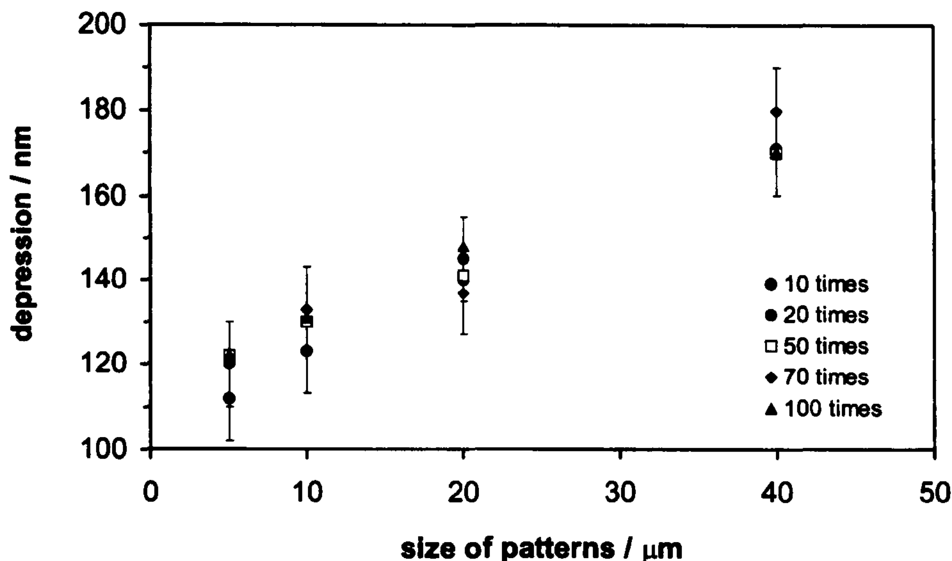

Figure 5.19. Influence of the number of scans: Depression measured on the surface with a Talystep profilometer versus the size of the pattern written, for different number of scans performed in order to deliver the same dose of 1 C·cm^{-2} to the sample.

5.5.6.2 Evolution of the depression on the surface with dose and germanium content.

Figure 5.20 shows the evolution of the depression measured on the surface of the material after electron-beam irradiation as a function of the irradiation dose for samples with different germanium contents. The process has been fitted with a saturating exponential (Equation 5.6) which produces the solid lines in Figure 5.20.

It can be observed that the greater the germanium level present in the sample, the less the value of the depression reached on saturation for the range of compositions studied here (4 – 14 % wt). It was not possible to analyze the effect on FHD silica with no germanium content, due to the fact that the sintering temperature for that material exceeded the 1400° C maximum value achieved in the furnace used. Larger germanium content was also not possible, because even when the flux of $GeCl_4$ gas to the torch was increased further, the amount of germanium present

in the sintered sample was not increased, possible due to out-gassing during the high-temperature sintering step, as it was measured by XPS (Chapter 4, Section 4.4.1). Therefore, a broader range of compositions was not available to be analyzed.

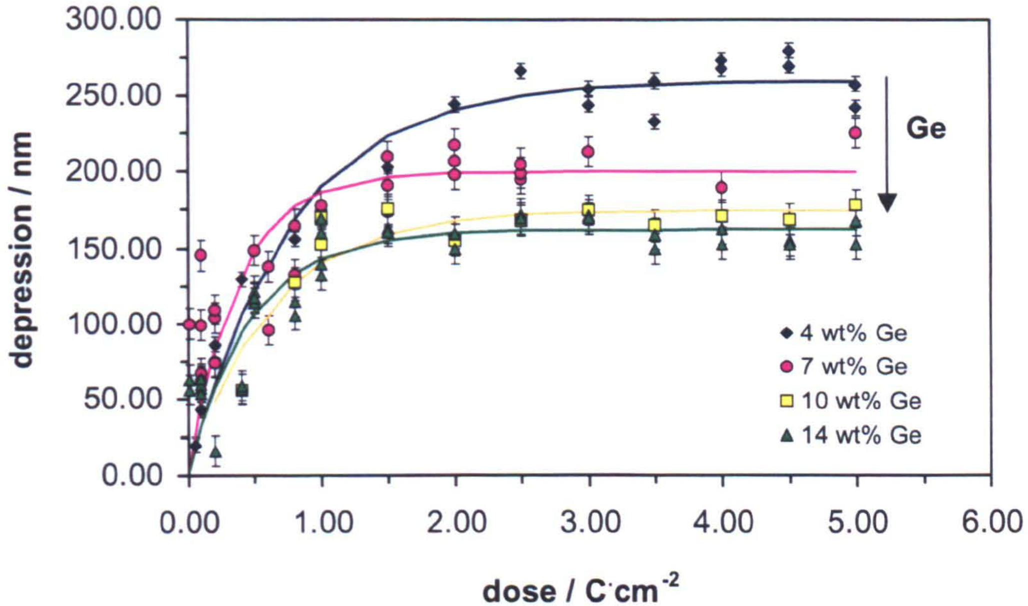

Figure 5.20. Influence of the germanium content on the densification: Depression observed on the surface after irradiation of germanium doped FHD silica layers with different contents of germanium as a function of electron irradiation dose. The solid lines represent the fitting with a saturating exponential function (Equation 5.6).

The same dependence of the densification of the silica structure upon electron-beam radiation on the germanium content was found by the author (in collaboration with the University of Paris-Sud) to happen in the case of germanium-doped MCVD silica [Jacqueline, 2003].

The studies of densification of silica induced by UV-irradiation usually report an increase in the sensitivity of the material as the germanium content is increased [Borrelli, 1999]. This is due to the decrease in the band-gap of the material following the introduction of germanium, thus increasing the absorption of the material at the irradiation wavelengths [Nishii, 1995]. A similar behavior to the one found for electron-beam irradiation in this work was reported by Chen *et al.* [Chen, 2003] after irradiation of germanium-doped silica with an F_2-laser. The similarities between electrons and the F_2-laser is that, in both cases, the reduction of the band-gap by

the introduction of defects in the network is not necessary for the transmission of energy to the material due to the larger energy of the photons and of the electrons.

The way in which the addition of more germanium decreases the electron-sensitivity of the material to the electron-irradiation is not clearly understood. A possible explanation could be that as the germanium concentration increases, the temperature for sintering the material decreases and therefore a more consolidated, i.e. dense, material is obtained. As the density of the initial material increases, less change in density is expected to be produced upon irradiation.

5.5.6.3 Dependence of the depression in the surface on the energy of the electrons used.

Figure 5.21 shows the measurements of the surface depression for a 7 % wt. average germanium concentration sample irradiated with different electron energies. It can be seen that the data corresponding to the 20 keV and 50 keV irradiations was already saturated, whereas the 100 keV depressions were still increasing with dose, for the range of doses characterized.

The difference lies probably in the way that the electrons with different energies deposit their energy into the sample, as was illustrated in Figure 5.6. In the 20 keV case, the total energy is deposited in the first ≈3.4 μm (Section 5.3, Equation 5.3). Therefore, the energy density deposited in that region is much higher than in the case of 50 keV irradiation. In this case, the energy is deposited in the outer 17 μm. For 100 keV electrons, the penetration range is approximately 57 μm. Since the amount of densification induced in the material was related to the amount of energy transferred into the material, and since saturation of the densification occurs (Section 5.5.2), it is logical to expect to arrive at saturation earlier in the 20 keV case than in the 50 keV or 100 keV irradiations cases.

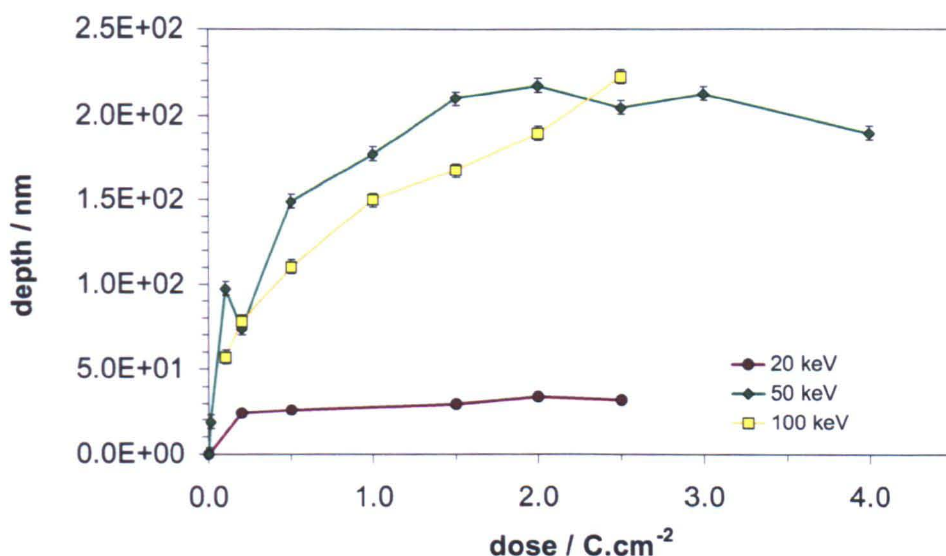

Figure 5.21. Influence of the electron-irradiation energy on the densification.

5.5.6.4 Dependence on the structure of the initial silica layers.

The change in density obtained after electron-beam irradiation was expected to be related to the particular structure of the as-deposited silica material. Different studies [Van Peski, 2000], [Liberman, 1999], [Sempolinski, 1996] compare the effect of UV-irradiation on different kinds of pure silica. Primak *et al.* have studied the effects of electron-irradiation on different kinds of pure silica [Primak, 1984]. In the present work, different kinds of germanium-doped silica films have been irradiated with a range of electron-doses and several different kinds of behaviours have been observed.

Figure 5.22 compares the depression on the surface obtained, as a function of the electron irradiation dose at 50 keV, for silica deposited via several different techniques: modified-chemical vapour deposition (MCVD), FHD, plasma-enhanced chemical vapour deposition (PECVD) and helicon activated reactive evaporation (HARE) [Charles, 95], [Cheylan, 01]. The compositions of the films vary from 5 to 8 wt% of germanium. The MCVD and PECVD samples were provided by A.S. Jacqueline, from the Laboratoire Physico-Chemie de l'Etat Solide, Université Paris-Sud, Orsay, France. The HARE deposited samples were provided by R. Jarvis from the University of Canberra. The Ge:SiO_2 FHD samples were deposited in Glasgow by the author. Due to the different deposition processes, the structure of the silica

deposited by using the different techniques was expected to be different, and so the response of the material to the electron-beam, as shown in Figure 5.22.

The densifications obtained for the case of the FHD and MCVD material follow the same kind of saturating behavior, with the depressions obtained for MCVD material at high doses being larger than for FHD. The behaviour of HARE and PECVD silica was slightly different: in both cases, for small electron-doses a small expansion of the material was observed, while for larger doses a net compaction occurs. An expansion after small irradiation doses has also been observed by Primak *et. al.* for the case of pile-exposed silica [Primak, 1969] and appeared to be due to a relaxation of the strained silica network caused by the energy deposited by the irradiation before the energy is large enough to produce compaction as the dominant process. For larger doses, the compaction obtained for PECVD material is larger than for the other silica materials studied. This could be due to the fact that PECVD is a technique for depositing silica at relatively low temperature. Therefore, the departing density of the material was expected to be smaller and, therefore, easier to densify.

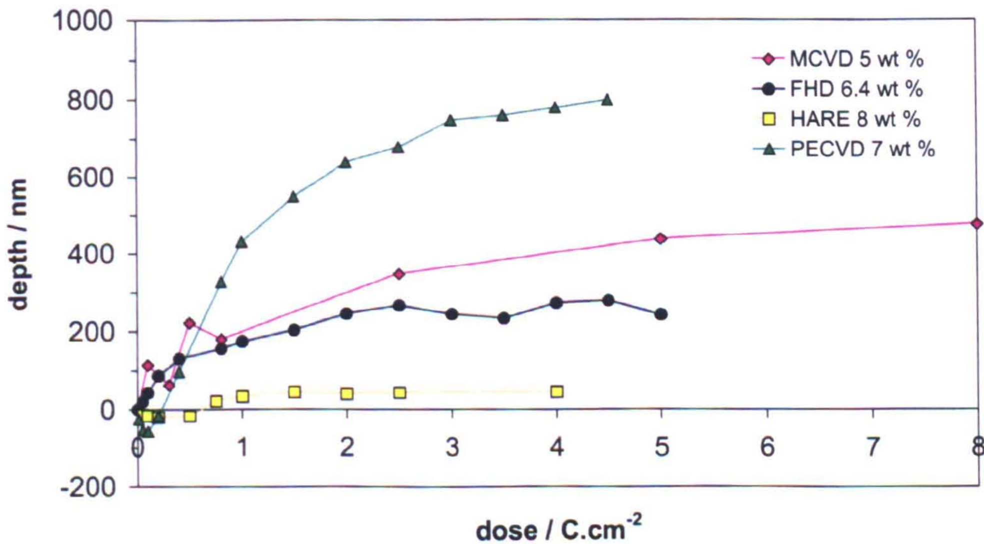

Figure 5.22. Influence of the silica structure on densification: Comparison of the depression measured on the surface of the material as a function of the irradiation electron-dose for different kind of silica deposited by different techniques: MCVD, FHD, HARE and PECVD.

The PECVD silica sample was subjected to a high temperature anneal (600 °C for 2.5 h in an air atmosphere and 700 °C for 2.5 h) before irradiation with the same

doses as described in Figure 5.23. A higher temperature was not possible due to the generation of bubbles in the PECVD silica structure. The annealing treatment was expected to produce a relaxation of the PECVD structure. Figure 5.23 shows the depression on the surface measured as a function of irradiation dose for the as-deposited and pre-annealed samples. It should be noted, that the amount of depression obtained after large doses was the same for the three samples. For low doses, the behavior has changed after pre-annealing: a reduction in the expansion obtained was observed. This result was consistent with a relaxation of the structure due to the annealing, thus limiting the amount of relaxation that can occur after low-dose irradiation. This result further confirms the hypothesis that the expansion observed for low doses was due to relaxation of the strained as-deposited structure. In that direction, PECVD and HARE silica samples must have a more strained structure after deposition, which is consistent with their low-temperature deposition processes [Li, 2002].

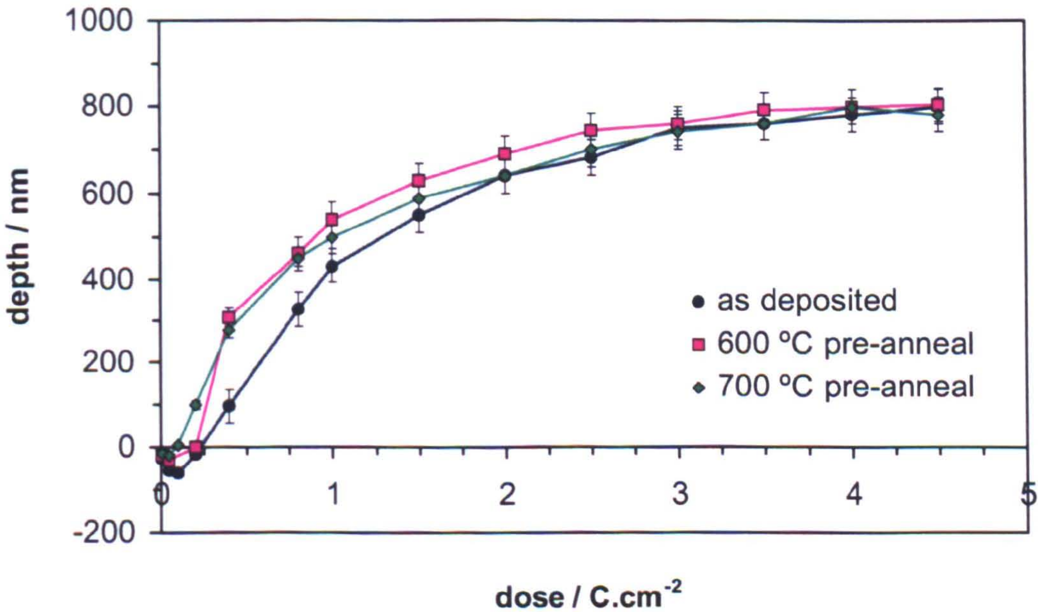

Figure 5.23. Effect of anneal in the densification of PECVD silica: Depression measured on the surface of a PECVD sample after different irradiation electron-doses. PECVD silica samples subjected to different pre-annealing temperatures (600 °C and 700 °C for 2.5 h) were compared with the as deposited PECVD silica.

A similar experiment was carried out for the case of FHD silica: the material was sintered for different times at high temperature (1350 °C), as described in previous sections when analyzing the properties of the as-deposited FHD silica layers (Sections 4.3.7, 4.4.3, 4.6.2). The results of this experiment are shown in Figure

5.24. Comparing the values obtained for a sample sintered for 30 min and for 2 h, it can be seen that for high doses, the amount of depression measured for the 2 h sintered sample was smaller. This result is consistent with the fact that a sample sintered during 2 h will have achieved a larger degree of consolidation than if the sintering time is only 30 min and, therefore, the initial density will be larger (as demonstrated from X-ray reflectivity measurements of the density in these samples in Chapter 4 Section 4.6). As a consequence, a smaller change in volume was expected. As for the case of the sample left in the furnace at 600 °C overnight, due to depletion of germanium out of the sample, a smaller density was expected for the as-deposited sample (as measured in Chapter 4 Section 4.6) and therefore a larger amount of densification can be produced after electron-beam irradiation, as shown in Figure 5.24.

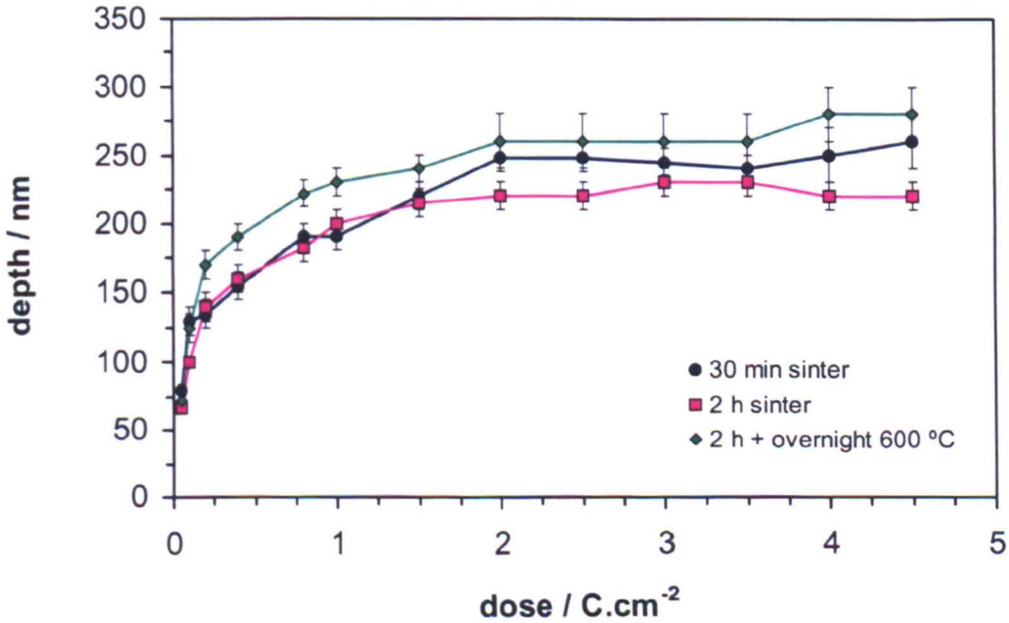

Figure 5.24. Influence of the sintering condition on the densification of FHD silica: Evolution with dose of the depression on the surface induced in FHD silica sintered for different times at 1350 °C.

The results obtained in this section reveal how sensitive the degree of densification obtained after irradiation is to the structure of the original material. Therefore, the selection of adequate material for each application is important in order to achieve the desired result. In this work, only the densification has been studied for different materials. Further work studying the induced refractive index change, structural changes and losses of different silica subjected to irradiation will

help to understand the intrinsic phenomena produced in the material by the irradiation.

5.6 Refractive index change induced in Ge-doped FHD silica by electron-beam irradiation.

The increase of refractive index after electron-beam irradiation of germanium-doped FHD silica is the property that makes this technique appropriate for the fabrication of optical waveguides. In order to design an optical waveguide-based integrated optical device, more information concerning the change in refractive index obtained is desirable.

The evolution of the effective refractive index of the different modes of propagation supported by an electron-beam irradiated slab waveguide is thus presented. The influence of the germanium concentration and the evolution of the change in effective index with the irradiation dose was studied. The refractive index change after irradiation can be calculated from the induced change in density by using the Lorentz-Lorenz equations and the photo-elastic effect. Using these calculations, the evolution of the change in refractive index with dose calculated from the evolution with dose of the relative change in volume was presented. The profile of refractive index expected from the density measurement was compared with a profile supporting the measured propagation modes. The evolution of the profile with dose is also analyzed. Finally, the change in the birefringence of the slab waveguides fabricated by this technique was described.

5.6.1 Evolution of the effective refractive index of the different propagation modes with irradiation dose and germanium content.

FHD silica layers with different germanium contents, ranging from 7 to16 % wt., were deposited on top of a silicon substrate with 15 μm of thermal oxide already grown on it. Gratings of periodicity 680 nm were fabricated, as described in Chapter 3 (Section 3.2.3). The dimensions of the gratings were 500x1000 μm^2. The effective refractive index of the different propagating modes supported by the structure were determined by measuring the coupling angle of the incident He-Ne laser (at 632.8 nm wavelength) beam into the slab waveguide. For this wavelength and this periodicity, the coupling angles are around 32 deg (see Equation 3.2 in Chapter 3). The samples were then irradiated repeatedly with a 50 keV electron-beam at different doses (as described in Section 5.2) and the effective refractive indices

were measured after each irradiation. A maximum dose of 1 C·cm^{-2} was used due to the large area that required to be irradiated for the experiment, which will imply a too large irradiation time, non-practical for this experiment.

The evolution with irradiation dose of the effective refractive indices for the modes 0 and 1 of the slab waveguides prepared as just described, for different germanium contents, is shown in Figure 5.25. The solid lines represent the averaged values.

It is possible to observe that there is no obvious trend of the change in the effective refractive index of the modes 0 and 1 on the germanium content, as opposed to that has been reported in the past for UV-irradiated silica [Chen, 2003]. In the case of germanium-doped FHD silica, the evolution with dose of the different effective refractive indices of the different modes of propagation was the same for the different compositions, in the range of compositions studied in this work. A possible explanation could be that as the germanium concentration increases, the relative change in volume obtained after electron-beam irradiation is smaller. On the other hand, a higher germanium content increases the refractive index of the initial silica. In the Lorentz-Lorenz equation (Equation 5.17), a higher degree of compaction leads to a higher change in refractive index. However, this effect can be compensated by the higher initial refractive index of the material, thus explaining the result of Figure 5.25.

It should also be noted from Figure 5.25 that, for all the different compositions studied, a saturation of the change of effective refractive index attained occurs at a value of around $7x10^{-3}$. This saturation was almost complete at a dose of around 0.2 C·cm^{-2}. The value of the maximum effective refractive index change and the dose for which saturation occurs agree with the values reported by Syms *et. al.* [Syms, 1994].

From the results shown for the evolution of the depression of the surface after irradiation as a function of electron-dose, Figure 5.20, it was observed that saturation appears after a dose of around 2 C·cm^{-2}. This result suggests different kinetics in the case of the change in density as compared with those for the change in refractive index, which can be related to the formation of colour centres. In the following subsection, the refractive index expected from the depression on the surface will be evaluated.

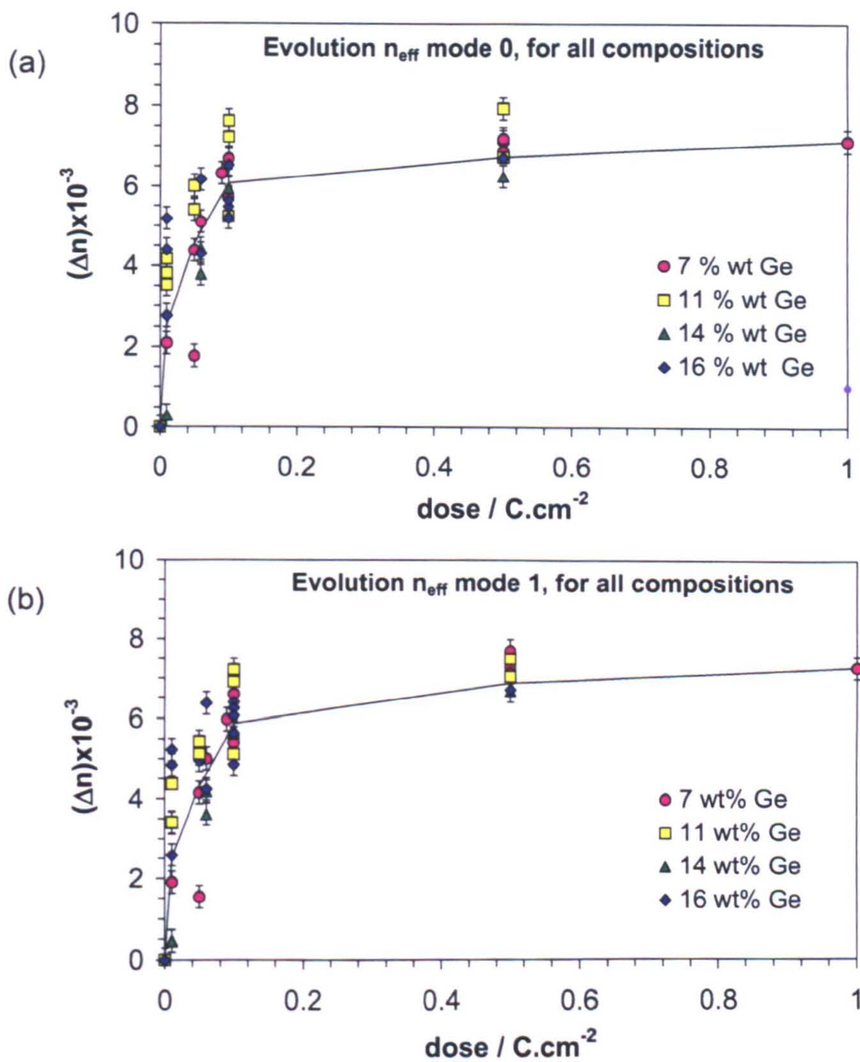

Figure 5.25. Evolution of the effective refractive index as a function of electron-dose for samples with different germanium contents: (a) Evolution of the effective refractive index of mode 0; (b) Evolution of effective refractive index of mode 1. It can be seen that the amount of change of the effective refractive index is independent of the composition.

5.6.2 Calculation of the refractive index change from the relative change in density.

5.6.2.1 Theoretical model.

In Section 5.5, how the irradiation of silica with an energetic electron-beam produces densification of the material was discussed. The relative change in volume was demonstrated to have two components: a "permanent" component also known as "unconstrained densification", appearing from the structural rearrangements

produced after the transference of the energy from the electron-beam to the silica matrix by ionization events and that leads to an isotropic change of volume of the irradiated material, and an elastic component, appearing as an elastic reaction of the material to the first, "unconstrained" densification component.

Each of these components of the change in volume will introduce a change in refractive index, the "permanent" component through a differential form of the Lorentz-Lorenz equations whilst the elastic component can be characterized by stress-optical equations [Poumellec, 1996a], [Poumellec, 2002], [Kerbouche, 1999], [Gusarov, 2000]. These changes are represented in the following schematic:

$$\left(\frac{\Delta V}{V}\right)^{T} = \left(\frac{\Delta V}{V}\right)^{p} + \left(\frac{\Delta V}{V}\right)^{e}$$

$$\Downarrow \qquad 1\Downarrow \qquad 2\Downarrow$$

$$(\Delta n)^{T} = (\Delta n)^{p} + (\Delta n)^{e}$$

where "1" represents the differential form of the Lorentz-Lorenz equation [Born, 1959], [Dellin, 1977], [Bazylenko, 1997], [Barbier, 1991], [Schenker, 1997]:

$$(\Delta n)^{p} = \frac{\left(n^{2}-1\right)\left(n^{2}+2\right)}{6n}(1+\Omega)\left(-\frac{\Delta V}{V}\right)^{p} \tag{5.17}$$

with Ω being a polarizability change due to the densification. Schenker *et. al.* performed a study relating the change in refractive index with densification for different kinds of pure silica and concluded that the density-induced polarizability changes are material dependent.

The photo-elastic equations, number "2" in the previous schematic, can be re-written as

$$\begin{aligned}\Delta n^{e}_{\perp z} &= -\frac{n^{3}}{2}\left[p_{11}\varepsilon^{e}_{\perp z} + p_{12}\left(\varepsilon^{e}_{\perp z} + \varepsilon^{e}_{\parallel z}\right)\right]\\ \Delta n^{e}_{\parallel z} &= -\frac{n^{3}}{2}\left[p_{11}\varepsilon^{e}_{\parallel z} + p_{12}\left(2\varepsilon^{e}_{\perp z}\right)\right]\end{aligned} \tag{5.18}$$

where p_{11} and p_{12} are the strain-optical constants, the values of which for silica are 0.12 and 0.27 respectively [Jeunhomme, 1990], and $\varepsilon_{\|z}$ and $\varepsilon_{\perp z}$ are the linear strains in the direction parallel to z (the z-direction) and normal to z (the x- and y-directions) respectively, as defined in Section 5.5.3, corresponding to the TM and TE polarizations respectively.

Therefore, the total change in refractive index for the TE modes will be given by

$$(\Delta n)_{TE}^{T} = \Delta n_{\perp z}^{e} + \Delta n^{P} \tag{5.19}$$

And the total change in refractive index for the TM polarization

$$(\Delta n)_{TM}^{T} = \Delta n_{\|z}^{e} + \Delta n^{P} \tag{5.20}$$

5.6.2.2 Refractive index profile expected from density change measurement in Ge:SiO$_2$ FHD layers.

As explained in the densification section, the surface profile after irradiation for different doses and for different sizes of patterns has been measured. From measurements of the surface depression, the permanent component of strain, ε^{P}, can be obtained as a function of depth (Equation 5.15). In the case of germanium-doped silica, the existence of a more highly densified region near the surface of the material was observed. A higher change in refractive index is expected for that layer.

From the values of permanent linear strain obtained in Table 5.4 of Section 5.5, the calculations carried out in the previous section were performed in order to obtain the total refractive index induced by densification, for TE polarization (Equation 5.19). The results of these calculations are shown in Figure 5.26, in which the profile for refractive index with depth derived from the measured densification for the TE polarization is depicted. The change in polarizability due to relative change in density, Ω, was assumed to be zero in these calculations.

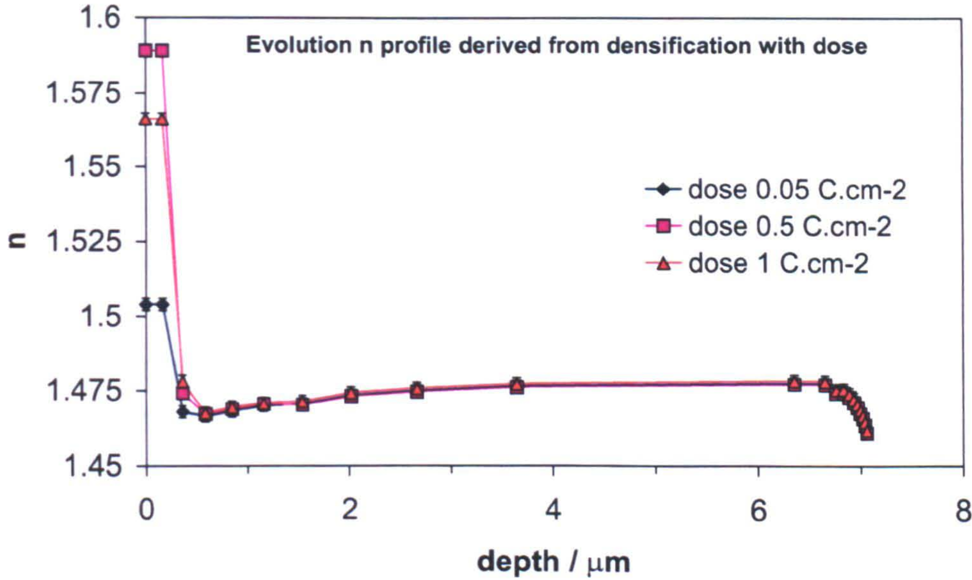

Figure 5.26. Calculation of the refractive index profile of a 9.4 % wt. Ge FHD silica sample from the densification for 3 irradiation doses. The polarizability change due to densification was considered $\Omega=0$ in these calculations.

It is appropriate to point out here the uncertainty intrinsic to these calculations: in the calculations of the permanent component of the linear strains (Section 5.5), several assumptions have been made, such as the assumption that the elastic constants are the same in all the material, the assumption that the silicon substrate is far enough from the area of interest so that it does not affect the calculations and the assumption that the elastic constants stay un-modified after irradiation. Furthermore, the parameters required in the formulae, i.e. the Poisson's ratio and the photo-elastic constants, were taken from the literature. These parameters are material and structure dependent and, thus, it is logical to question whether they adopt a different value for the germanium-doped flame-hydrolysis silica analyzed in this work. As an example, different authors have utilized a different values for the photo-elastic constants of silica: Dellin *et. al.* [Dellin, 1977] proposed a value of 0.193 and 0.088 for p_{11} and p_{12} respectively, while Primak [Primak, 1958] used 0.197 and 0.088. The Poisson's ratio has also been reported to adopt different values depending on the structure of the material under study. Primak [Primak, 1958] used a value of 0.164 for vitreous silica while Dellin [Dellin, 1977] used 0.17. From these considerations, an error of approximately $2\text{-}3\times10^{-3}$ has been assumed for the refractive index estimated from densification. This estimated value could be improved by measuring the elastic constants of the material and by making a more elaborated model for the densification. Furthermore, the density-induced

polarizability changes are material dependent and in the calculations presented above they have been considered to be zero.

The calculations were performed for the 100 sccm sample from batch Apr'01, with a germanium content of approximately 9.4 % wt., for which the density profile was evaluated in Section 5.5. In Figure 5.26 an outer more highly densified region is observed, derived from the one obtained from the density measurements.

5.6.2.3 Analysis of the refractive index profile from the study of the modes of propagation.

The profile of refractive index was analyzed from the measured effective refractive index of the modes of propagation. In Figure 5.27, plots of the effective refractive index squared versus the square of the mode number plus one are shown. It should be noted that a straight line for this kind of plot would represent a step index profile [Section 3.3.2.1].

In Figure 5.27, it is clear that the plots are not simple straight lines, thus discounting the possibility of a step profile index distribution. As was discussed previously (Chapter 3), the *inverse*-WKB method does not allow the reconstruction of profiles that are neither monotonically decreasing of increasing. On the other hand, from a limited set of modes it is not possible to determine a unique refractive index profile that supports this particular set of modes. Therefore, some other information about the profile is needed.

In the case of the present study, as was shown in the density measurements (Section 5.5), a more highly densified layer was observed in the outer region of the material after irradiation, due to the particular compositional and structural characteristics of the as-deposited FHD silica layers used. It was then logical to expect that an outer region with a higher refractive index will be present in the refractive index profile, based on the Lorentz-Lorenz equations.

The profiles obtained from the density measurements were used as the starting point in a direct search minimization algorithm ("fminsearch", implemented in the Optimization toolbox of Matlab). The best fits to the experimental values for the different modes, at the different doses characterized, are shown in Figure 5.28. The effective refractive indices of the fitted profiles are compared with the measured ones in Table 5.5.

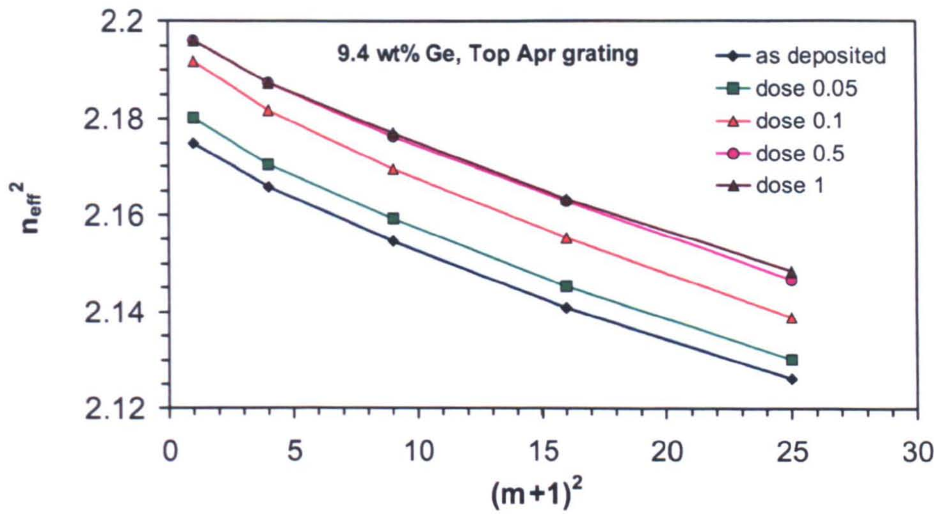

Figure 5.27. Plot of the squared effective refractive index as a function of $(m+1)^2$: Evolution with the different irradiation doses for a sample with germanium content 9.4 % wt. from batch Apr'01.

It is necessary to remark again that, even when the effective refractive indices supported by these profiles fit perfectly to the effective indices measured experimentally (Table 5.5), it was not possible to say that the actual index profile of the waveguide has been specified. In the present case, the density distribution inside the waveguide was known and was used to generate an approximate shape for the profile that was then refined to get a good fit solution.

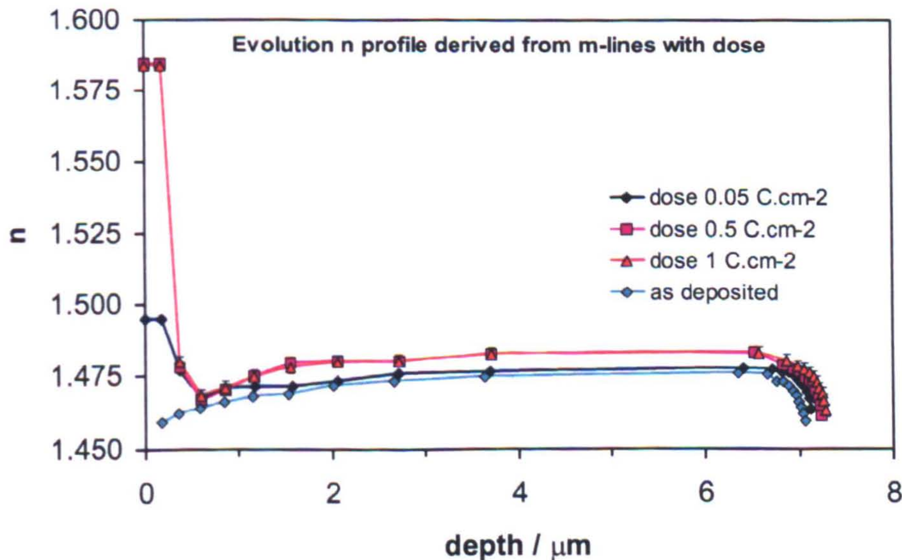

Figure 5.28. Evolution with dose of the measured refractive index profile: The effective refractive indices supported by these profiles fit the experimental values within the experimental error of the measurements.

Dose (C·cm^{-2})	neff measured	neff fitted	fit
0.05	1.4765±0.0002 1.4732±0.0002 1.4694±0.0002 1.4647±0.0002 1.4595±0.0002	1.4765 1.4733 1.4694 1.4648 1.4593	0.12
0.5	1.4819±0.0002 1.4790±0.0002 1.4753±0.0002 1.4707±0.0002 1.4651±0.0002	1.4820 1.4789 1.4752 1.4706 1.4652	0.1
1	1.4819±0.0002 1.4790±0.0002 1.4755±0.0002 1.4709±0.0002 1.4657±0.0002	1.4819 1.4790 1.4755 1.4709 1.4657	0.24

Table 5.5. Effective refractive index of the modes measured by the m-line technique and comparison with the effective indices obtained for the fitted profiles.

5.6.2.4 Comparison of the refractive index profiles obtained from densification with the ones from optical measurements.

Figures 5.29-5.30 compare the profiles of refractive index obtained from the application of the Lorentz-Lorenz formula and the photo-elastic effect to the measured densification and the profiles obtained from optical measurements. The density-induced polarizability change, Ω, was considered zero in these calculations.

Observing Figures 5.29 and 5.30, two different behaviours could be observed for the relative magnitude of the refractive index deduced from density changes and the refractive index obtained from optical measurements. In the outer higher densified region, the refractive index calculated from the measured densification was larger than the obtained by optical measurement for the lower dose case (0.05 C·cm^{-2}). As the dose increased, the relative magnitude of the densification calculated refractive index decreased and for the larger dose applied, 1 C·cm^{-2}, it was smaller than the refractive index obtained optically. A further effect not considered in the calculation might be responsible for this behaviour. On the other hand, a different evolution with dose was observed in the bulk: as the dose increased, the densification-induced refractive index was observed to decrease in comparison with the optically characterized refractive index.

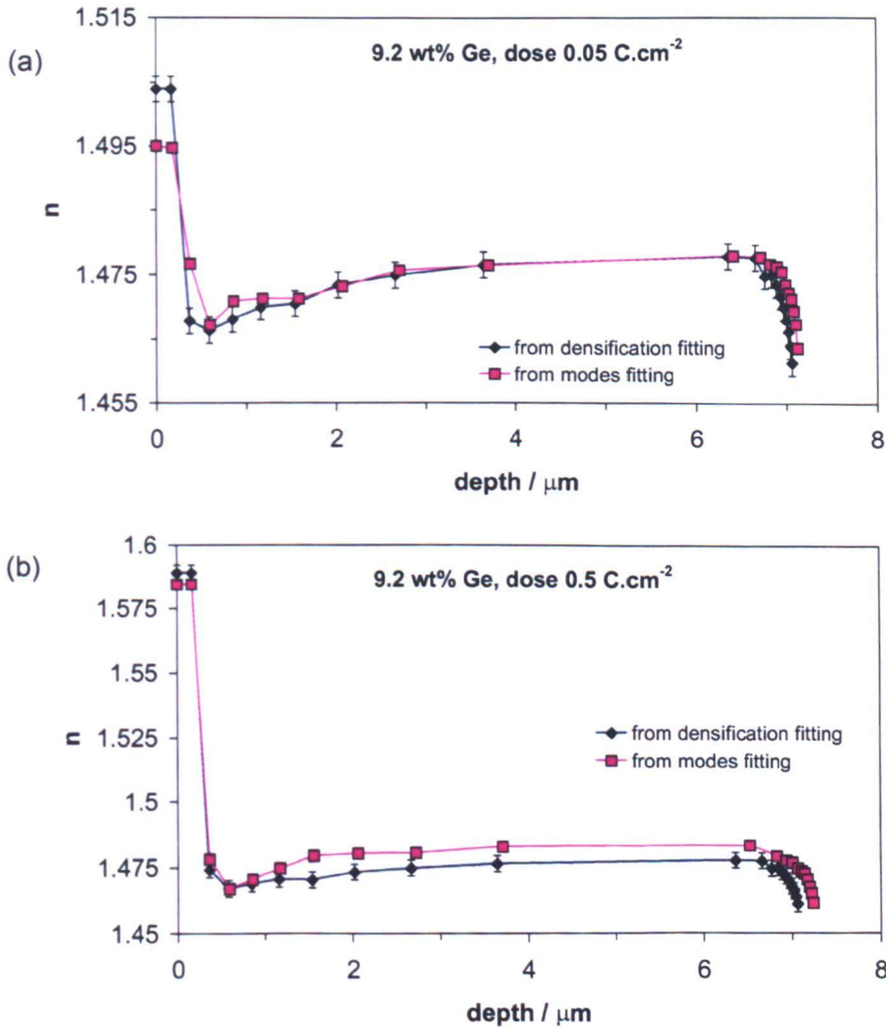

Figure 5.29. Comparison of calculated (from densification) versus measured refractive index profiles: (a) for a dose of 0.05 C·cm^{-2}; (b) for a dose 0.5 C·cm^{-2}.

Dellin *et. al.* [Dellin, 1977] reported a variation with electron-dose of the density-induced polarizability change, which varies the relationship between relative change in density and refractive index (Equation 5.17). Schenker *et. al.* found a material-dependency of the density-induced polarizability [Schenker, 1997]. The variation of Ω irradiation doses could be related to the formation of different defects in the material, such as colour centres, which would contribute to the way in which the polarizability changes [Bazylenko, 1997].

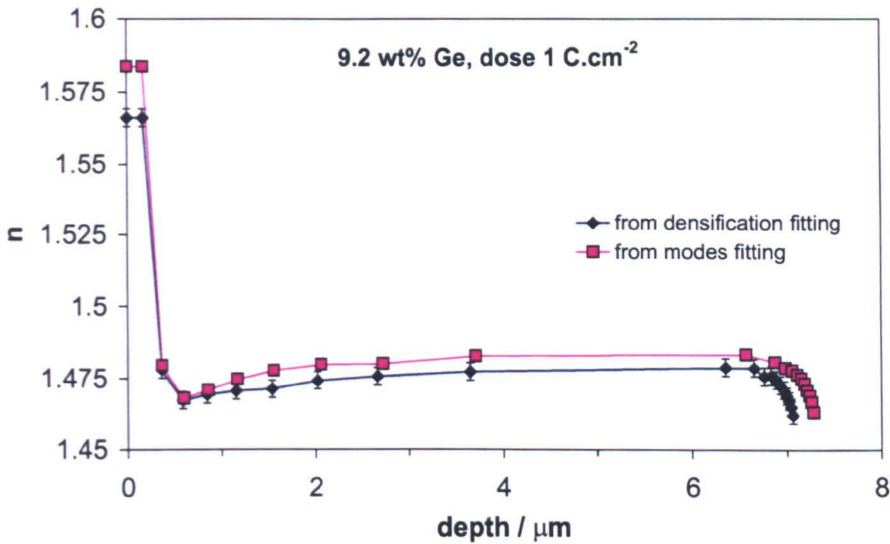

Figure 5.30. Measured and calculated (from densification) profiles of refractive index after an irradiation dose of 1 C·cm^{-2}: Comparison of the profile obtained from densification and the one from fitting the modes measured by the m-line technique.

If the value of Ω were varied with the irradiation dose in a different way for the two regions, i.e. the outer higher densified layer and the bulk, a better fit between the refractive index obtained from the measured densification and the one measured optical would be obtained, as can be seen in Figures 5.31-5.32. The variation of Ω with the dose assumed in order to get a good fit of the profiles is shown in Table 5.6.

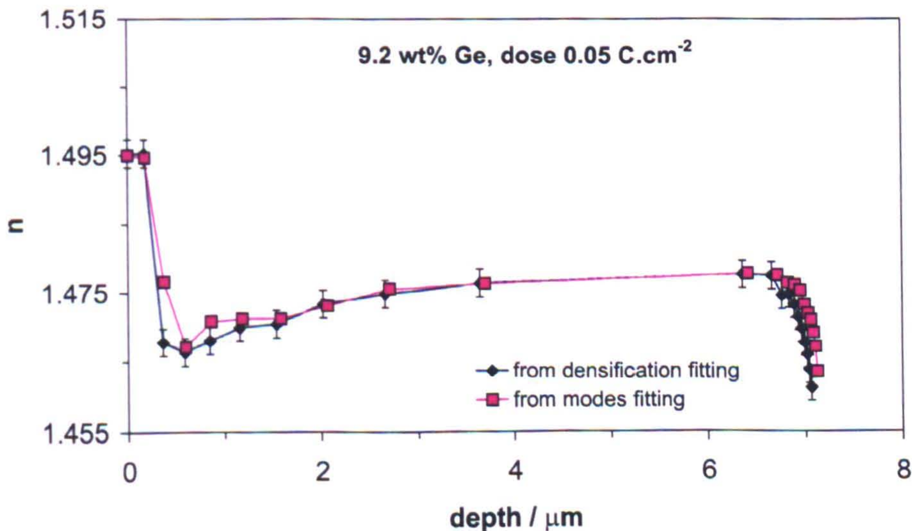

Figure 5.31. Comparison of the profiles of refractive index derived from densification and optical measurements: For a dose 0.05 C·cm^{-2}, values of Ω of –0.09 for the outer region and 0 for the bulk were taken.

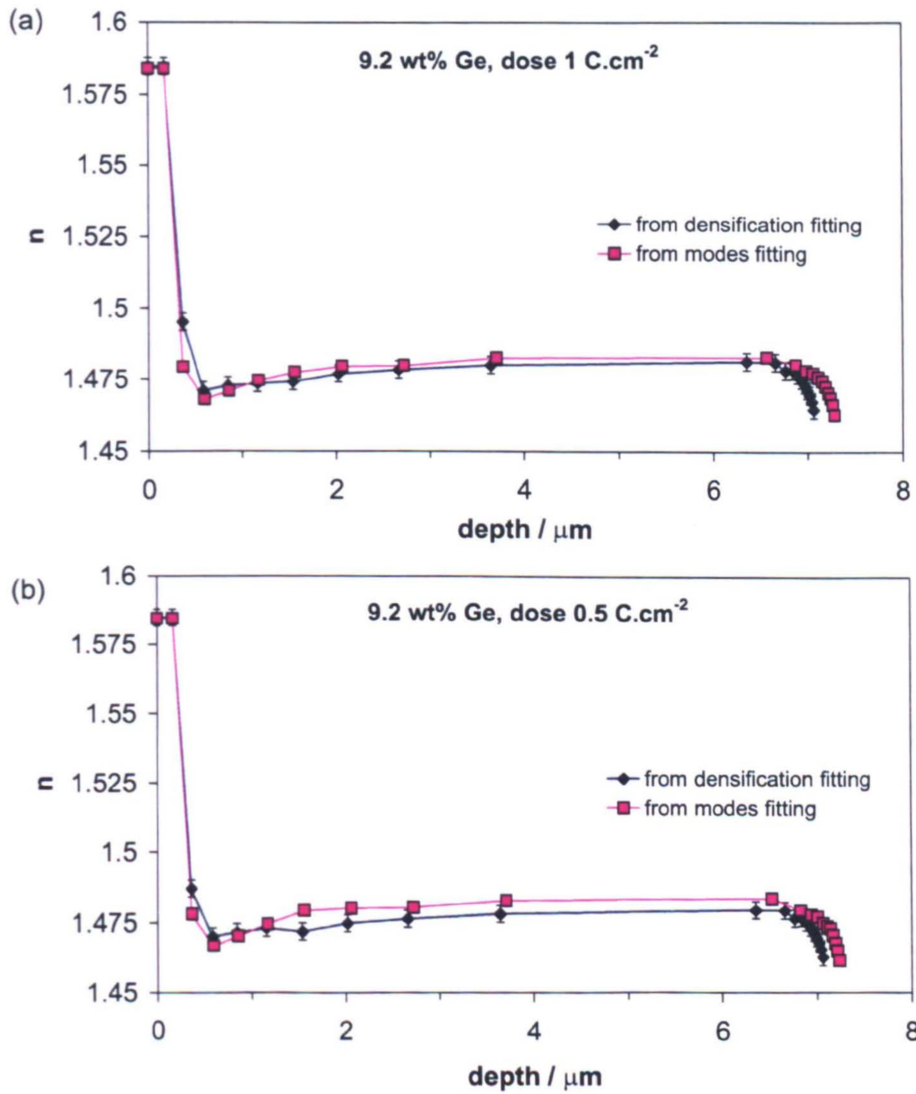

Figure 5.32. Comparison of the refractive index profile from densification with the one obtained optically: (a) For a dose 1 C·cm^{-2} Ω was taken 0.08 for the outer region and 0.5 for the bulk; (b) For a dose 0.5 C·cm^{-2}, Ω was taken as –0.015 for the outer region and 0.5 for the bulk.

It can be observed in Table 5.6. that, as the irradiation dose increases, the polarizability change contributes positively to the refractive index change.

dose	Ω (outer region)	Ω (bulk)
0.05	-0.09	0
0.5	-0.015	0.5
1	0.08	0.5

Table 5.6. Variation of the density-induced polarizability change with irradiation dose.

From the previous graphs, it appears that the main contribution to the change of refractive index is the densification induced by the irradiation accompanied by a change in polarizability associated with the densification, probably due to the formation of colour centres. It has been proposed that breakage of Ge-Si "wrong bonds" produces a positively charged site and a free electron [Poumellec, 1996b], which relaxes the structure producing densification [Bazylenko, 1997], i.e. mainly by forming low-membered ring structures in the silica structure and reducing the angle between tetrahedra. The positively charged site is fixed to the matrix while the electron can escape and get trapped at a neighboring site, producing a dc-electric dipole that will affect the polarizability of the material. Furthermore, densification of the material varies the distances of the different bonds, also inducing a change in the polarizability. From the EXAFS analysis (Section 5.4.2) breakage of the Si-Ge bonds was observed, which is reported to induce colour centres [Poumellec, 1996b]. A reduction of the Ge-O bond length was also observed. The results presented here deduced the density-related polarizability change, due to the factors described, by simply fitting the densification to the optical measurements, using the model described in Section 5.6.2.1. An independent measurement of the polarizability change after irradiation and its relation with the colour centre concentration and bond distances would be desirable in order to fully confirm the results presented here.

5.6.3 What happens with the birefringence.

The effective refractive indices of the different samples analyzed were measured for both TE and TM polarization in order to have some information concerning how the electron-beam irradiation affects the birefringence of the material (this is an important parameter for the design of integrated optical circuits).

The birefringence of the as-deposited layers has been reported to be smaller than 3×10^{-4} in Chapter 4 Section 4.3.8, a value that is below the experimental error of the measurements carried out in this work. After irradiation with different doses, the values of birefringence obtained are plotted in Figures 5.33 (for the Apr'01 series samples) and 5.34 (samples from the May'01 series). The values measured appear to vary from sample to sample, possibly due to a variation of the initial stresses present in the as-deposited layers, which will determine their birefringence. In all cases, the values for the birefringence vary after different irradiation doses, increasing or decreasing with respect to the previous dose. The variation of the

values of the birefringence might be related with the structural rearrangements occurring in the material during irradiation, probably leading to an increased release of stresses within the structure. In order to obtain more insight into the processes involved, further birefringence measurements using a more sensitive technique, such as a standard null technique as described by Borrelli *et al.* [Borrelli, 1997], together with structural analyses, should be carried out.

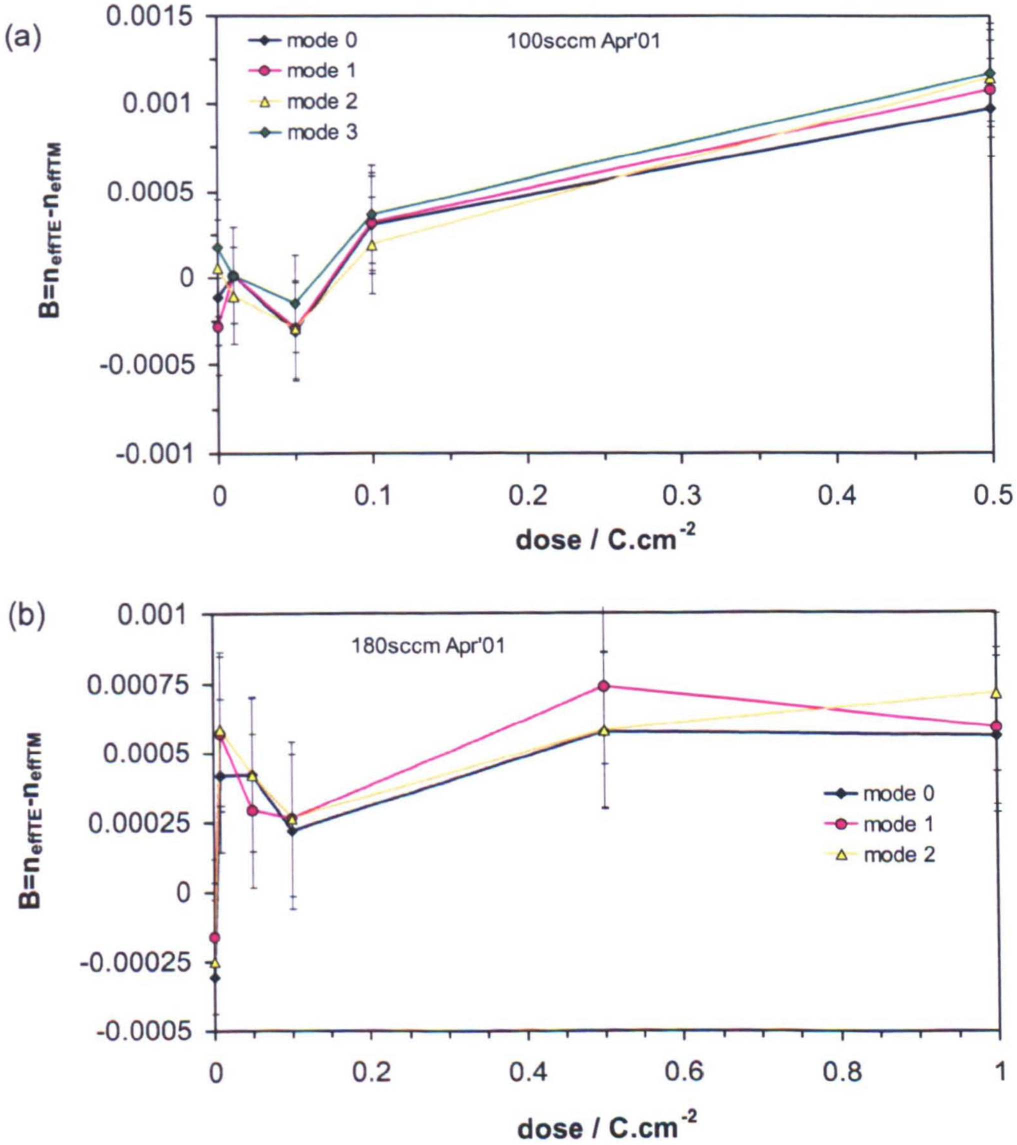

Figure 5.33. Evolution of the birefringence after irradiations as a function of dose: (a) for the 100 sccm Apr'01 (9.38 % wt. Ge); (b) 180 sccm Apr'01 (14.45 % wt. Ge) samples.

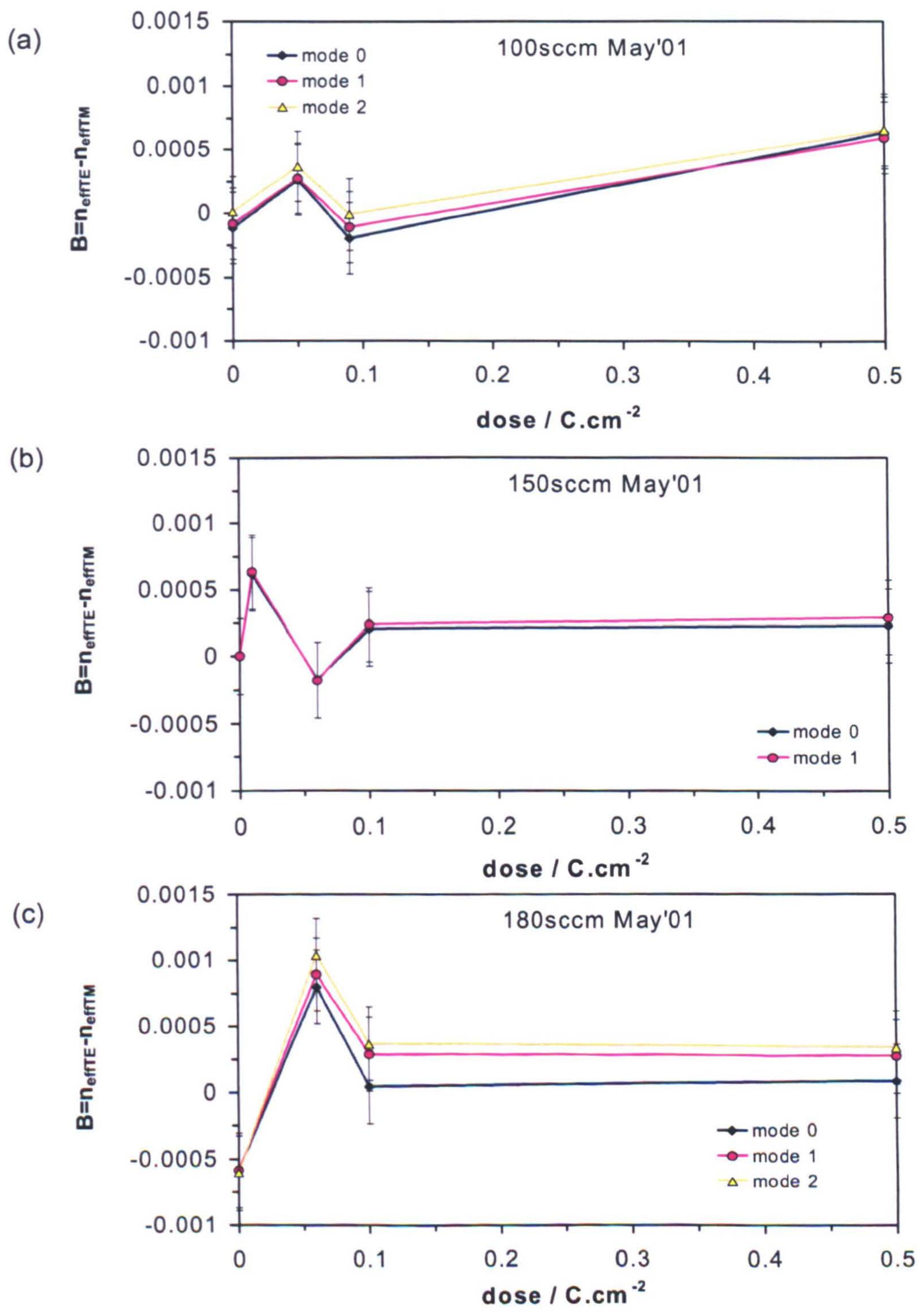

Figure 5.34. Evolution of the birefringence with irradiation dose: (a) 6.39 % wt. germanium; (b) 11.22 % wt. germanium; (c) 12.24 % wt. germanium samples from the May'01 series.

From the data measured in this work it was possible to deduce that there is a variation of the birefringence with dose. If well characterized, this phenomenon can

be useful, as optical devices with the desired birefringence characteristics could be designed and fabricated by selecting the appropriate irradiation dose [García-Blanco, 2002].

Another application could be the trimming of integrated optical circuits, as reported previously for UV-irradiation [Kashyap, 1993], in which a technique capable of producing a controlled change in birefringence is desired.

5.7 Stability of the changes induced by irradiation: isochronal annealing experiments.

From the results shown previously in Section 5.4, electron-beam irradiation produces changes in the structure of the flame-hydrolysis silica, which lead to an increase in the index of refraction. Therefore, electron irradiation can be a useful technique for direct-writing of integrated optical circuits, the characteristics of which will be addressed in the next chapter.

Nevertheless, it is important to study the thermal stability of the electron-beam induced changes in the silica, because it will determine the viability of this technique for the fabrication of optical circuits with applications in various different environments.

The stability of the refractive index change is studied next by means of isochronal (same time at different temperatures) annealing experiments.

Different studies have been published describing the analysis of the thermal-annealing of gratings written by UV-irradiation in silica fibers [Erdogan, 1994], [Razafimahatratra, 2000], [Kannan, 1996], [Baker, 1997]. Thermal annealing of the compaction produced by 193-nm excimer laser radiation has also been the subject of study [Piao, 1998]. Thermal decay of the effect of UV-irradiation on silica has been found to be dependent on the structure and composition of the irradiated material [Baker, 1997].

The mechanism of the refractive index change induced by electron-beam irradiation is not yet very well understood. As was discussed earlier in this chapter, the transfer of energy from the energetic electrons to the silica structure leads to structural rearrangements that produce densification, among other processes. Densification is believed to be the main contributor to the refractive index change in the case of large irradiated areas. The irradiated material is in a metastable state. Assuming that the relaxational process from the metastable state is thermally activated, it is possible to consider that it will be dominated by the limiting reaction of the process. Therefore, the annealing of the densification and refractive index change due to electron-beam irradiation could be characterized by a single activation energy [Razafimahatratra, 2000].

The decay of the effects of the electron-beam in the silica structure, i.e. densification and refractive index, could then be described by [Piao, 1998], [Syms, 1994b]

$$recovery = exp[-\nu(T)t] \tag{5.21}$$

where $\nu(T)$ is the rate constant, which depends on the temperature and t is the time. Assuming a thermally activated decay, $\nu(T)$ can be described as

$$\nu(T) = \nu_0 \, exp\left(-\frac{E_a}{K_B T}\right) \tag{5.22}$$

where E_a is the activation energy of the process, K_B is the Boltzmann constant, 8.63×10^{-5} eV·K^{-1}, and ν_0 is a constant.

It is necessary to note here that, due to the way in which the experiment was carried out, the same sample was subjected to successive temperature steps, i.e. when the sample was subjected to 30 min at 250 °C it had already been annealed for 30 min at 200 °C. Using a new sample for each annealing step was not practical due to the large preparation time required for each sample. It is possible, however, to make a correction to the data in order to take into account the previous thermal annealing steps, assuming that the annealing effects produced in the sample at a temperature T_1 during a time t_1 will be equivalent to an anneal at temperature T_2 during a time t_2. This procedure has been previously demonstrated to yield good approximated results [Razafimahatratra, 2000].

5.7.1 Thermal annealing experiments of the refractive index.

Gratings that were previously irradiated with doses 0.1 C·cm^{-2} and 0.5 C·cm^{-2} were subjected to high temperature annealing in a furnace in air. For the isochronal annealing experiments, the same sample was introduced for 30 min at temperatures ranging from 200 to 750 °C, varying the temperature at steps of 50 °C. After each annealing stage, m-line measurements of the effective refractive indices of the different modes were taken (as described in Chapter 3, Section 3.2.1) and the sample was again introduced into the furnace for 30 min at the next temperature.

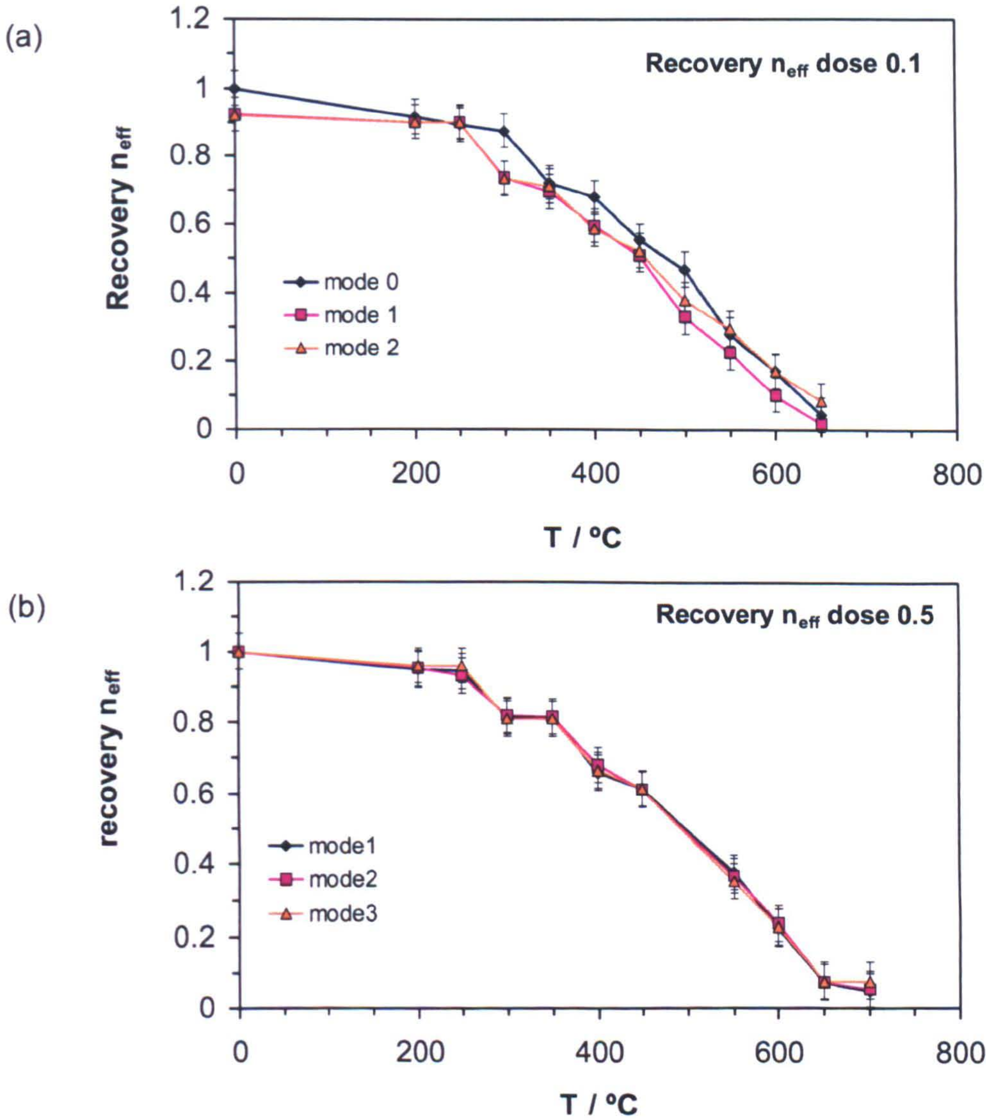

Figure 5.35. Isochronal annealing of the refractive index induced by irradiation: (a) dose 0.1 C·cm^{-2}; (b) dose 0.5 C·cm^{-2}.

In Figure 5.35, the isochronal annealing of two samples irradiated with two different electron doses is presented. It can be seen that the change in refractive index decreases very slowly with temperature for temperatures below 250 °C and is completely annealed at 700 °C. The germanium content of all the samples was ≈ 11 % wt.

The recovery of the refractive index due to annealing can be calculated as

$$re\,covery = \frac{n_{anneal} - n_{asdepos}}{n_{ebeam} - n_{asdepos}} \tag{5.23}$$

where the first term, n_{anneal}, is the refractive index of the material after the different annealing steps, $n_{asdepos}$ is the refractive index of the as-deposited material, n_{ebeam} is the refractive index of the material after irradiation. The recovery of the refractive index can be fitted as described in Equation 5.22. The results of this calculation are shown in Figure 5.36 for the recovery of the effective refractive index of the fundamental mode after 0.5 C·cm^{-2} of irradiation dose, shown previously in Figure 5.35 (b).

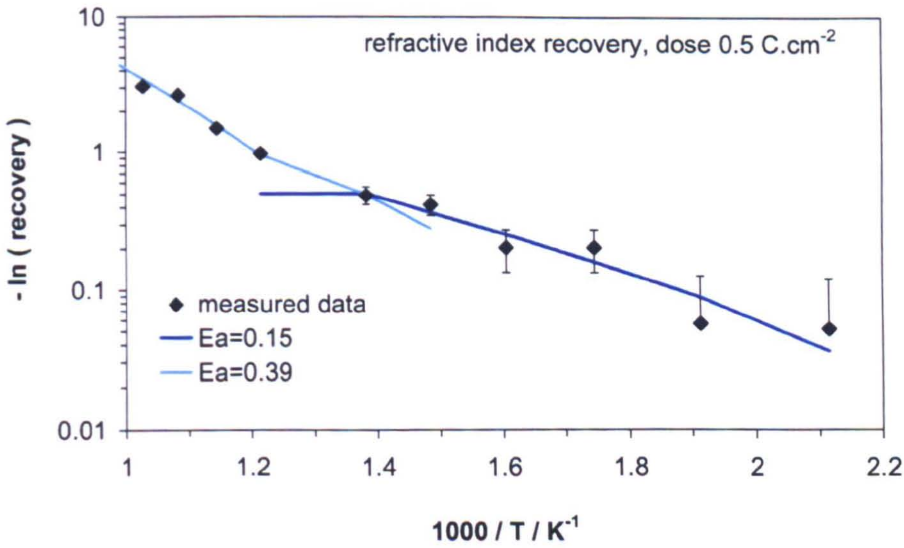

Figure 5.36. Isochronal anneal of refractive index induced by electron-beam irradiation: Recovery is calculated as $(n_{anneal}-n_{asdepos})/(n_{ebeam}-n_{asdepos})$ for an 11 % wt. sample irradiated with an electron dose of 0.5 C·cm^{-2}. An activation energy of ≈ 0.39 eV was obtained from the fit for T>800°C whilst for smaller T a value of 0.15 eV was found.

In Figure 5.36, the error bars were calculated considering the errors in the measurement of the effective refractive indices (2×10^{-4}). The fit line is not exactly a straight line as would be expected for an Arrhenius plot, because the time in Equation 5.21 is not a constant, but varies from point to point due to the correction carried out to take into account the effect of the previous temperatures. Two regions can be observed in Figure 5.36, the first one, for high temperatures, yielding an activation energy of 0.39 eV (and value of ν_0 of 9.1×10^{-4}, Equation 5.22). In the low temperature region, an activation energy of 0.15 eV (and ν_0 of 6.33×10^{-2}) was found to best fit the data. The presence of two activation energies implies the existence of

two mechanisms responsible for the change in refractive index. As it has been discussed previously (Section 5.6.2), the change in refractive index induced by electron-beam irradiation could be divided into two components, one of them, called "unconstrained densification" appearing as a consequence of the structural rearrangements induced by the electron-beam and the second one, called "elastic" contribution, being the result of the elastic reaction of the unexposed material. It could possible to consider that these two mechanisms responsible for the change in refractive index would anneal with different activation energies, being the smaller one the one corresponding to the "elastic" transformation. But in that case, for small temperatures, the anneal of the elastic components would produce a net expansion of the material not observed experimentally. The presence of a more highly damaged region near the surface has been demonstrated before (Sections 5.5.5.1 and 5.6.2). It could be considered that further structural modifications have been produced in that region, increasing the activation energy for annealing. Nevertheless further annealing experiments accompanied by structural analyses should be carried out in order to clarify the origin of the two different activation energies.

Despite the good fit to the data, this model does not predict, however, the behaviour of the irradiated sample with time at room temperature. Using the values obtained from the fit in Equation 5.21, after one year at room temperature, the refractive index change would completely anneal. This was not what was observed experimentally. Along the development of this work, the same electron-beam irradiated samples were measured several times. The time between measurements was sometimes several months. The measured refractive index of the irradiated samples lay always within the experimental error of the measurements. This result could be indicative of a threshold energy for the annealing of the electron-beam induced damage. Further isothermal annealing experiments could be carried out and the methodology proposed by Erdogan *et al.* [Erdogan, 1994] could be applied in order to obtain more information concerning the aging of the refractive index change produced by electron-beam irradiation of FHD silica.

The previously described model is useful to obtain information on the activation energy involved in the annealing process. This activation energy can be compared with the activation energies obtained after applying the same model to the recovery of the densification induced after irradiation for a sample of similar composition, as

will be shown in the following subsection, in order to gain some insight into the similarity of both processes.

5.7.2 Thermal recovery of the electron-beam induced densification.

The same kind of isochronal annealing experiments as described in Section 5.7.1 were performed here on an 11 % wt. germanium content sample in which densification patterns 40 μm wide were written by irradiation with different electron-beam doses. By analyzing the data assuming that the recovery of the densification is thermally activated and follows Equation 5.21, the following fits were obtained (Figures 5.36 to 5.37).

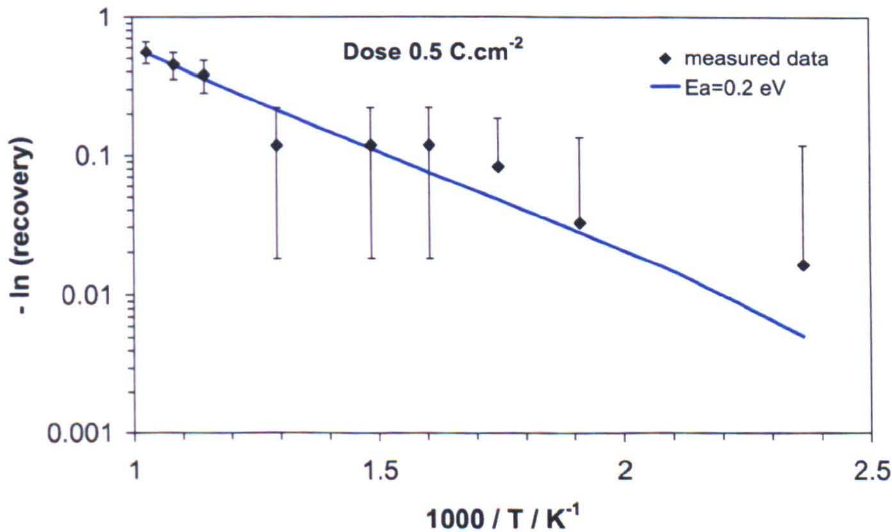

Figure 5.37. Recovery of the densification after 0.5 C·cm^{-2} electron-beam irradiation, at 50 KeV in a FHD sample with 11 % wt. germanium concentration submitted to isochronal anneal.

The measurement of the densification was carried out by characterizing the surface profile after irradiation with a Talystep profilometer after each annealing period. The depth of the depression was observed to decrease until its disappearance for T > 700°C. The value “recovery”, plotted in Figures 5.37-5.39, was calculated as

$$recovery = (depth\ after\ anneal)/(depth\ after\ irradiation) \qquad (5.23)$$

In Figure 5.37, the experimental data can be fitted with Equation 5.21, obtaining an activation energy of 0.2 eV (ν_0 of 5.79x10^{-4}). In Figure 5.38 it can be seen that, as the dose increases, two temperature regions, with different activation energies, occur. The same explanation given in the previous section (Section 5.7.1) for the annealing of the refractive index could be used here.

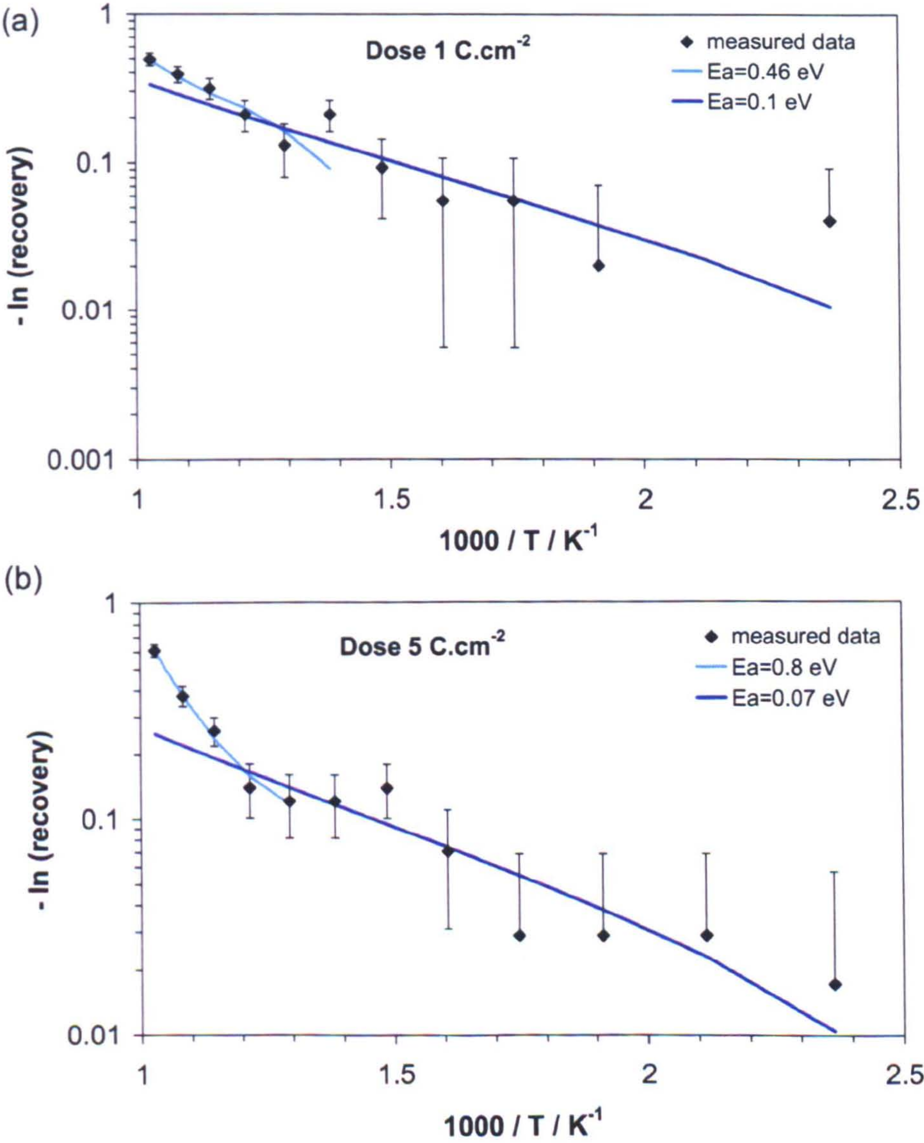

Figure 5.38. Isochronal annealing experiments for samples densified after doses of 1 and 5 C·cm^{-2}.

The values of activation energies obtained for the recovery of the densification (Figure 5.38) are comparable to the ones obtained for the recovery of the refractive index (Figure 5.36), taking into account the large errors associated with the

experimental method. This suggests once more that densification and change in refractive index are related and confirms the hypothesis that the densification is the principal contributor to the change in refractive index.

Furthermore, from these annealing experiments it is possible to see that the effects produced by the electron-beam in the silica structure and that make possible the fabrication of optical waveguides, will disappear if the samples are submitted to high temperatures. Therefore, it has been demonstrated that the depressions observed on the surface are due to densification and not to loss of matter.

The annealing of the irradiation effects at high temperatures limits the kind of processes that the samples can be subjected to after the formation of the waveguides. Measurements of the same sample taken during a time-period larger than one year suggest a very good stability of the refractive index at room temperature. Nevertheless, further experiments need to be carried out in order to fully understand the aging process of the direct electron-beam written waveguides.

5.8 Conclusions.

The effects of electron-beam irradiation of $Ge:SiO_2$ FHD silica were studied in this chapter.

A reorganization of the structure upon irradiation was obtained. Breakage of Si-Ge bonds, formation of low-order membered rings (3- and 4-fold order rings) in the silica structure and reduction of the bridging-oxygen inter-tetrahedral angle and of the Ge-O bond angle were experimentally observed. The main effect derived from the previous structural rearrangements was densification, accompanied probably by formation of colour centres and polarizability change.

The densification depth profile was characterized. Electron-beam irradiation of FHD silica produced a highly densified outer region, confirmed by X-ray reflectivity measurements. The origin to that region was thought to be the germanium-depleted lower-density, probably not completely consolidated, outer layer observed in the initial FHD material, which was likely to vary its density easier than the bulk material.

The change in density was found to decrease with germanium content, as opposed to UV-irradiated silica. The change in refractive index was found to be independent of the germanium content, due to the opposite effects of the increased refractive index of the original material as the germanium concentration increases and the reduced amount of relative density change obtained. Saturation of the refractive index change began at a dose of $\approx 0.2\ C{\cdot}cm^{-2}$, being the value of the maximum refractive index change obtained $\approx 7\times10^{-3}$.

The relative change in volume was considered to have two components: a "permanent" component resulting from the structural rearrangements suffered by the silica structure due to irradiation, and an "elastic" one appearing as a reaction of the material to the "permanent" component. Each component of the relative change in volume contributes to the relative refractive index change: the "permanent" component through the Lorentz-Lorenz equations, in which the effects of the possible density-induced polarizability change in the material are considered, and the "elastic" component through the strain-optical equations. The refractive index profile calculated from the densification profile fitted the profile obtained from optical

measurements if a density-induced polarizability factor, varying with the irradiation dose, was chosen.

Isochronal-annealing of the change in density and refractive index showed two regions with two different activation energies, indicating the presence of two mechanisms of damage, one of them probably related to the more highly densified surface region. The activation energy corresponding to the "bulk" of the damaged region, 0.1 eV, stays approximately constant with the dose, whilst the component associated to the further structural modification induced in the outer region increases with dose. The patterns written completely disappear after been subjected to 700ºC, thus limiting the range of applications of he optical waveguides written with this technique. A large stability at room temperature was found for the electron-beam written waveguides (the refractive index stayed unaltered for more than one year).

Chapter 6

Fabrication of integrated optical devices with electron-beam direct writing of germanium-doped flame-hydrolysis silica

Chapter summary.

Electron-beam irradiation of $Ge:SiO_2$ FHD layers was demonstrated in the previous chapters as a useful technique for the fabrication of optical waveguide circuits. The interaction of the electron-beam with the silica structure and the effects induced in it leading to an increase of refractive index were discussed. The properties of the optical devices fabricated with this technique also need to be addressed, in order to know its possibilities and limitations. The propagation in multimode waveguides, monomode waveguides and Y-junctions was characterized in this chapter and compared with the expected simulated values.

6.1 Introduction.

In this Chapter, the use of direct electron-beam writing for the fabrication of different devices in germanium-doped FHD silica is described. Firstly, multimode waveguides were demonstrated. The losses in monomode waveguides were characterized at a wavelength of 1.55 μm and were found to be typically as low as 0.3 $dB \cdot cm^{-1}$. The validity of this technique for the fabrication of optical sensors was demonstrated by the fabrication and characterization of an asymmetric optical Y-branch, basis of a simple optical sensor.

6.2 Fabrication of multimode waveguides.

Multimode waveguide are useful devices in certain applications, such as when large amount of light needs to be carried. In this Section, a simple multimode waveguide has been fabricated and demonstrated as the most simple example of optical device.

6.2.1 Fabrication method.

Waveguides 6 μm deep and 10 μm wide were written with a 50 keV electron-beam, as described in Chapter 5, Section 5.2.3 on a 7 % wt. germanium concentration FHD silica layer 6 μm thick (deposited as described in Chapter 4, Section 4.2) on top of 15 μm thick thermal oxide. The length of the waveguide was 1 cm (the size of the sample was 1 cm^2). The ends of the sample were polished to optical finishing in order to being able to couple light into the channel waveguide structure.

6.2.2 Characterization of the multimode waveguides.

Light from a He-Ne laser at 632.8 nm of wavelength was end-fired into the waveguide and the light was observed to propagate through the structure, thus demonstrating its functioning. Figure 6.1 shows an optical micrograph of the cross-section of the structure, as light is passed through it.

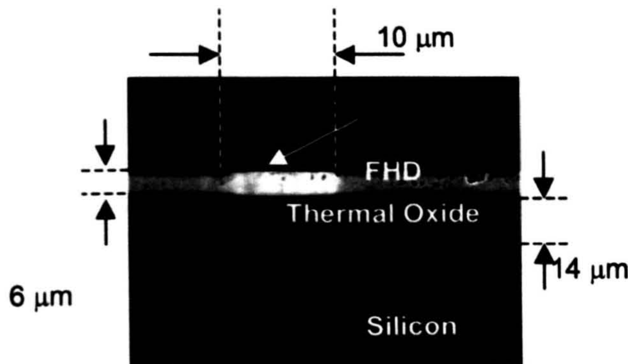

Figure 6.1. Optical micrograph of the electron beam written waveguide cross-section: It is possible to see the irradiated area, which forms a multimode waveguide, leading to the bright region.

6.3 Fabrication of monomode waveguides: characterization of the propagation losses.

Monomode waveguides are necessary for many applications, such as the fabrication of Y-branches and more complex integrated optical circuits. It is therefore interesting to prove the capability of this fabrication technique to produce monomode waveguides.

6.3.1 Fabrication of the waveguides.

FHD silica layers 2.5 μm thick and different germanium contents (from 7 to 15 % wt. Ge) were deposited on top of silicon substrates (Chapter 4, Section 4.2) on which a layer 15 μm thick of thermal oxide had previously been grown. Waveguides 3 μm wide were then written using different doses (ranging from 0.01 to 0.5 C $\cdot cm^{-2}$) of 50 keV electrons, as described in Chapter 5, Section 5.2.3. The Sellmeier equation for fused silica [Gowar, 1983] was used in order to convert the known refractive index values at a wavelength of 632.8 nm to the refractive indices at 1.55 μm wavelength. From theoretical calculations, the waveguides fabricated with these parameters were expected to be monomode at 1.55 μm wavelength (Chapter 3, Section 3.3.1.3). No upper-cladding layer was used for these structures.

In order to compare the losses of the waveguides fabricated by electron-beam direct-writing with the losses of waveguides fabricated by the conventional photolithography and dry-etch technique, some waveguides of the same dimensions than the ones fabricated by irradiation with an electron-beam were fabricated. The same substrates than for the electron-beam written waveguides were used. Waveguides 3 μm wide were then patterned by photolithography, using 75 nm of evaporated nichrome and photoresist Shipley S1818 as a mask for dry-etch. Dry-etch of the FHD material in a BP80 dry-etch machine was then performed using CHF_3 as the active gas until the correct depth was reached (the thickness of the FHD layers was 2.5 μm).

6.3.2 Characterization of the monomode waveguides: study of the propagation loss.

In order to investigate the suitability of this technique for the fabrication of optical waveguides, a study of the propagation losses was carried out. The main possible contributors to the propagation losses at 1.55 μm wavelength in the waveguides fabricated by electron-beam irradiation of germanium doped FHD silica (see discussion in Chapter 3, Section 3.5) were considered to be: surface imperfections, which produce scattering of the light out of the waveguide; absorption due to the presence of O-H and Si-H groups in the structure of the glass; and absorption due to the proximity of the substrate [Syms, 1994a], [Syms, 1994b], [Madden, 1990], [Barbier, 1991]. This last contribution, losses by coupling of light to the substrate, could be neglected in the particular case considered in this work, as the lower-SiO_2-cladding thickness, 15 μm, was enough to make the evanescent field of the light propagating in the waveguide negligible at the silicon substrate. Furthermore, it is important to realize that the losses depend on the dimensions of the waveguide, as these determine the confinement of the field inside it. In the case of FHD glass, absorption due to O-H and H groups is substantially eliminated due to the high temperatures produced during the sintering process and the losses are reported in the literature as being as low as < 0.1 dB·cm^{-1} [Kominato, 1990]. However, the buried waveguides formed by this technique were very close to the surface, making the effect of the surface roughness more critical.

Measurements of the losses in waveguides fabricated by electron-beam irradiation of different types of silica have been reported previously. Barbier *et al.* [Barbier, 1991] characterized the losses of their slab waveguides by measuring the light scattered from the waveguide using a traveling microscope with a photodiode placed at the eyepiece. They measured a minimum propagation loss at 632.8 nm wavelength of 0.3 ±0.1 dB·cm^{-1} for a slab waveguide of thickness 7.5 μm. Syms *et al.* [Syms, 1994b] used the cutback method in which the propagating losses are separated from the coupling losses by cutting the waveguides to different lengths and measuring the transmitted power versus the incident power in each waveguide. They obtained losses as small as 0.12 dB·cm^{-1} for a 7 x 7 μm^2 cross-section waveguide in 32 μm thick PECVD silica material provided by BNR Ltd.

In this work, losses measurements were carried out in directly electron-beam written monomode waveguides at 1.55 μm wavelength by using the modified Fabry-Perot technique described in Chapter 3, section 3.5. The Fabry-Perot fringes measured for the transmitted and reflected powers are shown, as an example, in Figure 6.2. The results of these measurements are shown in Table 6.1.

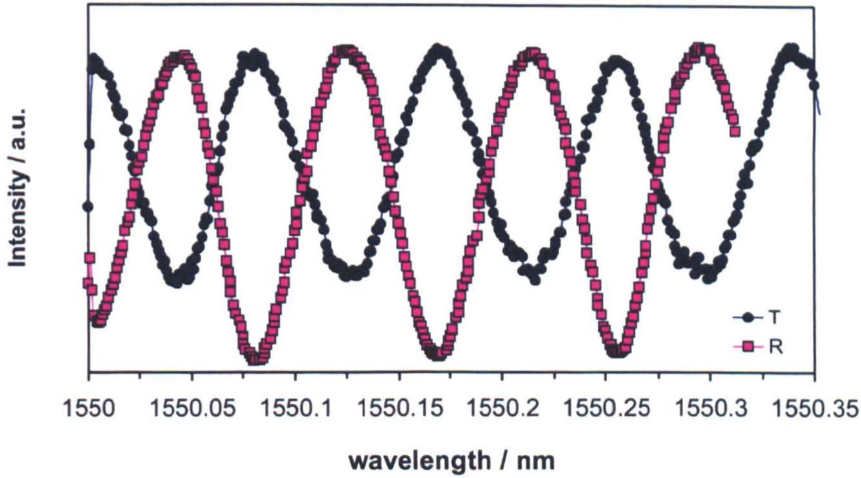

Figure 6.2. Example of Fabry-Perot losses measurements: Transmitted and reflected intensities from a waveguide written on 15 % wt. Ge content FHD sample with an electron-dose of 0.1 $C \cdot cm^{-1}$ and energy 50 keV. Measurement performed for the TE-polarization.

Losses as low as 0.2 ± 0.04 $dB \cdot cm^{-1}$ were measured. Nevertheless, a substantial scatter in the values measured could be observed. There is not a clear correlation between electron-dose and composition, contrary to what was found by Barbier *et al.* [Barbier, 1991], thus suggesting that the factor dominant in the magnitude of the losses was not the composition of the film or the writing parameters, but the local characteristics of the deposited material. Table 6.2 shows the measured losses for waveguides fabricated in a 7 % wt. Ge content FHD layer by using conventional photolithography, followed by dry-etch. The dimensions of the waveguides were designed to be similar to those of the waveguides fabricated by electron-beam writing, so that the measured losses could be compared.

In Table 6.2 it can be observed that the losses measured for the dry-etch waveguides fabricated as described in Section 6.3.1 are similar to the ones obtained for electron-beam direct-written waveguides (Table 6.1).

Composition	Dose / $C.cm^{-2}$	Waveguide	Propagation loss / $dB.cm^{-1}$
7 wt% Ge	0.01	1	0.30 ± 0.03
		2	0.14 ± 0.03
		3	0.66 ± 0.06
		4	0.31 ± 0.02
	0.05	1	1.44 ± 0.03
		2	2.17 ± 0.02
		3	2.99 ± 0.02
		4	0.95 ± 0.03
	0.1	1	0.27 ± 0.04
		2	0.27 ± 0.04
		3	1.22 ± 0.03
		4	0.74 ± 0.03
		5	0.26 ± 0.02
10 wt% Ge	0.01	1	1.52 ± 0.05
		2	0.76 ± 0.02
		3	0.33 ± 0.03
		4	0.57 ± 0.01
	0.05	1	1.78 ± 0.02
		2	1.78 ± 0.02
		3	1.5 ± 0.01
		4	0.003 ± 0.04
	0.1	1	1.85 ± 0.01
		2	2.01 ± 0.02
		3	1.18 ± 0.02
		4	1.17 ± 0.01
		5	1.14 ± 0.03
	0.5	1	1.07 ± 0.01
		2	1.79 ± 0.01
15 wt% Ge	0.05	1	0.46 ± 0.01
	0.075	1	0.58 ± 0.01
		2	0.2 ± 0.005
		3	0.2 ± 0.007
	0.1	1	0.22 ± 0.02
		2	0.07 ± 0.01
	0.5	1	1.27 ± 0.01
		2	1.69 ± 0.02

Table 6.1 Losses measured for directly electron-beam written waveguides fabricated by using different electron-dose in samples with different composition.

Sample	Waveguide	Losses / $dB.cm^{-1}$
Sample 1	1	0.49 ± 0.01
Sample 2	1	0.35 ± 0.035
	2	0.45 ± 0.02
Sample 3	1	1.04 ± 0.02
	2	0.38 ± 0.01
	3	0.64 ± 0.02
	4	0.39 ± 0.01

Table 6.2. Losses measured for waveguides fabricated on a 7 wt% Ge FHD silica layer by photolithography followed by dry-etch in a BP80 dry-etch machine using CHF_3 as the active gas.

It is possible to conclude that, probably, the main contribution to the losses in the case of electron-beam written waveguides in the material used in this work was the propagation characteristics of the initial material, dominating over the possible absorption introduced by the electron-beam irradiation process.

6.4 Fabrication of Y-branches.

Y-branches are a basic element in the fabrication of integrated optical circuits such as Mach-Zehnder interferometers, beam splitters and arrayed-waveguide gratings. Y-branches have also found utility in the design of optical-biosensors, in which, thanks to the functionality of the Y-branches, light can be split into different analysis chambers where different analytes could be characterized [Ruano, 2003].

The fabrication technology used in order to fabricated optical sensors in FHD silica glass consisted of a combination of photolithography and dry-etching in order to pattern the waveguides and dry-etching in order to define the microfluidics system [Ruano, 2003]. The system was sealed with a layer of PDMS (poly(dimethylsiloxane)). The drawbacks of this fabrication method were mainly that after the fabrication of the waveguide core by dry-etch a FHD silica cladding needed to be deposited. The cladding was subsequently dry-etched in order to define the microfluidics channels and chamber.

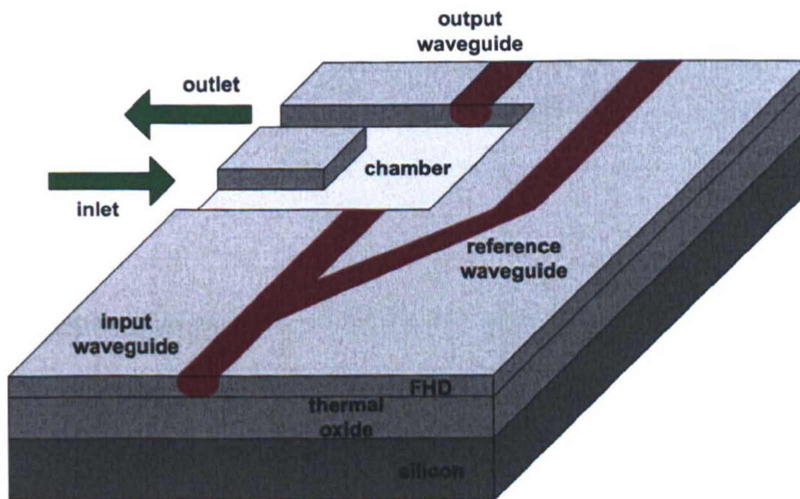

Figure 6.3. Example of optical sensor realized with electron-beam direct-written waveguides: After the waveguide is fabricated, a single dry-etch step is needed to perform the microfluidics to bring the analyte in and out the analysis chamber. The device will be sealed with a PDMS layer that will act as the cladding ($n \approx 1.43$ at 632.8 nm of wavelength).

Electron-beam direct-writing of the optical circuits considerably reduces the fabrication steps in this application, since, after the waveguide is formed, only a dry-etch step is required in order to form the microfluidics system, as described in

Figure 6.3. A PDMS layer will act as both cladding (n ≈ 1.43 at 632.8 nm) and sealing of the microfluidics system.

In the present work, the asymmetric Y-branches for the realization of optical bio-sensors have been studied. In these devices, a straight branch was required to guide the light from the input to the analysis chamber. The second branch, which should carry less power, was used as a reference for the power conducted to the analysis chamber [Ruano, 2000].

6.4.1 Preparation of the samples.

A Y-branch as the one shown in Figure 6.3 was written into a 7 % wt. germanium FHD silica layer by using 50 keV electrons with a dose of 0.1 $C \cdot cm^{-2}$. These conditions were expected to produce a change of the effective refractive index of 5×10^{-3}. The refractive index of the as-deposited material was 1.4679 and the refractive index for the thermal oxide was 1.4582. The layer was 2.4 μm thick and the width of the waveguides was 2 μm. Those conditions were supposed to lead to monomode waveguides at the analysis wavelength (632.8 nm), necessary for the correct functioning of the Y-branch. However, it is necessary to note here that previous studies in UV-written waveguides have suggested the formation of waveguides wider than the writing-spot. Further studies need to be carried out in order to verify whether the same effect occurs in electron-beam irradiated waveguides.

6.4.2 Beam propagation method (BPM) simulation of the Y-branch.

Figure 6.4 (a) shows the simulated propagation of 633 nm laser light in the structure, calculated with beam-propagation method (BPM) software. In (b) the modal electric field strength in each branch is shown at the output of the device. Two different Y-branches were designed with different splitting ratio, in order to verify the consistence of the simulations with the measured data. To that aim, two different separation of the output waveguide were used: 58.25 and 65 μm. The simulated percentage of light expected in each output waveguide is indicated in Table 6.3. It can be observed that the measurements agree with the calculations within the experimental errors.

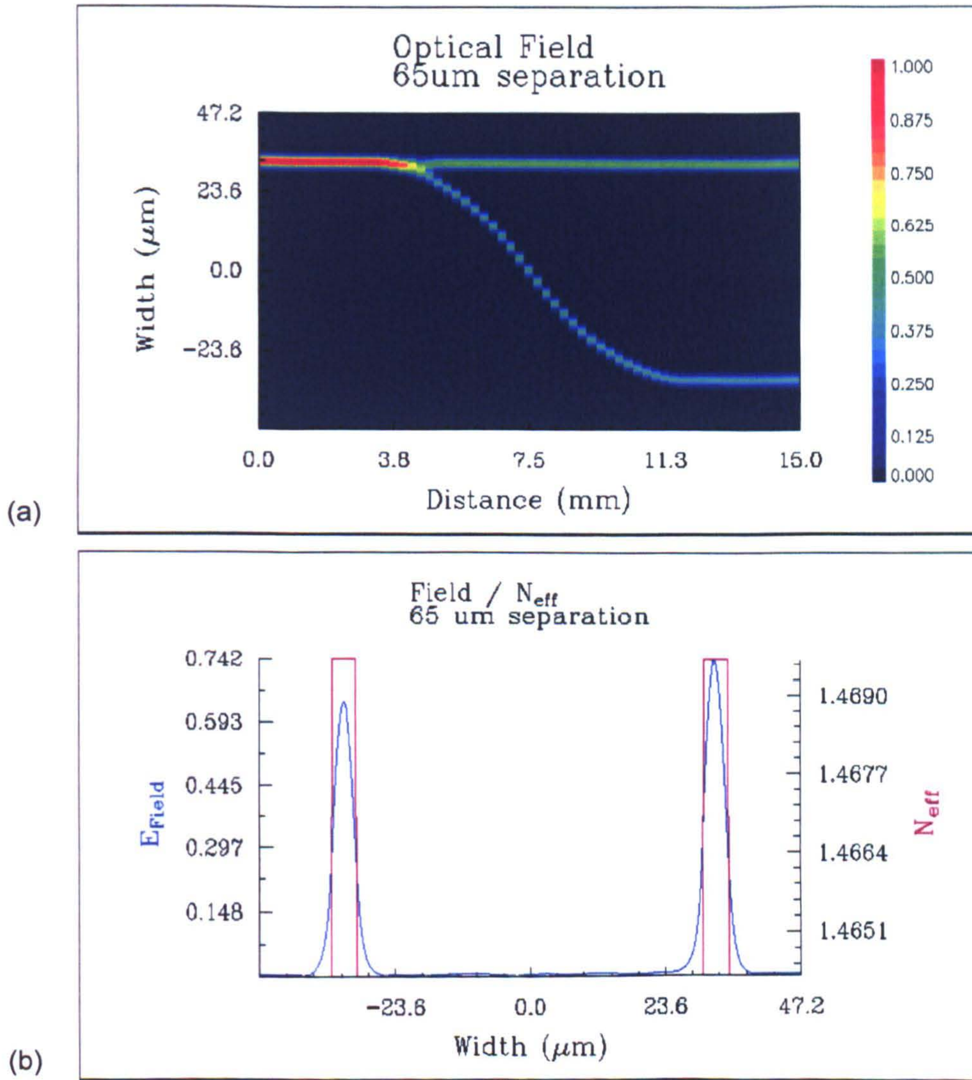

Figure 6.4. BPM simulations of an asymmetric Y-junction: (a) Field propagation image of 632.8 nm wavelength light in the Y-branch structure, calculated using the BPM software; (b) Splitting of the output electric field between the two branches of the Y-branch.

It is necessary to notice that, in the design of the Y-branches, the branching angle determines the amount of losses produced in the split. In order to illustrate this effect, several Y-branches have been simulated in which the same final separation between the output waveguides, 65 μm, was kept in all the cases but reached after different distances in the propagation direction, 2, 3, 5 and 6 mm (Figure 6.5).

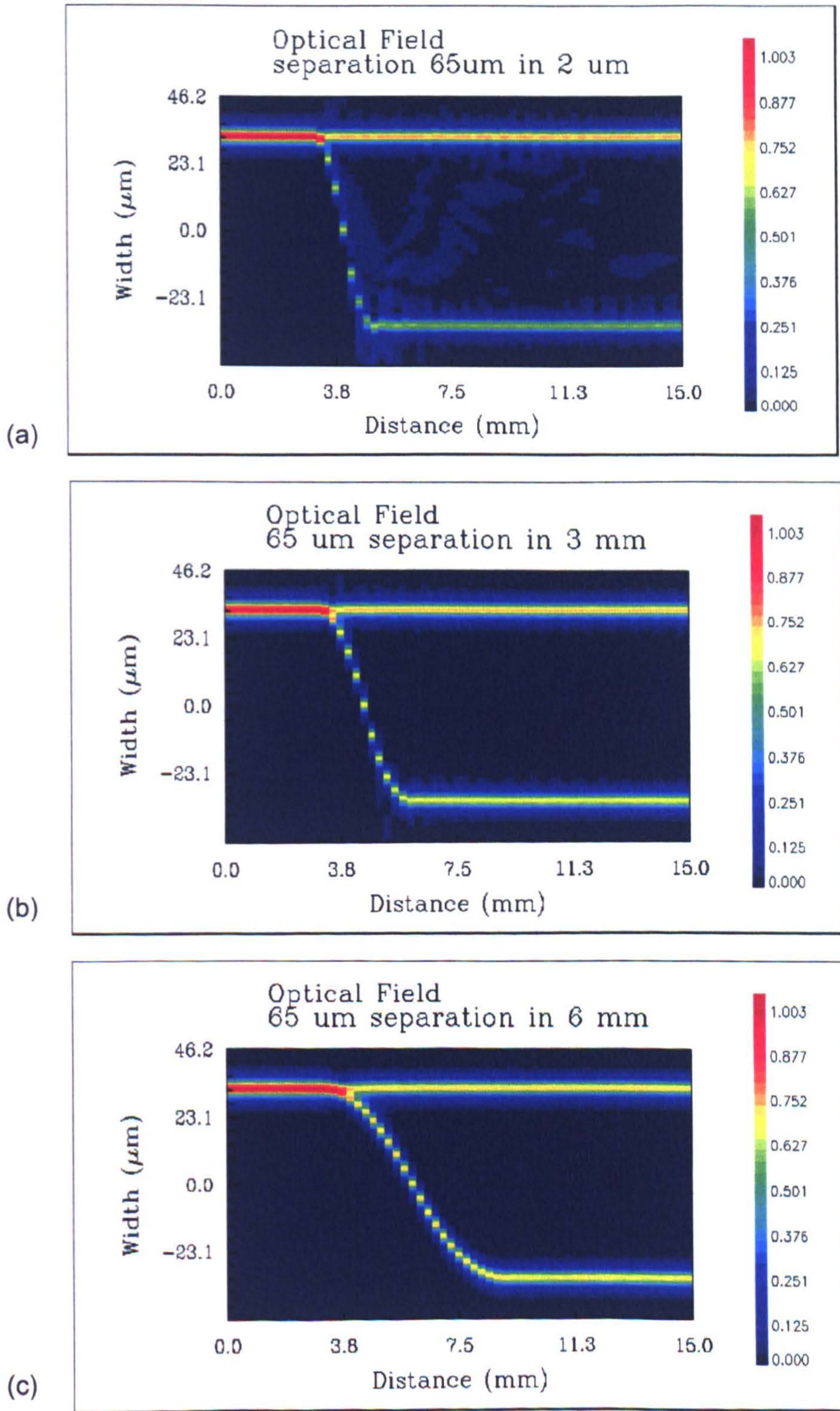

Figure 6.5. Effect of the branching angle in the losses in the Y-junction: (a) 65 μm separation in a distance of 2 mm; (b) 65 μm separation in 3 mm; (c) 65 μm separation in 6 mm.

6.4.3 Experimental characterization of the Y-branches.

The Y-branches were characterized experimentally with the following simple optical setup:

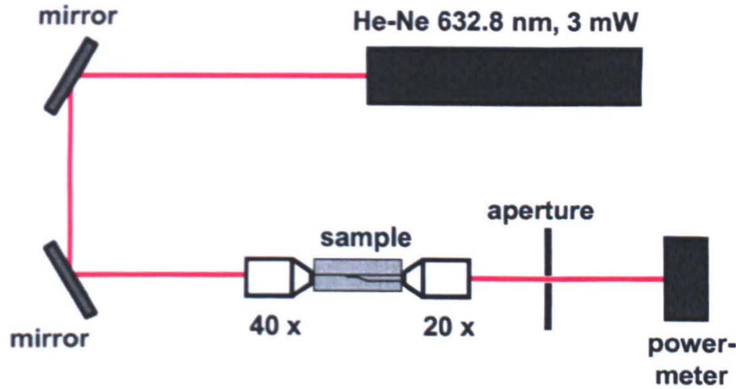

Figure 6.6. Experimental optical setup used to characterize the Y-branches.

The power measured in front of the 40x lens was 2.7 mW. The aperture was aligned so as to measure only the power in each branch of the junction structure. In Table 6.3, the percentage of the power in each branch measured is compared with the results of the BPM simulations. The errors shown in the experimental values were calculated by averaging all the measurements taken for each branch and calculating the maximum deviation from the individual values and from these measurement errors the error for the percentage of power in each branch was calculated.

Separation between output branches (μm)	Power in the output of straight waveguide (%) $(100xP_s/(P_s+P_w))$		Power in the output of the branch waveguide (%) $(100xP_w/(P_s+P_w))$	
	calculated	measured	calculated	measured
58.25	53	56 ± 3.4	47	44 ± 3.4
65	54	61.0 ± 7.3	46	39.0 ± 7.3

Table 6.3. Comparison of the calculated power splitting ratio at the output of the Y-branches using BPM calculations and measured values. Two different output separations of the branches were used.

It can be seen that the Y-branches fabricated using this technique worked according to the expectations. Therefore, it is possible to conclude that this technique is suitable for the fabrication of optical bio-sensors, presenting advantages over other fabrication methods.

6.5 Conclusions.

Multimode and monomode waveguides have been fabricated by electron-beam direct-writing. The losses of the waveguides fabricated with this technique are comparables to the losses fabricated by the more conventional photolithography and dry-etching technique, suggesting that the factor limiting the losses are the losses of the as-deposited material. Losses as low as 0.3 $dB \cdot cm^{-1}$, in average, have been found.

Y-branches fabricated with this technique presented propagation characteristics consistent with BPM simulations, thus confirming the validity of electron-direct-writing for the fabrication of optical waveguide based devices. A possible application suggested in this work was the fabrication of optical biosensors.

Chapter 7

Another irradiation technique to fabricate optical waveguide on Ge:SiO_2 FHD: Ion implantation with 2 MeV Ar^+ ions.

Chapter summary.

Ion irradiation with 2 MeV Ar^+ ions was demonstrated in this chapter to produce a high enough refractive index change, 1.2×10^{-2}, to produce optical waveguides, placed from the surface of the material up to a depth of ≈ 2 μm. The refractive index change after different irradiation doses and its relation with the induced density change was studied. A good correlation between the two effects, refractive index and density, was found if the value of the density-induced polarizability change was considered to vary with the irradiation dose. The recovery of the refractive index change was studied by means of annealing experiments. The same activation energy as for the recovery of the refractive index change induced by electron-beam irradiation was found, implying similarities between both irradiation techniques.

7.1 Introduction.

Ion implantation of silica has been reported previously as a technique for the fabrication of optical waveguides [Townsend, 1994]. A number of different ions have been used in order to fabricate waveguides: silicon [Johnson, 1998], argon, nitrogen [Battaglin, 1999], krypton, xenon [Arnold,2000], [Snoeks, 1994], neon, erbium [Snoeks, 1995], hydrogen [Bindner, 2001], [von Bibra, 2000], [von Bibra, 1998], helium [Boudrioua, 2001]. By contrast to what happens in crystalline materials [Wang, 2000], [Boudrioua, 2001], [Bindner, 2001], ion implantation in bulk silica typically produces an increase in refractive index in the resulting damaged area.

In this work, the change in refractive index of Ge:SiO_2 FHD layers after irradiation with 2 MeV argon ions was investigated [García-Blanco, 2003]. Optical measurements of the modes supported by the structure, before and after ion implantation, were carried out by a grating coupler technique, which has been previously described in Chapter 3. A waveguide structure in the surface of the silica layer, not present in the as-deposited structure, appeared after irradiation. Fitting to a step-index distribution was carried out, which yielded an "equivalent" uniform

value for the refractive index across an effective thickness of the formed waveguide as if the different regions presented sharp interfaces.

Step-height measurements of the depression on the surface obtained after irradiation through a > 3 μm thick gold mask, with different irradiation doses, were also carried out in order to see the evolution of the relative change in density with dose and its relation with the change in refractive index. To that aim, the refractive index expected from the measured densification was calculated. The results found were essentially the same than the ones found previously in this work for electron-beam irradiation of FHD silica. Furthermore, annealing experiments of the ion-implanted waveguides shows that the same kind of processes responsible for the change in refractive index after electron-irradiation must be present for the case of irradiation with argon ions.

7.2 Preparation of the samples.

Layers of germanium-doped FHD silica, ≈10 μm thick and 7 % wt. germanium concentration, were deposited directly on top of a polished silicon wafer (as described in Chapter 4, Section 4.2 and Chapter 2, Section 2.2.2).

For the optical characterization, gratings were etched on the surface of the samples (as explained in Chapter 3, Section 3.2.3) in order to apply the m-line technique (Chapter 3, Section 3.2) for the characterization of the refractive index. Optical measurements were carried out before and after irradiation with the ion-beam. A different sample was used for each ion-dose. All the samples belonged to the same batch.

For the step-height measurements sample from the same batch were used. Patterns 1 mm^2 were transferred into a thin Ti/Au (titanium/gold) layer, 10 nm / 30 nm, evaporated on to of the samples, by photolithography followed by wet etch of the gold and titanium layer. A gold layer, 3.5 μm thick, was then electroplated on top of the FHD silica layers with the thin metal layer on them. The thickness of the gold mask was enough to protect the Ar^+ ions to arrive to the FHD silica in the regions that were not to be irradiated, based on Monte-Carlo TRIM simulations. The gold mask was removed, after irradiation, by wet etch. The step-height produced by the irradiation was measured by a Talystep profilometer.

For the X-ray reflectivity measurements, Ge:SiO_2 FHD layers were deposited, using the same parameters than in the samples used for the other experiments, on top of 5 mm thick polished silicon wafers.

The irradiations were performed at the IBM Almaden Research Center by Dr. Andrew Kellock and Dr. John E.E. Baglin. The instrument used for the irradiations was an NEC Pelletron-particle accelerator, which can accelerate argon ions to energies of up to 3 MeV. The ion-beam is focused and directed toward the target chamber by means of a system of magnets, quadrupoles, and collimators through an evacuated line. Ar^+ ions at 2 MeV energy and doses ranging from 1×10^{12} to 1×10^{17} ions·cm^{-2} were used in the experiments.

7.3 Deposition of energy into the FHD silica after Ar^+ implantation.

The software SRIM/TRIM (The Stopping and Range of Ions in Matter) was used in order to simulate the deposition of energy by nuclear collisions and ionization events for 2 MeV Ar^+ ions in germanium-doped FHD silica. The results from the SRIM software are given in eV·Å^{-1}·ion^{-1} and they need to be multiplied by the dose (ions·cm^{-2}) and integrated over each depth step in order to obtain values in eV·cm^{-2}.

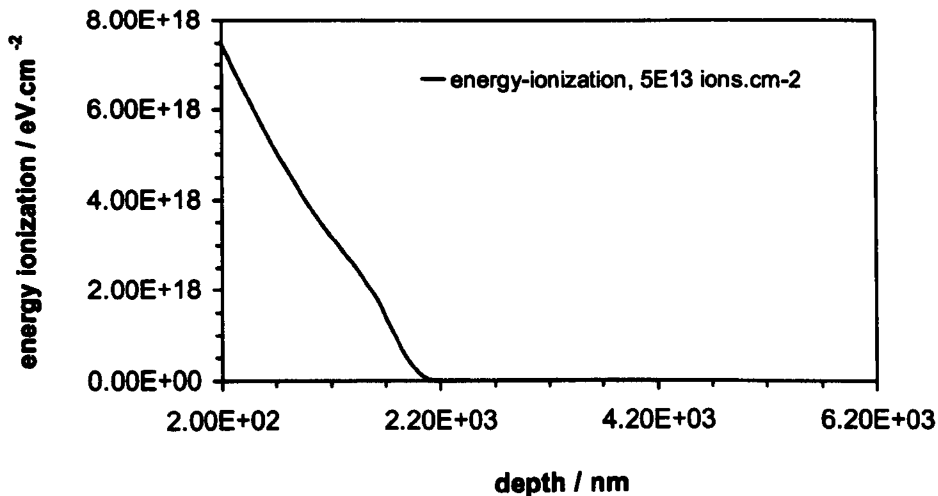

Figure 7.1. TRIM calculation of the energy deposited as a function of depth by ionization into the FHD silica structure: irradiation performed with 2 MeV Ar^+ ions with dose 5×10^{13} ions·cm^{-2} by ionization events.

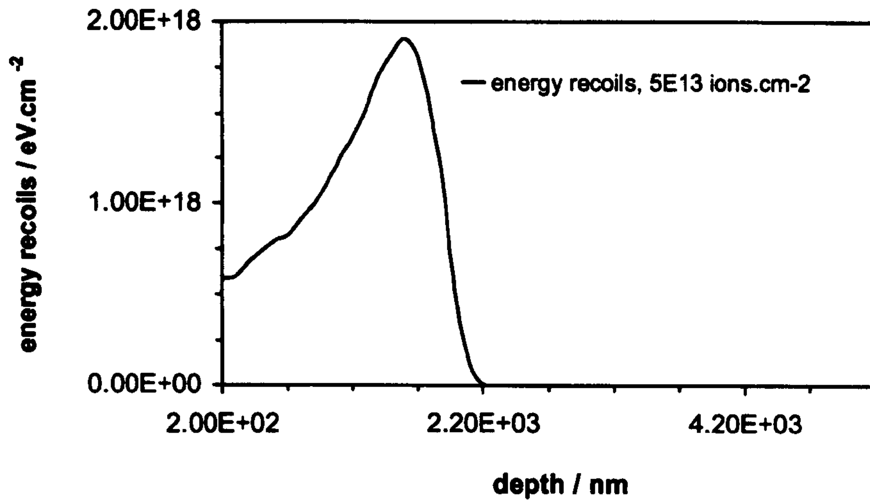

Figure 7.2. Energy transferred to the FHD silica structure by collisions: Calculated using the software TRIM for a 2 MeV Ar^{+} irradiation with dose 5×10^{13} ions·cm^{-2}.

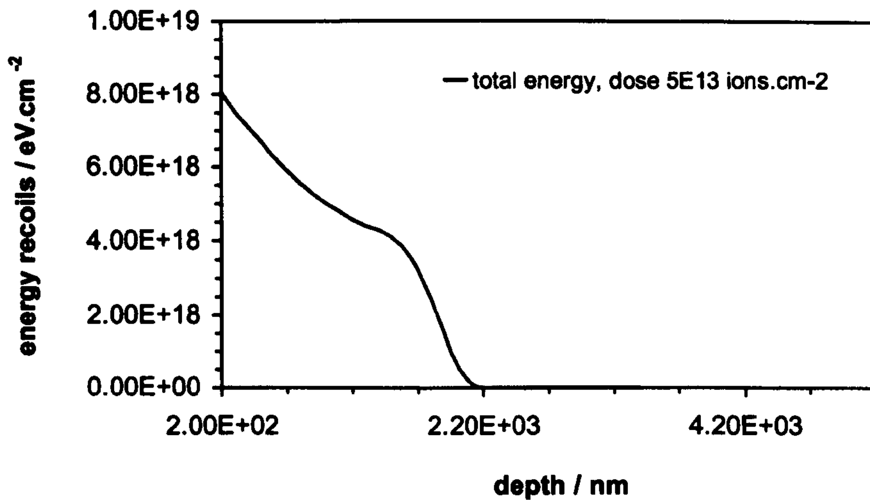

Figure 7.3. Total energy deposited into the silica structure, ionization plus recoils, as a function of depth.

The results are shown in Figures 7.1 to 7.3. Figure 7.3 is simply the sum of Figures 7.1 and 7.2, in order to represent the total energy deposited in the material.

7.4 Optical measurements after irradiation with 2 MeV Ar^+.

An m-lines technique based on grating couplers (Chapter 3) has been used to measure the coupling angles for the different propagation modes of the structure before and after irradiation.

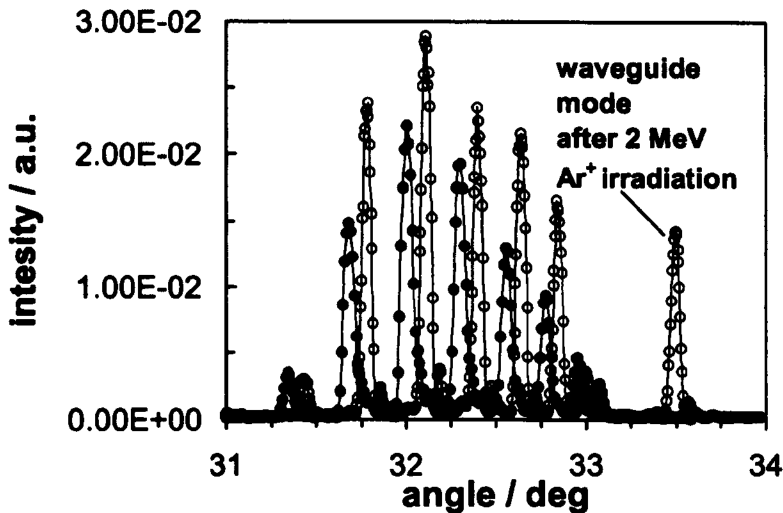

Figure 7.4. Measurement of the modes of propagation before and after 2 MeV Ar^+ irradiation: The peaks correspond to the intensity measured at the output of the waveguide structure as a function of the angle of incidence of the light into the grating coupler, before (dark circles) and after (open circles) irradiation.

After irradiation, a new mode appears at a higher coupling angle, meaning that it has a higher effective refractive index, as it can be seen in Figure 7.4.

As a first approximation, a step profile was assumed for the refractive index change due to irradiation, as shown in Figure 7.5 (a) in order to fit the results from the measurements of the grating coupler described in the previous paragraph [García-Blanco, 2003]. This model makes the assumption that sharp boundaries separate the different regions and that the waveguiding region extends from the surface up to an effective depth t_g with an "average" refractive index value $n_{FHD_implanted}$. The results from these fits can be seen in Figure 7.5 (b).

In Table 7.1, the numerical results obtained from the fits can be observed. The thickness obtained for the irradiated region that forms the waveguide varies with the irradiation dose. This can be related to the fact that a step profile has been assumed for the calculations, the thickness of which represents an "effective" thickness to account for an "average" value of refractive index change assumed by the model.

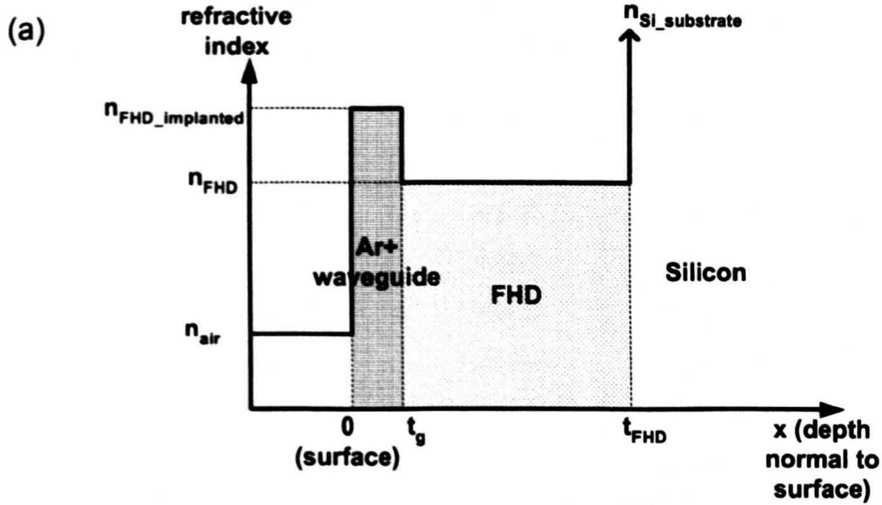

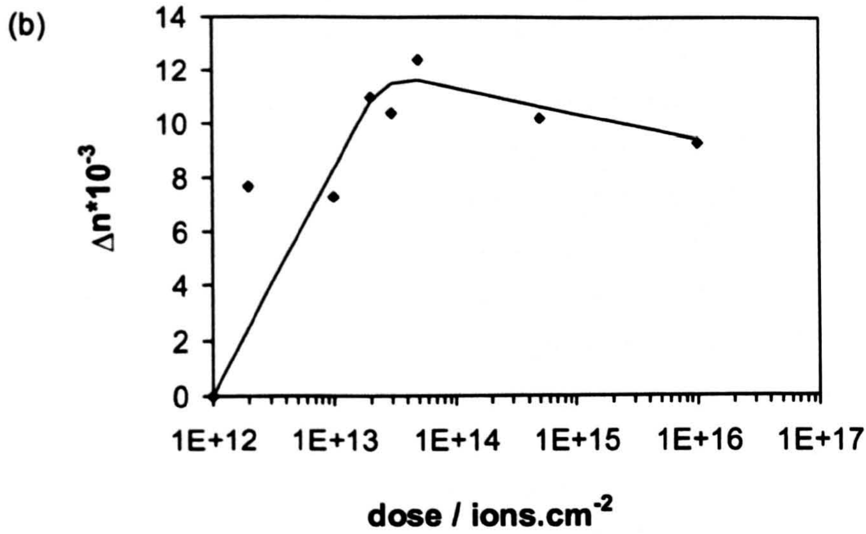

Figure 7.5. Refractive index calculations after irradiation with different ion doses: (a) Schematic structure of the waveguide formed after irradiation with 2 MeV Ar^{+} ions. The thickness of the waveguide formed due to the irradiation, t_g, and the refractive index $n_{FHD_implnated}$ are left as parameters for the fitting while the n_{FHD} value is taken from the measurement of the as-deposited layers, analysed assuming again a step index profile; (b) The change in refractive index obtained after different doses from the fittings.

dose / ions·cm^{-2}	n (as deposited)	n (after irradiation)	Δn (n_{impl}-n_{FHD})	t (μm)
1x10^{12}	1.4759	1.4759	0	--
2x10^{12}	1.4756	1.4833	7.7x10^{-3}	1.4
1x10^{13}	1.4767	1.4840	7.3x10^{-3}	1.3
2x10^{13}	1.4754	1.4864	1.1x10^{-2}	1.4
3x10^{13}	1.4765	1.4869	1.0x10^{-2}	1.6
5x10^{13}	1.4762	1.4886	1.2x10^{-2}	1.6
5x10^{14}	1.4762	1.4864	1.0x10^{-2}	1.9
1x10^{16}	1.4764	1.4857	9.3x10^{-3}	2

Table 7.1. Change in refractive index due to irradiation with 2 MeV Ar^{+} ions at different doses. The thickness indicated has been calculated by assuming a step index profile.

The change in refractive index obtained after irradiation is supposed to be related to the amount of energy transferred to the structure of the silica by ionizations and atomic collisional events. The increase of thickness found from the fittings performed here is related to the change of refractive index mainly due to ionization events. From the shape of the curve of transference of energy to the silica structure by ionizations, Figure 7.1, it can be seen a higher energy transfer at the surface and a decrease in depth. A similar shape for the change in refractive index could be expected. If the change in refractive index were considered uniform, the "effective" thickness obtained should be smaller than the actual penetration of the ions. A threshold energy deposited exists, below which not enough changes in the structure are produced in order to observe a change in refractive index. Here, no refractive index change was observed, for the measurement technique utilized, below doses of ≈2x10^{12} ions·cm^{-2}. Furthermore, a saturation energy deposition has been reported by several authors [Battaglin, 1999], [Arnold, 2000], for which compaction of the structure, which leads to an increase in refractive index, is followed by relaxation of the structure. Continuing with the results of Table 1, when the dose is increased, the refractive index change will be expected to saturate in the region where more energy deposition occurs, i.e. the surface, while an increase in refractive index is expected for the tail of the energy deposition profile. This process can account for the increase in "effective" thickness observed from the uniform refractive index model.

7.5 Measurement of the densification induced by 2 MeV Ar^+ irradiation.

7.5.1 X-ray reflectivity measurements of the change in density.

Two Ge:SiO_2 FHD films were prepared as described in Section 7.2. One of the samples was irradiated with a dose of $5x10^{13}$ ion·cm^{-2} uniformly across the surface of the wafer (Section 7.2). X-ray reflectivity measurements (Chapter 2, Section 2.5.1) at a wavelength 1.36 Å were performed in both non-irradiated and irradiated samples.

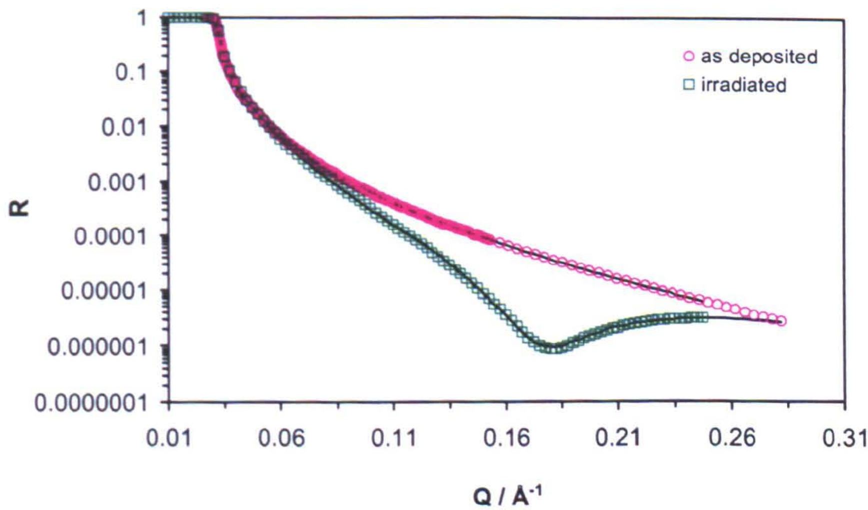

Figure 7.6. Reflectivity curves before and after 2 MeV Ar^+ ion implantation: the reflectivity is represented as a function of q (= $(4\pi/\lambda)\sin\theta$), where θ is the angle of incidence.

The results of the fitting by using the Parratt32 software (as described in Chapter 2, Section 2.5.1) can be seen in Figure 7.6. The density of the film changed from 2.39 g·cm^{-3} to 2.44 g·cm^{-3} after irradiation.

7.5.2 Measurement of the densification from height-step measurements.

Samples were prepared as described in Section 7.2. After irradiation with different doses (between $1x10^{12}$ to $1x10^{16}$ ion·cm^{-2}), profilometry measurements of the step-height obtained after irradiation were performed.

The results from these measurements are shown in Figure 7.7. The depression produced for each dose was measured at different points, from the different patterns irradiated with the same dose and the average is represented in Figure 7.7. The error bars represent the maximum deviation from the averaged value. For doses >10^{16} ions·cm^{-2}, damage of the surface occurred, making it impossible to perform the profilometer measurements.

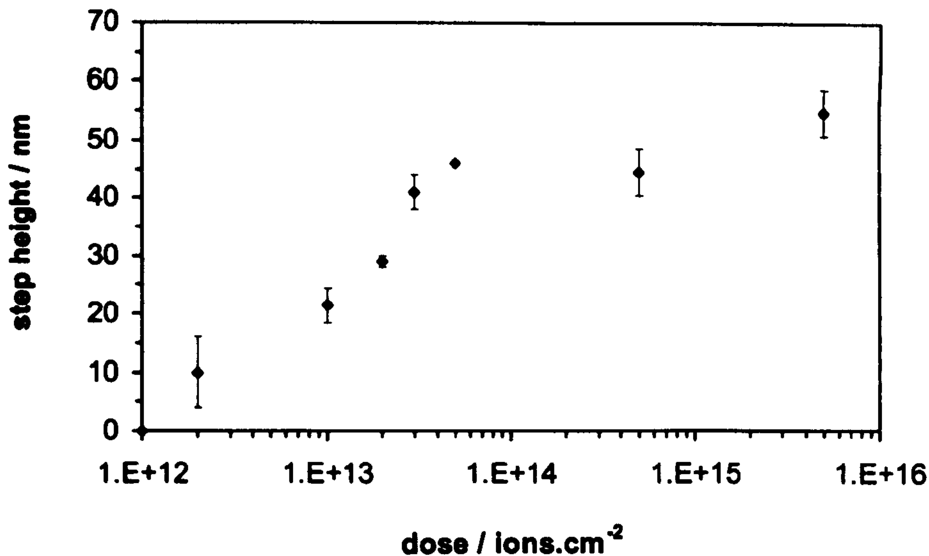

Figure 7.7. Profilometer measurements of the depression in the surface as a consequence of different Ar^+ irradiation doses.

7.6 Calculation of the change in refractive index expected from the change in density.

As it was discussed in Chapter 5 (Section 5.6.2), the change in refractive index suffered by the material after irradiation can be calculated from the change in density suffered by the material. The change in density of a material after irradiation can be divided into two components: a "permanent" densification component, which is isotropic, and an "elastic" component, appearing as a reaction to the permanent component. The first component, the "permanent" densification, produces a change in refractive index through the Lorentz-Lorenz derivative formula and the second one, the elastic reaction, produces a change in refractive index by the photo-elastic effect (Chapter 5, Section 5.6.2).

The same calculations described in Chapter 5, Section 5.6.2 were carried out in this chapter in order to calculate the refractive index change expected from the densification, measured by X-ray reflectivity and profilometry. It is important to note that several assumptions were made here. First, the strains induced by the irradiation were considered to be uniform in the depth of the irradiation, thus obtaining a value for the average densification in depth. The elastic constants used in the calculations were taken from the values reported in the literature for fused silica and they were considered to keep the same in the case of germanium-doped FHD silica and after 2 MeV Ar^+ ions irradiation (the values of the different parameters used in these calculations are the same used in Chapter 5, Section 5.6.2).

After performing these calculations, the change in the refractive index calculated from the densification measured by X-ray reflectivity is given by 1.14×10^{-2}, which closely agrees with the optical measurement of 1.2×10^{-2} (Table 7.1 for dose 5×10^{13} ions·cm^{-2}). For that calculation, a value of Ω of 0 was utilized.

Calculations as the ones described in Chapter 5, Section 5.5.3 and Section 5.6.2 were carried out in order to obtain the refractive index change expected from profilometry measurements of the densification. It is important to note that the penetration of 2 MeV Ar^+ ions is $\approx$ 1.7 μm, derived from TRIM Monte-Carlo simulations and the composition (XPS) and density (X-ray reflectivity) measured for the films.

Figure 7.8 shows the results of these calculations performed on the data depicted in Figure 7.7, in comparison with the refractive index change from optical measurements (Section 7.4, Figure 7.5). It is again necessary to be aware of all the assumptions made in these calculations, as discussed previously.

It can be seen that both sets of data are very similar for doses $\leq 5\times10^{13}$ ions·cm^{-2}. In Figure 7.8, Ω=0 (Equation 5.17) has been used for all the dose values, implying that the densification is not accompanied by a change in the polarizability. Dellin *et. al.* [Dellin, 1977] reported a variation in Ω after electron-beam irradiation of fused silica. In Chapter 5, the value of Ω was also found to increase with irradiation dose. If a value of +0.2 for doses below 2×10^{13} ion·cm^{-2}, a value of –0.15 for doses above 5×10^{13} ion cm^{-2} and a value of 0 for the transition were used, the results shown in Figure 7.9 would be obtained.

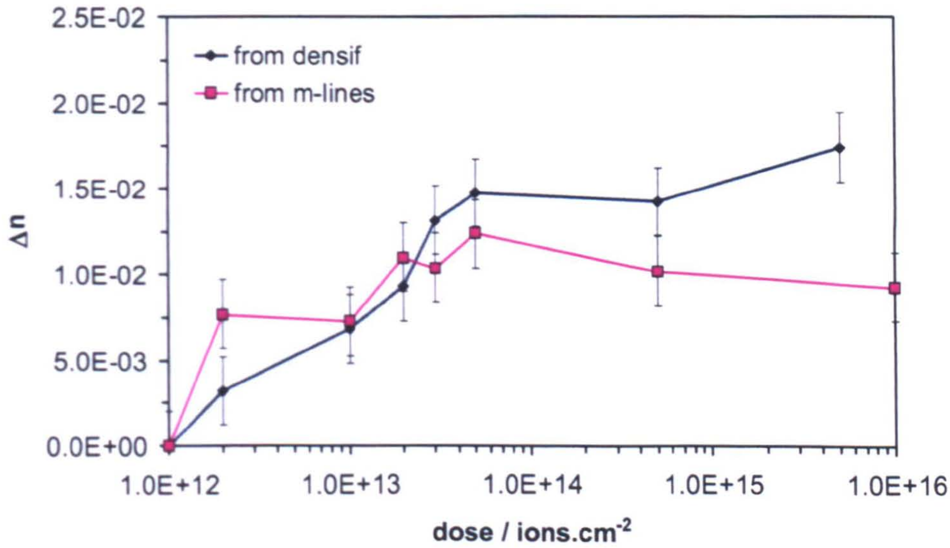

Figure 7.8. Calculations and measurements of the refractive index versus irradiation dose: The squares represent the refractive index values obtained from the m-lines techniques following by a fitting routine assuming a step index profile; the diamonds correspond to the refractive index change expected from the depressions measured on the surface.

It can be observed a better agreement between the data obtained from optical measurements, m-lines, and the data derived from the measurement of the depression on the surface. A decrease of the value of Ω with dose, passing from positive to negative values was obtained for 2 MeV Ar^+ irradiation whilst an increase in Ω, passing from negative to positive values was found for electron-beam irradiation of the same material (Chapter 5, Section 5.6.2.4). This result suggests a different polarizability change mechanisms in both kinds of irradiation, probably due to a different kind of structural reorganization of the silica matrix accompanied by different defect formation. However, structural analysis should be carried out on Ar^+ irradiated samples in order to compare the differences in structural changes occurring after both kind of irradiation.

After a dose $5x10^{13}$ ions·cm^{-2}, a decrease in refractive index was observed. Some authors have reported a similar mechanism [Battaglin, 1999]. Battaglin *et. al.* used fused silica and soda-lime glass for their investigations and found an saturation of the increase in density until a deposited energy of approximately 1-2x10^{20} keV·cm^{-3}. After a deposition of 1x10^{23} keV·cm^{-3}, a decrease in the density accompanied by further expansion of the material was found. The authors explained the increase in density as related with the formation of 3-membered rings in the silica structure. For higher irradiation doses, further damage of the structure might occur, probably leading to a relaxation of the silica structure, accompanied by a decrease in the

density. In the present work, a maximum in the change of refractive index was found, followed by a slight reduction. This effect was not followed by the data obtained for the change in density (Figure 7.7), for which a reduction in density or even expansion could not be found for higher doses before damage of the structure occurred (doses above $1x10^{16}$ ion·cm^{-2}). Nevertheless, Figure 7.9 suggests that the refractive index change derived from densification can follow the values obtained from optical measurements if the appropriate density-induced polarizability change factor were considered, thus implying a second mechanism, probably related to defect formation, involved in the refractive index change. Further work is needed in order to better understand the relation between refractive index change and density change and the structural modification leading to each of them.

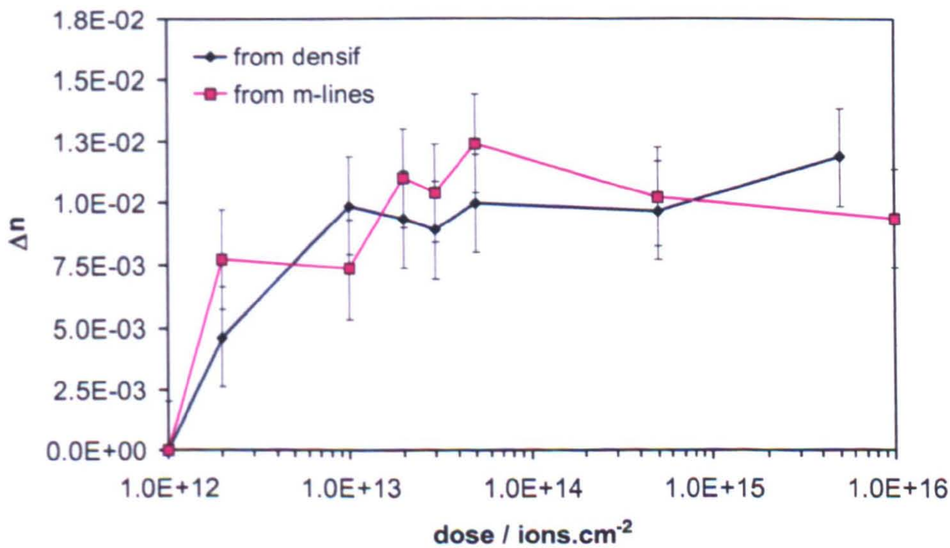

Figure 7.9. Evolution of the refractive index with dose: Squares represent the values obtained from the m-lines measurement followed by a fitting algorithm, The squares are calculations of the refractive index change from profilometry measurements of the change in density, with Ω=0.2 for doses below $2x10^{13}$ ions·cm^{-2} and –0.15 for doses over $5x10^{13}$ Ions·cm^{-2}.

7.7 Isochronal annealing experiments.

In order to investigate the stability of the changes induced in the material by the irradiation and get some insight into the possible nature of the mechanisms involved, annealing experiments have been performed, described in greater detail in Chapter 5.7.

A sample irradiated with a dose of 5×10^{13} ions·cm^{-2} was submitted to successive 30 min high-temperature steps. The temperature was varied from 200 to 550 °C at increments of 50 °C. The annealing was performed in a furnace at air atmosphere. The refractive index was measured after each high-temperature step by means of the m-lines technique following by the step-index profile approximation. The results are shown in Figure 7.10.

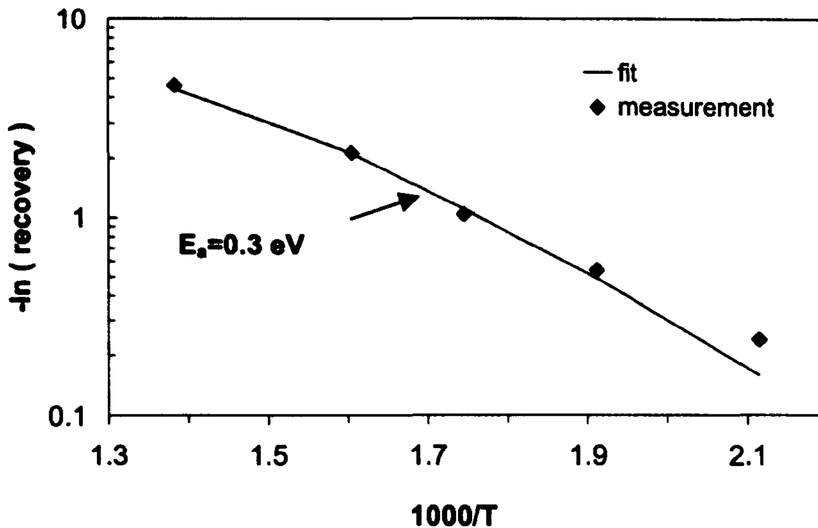

Figure 7.10. Isochronal annealing of the refractive index induced by Ar^+ irradiation: An activation energy of 0.3 eV has been found for the recovery of the damage produced by 2 MeV Ar^+ ions irradiation.

A similar activation energy for the recovery of the damage to the one found in the case of electron-beam irradiation of FHD silica layers (Chapter 5, Section 5.7.1) was found for the recovery of the damage after 2 MeV Ar^+ ions irradiation. An activation energy for low temperatures of 0.39 eV was found for the recovery of the refractive index change induced by electron-beam irradiation, which is comparable to the 0.3 eV obtained here. The damage was totally recovered after the experiment. This result implies that the structural rearrangements that lead to the change in refractive index are fully reversible. This suggests that no permanent modifications of the silica structure, including breakage of the silica tetrahedra structure, were produced by the irradiation, or at least are not responsible for the change in refractive index. Furthermore, the similarity with the electron-beam irradiation case suggests a similar mechanism of producing the damage. In the case of electron-beam irradiation, atomic displacements produced by atomic collisions are not possible,

being all the damage produced by ionization. It is consistent, therefore, to think that energy deposited by ionization events is the main contributor to the change in refractive index.

7.8 Conclusions.

Irradiation of $Ge:SiO_2$ FHD silica with 2 MeV Ar^+ ions was found to lead to a large refractive index change in the region from the surface of the material up to a depth of ≈ 2 μm, which correspond to the penetration range of the ions. The refractive index change induced was found to increase with irradiation dose to a maximum at a dose of $\approx 5x10^{13}$ $ion{\cdot}cm^{-2}$. Further increase of the irradiation dose led to a decrease of the effect, probably due to further change in the silica structure by collision damage.

The refractive index variation after irradiation was found to be derived from the change in density undergone by the material, as calculated from profilometry measurements. A variation of the density-induced polarizability change of opposite sign than the one found for electron-beam irradiation was obtained, related to the kind of structural rearrangements produced in the structure.

The refractive index change induced by the irradiation was found to be reversible if enough temperature were applied. The same activation energy than obtained for the recovery of the electron-beam irradiated silica was obtained here, further confirming the similarities between the nature of the damage induced by the two irradiation processes.

Chapter 8

Conclusions and suggestions for further work

8.1 Conclusions.

In this work, the effects induced by electron-beam irradiation in layers of flame-hydrolysis deposited silica doped with germanium were studied, in order to create the tools necessary for the development of novel devices for the communications and bio-sensing industries.

The germanium-doped as-deposited layers were first characterized optically. Two methodologies for obtaining the refractive index profile from optical measurements of the effective refractive indices of the different propagation modes were developed. The first one implies a first analysis using an inverse-WKB method, followed by a simplex fitting routine. The second implies an inverse reflectivity calculation method followed by the use of genetic algorithms and a simplex fitting routine. The two different methods were shown to give similar results.

The refractive index profile of the germanium-doped FHD silica layers deposited in this work was found to be non-uniform, showing a decrease in the refractive index towards the surface and also towards the interface with the thermal oxide underneath the FHD silica layer. XPS compositional analyses showed a negative gradient in the germanium profile in the interface towards the surface and at the interface with the substrate, further confirmed by RBS analyses. X-ray reflectivity measurements of the variation of the density of the material with depth showed an increase away from the surface. The origin of these results has been proposed to be the high-temperature sintering step performed on the germanium doped films after soot deposition. This result was confirmed by comparing the surface composition of the soot before and after the high temperature sintering step. This behaviour is consistent with the explanation that the refractive index profile, which is closely related to the germanium concentration profile, is dependent on the length of time that the films are subjected to the high-temperature sintering step.

The non-uniformity of the $Ge:SiO_2$ FHD films affects the way in which the electron-beam irradiation interacts with the material. After irradiation, a more highly densified region was found in the outer region (near the surface of the material), but was not observed when irradiating other materials such as germanium-doped MCVD silica or thermally grown silicon oxide. Structural analyses also showed that higher degree of compaction was occurring near the surface, based on a higher concentration of low-membered rings and higher reduction of the inter-tetrahedra angles in that region in comparison with the bulk. The refractive index profile was found to follow the densification profile, finding a variation with dose of the density-induced polarizability change of the material, probably related to the kind of defects generated during the irradiation.

The magnitude of the relative change in density was found to decrease as the germanium content of the material increased. Contrarily, no variation in the refractive index change was found after electron-beam irradiation between different germanium content FHD silica films. A possible explanation that has been given was that, as the germanium content of the glass increases, the temperature needed for the sintering of the material decreases, thus producing a more consolidated material in the sintering step, therefore allowing less additional compaction. On the other hand, as the germanium content increases, so does the refractive index of the initial material. In the formula relating densification with refractive index change, an increase in the original refractive index of the material will decrease the amount of refractive index change obtained. This is an important result as it indicates that the same amount of relative change in refractive index is obtained independently of the germanium content, increasing the flexibility in the selection of the material, as opposed to UV-irradiation of silica, for which a higher germanium content is desirable to increase the sensitivity.

The study of the evolution of the densification and change in refractive index with the irradiation dose showed a saturation of the effects of the electron-beam at a dose of 2 $C\cdot cm^{-2}$ for the change in density and 0.2 $C\cdot cm^{-2}$ for the relative change in refractive index. The saturation value of the effective refractive index change for the different modes was $7x10^{-3}$.

The stability of the changes induced by irradiation was investigated. The effect of the electron-beam irradiation was found to be annealing with two different activation energies, a smaller energy (around 0.1 eV) for low temperatures and a larger one

for higher temperatures (increasing with irradiation dose), the effect of the electron-beam disappearing completely after 700 °C. The number of processes occurring simultaneously in the material is too large to be able to determine the origin of the two activation energies. However, it is clear that two competing thermally-activated mechanisms must be present.

The losses of monomode waveguides were characterized and compared with the typical losses of waveguides fabricated in the same material with the more conventional fabrication technique of photolithography followed by dry-etching. Propagation loss values around 0.3 $dB \cdot cm^{-1}$ were found in both cases, suggesting that the factor determining the losses is the FHD material employed. Therefore, the technique is suitable for the fabrication of optical circuits, as was demonstrated by the fabrication of asymmetric Y-branches, which exhibited propagation characteristics consistent with the BPM-simulations performed.

Finally, 2 MeV Ar^+ irradiation was found to produce a considerably larger refractive index change, 1.2×10^{-2}, than the electron-beam irradiation. The relation between densification and refractive index change was studied, obtaining a variation in the density-induced polarizability change with dose opposite to that found for electron-beam irradiation, suggesting that different kinds of defect must be generated by the ion irradiation. However, the activation energy found for the recovery of the refractive index is similar to that found in the case of the electron-beam irradiation, implying that the defects generated are of the same kind as after electron-beam irradiation and do not involve breakage of the Si-O bonds as that would involve activation energies in the several eV range.

8.2 Suggestions for further work.

The work presented in this thesis could lead to a number of further experiments in order to increase understanding of the various processes involved. For example, an analysis of the annealing of the structural changes in depth induced by electron-beam irradiation would be useful to complete the series of densification and refractive index change annealing experiments performed in this work and to understand further the origin of the two activation energies. For that purpose, confocal Raman spectroscopy could possibly be used to profile the structural changes in depth after each annealing step.

The sensitivity to the electron-beam irradiation of flame-hydrolysis deposited silica with different dopants, such as phosphorus, could be studied in order to find the dopant that allows the highest refractive index change at the lowest dose, thereby increasing the possibilities of the technique.

The refractive index change studied in this work was investigated for large irradiated areas. When the irradiated area is reduced, changes in the local stresses will be introduced in the structure. Further work could involve the analysis of the refractive index profile in small waveguides, probably using different techniques, such as the ones based on observation of near-field modal patterns.

Another interesting subject is the birefringence induced after the electron-beam irradiation. In this work, it was shown that the birefringence varied with the applied dose. A larger range of doses should be investigated in order to discover the real trend of the birefringence. The possibility of writing waveguides with tailored birefringence by selecting the irradiation dose would be useful for a large range of optical devices, such as polarization splitters, which could be integrated in the same fabrication step with devices for which an absence of birefringence is desired.

As described in Chapter 7, this technique of fabrication of waveguide could find direct application in the development of optical bio-sensors, where a flat substrate is desired for integration with micro-fluidics. The further development of this type of device, including fluorescence sensors or evanescent-field sensors, would make it possible to combine a high-optical quality material, an easy optical fabrication technique and a fast integration capability with microfluidics, providing a convenient platform for the fabrication of optical sensors.

The study of the resolution limits of the patterns written with the electron-beam in silica would be useful in order to being able to modify the material to produce very fine structures, such as gratings. Probably, a limiting factor to the fabrication of these devices would be the lateral scattering of the electrons in the material.

References

Chapter 1.

[Albert, 1999] Albert J., Bilodeau F., Johnson D.C., Hill K.O., Hattori K., Kitagawa T., Hibino Y., Abe M., Low-loss planar lightwave circuit OADM with high isolation and no polarization dependence, IEEE Photon. Technol. Lett., 11, 3, 346-348, 1999.

[Almeida, 1994] Almeida R.M., Sol-gel silica films on silicon substrates, Int. J. Optoelectron., 9, 2, 135-142, 1994.

[Åslund, 1999] Åslund M., Canning J., Yoffe G., Locking in photosensitivity within optical fiber and planar waveguides by ultraviolet preexposure, Opt. Lett., 24, 24, 1826-1828, 1999.

[Åslund, 2000] Åslund M., Canning J., Annealing properties of gratings written into UV_presensitized hydrogen-outdifussed optical fiber, Opt. Lett., 25, 10, 692-694, 2000.

[Barbier, 1991] Barbier D., Green M., Madden S.J., Waveguide fabrication for integrated optics by electron beam irradiation of silica, J. Lightwave Technol., 9, 6, 715-720, 1991.

[Bell, 1991] Bell J., Ironside C.N., Channel optical waveguides directly written in glass with an electron-beam, Electron. Lett., 27, 5, 448-450, 1991.

[Bernardin, 1990] Bernardin J.P., Lawandy N.M., Dynamics of the formation of Bragg gratings in germanosilicate optical fibers, Opt. Commun., 79, 3-4, 194-199, 1990.

[Bilodeau, 1993] Bilodeau F., Malo B., Albert J., Johnson D.C., Hill K.O., Hibino Y., Abe M., Kawachi M. Photosensitization of optical fiber and silica-on-silicon silica waveguides, Opt. Lett., 18, 12, 953-955, 1993.

[Brambilla, 1999] Brambilla G., Pruneri V., Reekie L., Payne D.N., Enhanced photosensitivity in germanosilicate fibers exposed to CO_2 laser radiation, Opt. Lett., 24, 15, 1023-1025, 1999.

[Bretoiu, 2002] Bretoiu S., Di Mola D., Fiovaranti E., Visona S., Inductively coupled plasma etching for arrayed waveguide gratings fabrication in silica on silicon technology, J. Vac. Sci. Technol. B., 20, 5, 2085-2090, 2002.

[Canning, 2000a] Canning J., Aslund M., Ankiewicz A., Dainese M., Fernando H., Sahu J.K., Wosinski L., Birefringence control in plasma-enhanced chemical vapor deposition planar waveguides by ultraviolet irradiation, Appl. Opt., 39, 24, 4296-4299, 2000.

[Canning, 2000b] Canning J, Summer School on Photosensitivity in optical waveguides and glasses, POWAG2000, Giens Peninsula, France, 2000.

[Chao, 2002] Chao H.J., Next generation routers, Proc. IEEE, 90, 9, 1518-1558, 2002.

[Chen, 2000] Chen K.P., Herman P.R., Tam R., Zhang J., Rapid long-period grating formation in hydrogen-loaded fiber with 157-nm F_2-laser irradiation, Electron. Lett., 36, 2000-2001, 2000.

[Chen, 2002] Chen K.P., Herman P.R., Trimming and birefringence control in planar waveguide circuits using photosensitivity locking, IEEE Photon. Technol. Lett., 14, 71-73, 2002.

[Chen, 2003] Chen K.P., Herman P.R., Taylor R., Photosensitivity and application with 157 nm F_2 laser radiation in planar lightwave circuits, accepted for publication in J. Lightwave Technol., 2003.

[Dellin, 1977] Dellin T.A., Tichenor D.A., Barsis E.H., Volume, index of refraction and stress changes in electron irradiated silica, J. Appl. Phys., 48, 3, 1131-1138, 1977.

[Dianov, 1997] Dianov E.M., Stardubov D.S., Vasiliev S.A., Frolov A.A., Medvedkov O.I. Refractive-index gratings written by near-ultraviolet radiation, Opt. Lett., 22, 4, 221-223, 1997.

[Dong, 1995] Dong L., Archambault J.L., Reekie L., Russell P.S.J., Payne D.N., Photoinduced absorption change in germanosilicate preforms: evidence for the color-center model of photosensitivity, Appl. Opt., 34, 18, 3436-3440, 1995.

[Douay, 1997] Douay M., Taunay T., Bernage P., Niay P., Cordier P., Poumellec B., Dong L., Bayon J.F., Poignant H., Delevaque E., Densification involved in the UV-based photosensitivity of silica glasses and optical fibers, J. Lightwave Technol., 15, 8, 1329-1342, 1997.

[Douay, 2000] Douay M, Summer School on Photosensitivity in optical waveguides and glasses, POWAG2000, Giens Peninsula, France, 2000.

[Eldada, 2001] Eldada L., Advances in telecom and datacom optical components, Opt. Eng., 40, 7, 1165-1178, 2001.

[Erdogan, 1994] Erdogan T., Mizrahi V., Lemaire P.J., Monroe D., Decay of ultraviolet-induced fiber Bragg gratings, J. Appl. Phys., 76, 1, 73-80, 1994.

[Everhart, 1971] Everhart T.E., Hoff P.H., Determination of kilovolt electron energy dissipation vs penetration distance in solid materials, J. Appl. Phys., 42, 13, 5837-5846, 1971.

[Færch, 2002] Færch K., Svalgaard M., Symmetrical waveguide devices fabricated by direct UV writing, IEEE Photon. Technol. Lett., 14, 2, 173-175, 2002.

[Fardad, 1996] Fardad M.A., Yeatman E.M., Dawnay E.J.C., Green M., Fick J., Guntau M., Vitrant G., Fabrication and characterization of a CdS doped silica-on-silicon planar waveguide, IEE Proc. Optoelectron., 143, 5, 298-302, 1996.

[Ferraris, 2000] Ferraris M, Summer School on Photosensitivity in optical waveguides and glasses, POWAG2000, Giens Peninsula, France, 2000.

[Fokine, 2000] Fokine M., Margulis W., Large increase in photosensitivity through massive hydroxyl formation, Opt. Lett., 25, 5, 302-304, 2000.

[Goell, 1985] Goell J.E., Stanley R.D., Sputtered glass waveguide for integrated optics circuits, Bell Syst. Tech. J., 48, 230, 1985.

[Gowar, 1983] Gowar J., Optical communication systems, Prentice-Hall Intern. Series in Optoelectronics, London, 1983.

[Grand, 1990] Grand G., Jadot J.P., Denis H., Valette S., Fournier A., Grouillet A.M:, Low-loss PECVD silica channel waveguides for optical communications, Electron. Lett., 26, 25, 2135-2137, 1990.

[Grant, 1994] Grant M.F., Day S., Bellerby R., Wensley P.R., Rosser S.A., Cannell G.J., Wilson I.W., Lambert N.J., Low-cose MxN couplers in silica-on-silicon for passive optical networks, Int. J. Optoelectron., 9, 2, 159-170, 1994.

[Grubsky, 1999] Grubsky V., Starodubov D.S., Feinberg J., Photochemical reaction of hydrogen with germanosilicate glass initiated by 3.4-5.4 eV ultraviolet light, Opt. Lett., 24, 11, 729-731, 1999.

[Hanafusa, 1985] Hanafusa H., Hibino Y., Yamamoto F., Formation mechanism of drawing-induced E centers in silica optical fibers, J. Appl. Phys., 58, 3, 1356-1361, 1985.

[Hand, 1990] Hand D.P., Russell P.S.J., Photoinduced refractive-index changes in germanosilicate fibers, Opt. Lett., 15, 2, 102-104, 1990.

[Heaney, 1999] Heaney A.D., Erdogan T., Borrelli N., The significance of oxygen-deficient defects to the photosensitivity of hydrogen-loaded germano-silicate glass, J. Appl. Phys., 85, 11, 7573-7578, 1999.

[Henry, 1989] Henry C.H., Blonder G.E., Kazarinov R.F., Glass waveguides on silicon for hybrid optical packaging, J. Lightwave Technol., LT-7, 10, 1530-1539, 1989.

[Hill, 1978] Hill K.O., Fujii Y., Johnson D.C., Kawasaki, B.S., Photosensitivity in optical fiber waveguides: application to reflection filter fabrication, Appl. Phys. Lett., 32, 10, 647-649, 1978.

[Hill, 1993] Hill K.O., Malo B., Bilodeau F., Johnson D.C., Albert J., Bragg gratings fabricated in monomode photosensitive optical-fiber by UV exposure through a phase mask, Appl. Phys. Lett., 62, 10, 1035-1037, 1993.

[Holmes, 1993] Holmes A.S., Syms R.R.A., Li M., Green M., Fabrication of buried channel waveguides on silicon substrates using spin-on-glass and rapid thermal annealing, Appl. Opt., 32, 25, 4916-4921, 1993.

[Homoelle, 1999] Homoelle D., Wielandy S., Gaeta A.L., Borrelli N.F., Smith C., Infrared photosensitivity in silica glasses exposed to femtosecond laser pulses, Opt. Lett., 24, 18, 1311-1313, 1999.

[Hosono, 1992] Hosono H., Abe Y., Kinser D.L., Weeks R.A., Muta K., Kawazoe H., Nature and origin of the 5-eV band in SiO_2-GeO_2 glasses, Phys. Rev. B, 46, 18, 11445-11451, 1992.

[Hosono, 1996] Hosono H., Mizuguchi M., Kawazoe H., Nishii J., Correlation between GeE centers and optical absorption bands in SiO_2:GeO_2 glasses, Jap. J. Appl. Phys., 35, 2B, L234-L236, 1996.

[Hosono, 1999a] Hosono H., Kurita M., Kawazoe H., Excimer laser crystallization of amorphous indium-tin oxide thin films and application to fabrication of Bragg gratings, Thin Solids Films, 351, 1-2, 137-140, 1999.

[Hosono, 1999b] Hosono H., Mizuguchi M., Kawazoe H., Ogawa T., Effects of fluorine dimer excimer laser radiation on the optical transmission and defect formation of various types of synthetic SiO_2 glasses, Appl. Phys. Lett., 74, 19, 2755-2757, 1999.

[Houghton, 1976] Houghton A.J.,Townsend P.D., Optical waveguides formed by low-energy electron irradiation of silica, Appl. Phys. Lett., 29, 9, 565-566, 1976.

[Hunsperger, 1991] Hunsperger R.G., Integrated optics: theory and technology, Springer-Verlag, New York, 1991, 3rd edition.

[Hyde, 1942] Hyde J.H, Method of making a transparent article of silica, US patent N° 2 272 342, 1942.

[Inada, 2002] Inada Y., Sugahara H., Fukuchi K., Ogata T., Aoki Y., 32x40-Gb/s dense WDM transmission over 3000 km using "double-hybrid" fiber configuration, IEEE Photon. Technol. Lett., 14, 9, 1366-1368, 2002.

[Izawa, 1981] Izawa T., Mori H., Murukami Y., Shimizu N., Deposited silica waveguide for integrated optical circuits, Appl. Phys. Lett., 38, 7, 483-485, 1981.

[Jalali, 1996] Jalali B., Trinh P.D., Yegn S. Coppingen F. Guided wave optics in silicon-on-insulator technology, IEE Proc. Optoelectronics, 143, 5, 307-311, 1996.

[Jones, 1996] Jones C.A., Cooper, K., Hybrid integration onto silicon motherboards with plana silica waveguides, IEE Proc. Optoelectronics, 143, 5, 316-321, 1996.

[Kao, 1966] Kao K.C., Hockman G.A., Dielectric-fibre surface waveguides for optical frequencies, Proc. IEE, 113, 1151-1158, 1966.

[Kashyap, 1993] Kashyap R., Maxwell G.D., Ainslie B.J., Laser-trimmed four-port bandpass filter fabricated in single-mode photosensitive Ge-doped planar waveguide, IEEE Photon. Technol. Lett., 5, 2, 191-194, 1993.

[Kawachi, 1983] Kawachi M., Yasu M., Edahiro T., Fabrication of SiO_2-TiO_2 glass planar optical waveguides by flame hydrolysis deposition, Electron. Lett., 19,15, 583, 1983.

[Kawachi, 1990] Kawachi M., Silica waveguides on silicon and their application to integrated optics components, Opt. Quantum Electron., 22, 5, 391-416, 1990.

[Kawachi, 1996] Kawachi M., Recent progress in silica-based planar lightwave circuits on silicon, IEE Proceedings in optoelectronics, 143, 5, 257-262, 1996.

[Keiser, 2000] Keiser G., Optical fiber communications, Mc-Graw Hill, Singapore, 2000.

[Kominato, 1990] Kominato T., Ohmori Y., Okazaki H., Yasu M., Very low-loss GeO_2-doped silica waveguides fabricated by flame hydrolysis deposition method, Electron. Lett., 26, 5, 327-328, 1990.

[Kuzuu, 1997] Kuzuu N., Taga T., Kamisugi N., Effect of SiOH and SiCl on ArF-excimer laser-induced absorption in soot-remelted silica, J. Appl. Phys., 81, 12, 8011-8017, 1997.

[Kyle, 1995] Kyle D.J., Weiss B.L., Maxwell G.D., Photosensitivity of proton-implanted germania-doped planar silica structures, J. Appl. Phys., 77, 3, 1207-1210, 1995.

[Leconte, 1997] Leconte B., Xie W.X., Douay M., Bernage P., Niay P., Bayon J.F., Delevaque E., Poignant H., Analysis of color-center-related contribution to Bragg grating formation in Ge:SiO_2 fiber based on a local Kramers-Kronig transformation of excess loss spectra, Appl. Opt., 36, 24, 5923-5930, 1997.

[Lee, 1999] Lee B.H., Nishii J., Dependence of fringe spacing on the grating separation in a long period fiber grating pair, Appl. Opt., 38, 16, 3450-3459, 1999.

[Lewandowski, 1991] Lewandowski J., Syms R.R.A., Madden S., Green M., Buried channel waveguides in PECVD silicon oxynitride layers on Si substrates, formed by electron-beam irradiation, Opt. Quantum Electron., 23, 6, 703-711, 1991.

[Lewandowski, 1994] Lewandowski J., Syms R.R.A., Grant M., Bailey S., Controlled formation of buried channel waveguides by electron-beam irradiation of glassy layers on silicon, Int. J. Optoelectron., 9, 2, 143-149, 1994.

[Li, 1996] Li Y.P., Henry C.H., Silica-based optical integrated circuits, IEE Proc. Optoelectron., 143, 5, 263-280, 1996.

[Liu, 1997] Liu F.X., Qian J.Y., Wang X.L., Liu L., Ming H., UV irradiation-induced defect study of GeO_2-SiO_2 glasses by Raman spectroscopy, Phys. Rev. B, 56, 6, 3066-3071, 1997.

[Madden, 1990] Madden S.J., Green M., Barbier D., Optical channel waveguide fabrication based on electron beam irradiation of silica, Appl. Phys. Lett., 57, 27, 2902-2903, 1990.

[Marques, 2000] Marques P.V.S., Silica-on-silicon integrated optics by flame hydrolysis deposition, PhD thesis, University of Porto, 2000.

[Maxwell, 1993] Maxwell G.D., Ainslie B.J., Williams D.L., Kashyap R., UV written 13 dB reflection filters in hydrogenated low-loss planar silica waveguides, Electron. Lett., 29, 5, 425-426, 1993.

[Maxwell, 1995] Maxwell G.D., Ainslie B.J., Demonstration of a directly written directional coupler using UV-induced photosensitivity in a planar silica waveguide, Electron. Lett., 31, 2, 95-96, 1995.

[McLauglhin, 1998] McLaughin A.J., Hybrid silicon optoelectronic technologies, PhD Thesis, University of Glasgow, 1998.

[Meltz, 1989] Meltz G., Morey W.W., Glenn W H., Formation of Bragg gratings in optical fibers by a transverse holographic method, Opt. Lett., 14, 15, 823-825, 1989.

[Miller, 1969] Miller S.E., Integrated optics: an introduction, Bell Syst. Tech. J., 48, 7, 2059-2069, 1969.

[Monro, 1996] Monro T.M., de Sterke C.M., Poladian L., Investigation of waveguide growth in photosensitive germanosilicate glass, J. Opt. Soc. Am., B13, 12, 2824-2832, 1996.

[Monro, 1998] Monro T.M., Moss D., Bazylenko M., Martijn de Sterke C., Poladian L., Observation of self-trapping of light in a self-written channel in a photosensitive glass. Phys. Rev. Lett., 80, 18, 4072-4075, 1998.

[Monro, 1999] Monro T.M., de Sterke C.M., Poladian L., Analysis of self-written waveguide experiments, J. Opt. Soc. Am., B16, 10, 1680-1685, 1999.

[Montero, 1999] Montero C., Gomez-Reino C., Brebner J.L., Planar Bragg-gratings made by excimer-laser modification of ion-exchanged waveguides, Opt. Lett., 24, 21, 1487-1489, 1999.

[Morimoto, 1999] Morimoto Y., Yasuda Y., Nasu S., Photon dependence of vacuum ultraviolet light-induced stress in silica glass, J. Appl. Phys., 85, 10, 7385-7391, 1999.

[Nakanishi, 1999] Nakanishi M., Sugihara O., Okamoto N., Fujimura H., Egami C., Electron-beam irradiation-induced nonlinearity in silicate glass films and fabrication of nonlinear optical gratings, J. Appl. Phys., 86, 5, 2393-2396, 1999.

[Niay, 1999] Niay P., Douay M., Bernage P., Xie W.X., Leconte B., Ramecourt D., Delavaque E., Bayon J.F., Poignant H., Poumellec B., Does photosensitivity pave the way towards the fabrication of miniature coherent light sources in inorganic glass waveguides?, Opt. Materials, 11, 2-3, 115-129, 1999.

[Nishii, 1995] Nishii J., Kitamura N., Yamanaka H., Hosono H., Kawazoe H., Ultraviolet-radiation-induced chemical reactions through one and two-photon absorption processes in GeO_2-SiO_2 glasses, Opt. Lett., 20, 10, 1184-1186, 1995.

[Nishii, 1996] Nishii J., Yamanaka H., Hosono H., Kawazoe H., Preparation of Bragg gratings in sputter-deposited GeO_2-SiO_2 glasses by excimer laser irradiation, Opt. Lett., 21, 17, 1360-1362, 1996.

[Nishii, 1997] Nishii J., Yamanaka H., Bragg gratings printed upon thin glass films by excimer laser irradiation and selective chemical etching, Appl. Opt., 36, 27, 6852-6856, 1997.

[Nishii, 1999] Nishii J., Kintaka K., Hosono H., Kawazoe H., Kato M., Muta K., Pair generation of Ge electron centers and self-trapped hole centers in GeO_2-SiO_2 glasses by KrF excimer laser irradiation, Phys. Rev. B, 60, 10, 7166-7169, 1999.

[Poumellec, 1996] Poumellec B., Niay P., Douay M., Bayon J.F., The UV-induced refractive index grating in Ge:SiO_2 preforms: additional CW experiments and the macroscopic origin of the change in index, J. Phys. D., 29, 7, 1842-1856, 1996.

[Poumellec, 2002] Poumellec B., Niay P., Direct measurement of 248- and 193- nm excimer-induced densification in silica-germania waveguide blanks: comment, J. Opt. Soc. Am. B., 19, 9, 2039-2041, 2002.

[Primak, 1968] Primak W., Kampwirth R., The radiation compaction of vitreous silica, J. Appl. Phys., 39, 12, 5651-5658, 1968.

[Schenker, 1997] Schenker R.E., Oldham W.G., Ultraviolet induced densification in fused silica. J. Appl. Phys., 82, 3, 1065-1071, 1997.

[Selvarajan, 2001] Selvarajan A., Srinivas T., Optical amplification and photosensitivity in sol-gel based waveguides, IEEE J. Quantum Electron., 37, 9, 1117-1126, 2001.

[Shigemura, 1999] Shigemura H., Kawamoto Y., Nichii J., Takahashi M., Ultraviolet-photosensitive effect of sol-gel derived GeO_2-SiO_2 glasses, J. Appl. Phys., 85, 7, 3413-3418, 1999.

[Simmons, 1991] Simmons K.D., LaRochelle S., Mizrahi V., Stegeman G.I., Griscom D.L., Correlation of defect centes with a wavelength-dependent photosensitive response in germania-doped silica optical fibers, Opt. Lett., 16, 3, 141-143, 1991.

[Song, 2002] Song Z.T., Chong N., Chan L.W.H.W., Choy C.L., Lin C.L., Thermal stability of electrode stacks for application in oxide film devices, Thin Solid Films, 406, 1-2, 268-274, 2002.

[Soref, 1993] Soref S.A., Silica based optoelectronics, Proc. IEEE, 81, 12, 1687-1706, 1993.

[Spaargaren, 2000] Spaargaren S.M.R., Syms R.R.A., Characterization of defects in waveguides formed by electron irradiation of silica-on-silicon, J. Lightwave Technol., 18, 4, 555-561, 2000.

[Stewart, 1979] Stewart G., Refractive index modification by ion-exchange, PhD Thesis, University of Glasgow, 1979.

[Svalgaard, 1997] Svalgaard M., Direct writing of planar waveguide power splitters and directional couplers using a focused ultraviolet laser beam, Electron. Lett., 33, 20, 1694-1695, 1997.

[Syahriar, 1998] Syahriar A., Syms R.R.A., Tate T.J., Thermooptic interferometric switches fabricated by electron beam irradiation of silica-on-silicon, J. Lightwave Technol., 16, 5, 841-846, 1998.

[Syms, 1994a] Syms R.R.A., Tate T.J., Grant M.F., Reduction of propagation loss in silica-on-silicon channel waveguides formed by electron beam irradiation, Electron. Lett., 30, 18, 1480-1481, 1994.

[Syms, 1994b] Syms R.R.A., Tate T.J., Lewandowski J.J., Near-infrared channel waveguides formed by electron-beam irradiation of silica layers on silicon substrates, J. Lightwave Technol., 12, 12, 2085-2091, 1994.

[Syms, 1995] Syms R.R.A., Tate T.J., Bellerby R., Low-loss near-infrared passive optical waveguide components formed by electron-beam irradiation of silica-on-silicon, J. Lightwave Technol., 13, 8, 1745-1749, 1995.

[Tang, 1996] Tang G.K., Kewell A.K., Reed G.T., Rickman A.G., Namavar F., Development of a library of low-loss silicon on insulator optoelectronic devices, IEE Proc. Optoelectronics, 143, 5, 312-315, 1996.

[Takahashi, 1997] Takahashi M., Fujiwara T., Kawachi T., Ikushima A.J., Defect formation in GeO_2-SiO_2 glass by poling with ArF laser excitation, Appl. Phys. Lett., 71, 8, 993-995, 1997.

[Takada, 2000] Takada K., Tanaka T., Abe M., Yanagisawa T., Ishii M., Okamoto K., Beam-adjustment-free crosstalk reduction in 10 GHz-spaced arrayed-waveguide grating via photosensitivity under UV laser irradiation through metal mask, Electron. Lett., 36, 1, 60-61, 2000.

[Taunay, 1997] Taunay T., Niay P., Bernage P., Douay M., Xie W.X., Pureur D., Cordie, P., Bayon J.F., Poignant H., Delevaque E., Poumellec B., Bragg grating inscriptions within strained monomode high NA germania-doped fibers: part I. Experimentation, J. Phys. D: Applied Physics., 30, 1, 40-52, 1997.

[Townsend, 1994] Townsend P.D., Chandler P.J., Zhang L., Optical effects of ion implantation, Cambridge Studies in Modern Optics, Cambridge University Press, 1994.

[Tsai, 1993] Tsai T.E., Friebele E.L., Griscom D.L., Thermal stability of photoinduced gratings and paramagnetic centers in Ge-doped and Ge-P-doped silica optical fibers, Opt. Lett., 18,12, 935-937, 1993.

[Tsai, 1997] Tsai T.E., Williams G.M., Friebele E.J. Index structure of fiber Bragg gratings in Ge-SiO_2 fibers, Opt. Lett., 22, 4, 224-226, 1997.

[Tyndall, 1851] Tyndall J., Royal Institution of Great Britain Proceedings, 189, 6, 1870-1872, 1851.

[Xie, 1993] Xie W.X., Niay P., Bernage P., Douay M., Bayon J.F., Georges T., Monerie M., Poumellec B., Experimental evidence of two types of photorefractive effects occurring during photoinscriptions of Bragg gratings within germanosilicate fibres, Opt. Commun., 104, 1-3, 185-195, 1993.

[Zauner, 1998a] Zauner D.A., Hubner J., Malone K.J., Kristensen M., UV trimming of arrayed-waveguide grating wavelength division demultiplexers, Electron. Lett., 34, 8, 780-781, 1998.

[Zauner, 1998b] Zauner D., Kulstad K., Rathje J., Svalgaard M., Direct UV-written silica-on-silicon planar waveguides with low-insertion loss, Electron. Lett., 34, 16, 1582-1584, 1998.

[Zelmon, 1983] Zelmon, D.E., Jackson, H.E., Boyd J.T., Naumaan A., Anderson D.B., A low-scattering graded-index SiO_2 planar optical waveguide thermally grown on silicon, Appl. Phys. Lett., 42, 7, 565-567, 1983.

[Zhao, 1998] Zhao G., Tohge N., Nishii J., Fabrication and characterization of diffraction gratings using photosensitive Al_2O_3 gel films, Jap. J. Appl. Phys., 37, 4A, 1842-1846, 1998.

Chapter 2.

[Als-Nielsen, 1991] Als-Nielsen J., X-ray reflectivity studies of liquid surfaces, Handbook of synchrotron radiation, vol. 3, Chapter 12, Elsevier Science Publishers B.V., 1991.

[Barbarossa, 1992] Barbarossa G., Planar silica optical devices technology, PhD Thesis, University of Glasgow, 1992.

[Bazylenko, 1997] Bazylenko M.V., Gross M., Moss D., Mechanisms of photosensitivity in germanosilica films, J. Appl. Phys., 81, 11, 7497-7505, 1997.

[Bebbington, 1993] Rare earth doped silica for integrated optical waveguide lasers and amplifiers, PhD Thesis, University of Glasgow, 1993.

[Binnig, 1986] Binnig G., Quate C.F., Gerber C., Atomic force microscope, Phys. Rev. Lett. 56, 9, 930-933, 1986.

[Binsted, 1998] Binsted N., EXCURV98, CCLRC Daresbury Laboratory Program, 1998.

[Blanco, 2001] Blanco S.G., Glidle A., Davies J.H., Aitchison J.S., Cooper J.M., Electron-beam induced densification of Ge-doped flame hydrolysis silica for waveguide fabrication, Appl. Phys. Letts, 79, 18, 2889-2891, 2001.

[Bonar, 1995] Bonar J.R., Waveguide lasers in rare earth doped planar silica, PhD Thesis, University of Glasgow, 1995.

[Born, 1959] Born M., Wolf E., Principles of optics, Pergamon Press, 1959.

[Braun, 1999] Braun C., The reflectivity tool or Parratt32 version 1.5.2., HMI Berlin, 1997-1999.

[Briggs, 1990] Briggs D., Practical surface analysis, vol. 1, John Wiley and Sons, 1990.

[Carlson, 1975] Carlson T.A., Photoelectron and Auger spectroscopy, Plenum Press, New York, 1975.

[Chan, 2001] Chan J.W., Huser T., Risbud S., Krol D.M., Structural changes in fused silica after exposure to focused femtosecond laser pulses, Opt. Lett., 26, 21, 1726-1728, 2001.

[Chan, 2003] Chan J.W., Huser T.R., Risbud S.H., Krol D.M., Modification of the fused silica glass network associated with waveguide fabrication using femtosecond laser pulses, Appl. Phys. A, 76, 3, 367-372, 2003.

[Compton, 1923] Compton A.H., The total reflection of X-rays, Philos. Mag., 45, 1121-1131, 1923.

[Crist, 1999] Crist B.V., Handbooks of monochromatic XPS spectra, XPS International, Kawasaki, Japan, 1999.

[Dianov, 1997] Dianov E.M., Plotnichenko V.G., Koltachev V.V., Pyrkov Y.N., Ky N.H., Limberger H.G., Salathe R.P., UV-irradiation-induced structural transformation of germanosilicate glass fiber, Opt. Lett., 22, 23, 1754-1756, 1997.

[Doolittle, 1985] Doolittle L.R., Algorithms for the rapid simulation of Rutherford Backscattering spectra, Nucl. Instrum. Meth. B., 9, 3, 344-351, 1985.

[Ellis, 1995] Ellis P., PhD Thesis, University of Sydney, 1995.

[England, 1999] England K.E.R., Charnock J.M., Pattrick R.A.D., Vaughan D.J., Surface oxidation studies of chalcopyrite and pyrita by glancing-angle X-ray absorption spectroscopy (REFLEXAFS), Mineral. Mag., 63, 4, 559-566, 1999.

[Galeener, 1979] Galeener F.L., Band limits and the vibrational spectra of tetrahedral glasses, Phys. Rev. B, 19, 8, 4292-4297, 1979.

[Galeener, 1982a] Galeener F.L., Planar rings in vitreous silica, J. Non-Cryst. Solids, 49, 1-3, 53-62, 1982.

[Galeener, 1982b] Galeener F.L., Planar rings in glasses, Solid State Commun., 44, 7, 1037-1040, 1982.

[Galeener, 1983] Galeener F.L., Geissberger A.E., Vibrational dynamics in 30Si-substituted vitreous SiO_2, Phys. Rev. B, 27, 10, 6199-6204, 1983.

[Gowar, 1983] Gowar J., Optical communication systems, Prentice-Hall Intern. Series in Optoelectronics, London, 1983.

[Liu, 1997] Liu F.X., Qian J.Y., Wang X.L., Liu L., Ming H., UV irradiation-induced defect study of GeO_2-SiO_2 glasses by Raman spectroscopy, Phys. Rev. B, 56, 6, 3066-3071, 1997.

[Marques, 2000] Marques P.V.S., Silica-on-silicon integrated optics by flame hydrolysis deposition, PhD thesis, University of Porto, 2000.

[Maxwell, 1990] Optical waveguide fabrication in silica using flame hydrolysis, PhD Thesis, University of Glasgow, 1990.

[McLaughlin, 1998] McLaughlin A.J., Hybrid silicon optoelectronics technologies, PhD Thesis, University of Glasgow, 1998.

[Meyer, 1988] Meyer G., Amer N.M., Novel optical approach to atomic force microscopy, Appl. Phys. Lett., 53, 12, 1045-1047, 1988.

[Midha, 1999] Midha A., Batch-fabrication of novel nanoprobes for SPM, PhD Thesis, University of Glasgow, 1999.

[Nevot, 1980] Nevot L., Croce R., Characterisation of surfaces by grazing X-ray reflection. Application to the study of polishing some silicate glasses, Rev. Phys. Appl., 15, 761-779, 1980.

[Parrat, 1954] Parrat L.G., Surface studies of solids by total reflection of X-rays, Phys. Rev., 95, 2, 359-369, 1954.

[Pasquarello, 1998] Pasquarello A., Car R., Identification of raman defects lines as signatures of ring structures in vitreous silica, Phys. Rev. Lett., 80, 23, 5145-5147, 1998.

[Ruano, 2000] Ruano-López J.M., Optical devices for biosensing, microfabricated in flame hydrolysis deposited glasses, PhD Thesis, University of Glasgow, 2000.

[Sen, 1977] Sen P.N., Thorpe M.F., Phonons in AX_2 glasses: from molecular to band-like modes, Phys. Rev. B, 15, 8, 4030-4038, 1977.

[Seward III, 1997] Seward III T.P., Densification of synthetic fused silica under ultraviolet irradiation, J. Non-Cryst. Solids, 222, 407-414, 1997.

[Shirley, 1972] Shirley D.A., High resolution X-ray photoemission spectrum of the valence bands of gold, Phys. Rev. B, 5, 4709-4714, 1972.

[Stoev, 1997] Stoev K., Sakurai K., Recent theoretical models in grazing incidence X-ray reflectometry, The Rigaku Journal, 14, 22-37, 1997.

[Umari, 2002] Umari P., Pasquarello A., Modelling of the Raman spectrum of vitreous silica: concentration of small ring structures, Physica B, 316-317, 572-574, 2002.

[Vickerman, 1997] Vickerman J.C., Surface analysis: the principal techniques, Wiley and Sons, West Sussex, England, 1997.

[Wallace, 1995] Wallace W.E., Wu W.L., A novel method for determining thin-film density by energy-dispersive X-ray reflectivity, Appl. Phys. Lett., 67, 9, 1203-1205, 1995.

[Walls, 1989] Walls J.M, Methods of surface analysis, Cambridge University Press, England. 1989.

[Wolf, 1989] Wolf S., Tauber R.N., Silicon processing for the VLSI era, vol. 1, Lattice Press, Sunset Beach, California, 1989.

[Yates, 1987] Yates J.T., Madey T.E., Vibrational spectroscopy of molecules on surfaces, Methods of surface characterization, vol 1, Plenum Press, New York, 1987.

[Ziegler, 1985] Ziegler J., Biersack J., Littmark U., The stopping and ranges of ions in matter, vol. 1, Pergamon Press, New York, 1985.

Chapter 3.

[Adams, 1979] Adams A.C., Schinke D.P., Capio C.D., An evaluation of the prism coupler for measuring the thickness and refractive index of dielectric films on silicon substrates, J. Electrochem. Soc., 126, 9, 1539-1543, 1979.

[Adams, 1981] Adams M.J., An introduction to optical waveguides, J.Wiley&Sons, 1981.

[Adar, 1991] Adar R., Shani Y., Henry C.H., Kistler R.C., Blonder G.E., Olsson N.A., Measurement of very low-loss silica on silicon waveguide with a ring resonator, Appl. Phys. Lett., 58, 5, 444-445, 1991.

[Alfaro-Cid, 2001a] Alfaro-Cid E., McGookin E.W., Murray-Smith, D.J., Genetic Algorithm Optimisation of a Ship Navigation System, Acta Polytechnica, 41, 4-5, 13-9, 2001.

[Alfaro-Cid, 2001b] Alfaro-Cid E., McGookin E.W., Murray-Smith D.J., Genetic Algorithm Optimisation of a Supply Ship Propulsion and Navigation Systems, Proceedings of the MTS/IEEE Oceans Conference, Honolulu, USA, 2645-52, 2001.

[Bazylenko, 1996] Bazylenko M.V., Gross M., Faith M., Effect of reactive ion etching generated sidewall roughness on propagation loss of buried channel silica waveguides, Appl. Phys. Lett., 69, 15, 2178-2180, 1996.

[Born, 1959] Born M., Wolf E., Principles of optics, Pergamon Press, 1959.

[Campbell, 1996] Campbell S.A., The science and engineering of microelectronic fabrication, Oxford University Press, p. 206, 1996.

[Chandler, 1986] Chandler P.J., Lama F.L., A new approach to the determination of planar waveguide profiles by means of a non-stationary mode index calculation, Optica Acta, 33, 2, 127-143, 1986.

[Chandler, 1990] Chandler P.J., Lama F.L., Townsend P.D., Zhang L., Analysis of doped layer step waveguides *using dark* modes, J. Lightwave Technol., 8, 6, 917-921, 1990.

[Chiang, 1984] Chiang K.S., Finite element method for cutoff frequencies of weakly guiding fibers of arbitrary cross-section, Opt. Quantum. Electron., 16, 6, 487-493, 1984.

[Chiang, 1985] Chiang K.S., Construction of refractive-index profiles from the distribution of refractive indexes, J. Lightwave Technol., LT3, 2, 385-391, 1985.

[Clark, 1990] Clark D.F., Iqbal M.S., Simple extension to the Fabry-Perot technique for accurate measurement of losses in semiconductor waveguides, Opt. Lett., 15, 22, 1291-1293, 1990.

[Dakss, 1970] Dakss M.L., Kuhn L., Heidrich P.F., Scott B.A., Grating coupler for efficient excitation of optical guided waves in thin films, Appl. Phys. Lett., 16, 12, 523-525, 1970.

[Deri, 1991] Deri R.J., Kapon E., Low-loss III-V semiconductor optical waveguides, IEEE J. Quantum. Electron., 27, 3, 626-640, 1991.

[Ding, 1983] Ding T., Garmire E., Measurement of thin film parameters using substrate excitation of leaky modes, Opt. Commun., 48, 2, 113-115, 1983.

[Djurisic, 1997] Djurisic A.B., Elazar J.M., Rakic A.D., Genetic algorithms for continuous optimization problems-a concept of parameter-space size adjustment, J. Phys. A: Math. Gen., 30, 22, 7849-7861, 1997.

[Djurisic, 1998] Djurisic A.B., Elite genetic algorithms with adaptive mutations for solving continuous optimization problems-application to modeling of the optical constants of solids, Optics Commun., 151, 1-3, 147-159, 1998.

[Gedeon, 1974] Gedeon, A., Comparison between rigorous theory and WKB-analysis of modes in graded-index waveguides, Opt. Commun., 12, 3, 329-332, 1974.

[Goldberg, 1989] Goldberg D.E., Genetic algorithms in search, optimization and machine learning, Addison-Wesley, Reading, 1989.

[Henry, 1989] Henry C.H., Verbeek B.H., Solution of the scalar wave equation for arbitrarily shaped dielectric waveguides by two-dimensional Fourier analysis, J. Lightwave Technol., LT-7, 2, 308-131, 1989.

[Hocker, 1975] Hocker G.B., Burns W.K., Modes in diffused optical waveguides of arbitrary index profile, IEEE J. Quantum. Electron., QE-11, 6, 270-276, 1975.

[Holland, 1992] Holland J.H., Genetic Algorithms, Scientific American, 267, 1, 44-50, 1992.

[Hotate, 1979] Hotate K., Okoshi T., Measurement of refractive index profile and transmission characteristics of single-mode optical fiber from its exit-radiation pattern, Appl. Opt., 18, 19, 3265-3271, 1979.

[Hunsperger, 1991] Hunsperger R.G., Integrated optics: theory and technology, Springer-Verlag, New York, 1991, 3rd edition.

[Ingber, 1992] Ingber L., Rosen B., Genetic algorithms and very fast simulating annealing: a comparison, Mathl. Comput. Modelling, 16, 11, 87-100, 1992.

[Ladouceur, 1994] Ladouceur F., Love J.D., Senden T.J., Effect of sidewall roughness in buried channel waveguides, IEE Proc. Optoelectron., 141, 4, 242-248, 1994.

[Lee, 1986] Lee D.L., Electromagnetic principles of integrated optics, Wiley, New York, 1986.

[Lee, 1998] Lee C-T, Nondestructive measurement of separated propagation loss for multimode waveguides, Appl. Phys. Lett., 73, 2, 133-135, 1998.

[Marcaliti, 1974] Marcaliti E.A.J., Slab-coupled waveguides, Bell Syst. Tech. J., 53, 4, 645-674, 1974.

[Marcuse, 1973] Marcuse D., TE modes of graded-index slab waveguides, IEEE J. Quantum. Electron., QE-9, 10, 1000-1006, 1973.

[McCaughan, 1983] McCaughan L., Bergmann E.E., Index distribution of optical waveguides from their mode profile, J. Lightwave Technol., LT1, 1, 241-244, 1983.

[Ogawa, 1972] Ogawa K., Chang W.S.C., Sopori B.L., Rosenbaum F.J., A theoretical analysis of etched grating couplers for integrated optics, J. Quantum Electron., QE-9, 1, 29-42, 1972.

[Okamura, 1986] Okamura Y., Miki A., Yamamoto S., Observation of wave propagation in integrated optical circuits, Appl. Opt., 25, 19, 3405-3408, 1986.

[Sarid, 1980] Sarid D., Recovery of the refractive-index profile of an optical waveguide from the measured coupling angles, Appl. Opt., 19, 10, 1606-1608, 1980.

[Shiozawa, 1990] Shiozawa T., Miyamoto H., Ohta H., Yamaguchi M., Oki T., Determination of two-dimensional optical waveguide index distribution function parameters from effective indexes, J. Lightwave Technol., 8, 4, 497-505, 1990.

[Schulz, 1990] Schulz N., Bierwirth K., Arndt F., Koster U., Finite defference method without spurious solutions for the hybrid mode analysis of diffused channel waveguides, IEEE Trans. Micr. Theory and Tech., MTT-38, 6, 722-729, 1990.

[Snyder, 1983] Snyder A.W., Love J.D., Optical waveguide theory, Chapman and Hall, 1983.

[Takeuchi, 1989] Takeuchi H., Oe, K., Low-loss single-mode GaAs/AlGaAs miniature optical waveguides with straight and bending structures, J. Lightwave Technol., 7, 7, 1044-1054, 1989.

[Tien, 1971] Tien P.K., Light waves in thin films and integrated optics, Appl. Opt., 10,11, 2395-2413, 1971.

[Tien, 1970] Tien P.K., Ulrich R., Theory of prism-film coupler and thin-film light guides, J. Opt. Soc. Am., 60, 10, 1325-1337, 1970.

[Tien, 1974] Tien P.K., Riva-Sanseverino S., Martin R.J., Ballman A.A., Brown H., Optical waveguide modes in single-crystalline $LiNbO_3$-$LiTaO_3$ solid solution films, Appl. Phys. Lett., 24, 10, 503-506, 1974.

[Townsend, 1994] Townsend P.D., Chandler P.J., Zhang L., Optical effects of ion implantation, Cambridge Studies in Modern Optics, Cambridge University Press, 1994.

[Ulrich, 1970] Ulrich R., Theory of the prism-film coupler by plane-wave analysis, J. Opt. Soc. Am., 60, 10, 1337-1350, 1970.

[Ulrich, 1973] Ulrich R., Torge R., Measurement of thin film parameters with a prism coupler, Appl. Opt., 12, 12, 2901-2908, 1973.

[Walker, 1983] Walker R.G., Wilkinson C.D.W., Integrated optical ring resonators made by silver ion-exchange in glass, Appl. Opt., 22, 7, 1029-1035, 1983.

[Walker, 1985] Walker R.G., Simple and accurate loss measurement technique for semiconductor optical waveguides, Elec. Lett., 21, 13, 581-583, 1985.

[Weber, 1973] Weber H.P., Dunn F.A., Leibolt W.N., Loss measurement in thin film optical waveguides, Appl. Opt., 12, 4, 755-757, 1973.

[White, 1976] White J.M., Heidrich P.F., Optical waveguide refractive index profiles determined from measurements of mode indices: a simple analysis, Appl. Opt., 15, 1, 151-155, 1976.

[Wolfe, 1978] Wolfe M.A., Numerical methods for unconstrained optimization and introduction, Van Nostrand Reinhold Company, England, 1978.

[Won, 1980] Won Y.H., Jaussaud P.C., Chartier G.H., Three-prism loss measurements of optical waveguides, Appl. Phys. Lett, 37, 3, 269-271, 1980.

Chapter 4.

[Battaglin, 1998] Battaglin G., Cattaruzza E., DAcapito F., Gonella F., Mazzoldi P., Mobilio S., Priolo F., EXAFS study on metal cluster doped silica glass obtained by ion implantation procedures, Nucl. Instrum. Meth. B, 141, 1-4, 252-255, 1998.

[Bonar, 1995] Bonar J.R., Waveguide lasers in rare earth doped planar silica, PhD Thesis, University of Glasgow, 1995.

[Born, 1959] Born M., Wolf E., Principles of optics, Pergamon Press, 1959.

[Brinker, 1986] Brinker C.J., Tallant D.R., Roth E.P., Ashley C.S., Sol-gel transition in simple silicates. 3. Structural studies during densification, J. Non-Cryst. Solids, 82, 1-3, 117-126, 1986.

[Brückner, 1970] Brückner R., Properties and structure of vitreous silica I, J. Non-Cryst. Solids, 5, 2, 123-175, 1970.

[Chandler, 1986] Chandler P.J., Lama F.L., A new approach to the determination of planar waveguide profiles by means of a non-stationary mode index calculation, Optica Acta, 33, 2,127-143, 1986.

[Chemarin, 1997] Chemarin C., Champagnon B., Panczer G, Effect of fictive temperature on medium range order in v-SiO_2, J. Non-Cryst. Solids, 216, 111-115, 1997.

[Chiang, 1985] Chiang K.S., Construction of refractive-index profiles from the distribution of refractive indexes, J. Lightwave Technol., LT3, 2, 385-391, 1985.

[Chiodini, 1999] Chiodini N., Meinardi F., Morazzoni F., Paleari A., Scotti R., Spinolo G., Tin doped silica by sol-gel method: doping effects on the SiO_2 Raman spectrum, Solid State Commun., 109, 3, 145-150, 1999.

[Dakss, 1970] Dakss M.L., Kuhn L., Heidrich P.F., Scott B.A., Grating coupler for efficient excitation of optical guided waves in thin films, Appl. Phys. Lett., 16, 12, 523-525, 1970.

[Dimitrov, 2002] Dimitrov V., Komatsu T., Classification of simple oxides: a polarizability approach, J. Solid State Chem., 163, 1, 100-112, 2002.

[Doolittle, 1985] Doolittle L.R., Algorithms for the rapid simulation of Rutherford Backscattering spectra, Nucl. Instrum. Meth. B., 9, 3, 344-351, 1985.

[Galeener, 1979] Galeener F.L., Band limits and the vibrational spectra of tetrahedral glasses, Phys. Rev. B, 19, 8, 4292-4297, 1979.

[Galeener, 1982a] Galeener F.L., Planar rings in vitreous silica, J. Non-Cryst. Solids, 49, 1-3, 53-62, 1982.

[Galeener, 1982b] Galeener F.L., Planar rings in glasses, Solid State Commun., 44, 7, 1037-1040, 1982.

[Gaskell, 1997] Gaskell P.H., Structure and properties of glasses – how far do we need to go?, J. Non-Cryst. Solids, 222, 1-12, 1997.

[Greegor, 1987] Greegor R.B., Lytle F.W., Kortright J., Fischer-Colbrie A, Determination of the structure of GeO_2-SiO_2 glasses by EXAFS and X-ray scattering, J. Non-Cryst. Solids, 89, 3, 311-325, 1987.

[Heimala, 1992] Heimala P., Aarnio J., Refractive index behaviour of phosphorus-doped planar silica waveguides, J. Phys. D: Appl. Phys., 25, 5, 733-739, 1992.

[Holland, 1992] Holland J.H., Genetic Algorithms, Scientific American, 267, 1, 44-50, 1992.

[Hussin, 1999] Hussin R., Dupree R., Holland D., The Ge-O-Ge bond angle distribution in GeO_2 glass: a NMR determination, J. Non-Cryst. Solids, 246, 3, 159-168, 1999.

[Johnson, 1998] Johnson C.M., Thompson T.D., Ridgway M.C., Gurarie V., Implantation-induced structural and surface modification of silica, Nucl. Instrum. Meth. B, 141, 1-4, 629-633, 1998.

[Leeuw, 1985] Leeuw S.W., He H., Thorpe M.F., Vibrational spectra of rings in vitreous silica, Solid State Commun., 56, 4, 343-346, 1985.

[Liu, 1997] Liu F.X., Qian J.Y., Wang X.L., Liu L., Ming H., UV irradiation-induced defect study of GeO_2-SiO_2 glasses by Raman spectroscopy, Phys. Rev. B, 56, 6, 3066-3071, 1997.

[Marques, 2000] Marques P.V.S., Silica-on-silicon integrated optics by flame hydrolysis deposition, PhD thesis, University of Porto, 2000.

[Morishita, 1986] Morishita K., Index profiling of three dimensional waveguides by the propagation-mode near-field method, J. Lightwave Technol., LT4, 8, 1120-1124, 1986.

[Nian, 1989] Nian X., Zhisan X., Decheng T., A Raman study of the ring defects in GeO_2-SiO_2 glasses, J. Phys: Condens. Matter, 1, 36, 6343-6346, 1989.

[Okumura, 1998] Okumura K., Asakura K:, Iwasawa Y., Characterization of GeO_2 submonolayers on SiO_2 prepared by chemical vapour deposition of $Ge(OMe)_4$ by EXAFS FT-IR and XRD, Langmuir, 14, 13, 3607-3613, 1998.

[Pasquarello, 1998] Pasquarello A., Car R., Identification of raman defects lines as signatures of ring structures in vitreous silica, Phys. Rev. Lett., 80, 23, 5145-5147, 1998.

[Pasquarello, 01] Pasquarello A., First-principles simulation of vitreous systems, Curr. Opinion in Solid State and Materials Science, 5, 6, 503-508, 2001.

[Phillips, 1984] Phillips J.C., Microscopic origin of anomalously narrow raman lines in network glasses, J. Non-Cryst. Solids, 63, 3, 347-355, 1984.

[Potkay, 1988] Potkay E., Clark H.R., Smyth I.P., Kometani T.Y., Wood D.L., Characterization of soot from multimode vapor-phase axial deposition (VAD) optical fiber preforms, J. Lightwave Technol., 6, 8, 1338-1347, 1988.

[Sakka, 1969] Sakka S., Mackenzie J.D., High pressure effect on glass, J. Non-Cryst. Solids, 1, 2, 107-142, 1969.

[Sharma, 1984] Sharma S.K., Matson D.W., Philpotts J.A., Roush T.L., Raman-study of the structure of glasses along the join SiO_2-GeO_2, J. Non-Cryst. Solids, 68, 1, 99-114, 1984.

[Skuja, 2000] Skuja L., Hosono H., Mizuguchi M., Guttler B., Silin A., Site-selective study of the 1.8 eV luminescence band in glassy GeO_2, J. Luminescence, 87-89, 699-701, 2000.

[Townsend, 1994] Townsend P.D., Chandler P.J., Zhang L., Optical effects of ion implantation, Cambridge Studies in Modem Optics, Cambridge University Press, 1994.

[Tien, 1970] Tien P.K., Ulrich R., Theory of prism-film coupler and thin-film light guides, J. Opt. Soc. Am., 60, 10, 1325-1337, 1970.

[Tien, 1974] P.K. Tien, S. Riva-Sanseverino, R.J. Martin, A.A. Ballman, H. Brown, Optical waveguide modes in single-crystalline $LiNbO_3$-$LiTaO_3$ solid-solution films, Appl. Phys. Lett., 24, 10, 503-506, 1974.

[Wefing, 1999] Wefing S, Modeling of continuous random networks: a case study for vitreous GeO_2. I. Model generation, J. Non-Cryst. Solids, 244, 89-111, 1999.

[Yoshikawa, 1997] Yoshikawa M., Iwagami K., Morita N., Matsunobe T., Ishida H., Characterization of fluorine-doped silicon dioxide film by Raman spectroscopy, Thin Solid Films, 310, 1-2, 167-170, 1997.

Chapter 5.

[Agawal, 1995] Agawal A., Davis K.M., Tomozawa M., A simple IR spectroscopic method for determining fictive temperature of silica glasses, J. Non-Cryst. Solids, 185, 191-198, 1995.

[Allan, 1996] Allan D.C., Smith C., Borrelli N.F., Seward III T.P., 193-nm excimer-laser-induced densification of fused silica, Opt. Lett., 21, 24, 1960-1962, 1996.

[Baker, 1997] Baker S.R., Rourke H.N., Baker V., Goodchild D., Thermal decay of fiber Bragg gratings written in boron and germanium codoped silica fiber, J. Lightwave Technol.., 15, 8, 1470-1477, 1997.

[Barbier, 1991] Barbier D., Green M., Madden S.J., Waveguide fabrication for integrated optics by electron beam irradiation of silica, J. Lightwave Technol., 9, 6, 715-720, 1991.

[Bartolotta, 2001] Bartolotta A., Carini G., DAngelo G., Ferrari M., Fontana A., Montagna M., Rossi F., Tripodo G., A study of Raman spectroscopy and low-temperature specific heat in gel-synthesized amorphous silica, J. Non-Cryst. Solids, 280, 1-3, 249-254, 2001.

[Bates, 1972] Bates J.B., Dynamics of beta-quartz structures of vitreous SiO_2 and BeF_2, J. Chem. Phys., 56, 5, 1910-1917, 1972.

[Bates, 1974] Bates J.B., Hendricks R.W., Shaffer L.B., Neutron irradiation effects and structure of non-crystalline SiO_2, J. Chem. Physics, 61, 10, 4163-4176, 1974.

[Bazylenko, 1997] Bazylenko M.V., Gross M., Moss D., Mechanisms of photosensitivity in germanosilica films, J. Appl. Phys., 81, 11, 7497-7505, 1997.

[Bell, 1991] Bell J., Ironside C.N., Channel optical waveguides directly written in glass with an electron beam, Electron. Lett., 27, 5, 448-450, 1991.

[Blanco, 2001] García Blanco S., Glidle A., Davies J.H., Aitchison J.S., Cooper J.M., Electron-beam-induced densification of Ge-doped flame hydrolysis silica for waveguide fabrication, Appl. Phys. Lett., 79, 2889-2891, 2001.

[Born, 1959] Born M., Wolf E., Principles of optics, Pergamon Press, 1959.

[Borrelli, 1997] Borrelli, N.F., Smith, C., Allan, D.C., Seward III, T.P., Densification of fused silica under 193-nm excitation, J. Opt. Soc. Am B, 14, 7, 1997, 1606-1615.

[Borrelli, 1999] Borrelli, N.F., Allan D.C., Modavis R.A., Direct measurement of 248- and 193-nm excimer-induced densification in silica-germania waveguide blanks, J. Opt. Soc. Am. B, 16, 10, 1672-1679, 1999.

[Braun, 1999] Braun C., The reflectivity tool or Parratt32 version 1.5.2., HMI Berlin, 1997-1999.

[Bridgman, 1953] Bridgman P.W., Simon I., Effects of very high pressures on glass, J. Appl. Phys., 24, 405-413, 1953.

[Chan, 2001] Chan J.W., Huser T., Risbud S., Krol D.M., Structural changes in fused silica after exposure to focused femtosecond laser pulses, Opt. Lett., 26, 21, 1726-1728, 2001.

[Chan, 2003] Chan J.W., Huser T.R., Risbud S.H., Krol D.M., Modification of the fused silica glass network associated with waveguide fabrication using femtosecond laser pulses, Appl. Phys. A, 76, 3, 367-372, 2003.

[Charles, 1995] Charles C., Boswell R.W., Effect of wall charging on an oxygen plasma created in a helicon diffusion reactor used for silica deposition, J. Vac. Sci. Technol. A, 13, 4, 2067-2073, 1995.

[Chen, 2003] Chen K.P., Herman P.R., Taylor R., Photosensitivity and application with 157 nm F_2 laser radiation in planar lightwave circuits, to be published in J. Lightwave Circuits, 2003.

[Cheylan, 2001] Cheylan S., Elliman R.G., Gaff K., Durandet A., Luminescence from Si nanocrystals in silica deposited by helicon activated reactive evaporation, Appl. Phys. Lett., 78, 12, 1670-1672, 2001.

[Craig, 1996] Craig R.R., Mechanics of materials, John Wiley & Sons, United States, 1996.

[Davies, 2003] Davies J.H., Elastic field in a semi-infinite solid due to thermal expansion or a coherently misfitting inclusion, accepted for publication in ASME J. Appl. Mech., 2003.

[Dellin, 1977] Dellin T.A., Tichenor D.A., Barsis E.H., Volume, index of refraction, and stress changes in electron-irradiated vitreous silica, J. Appl. Phys., 48, 3, 1131-1138, 1977.

[Devine, 1993] Devine, R.A.B., Ion implantation- and radiation-induced structural modifications in amorphous SiO_2, J. Non-Cryst. Solids, 152, 50-58, 1993.

[Dianov, 1997] Dianov E.M., Plotnichenko V.G., Koltachev V.V., Pyrkov Y.N., Ky N.H., Limberger H.G., Salathe R.P., UV-irradiation-induced structural transformation of germanosilicate glass fiber, Opt. Lett., 22, 23, 1754-1756, 1997.

[EerNisse, 1974a] EerNisse, E.P., Compaction of ion-implanted fused silica, J. Appl. Phys., 45, 1, 167-174, 1974.

[EerNisse, 1974b] EerNisse, E.P., Norris, C.B., Introduction rates and annealing of defects in ion-implanted SiO_2 layers on Si, J. Appl. Phys., 45, 12, 5196-5205, 1974.

[Erdogan, 1994] Erdogan T., Mizrahi V., Lemaire P.J., Monroe D., Decay of ultraviolet-induced fiber Bragg gratings, J. Appl. Phys., 76, 1, 73-80, 1994.

[Everhart, 1971] Everhart T.E., Hoff P.H., Determination of kilovolt electron energy dissipation vs penetration distance in solid materials, J. Appl. Phys., 42, 13, 5837-5846, 1971.

[Fisher, 1990] Fisher A.J., Hayes W., Stoneham A.M., Structure of the self-trapped exciton in quartz, Phys. Rev. Lett., 64, 2667-2670, 1990,

[Galeener, 1979] Galeener F.L., Band limits and the vibrational spectra of tetrahedral glasses, Phys. Rev. B., 19, 8, 4292-4297, 1979.

[Galeener, 1982a] Galeener F.L., Planar rings in vitreous silica, J. Non-Cryst. Solids, 49, 1-3, 53-62, 1982.

[Galeener, 1982b] Galeener F.L., Planar rings in glasses, Solid State Commun., 44, 7, 1037-1040, 1982.

[Galeener, 1985] Galeener F.L., Raman and electron-spin-resonance studies of the thermal history of amorphous SiO_2, J. Non-Cryst. Solids, 71, 1-3, 373-386, 1985.

[García-Blanco, 2002] García-Blanco S., Aitchison J.S., Cooper J.M., De La Rue R.M., Low-loss controlled-birefringence waveguides fabricated by electron-beam irradiation of germanium doped FHD silica, Proc. IPRC 2002, Vancouver, Canada, 2002.

[Griscom, 1991] Griscom, Optical-properties and structure of defects in silica glass, J. Ceramic Soc. Jpn., 99, 10, 923-942, 1991.

[Griscom, 1993] Griscom D.L., Gingerich M.E., Friebele E.J., Radiation-induced defects in glasses: Origin of the power-law dependence of concentration on dose, Phys. Rev. Lett., 71, 7, 1019-1022, 1993.

[Griscom, 2001] Griscom, D.L., Fractal kinetics of radiation-induced point-defect formation and decay in amorphous insulators: application to color center in silica-based optical fibers, Phys. Rev. B., 64, 17, 174201, 2001.

[Gusarov, 2000] Gusarov A.I., Doyle D.B., Contribution of photoinduced densification to refractive-index modulation in Bragg gratings written in Ge-doped silica fibers, Opt. Lett., 25, 12, 872-874, 2000.

[Hemley, 1986] Hemley R.J., Mao H.K., Bell P.M., Mysen B.O., Raman spectroscopy of SiO_2 glass at high pressure, Phys. Rev. Lett., 57, 6, 747-750, 1986.

[Hill, 1978] Hill K.O., Fujii Y., Johnson D.C., Kawasaki, B.S., Photosensitivity in optical fiber waveguides: application to reflection filter fabrication, Appl. Phys. Lett., 32, 10, 647-649, 1978.

[Hosono, 2001] Hosono H., Ikuta Y., Kinoshita T., Kajihara K., Hirano M., Physical disorder and physical properties in the vacuum ultraviolet region of amorphous SiO_2, Phys. Rev. Lett., 87, 17, 175501/1-4, 2001.

[Houghton, 1976] Houghton A.J.,Townsend P.D., Optical waveguides formed by low-energy electron irradiation of silica, Appl. Phys. Lett., 29, 9, 565-566, 1976.

[Jacqueline, 2003] Jacqueline A.S., García-Blanco S., Poumellec B., Aitchison J.S., Dependence on Ge doping of specific volume change in silica induced by e-beam irradiation, accepted in Journal of Non Crystalline Solids, 2003.

[Jeunhomme, 1990] Jeunhomme L.B., Single-mode fiber optics, principles and applications, Optical Enginnering, vol. 23, Marcel Dekker Inc., New York, 1990.

[Jian, 2002] Jiang N., Qiu J., Gaeta A.L., Silcox J., Nanoscale modification of optical properties in Ge-doped SiO_2 glass by electron-beam irradiation, Appl. Phys. Lett., 80, 11, 2005-2007, 2002.

[Kannan, 1996] Kannan S., Guo J.Z.Y., Lemaire P.J., Thermal stability analysis of UV-induced fiber Bragg gratings, J. Lightwave Technol., 15, 8, 1478-1483, 1997.

[Kashyap, 1993] Kashyap R., Maxwell G.D., Ainslie B.J., Laser-trimmed four-port bandpass filter fabricated in single-mode photosensitive Ge-doped planar waveguide, IEEE Photon. Technol. Lett., 5, 2, 191-194, 1993.

[Kerbouche, 1999] Kerbouche F., Modifications chimiques et des contraintes mécaniques induited par lirradiation UV des fibres optiques Germanosilicates, PhD Thesis no 6016, Université Paris XI, Orsay, 1999.

[Kristensen, 2001] Kristensen M., Ultraviolet-light-induced processes in germanium-doped silica, Phys. Rev. B, 64, 144201/1-12, 2001.

[Leconte, 1998] B. Leconte, Contribution à létude de la photosensibilité des fibres sous leffet dune insolation par un laser à ArF, PhD Thesis, University of Lille, 1998.

[Lemaire, 1993] Lemaire P.J., Atkins R.M., Mizrahi V., Reed W.A.,, High pressure H_2 loading as a technique for achieving ultra-high UV photosensitivity and thermal sensitivity in GeO_2 doped optical fibers, Electron. Lett., 29, 13, 1191-1193, 1993.

[Lewandowski, 1991] Lewandowski J., Syms R.R.A., Madden S., Green M., Buried channel waveguides in PECVD silicon oxynitride layers on Si substrates, formed by electron-beam irradiation, Opt. Quantum Electron., 23, 6, 703-711, 1991.

[Lewandowski, 1994] Lewandowski J., Syms R.R:A., Madden S., Green M., Controlled formation of buried channel waveguides by electron-beam irradiation of glassy layers on silicon, Int. J. Optoelectron., 9, 2, 143-149, 1994.

[Li, 2002] Li W.T., Bulla D.A.P., Charles C., Boswell R., Love J., Luther-Davies B., Ge-doped SiO_2 thin films produced by helicon activated reactive evaporation, Thin Solid Films, 419, 1-2, 82-87, 2002.

[Liberman, 1999a] Liberman V., Rothschild M., Sedlacek J.H.C., Uttaro R.S., Grenville A., Excimer-laser-induced densification of fused silica: laser-fluence and material-grade effect on the scaling law, J. Non-Cryst. Solids, 244, 2-3, 159-171, 1999.

[Liberman, 1999b] Liberman V., Rothschild M., Sedlacek J.H.C., Uttaro R.S., Grenville A., Bates A.K., Van Peski C., Excimer-laser-induced degradation of fused silica and calcium fluoride for 193-nm lithographic applications, Opt. Lett., 24, 1, 58-60, 1999.

[Liu, 97] Liu F.X., Qian J.Y., Wang X.L., Liu L., Ming H., UV irradiation-induced defect study of GeO_2-SiO_2 glasses by Raman spectroscopy, Phys. Rev. B, 56, 6, 3066-3071, 1997.

[Madden, 90] Madden S.J., Green M., Barbier D., Optical channel waveguide fabrication based on electron beam irradiation of silica, Appl. Phys. Lett., 57, 27, 2902-2903, 1990.

[Midlin, 50] Midlin R.D., Cheng D.H., Thermoelastic stress in the semi-infinite solid, J. Appl. Phys., 21, 931-933, 1950.

[Miller, 69] Miller S.E., Integrated optics: an introduction, Bell Syst. Tech. J., 48, 7, 2059-2069, 1969.

[Mozzi, 69] Mozzi R.L., Warren B.E., Structure of vitreous silica, J. Appl. Crystal., 2, 164-172, 1969.

[Nishii, 1995] Nishii J., Kitamura N., Yamanaka H., Hosono H., Kawazoe H., Ultraviolet-radiation-induced chemical reactions through one and two-photon absorption processes in GeO_2-SiO_2 glasses, Opt. Lett., 20, 10, 1184-1186, 1995.

[Norris, 1974] Norris C.B., EerNisse E.P., Ionization dilation effects in fused silica from 2 to 18-keV irradiation, J. Appl. Phys., 45, 9, 3876-3882, 1974.

[Okumura, 1998] Okumura K., Asakura K:, Iwasawa Y., Characterization of GeO2 submonolayers on SiO_2 prepared by chemical vapour deposition of Ge(OMe)4 by EXAFS FT-IR and XRD, Langmuir, 14, 13, 3607-3613, 1998.

[Okuno, 1999] Okuno M., Reynard B., Shimada Y., Syono Y., Willaime C., A Raman spectrscopy study of shock-wave densification of vitreous silica, Phys. Chem. Minerals, 26, 4, 304-311, 1999.

[Pasquarello, 1998] Pasquarello A., Car R., Identification of raman defects lines as signatures of ring structures in vitreous silica, Phys. Rev. Lett., 80, 23, 5145-5147, 1998.

[Piao, 1998] Piao F., Oldham W.G., Haller E.E., Thermal annealing of deep ultraviolet (193 nm) induced compaction in fused silica, J. Vac. Sci. Technol. B, 16, 6, 3419-3421, 1998.

[Piao, 2000] Piao, F., Oldham, W.G., Haller, E.E., The mechanism of radiation-induced compaction in vitreous silica, J. Non-Cryst. Solids, 276, 1-3, 61-71, 2000.

[Poumellec, 1996a] Poumellec, B., Niay, P., Douay, M., Bayon, J.F., "The UV-induced refractive index grating in Ge:SiO_2 preforms: additional CW experiments and the macroscopic origin of the change in index", J. Phys. D: Appl. Phys., 29, 7, 1842-1856, 1996.

[Poumellec, 1996b] Poumellec B., Kherbouche F., The photorefractive Bragg gratings in the fibers for telecommunications, J. Phys. III, 6, 12, 1595-1624, 1996.

[Poumellec, 2002] Poumellec B., Niay P., Direct measurement of 248- and 193- nm excimer-induced densification in silica-germania waveguide blanks: comment, J. Opt. Soc. Am. B., 19, 9, 2039-2041, 2002.

[Primak, 58] Primak W., Photoelastic constants of vitreous silica and its elastic coefficient of refractive index, J. Appl. Phys., 30, 5, 779-788, 1958.

[Primak, 1968a] Primak W., Kampwirth R., The radiation compaction of vitreous silica, J. Appl. Phys., 39, 5651-5658, 1968.

[Primak, 1968b] Primak, W., Kampwirth, R., Impurity effect in the ionization dilatation of vitreous silica, J. Appl. Phys., 39, 13, 6010-6017, 1968.

[Primak, 1969] Primak, W., Kampwirth, R., Ionization expansion of pile-exposed vitreous silica, J. Appl. Phys., 40, 6, 2565-2570, 1969.

[Primak, 1972] Primak, W., Mechanism for the radiation compaction of vitreous silica, J. Appl. Phys., 43, 6, 2745-2754, 1972.

[Primak, 1974] Primak, W., Electron-dose distribution and range in vitreous silica from the dilation determined photoelastically, Nucl. Instrum. Meth., 119, 3, 533-540, 1974.

[Primak, 1979] Primak, W., Monahan, E., Improved servo-polarimeter, Rev. Sci. Instrum., 50, 738-740, 1979.

[Primak, 1982] Primak, W., Stress relaxation of vitreous silica on irradiation, J. Appl. Phys., 53, 11, 7331-7342, 1982.

[Primak, 1983] Primak, W., Monahan, E., Cantilever and capacitor technique for measuring dilatation, Rev. Sci. Intrum., 54, 544-551, 1983.

[Primak, 1984] Primak W., Stress relaxation in electron bombarded silicate glasses, J. Appl. Phys., 55, 9, 3315-3321, 1984.

[Razafimahatratra, 2000] Razafimahatratra D., Niay P., Douay M., Poumellec B., Riant I., Comparison of isochronal and isothermal decays of Bragg gratings written through continuous-wave exposure of an unloaded germanosilicate fiber, Appl. Opt., 39, 12, 1924-1933, 2000.

[Revesz, 1972] Revesz A.G., Pressure-induced conformational changes in vitreous silica, J. Non-Cryst. Solids, 7, 1, 77-85, 1972.

[Ruano, 1999] Ruano J.M., Ortega D., Bonar J.R., McLaughin A.J., Jubber M.G., Cooper J.M., Aitchison J.S., Fabrication of integrated microanalytical chambers and channels for biological assays using flame hydrolysis deposition glass, Microelectronics Engineering, 46, 1-4, 419-422, 1999.

[Ruller, 1991] Ruller J.A., Friebele E.J., The effect of gamma-irradiation on the density of various types of silica, J. Non-Cryst. Solids, 136, 1-2, 163-172, 1991.

[Sempolinski, 1996] Sempolinski D.R., Seward T.P., Smith C., Borrelli N., Rosplock C., Effects of glass forming conditions on the KrF-excimer-laser-induced optical damage in synthetic fused silica, J. Non-Cryst. Solids, 203, 69-77, 1996.

[Seward III, 1997] Seward III, Smith C., Borrelli N.F., Allan D.C., Densification of synthetic fused silica under ultraviolet irradiation, J. Non-Cryst. Solids, 222, 407-414, 1997.

[Schenker, 1997] Schenker R.E., Oldham W.G., Ultraviolet-induced densification in fused silica, J. Appl. Phys., 82, 3, 1065-1071, 1997.

[Skuja, 1984] Skuja L.N., Streletsky A.N., Pakovich A.B., A new intrinsic defect in amorphous SiO_2: twofold coodinated silicon, Solid State Commun., 50, 12, 1069-1072, 1984.

[Skuja, 2000] Skuja L., Hosono H., Mizuguchi M., Guttler B., Silin A., Site-selective study of the 1.8 eV luminescence band in glassy GeO_2, J. Luminescence, 87-89, 699-701, 2000.

[Spaargaren, 2000] Spaargaren S.M.R., Syms R.R.A., Characterization of defects in waveguides formed by electron irradiation of silica-on-silicon, J. Lightwave Technol., 18, 4, 555-561, 2000.

[Svalgaard, 1997] Svalgaard M., Direct writing of planar waveguide power splitters and directional couplers using a focused ultraviolet laser beam, Electron. Lett., 33, 20, 1694-1695, 1997.

[Syahriar, 1998] Syahriar A., Syms R.R.A., Tate T.J., Thermooptic interferometric switches fabricated by electron beam irradiation of silica-on-silicon, J. Lightwave Technol., 16, 5, 841-846, 1998.

[Syms, 1994a] Syms R.R.A., Tate T.J., Grant M.F., Reduction of propagation loss in silica-on-silicon channel waveguides formed by electron beam irradiation, Electron. Lett., 30, 18, 1480-1481, 1994.

[Syms, 1994b] Syms R.R.A., Tate T.J., Lewandowski J.J., Near-infrared channel waveguides formed by electron-beam irradiation of silica layers on silicon substrates, J. Lightwave Technol., 12, 12, 2085-2091, 1994.

[Syms, 1995] Syms R.R.A., Tate T.J., Bellerby R., Low-loss near-infrared passive optical waveguide components formed by electron-beam irradiation of silica-on-silicon, J. Lightwave Technol., 13, 8, 1745-1749, 1995.

[Timoshenko, 1970] Timoshenko, S.P., Goodier, J.N., Theory of elasticity, McGraw-Hill, New York, 1970.

[Tsai, 1991] Tsai T.E., Griscom D.L., Dispersive diffusive transport of free excitons in high purity silica, J. Non-Cryst. Solids, 131, 1240-1244, 1991.

[Tugushev, 1998] Tugushev V.V., Golant K.M., Excited oxygen-deficient center in silicon-dioxide as a structurally non-rigid, mixed-valence complex, J. Non-Cryst. Solids, 241, 2-3, 166-173, 1998.

[Van Peski, 2000] Van Peski C.K., Morton R., Bor Z., Behavior of fused silica irradiated by low level 193 nm excimer laser for tens of billions of pulses, J. Non-Cryst. Solids, 265, 3, 285-289, 2000.

[Walrafen, 1981] Walrafen G.E., Krishnan P.N., Raman spectrum of pressure compacted fused silica, J. Chem. Phys., 74, 9, 5328-5330, 1981.

[Wackerle, 1962] Wackerle J., Shock wave compression of quartz, J. Appl. Phys., 33, 3, 922-937, 1962.

[Wefing, 1999] Wefing S., Modeling of continuous random networks: a case study for vitreous GeO_2. I. Model generation, J. Non-Cryst. Solids, 244, 2-3, 89-111, 1999.

[Williams, 1989] Williams, R.T., Optically generated lattice-defects in halide crystals, Opt. Eng., 28, 10, 1024-1033, 1989.

Chapter 6.

[Barbier, 1991] Barbier D., Green M., Madden S.J., Waveguide fabrication for integrated optics by electron beam irradiation of silica, J. Lightwave Technol., 9, 6, 715-720, 1991.

[Gowar, 1983] Gowar J., Optical communication systems, Prentice-Hall Intern. Series in Optoelectronics, London, 1983.

[Kominato, 1990] Kominato T., Ohmori Y., Okazaki H., Yasu M., Very low-loss GeO_2-doped silica waveguides fabricated by flame hydrolysis deposition method, Electron. Lett., 26, 5, 327-328, 1990.

[Madden, 1990] Madden S.J., Green M., Barbier D., Optical channel waveguide fabrication based on electron beam irradiation of silica, Appl. Phys. Lett., 57, 27, 2902-2903, 1990.

[Ruano, 2000] Ruano-López J.M., Optical devices for biosensing, microfabricated in flame hydrolysis deposited glasses, PhD Thesis, University of Glasgow, 2000.

[Ruano, 2003] Ruano J.M., Gligle A., Cleary A., Walmsley A., Aitchison J.A., Cooper J.M., Design and fabrication of a silica on silicon integrated optical biochip as a fluorescence microarray platform, Biosensors and Bioelectronics, 18, 175-184, 2003.

[Syms, 1994a] Syms R.R.A., Tate T.J., Grant M.F., Reduction of propagation loss in silica-on-silicon channel waveguides formed by electron beam irradiation, Electron. Lett., 30, 18, 1480-1481, 1994.

[Syms, 1994b] Syms R.R.A., Tate T.J., Lewandowski J.J., Near-infrared channel waveguides formed by electron-beam irradiation of silica layers on silicon substrates, J. Lightwave Technol., 12, 12, 2085-2091, 1994.

Chapter 7.

[Arnold, 2000] Arnold G.W., Battaglin G., Mattei G., Mazzoldi P., Zandolin S., Implantation-induced structural changes and hydration in silicate glasses, Nucl. Instrum. Meth. B, 166-167, 440-444, 2000.

[Battaglin, 1999] Battaglin G., Arnold G.W., Mattei G., Mazzoldi P., Dran J.C., Structural modifications in ion-implanted silicate glasses, J. Appl. Phys., 85, 12, 8040-8049, 1999.

[Bindner, 2001] Bindner P., Boudrioua A., Loulergue J.C., Moretti P., Formation of planar optical waveguides in potassium titanyl phosphate by double implantation of protons, Appl. Phys. Lett., 79, 16, 2558-2560, 2001.

[Boudrioua, 2001] Boudrioua A., Bakhouya Ch., Loulergue J.C., Moretti P., Polgar K., Low-loss optical planar waveguides in $Li_2B_4O_7$ crystal formed by He^+ implantation, J. Appl. Phys., 89, 12, 7716-7721, 2001.

[Dellin, 1977] Dellin T.A., Tichenor D.A., Barsis E.H., Volume, index of refraction and stress changes in electron irradiated silica, J. Appl. Phys., 48, 3, 1131-1138, 1997.

[García-Blanco, 2003] García-Blanco S., Kellock A.J., Baglin J.E.E., Glidle A., Cooper J.M., Aitchison J.S., Delarue R.M., Fabrication of optical waveguides by 2 MeV Ar^+ of germanium doped flame hydrolysis deposited silica, accepted for publication in Nucl. Instrum. Meth. B, 2003.

[Jeunhomme, 1990] Jeunhomme L.B., Single-mode fiber optics, principles and applications, Optical Enginnering, vol. 23, Marcel Dekker Inc., New York, 1990.

[Johnson, 1998] Johnson C.M., Ridway M.C., Kurver A., Leech P.W., Simpson P.J., Thermal annealing of waveguides formed by ion implantation of silica-on-silicon, Nucl. Instrum. Meth. B, 141, 670-674, 1998.

[Kerbouche, 1999] Kerbouche F., Modifications chimiques et des contraintes mécaniques induited par lirradiation UV des fibres optiques Germanosilicates, PhD Thesis no 6016, Université Paris XI, Orsay, 1999.

[Poumellec, 1996] Poumellec B., Niay P., Douay M., Bayon J.F., The UV-induced refractive index grating in $Ge:SiO_2$ preforms: additional CW experiments and the macroscopic origin of the change in index, J. Phys. D., 29, 7, 1842-1856, 1996.

[Poumellec, 2002] Poumellec B., Niay P., Direct measurement of 248- and 193- nm excimer-induced densification in silica-germania waveguide blanks: comment, J. Opt. Soc. Am. B., 19, 9, 2039-2041, 2002.

[Schenker, 1997] Schenker R., Oldham W.G., Ultraviolet induced densification in fused silica. J. Appl. Phys., 82, 3, 1065-1071, 1997.

[Snoeks, 1994] Snoeks E., Polman A., Volkert C.A., Densification, anisotropic deformation and plastic flow of SiO_2 during MeV heavy ion irradiation, Appl. Phys. Lett., 65, 19, 2487-2489, 1994.

[Snoeks, 1995] Snoeks E., Weber T., Cacciato A., Polman A., MeV irradiation-induced creation and relaxation of mechanical stress in silica, J. Appl. Phys., 78, 7, 4723-4732, 1995.

[Townsend, 1994] Townsend P.D., Chandler P.J., Zhang L., Optical effects of ion implantation, Cambridge Studies in Modern Optics, Cambridge University Press, 1994.

[von Bibra, 1998] von Bibra M.L., Canning J., Robert A., Mode profile modeification of H^+ ion beam irradiated waveguides using UV processing, J. Non-Cryst. Solids, 239, 121-125, 1998.

[von Bibra, 2000] von Bibra M.L., Roberts A., Dods S.D., Ion beam energy attenuation for fabrication of buried, variable-depth, optical waveguides, Nucl. Instrum. Meth. B, 168, 47-52, 2000.

[Wang, 2000] Wang K.M., Lu F., Hu H., Shi B.R., Wang F.X., Xie Z.X., Chen F., Wang W., Refractive index profiles in $LiNbO_3$ waveguide formed by 3.2 MeV He ions, Surface and Coatings Technol., 128-129, 465-469, 2000.

Appendix 1

Calculation of the losses by the Fabry-Perot resonator method

In this appendix, the calculations carried out in order to obtain the expression for the propagation losses of a waveguide using the Fabry-Perot resonator method are detailed. An estimation of the errors introduced by the slight variation of the angle at which the end-facets are polished will also be described.

3.1 Calculation of the transmitted and reflected power from a Fabry-Perot resonator.

Figure A.3.1. shows the fields propagating between the two end-facets of a Fabry-Perot resonator of length L and propagation loss α.

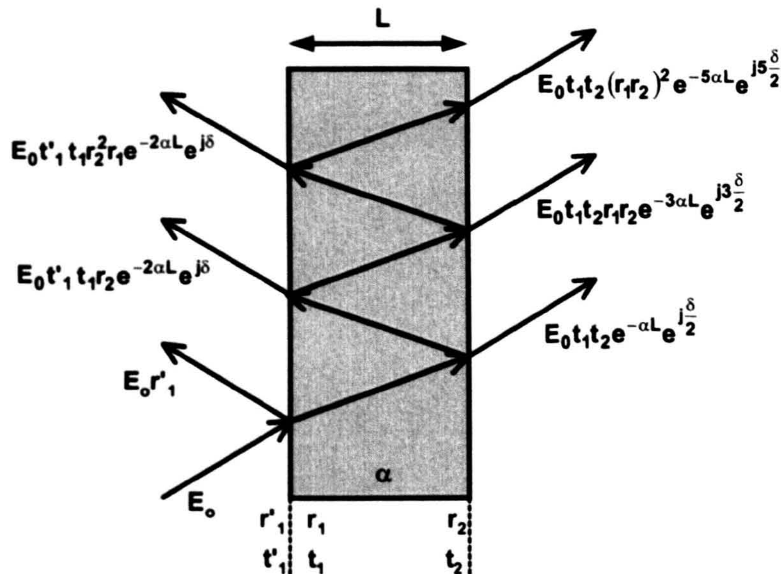

Figure A.3.1. Reflected and transmitted fields from a Fabry-Perot cavity of propagation loss α.

A similar resonator is formed by the end-facets of a channel waveguide: the field propagates along the waveguide and partially reflects at the end-facets. The rest of the light leaves the resonator after one, two, three, etc. round trips. The transmitted (or reflected) fields can be calculated as the sum of all those components.

Thus, the reflected field can be calculated as

$$
\begin{aligned}
E_R &= E_o r_1' + E_o t'_1 t_1 r_2 e^{-2\alpha L} e^{j\delta} + E_o t'_1 t_1 r_2^2 r_1 e^{-4\alpha L} e^{j2\delta} + E_o t'_1 t_1 r_2^3 r_1^2 e^{-6\alpha L} e^{j3\delta} + \ldots\ldots = \\
&= E_o r_1' + E_o t'_1 t_1 r_2 e^{-2\alpha L} e^{j\delta} \cdot \left(1 + r_2 r_1 e^{-2\alpha L} e^{j\delta} + (r_2 r_1)^2 e^{-4\alpha L} e^{j2\delta} + \ldots\ldots\right) = \\
&= E_o r_1' + E_o t'_1 t_1 r_2 e^{-2\alpha L} e^{j\delta} \sum_m \left(r_1 r_2 e^{-2\alpha L} e^{j\delta}\right)^m = -E_o \frac{r_1 - r_2 e^{-2\alpha L} e^{j\delta}}{1 - r_1 r_2 e^{-2\alpha L} e^{j\delta}}
\end{aligned}
\tag{A.3.1}
$$

where we have used $r_1 = -r'_1$, $t_1 = t'_1$ and $r_1^2 + t_1^2 = 1$. The transmitted field can be calculated in the same way as:

$$
\begin{aligned}
E_t &= E_o t_1 t_2 e^{-\alpha L} e^{j\frac{\delta}{2}} + E_o t_1 t_2 r_1 r_2 e^{-3\alpha L} e^{j3\frac{\delta}{2}} + E_o t_1 t_2 (r_1 r_2)^2 e^{-5\alpha L} e^{j5\frac{\delta}{2}} + \ldots\ldots = \\
&= E_o t_1 t_2 e^{-\alpha L} e^{j\frac{\delta}{2}} \cdot \left(1 + r_1 r_2 e^{-2\alpha L} e^{j\delta} + (r_1 r_2)^2 e^{-4\alpha L} e^{j2\delta} + \ldots\ldots\right) = \\
&= E_o t_1 t_2 e^{-\alpha L} e^{j\frac{\delta}{2}} \sum_m \left(r_1 r_2 e^{-2\alpha L} e^{j\delta}\right)^m = E_o \frac{t_1 t_2 e^{-\alpha L} e^{j\frac{\delta}{2}}}{1 - r_1 r_2 e^{-2\alpha L} e^{j\delta}}
\end{aligned}
\tag{A.3.2}
$$

From the expressions for the fields, the transmitted and reflected powers can be calculated as:

$$
\begin{aligned}
P_R &= E_R \cdot E_R^* = E_o^2 \frac{r_1^2 - 2 r_1 r_2 e^{-2\alpha L} \cos\delta + r_2^2 e^{-4\alpha L}}{1 - 2 r_1 r_2 e^{-2\alpha L} \cos\delta + (r_1 r_2)^2 e^{-4\alpha L}} \\
P_T &= E_T \cdot E_T^* = E_o^2 \frac{(t_1 t_2)^2 e^{-2\alpha L}}{1 - 2 r_1 r_2 e^{-2\alpha L} \cos\delta + (r_1 r_2)^2 e^{-4\alpha L}}
\end{aligned}
\tag{A.3.3}
$$

The transmitted power presents a maximum when $\cos\delta = 1$ and a minimum when $\cos\delta = -1$. For those points, the reflected power presents a minimum and a maximum respectively. Therefore,

$$P_{R\min} = E_o^2 \frac{r_1^2 - 2r_1r_2e^{-2\alpha L} + r_2^2e^{-4\alpha L}}{1 - 2r_1r_2e^{-2\alpha L} + (r_1r_2)^2 e^{-4\alpha L}}$$

$$P_{R\max} = E_o^2 \frac{r_1^2 + 2r_1r_2e^{-2\alpha L} + r_2^2e^{-4\alpha L}}{1 + 2r_1r_2e^{-2\alpha L} + (r_1r_2)^2 e^{-4\alpha L}}$$

$$P_{T\min} = E_o^2 \frac{(t_1t_2)^2 e^{-2\alpha L}}{1 + 2r_1r_2e^{-2\alpha L} + (r_1r_2)^2 e^{-4\alpha L}} \qquad \text{(A.3.4)}$$

$$P_{T\max} = E_o^2 \frac{(t_1t_2)^2 e^{-2\alpha L}}{1 - 2r_1r_2e^{-2\alpha L} + (r_1r_2)^2 e^{-4\alpha L}}$$

Doing

$$G = \frac{P_{R\min} \cdot P_{T\min}}{P_{R\max} \cdot P_{T\max}} = \frac{r_1^2 + r_2^2e^{-4\alpha L} - 2r_1r_2e^{-2\alpha L}}{r_1^2 + r_2^2e^{-4\alpha L} + 2r_1r_2e^{-2\alpha L}} = \frac{\left(r_1 - r_2e^{-2\alpha L}\right)^2}{\left(r_1 + r_2e^{-2\alpha L}\right)^2} \qquad \text{(A.3.5)}$$

Therefore, the propagation losses can be calculated as

$$\alpha = \frac{-1}{2L} \ln\left(\frac{r_1}{r_2} \frac{1-\sqrt{G}}{1+\sqrt{G}}\right) \qquad \text{(A.3.6)}$$

For this measurement, the end-facets are polished so that they are at 90 degrees with respect to the surface and at 90 degrees with respect to the propagation direction of the light in the waveguide. In that case, $r_1=r_2$, thus eliminating the reflectivity at the end-facets from the formula for the calculation of the losses, resulting in

$$\alpha = \frac{-1}{2L} \ln\left(\frac{1-\sqrt{G}}{1+\sqrt{G}}\right) \qquad \text{(A.3.7)}$$

which is the expression used in Chapter 3 Section 3.5 (Equation 3.41).

3.2 Estimation of the errors due to bad polishing of the end-facets.

In order for Equation A.3.7 to give a correct estimation of the propagation losses of a monomode channel waveguide, the two reflectivities of the end-facets must be equal. For that, extreme care needs to be taken to polish them so that they form

90 degrees with the surface and the propagation direction. If there is a slight deviation of the end-facet angle, the reflectivities will change and therefore the value of the propagation loss calculated with this method by using Equation A.3.7 will have some error. Furthermore, an angular deviation in the end-facets can degrade the functioning of the Fabry-Perot resonator, reducing the fringe visibility.

In this work, the end-facets could be polished with an accuracy better than one degree from orthogonality. Therefore, an error of 1 degree will be considered in order to calculate the maximum error that the misalignment of the angle is likely to introduce into the measurement of the losses, due to the change in the end-facet reflectivities and due to a mismatch between the angle of propagation of the incident light in the waveguide and the angle of the reflected light in the waveguide.

On the other hand, the losses introduced due to the mismatch between the reflected light and the waveguide mode must be considered. Using the effective index approximation and representing the reflected mode by an equivalent mode in an ongoing waveguide forming an angle twice the angle between the normal to the end-facet and the propagation direction, the misalignement between the incident and reflected propagation modes can be accounted for by adding an additional phase factor,

$$e^{j2\Delta\theta\beta x} \tag{A.3.8}$$

as described in [Sidorin, 2001], [Marcuse, 1989]. The efficiency of the propagation of the mode through the angled waveguide junction is given by the overlap integral

$$\tau = \frac{\beta}{2\omega\mu_o P_o}\int_{-\infty}^{+\infty}|E|^2 e^{j2\Delta\theta\beta x}dx \tag{A.3.9}$$

where E is the fundamental TE mode, P_o is the power transmitted in the mode, ω is the light angular frequency and μ_0 is the magnetic permeability of vacuum [Marcuse, 1989]. Approximating the TE mode distribution by a Gaussian profile with waist width w, gives $E = A\,exp(-x/w)^2$, the reflectance (power) in the tilted interface can be calculated from

$$R_{\Delta\theta} = R_F(\Delta\theta)\,exp\left(-\left(\frac{2\pi n_{clad} w\Delta\theta}{\lambda}\right)^2\right) \tag{A.3.10}$$

where n_{clad} is the effective refractive index of the cladding region in the effective index approximation [Marcuse, 1989].

Marcuse et. al. [Marcuse, 89] approximated the waist parameter of the gaussian beam as a function of the V parameter of the waveguide ($V = (2\pi\ d/\lambda)\sqrt{(n_1^2 - n_2^2)}$ where d is the thickness of the waveguide and n_1 and n_2 are the effective refractive indices of core and cladding slabs, respectively, as

$$\frac{w}{d} \approx 9.2063 \cdot 10^{-3} + \frac{1.7265}{\sqrt{V}} + \frac{0.38399}{V^3} - \frac{9.1691 \cdot 10^{-3}}{V^5} \qquad \text{(A.3.11)}$$

The reflectivity at the end-facets can be calculated by the Fresnel equations [Hecht, 87]. For TE-polarized light,

$$r_F = \frac{n_1 \cos\theta_i - n_2 \cos\theta_t}{n_1 \cos\theta_i + n_2 \cos\theta_t} \qquad \text{(A.3.12)}$$

where θ_i is the angle of incidence of the wave propagating into the waveguide and the perpendicular to the end-facet and θ_t is the angle formed by the transmitted light with the normal to the end-facet. As discussed above, $\theta_i = \Delta\theta$ and θ_t can be calculated by applying the Snell's law, resulting in

$$r_F = \frac{n_1 \cos\Delta\theta - \sqrt{n_2^2 - (n_1 \sin\Delta\theta)^2}}{n_1 \cos\Delta\theta + \sqrt{n_2^2 - (n_1 \sin\Delta\theta)^2}} \qquad \text{(A.3.13)}$$

The factor r_1/r_2 from Equation A.3.6 can be written as

$$\frac{r_1}{r_2} = \frac{r_{1F}}{r_{2F}} \cdot \frac{\sqrt{exp\left(-\left(\frac{2\pi n_1 w \Delta\theta_1}{\lambda}\right)^2\right)}}{\sqrt{exp\left(-\left(\frac{2\pi n_2 w \Delta\theta_2}{\lambda}\right)^2\right)}} \qquad \text{(A.3.14)}$$

where $\Delta\theta_1$ and $\Delta\theta_2$ are the angle of the input and output end-facets of the waveguide and r_{1F} and r_{2F} are the Fresnel reflectivities (field) for each of the end-facets.

Therefore, considering $r_1/r_2 = 1$ introduces some error in the measurement. The calculation below gives a typical magnitude for this error.

As an example, consideration is given to a typical waveguide 2 μm thick with core refractive index 1.474 (at a wavelength of 1.55 μm) surrounded by material with refractive index 1.469 and on top of a layer of thermal oxide of refractive index 1.4442. The refractive index of the cladding is 1 (i.e. air). The effective refractive index for the core layer can be calculated as 1.4699 (n_1 in the previous equations). The refractive index of the cladding layer, n_2, is 1.

From Equation A.3.14, it can be seen that if the magnitudes of $\Delta\theta_1$ and $\Delta\theta_2$ are the same, $r_1/r_2 = 1$. Therefore, the worse case will be when the difference in the magnitudes of $\Delta\theta_1$ and $\Delta\theta_2$ is maximum, i.e. $\Delta\theta_1$=1 deg and $\Delta\theta_2$=0 deg. In that case, Equation A.3.14 yields

$$\frac{r_1(\Delta\theta = 1\,deg)}{r_2(\Delta\theta = 0\,deg)} = 0.99207 \qquad \text{(A.3.15)}$$

Thus, the error introduced in r_1/r_2 by considering it to be unity will be $\sigma_{r1/r2}$=0.0078. This error will produce an error in the calculation of the losses as small as $\sigma_\alpha = \pm\, 3.96\cdot 10^{-3}/L = \pm\, 0.39/L$ %, where L is the length of the waveguide measured in cm.

Therefore, with the precision of the polishing of the samples that could be achieved in this work, no significant error is likely to be introduced by a modified reflectivity at the end-facets.

3.3 References.

[Hecht, 87] Hecht E., Optics, Addison-Wesley Ed., Second Ed., 1987.

[Marcuse, 1989] Marcuse D., Reflection loss of laser mode from tilted end mirror, J. Lightwave Technol., 7, 2, 1989, 336-339.

[Sidorin, 2001] Sidorin Y., On the accuracy of the measurement of propagation loss in channel waveguides using the Fabry-Perot resonance method, Opt. Commun., 194, 325-330, 2001.

Appendix 2

Material stack descriptors used in Sceleton

In the present case, the material stack used for the simulations is as follows. The stack file begins by a description of the stack in which the name of the stack, constituted by a succession of names of the different layers, and the number of layers are specified. Next, the description of each of the layers that constitute the stack is performed, indicating the material and the thickness of the different layers. An extract of a stack file is shown as follows.

```
# rem: stack description starts with topmost material...
#-----------------------------------------------------------

StackDescriptor: NiCr/FHDGedoped/SiO2/Si
NumberOfLayers:        4

#-----------------------------------------------------------
MaterialDescriptor:     NiCr
Thickness/nm:           30
LayFlag:                3

#-----------------------------------------------------------


MaterialDescriptor:    FHDGedoped
Thickness/nm:          4000
LayFlag:        2

#-----------------------------------------------------------

MaterialDescriptor:     SiO2
Thickness/nm:           14000
LayFlag:                1

#-----------------------------------------------------------

MaterialDescriptor:     Si
Thickness/nm:           300000
LayFlag:                0

#-----------------------------------------------------------
```

The materials used in the stack are described in another file, in which the name ('desc'), number of components ('nComp'), density ('rho') and the different elements ('Z') followed by their content ('c') are indicated. An example can be seen as follows for a FHD silica sample 2 % at. germanium concentration.

```
#-------------------------------------------------
desc        SiO2
nComp             2
rho         2.2
ioEn        0.0
Z[0]        Si
c[0]        1
Z[1]        O
c[1]        2
#-------------------------------------------------
desc             FHDGedoped
nComp            3
rho              2.5
ioEn             0.0
Z[0]             Si
c[0]             31
Z[1]             Ge
c[1]             2
Z[2]             O
c[2]             66
#-------------------------------------------------
desc             NiCr
nComp            2
rho              8.047
ioEn             0.0
Z[0]             Cr
c[0]             1
Z[1]             Ni
c[1]             1
#-------------------------------------------------
```